X-ray Telescopes: Development, Flight and Analysis

PhD Dissertation
by
Kristin Kruse Madsen

Advisors: Kristian Pedersen, DARK, NBI, KU
Finn E. Christensen, DNSC
Jens Hjorth, DARK, NBI, KU

The Niels Bohr Institute, Faculty of Science, University of Copenhagen
2007

Abstract

This thesis is divided into three parts as themes of the same general subject: the X-ray focusing telescopes.

On the 18'th of May 2005 the balloon borne High Energy Focusing Telescope, HEFT, was launched on its maiden voyage from Fort Sumner, New Mexico. For 24 hours the gondola remained afloat proving that it could successfully track and detect the galactic X-ray sources, Cygnus X-1 and the Crab, before plunging to a hard and brutal landing in the desert. In this thesis I describe the HEFT gondola platform, designed and build by LLNL to hold the HEFT payload, and discuss the sensor groups available for pointing, their performance and accuracy. I also outline the pointing strategy we adopted, and describe how the sensors worked in concert to achieve the required pointing stability. Based on the gondola configuration I present the aspect reconstruction procedures and use them to show a first data analysis of the HEFT flight observations of the Crab and Cygnus X-1.

In the second part of my thesis I present a method of simulating concept study designs of grazing incidence focusing X-ray telescopes used on the X-ray Evolving Universe Spectroscopy Mission, XEUS. Past and current X-ray missions have used single films of gold, platinum or iridium coatings, utilizing the critical angle to achieve high grazing incidence reflection. These coatings are, however, not efficient at energies above 20 keV. A method of pushing up the energy is by employing multilayers, or supermirrors, which is a stack of films of alternating low and high density material. Using a Figure of Merit code I step through a limited parameter space and find the optimal multilayer recipe that yields the best reflectivity for a given telescope design. This tool can be used to study the effects of different design parameters such as material selection and substrate thickness.

In the third part I analyze data of the QSO B1152+199 taken with the *Chandra* x-ray observatory. I present evidence of variability in the lightcurve of the lens, which is accompanied by movement in the Fe Kα line emitting region. A sudden redshift or broadening of the iron line is an indication of

strong gravitational effects. These effects are commonly seen in conjunction with a brightening or hardening of the source, as part of the accretion disc momentarily lights up, and can be used to constrain the parameters of the central black hole. I show there is a correlation between the lightcurve and movement of the iron line, and fit the spectrum with relativistic line model **kyrline** from **xspec**.

Preface

This thesis is submitted in partial fultillment of the PhD degree at the Niels Bohr Institute in Denmark. The thesis concludes three years of work, of which one year was spend at California's Institute of Technology under the supervision of Fiona A. Harrison, and two at the Dark Cosmology Center in Copenhagen, DARK, funded by the Danish National Space Center and the Instrument centre for Danish Astrophysics, iDA. The PhD project was carried out under the supervision of Kristian Pedersen at the DARK, and Finn E. Christensen from the Danish Space Research Center.

The main theme of this thesis concerns X-ray telescopes: Flight, Development and Analysis.

The 'flight' part concerns the practical work I did on the High Energy Focusing Telescope, HEFT, and the three Chapters dedicated to this mission are written as much to document its flight, as to provide a manual on how to operate it. Chapter 1 describes the gondola platform hardware and its operation. Chapter 2 describes the aspect reconstruction of the flight attitude. Chapter 3 uses the tools of Chapter 2 to show the aspect reconstruction of the flight, and the creation of images and spectra from the detected sources: Cygnus X-1 and the Crab.

The 'development' work I did on a concept study of the ESA XEUS mission, and Chapter 4 shows simulations of 4 high energy extension to the main XEUS optic.

The 'analysis' work was done on *Chandra* data of the lensed QSO B1152+199, and Chapter 5 presents evidence for variable iron Kα behavior in this QSO.

Acknowledgement

Building and flying a balloon instruments is damn hard work, and without some solid team work, we would never have achieved what we did in the time given to us. Blood, sweat and tears went into making this beast flight ready, not to mention a great deal of swearing, the occasional frozen margarita, and the cheese smothered chicken diet we all were committed to for many months, that only came in flavours of red and green.

Therefore, I would firstly like to thank my advisors for sending me out on an adventure. I would also like to thank Fiona Harrison and William Craig for trusting me with their precious instrument, and giving me the chance to fly and wreck it for them. A very special thanks also goes to Kurt Gunderson without whom I would never have deciphered the mystery known as the HEFTflight code, and to William Craig for making the HEFT code such an amusing read. I would like to thank Todd and Randy for ingenious solutions to mindboggling problems, Jim Chonko for bringing Gatorade and driving me around, Hubert Chen for remembering what I had forgotten, Matvey Farber for taking me places I should never have gone, Wayne Baumgartner for making tea, and Jill Burnham for making sure I lost my mind.

I am also grateful to my cats for warming my legs when the nights got long, and my family for knowing when to stay away.

Given the chance I would do it all again (but without the cheese please).

Contents

Chapter 1

The HEFT Payload

1.1 Introduction

On the 18'th of May 2005 the balloon borne High Energy Focusing Telescope, HEFT,launched on its maiden voyage from Fort Sumner, New Mexico. For 24 hours the gondola remained afloat proving that it could succesfully track and detect the galactic X-ray sources, Cygnus X-1 and the Crab, before plunging to a hard and brutal landing in the desert. Years of hard work preceeded this flight, developing ground breaking and competative detectors and optics, in a collaboration between the Danish National Space Center, Columbia University, Californias Institute of Technoloty and Lawrence Livermore National Laboratories. The 3 conical approximation grazing incidence optics, designed and coated with W/Si multilayers at DNSC, build at Columbia, are capable of focusing energies up to 70 keV at a spartial resoltion of $\sim$ 90". The detectors are room temperature low consumption CdZnTe hydrid pixel detectors, bonded to a custom build Application Specific Integrated Circuit (ASIC), designed and build at Caltech, and have an energy resolution of $\Delta E/E \sim 1\%$. With these kind of resolutions the requiremnts for the attitute control system of the gondola, that carried the payload, were demanding, and achieving positional stabilty better than 1 arcminute on a balloon platform was no trivial feat.

In this Chapter I will describe the gondola platform that was designed and build by LLNL to hold the HEFT payload and discuss the sensor groups available for pointing, their performance and accuracy. I will then outline the pointing strategy we adopted, and describe how the sensors worked in concert to achieve the required pointing stability. Finally I will review the science payload, optics and detectors, in more detail and document the

Figure 1.1: Left: side view. Right: front view. Numbers on the images are explained in the text.

preflight alignment of the system performed shortly before flight.

1.2 Payload overview

Figure 1.1 shows an image of the fully integrated HEFT payload shortly before its launch on May the 18th 2005. The hight of the gondola was 5 m and the length of the telescope structure 6 m - excluding the detector pressure vessel - which is the focal length of the optics. Its total weight came up to around 2.5 tonnes.

The curious looking HEFT gondola frame is designed to be resistant to thermal deformations caused by the large temperature gradient introduced by sun and shadow sides when the payload is at float altitude. The open structure also serves to reduce wind resistance, and to absorb the shocks experienced at the moment of parachute deployment and during ground impact.

Using the numbering of Figure 1.1 the main components of the payload are:

1. The science detector pressure vessel. Two Kevlar/Carbon domes were clamped together around a isothermal midflange supporting the detectors and hardware. Fans and heaters were used to regulate the temperature, which was held at -15 degrees during flight. It was pressurized to 1 psi with dry Ni^2.

2. The three HEFT optics were co-aligned and mounted in a triangular pattern to match the detector setup.

3. The pressurized Flight Computer housing vessel.

4. At the top of the gondola a massive H bar frame provided vital support and stability for the gondola. Suspended under it was the large azimuthal reaction wheel, and on top a motor which continually desaturated the torsion caused by the slow rotation of the balloon. Extended from the corners of the frame were the differential GPS antennas with back shields.

5. The elevation drive.

6. The cross coupling reaction wheel preventing pendulation.

7. The star trackers. One was on-axis while the other pointed off-axis by 30 deg. This separation is the angular extend of the balloon, so that a piece of sky was always visible to the trackers.

Not visible on Figure 1.1 are the sensors: two-axis gyroscope attached to the gondola frame, two-axis gyroscope attached to the telescope frame, and two magnetometers mounted on opposite sides of the gondola frame. Also a 105 radio provided the communication between ground control and the two onboard flight science and gondola control computers.

1.2.1 A few gondola definitions

The base of the gondola is called the platform and its average roll should be equal to 0. The moving frame mounted on a pivot - and holding the optics, detectors and star trackers - is called the telescope strut. When the gondola is in the configuration shown on Figure 1.1, up to the point where the telescope strut is pointing at zenith, then gondola is in un-flipped configuration. The telescope strut can move through zenith to the other side such that, going by the Figure, the detector end is underneath the gondola to the right and the optics are to the left. This configuration is called flipped.

1.3 Sensors

We employed five groups of sensor to provide the aspect. Alone none of the sensors could deliver the accuracy needed to stabilize the gondola at 1 arcmin in azimuth and 30 arcsec in elevation, but together they got the job done.

Sensor	AZ	EL	ROLL	MOUNT LOCATION	TYPE
Gyro 1		×		Telescope strut	relative
Gyro 2	×		×	Platform	relative
Encoder: Gurley A25S		×		Telescope strut	absolute
GPS	×	×[a]	×	Platform	absolute
Magnetometer	×	×[a]	×	Platform	relative
Star Tracker 1 and 2	×	×	×	Telescope strut	absolute
Accelerometer		×		Telescope strut	relative

Table 1.1: Overview of sensors, their position and type of detection. [a] This pitch is the platform pitch and not the elevation pitch.

In order of increasing accuracy we had: a differential GPS, magnetometers, star trackers, elevation encoders and two-axis gyroscopes. Additionally we flew an accelerometer, but it was not used in the pointing loop and only served as an absolute reference to cross check with the other sensors and back-up in case of encoder failure.

We distinguish between two types of sensors: absolute sensors which return a sky coordinate such as the differential GPS, the star trackers and encoders, and relative sensors which detect movement perturbations like the magnetometers, gyros and accelerometer. The Table 1.1 summarizes the locations and type of the sensors.

The relative sensors detect small movement perturbations well, but easily risk loosing track of the sky if the gondola moves much faster than 3 deg a second. In comparison the differential GPS is quite coarse, but does not risk getting lost. The star trackers are very accurate, but because of a limited field of view and their slow solution update, the star trackers can only be used once the gondola has obtained a rough stabilization and has a position estimate better than 4-5 deg. Any error larger than this causes the solution extraction of the trackers to take inconveniently long.

1.3.1 GPS

HEFT flew a military grade TANS Vector, Trimble Advanced Navigation Sensor[1]. It is a four antenna, six channel, global positioning system that can provide 3-dimensional attitude: azimuth, pitch and roll. The antennas were mounted on the top of the 'H' shaped frame, see Figure 1.1, with an approximate baseline of about 2 m. With this sort of baseline the positional accuracy in azimuth is 0.15 deg (RMS), and 0.25 deg (RMS) for Pitch/Roll. The position accuracy horizontally is 25-100 m and vertically 35-150 m. When the differential mode is enabled the accuracy is improved

to horizontally 5 m and vertically 8 m, for 95% of the time[1].

The GPS primary task was to provide the absolute azimuthal reference as well as longitude and latitude for the conversion between equatorial and horizontal coordinates. The GPS coordinate system is in a North East Up setting and returns euler angler such that azimuth is referenced to N, the roll goes from 180° to -180° and pitch from 90° to -90°. The roll and pitch information was not used during flight as it is too coarse and risks kicking up pendulations, but it was in post-flight reconstruction used to back up the gyro roll and pitch information.

1.3.2 Star Trackers

The design of the HEFT star cameras was based on the design used by the High Energy Replicated Optics (HERO) experiment developed at the Marshall Space Flight Center [2]. HEFT flew two star trackers: one mounted on-axis and the second mounted off-axis at an elevation separation of $\sim 30^\circ$ to ensure that a piece of sky was visible at all times no matter at what elevation we were pointing.

Each star camera consisted of a 2.86 meter stray light baffle and a pressure vessel containing a digital camera, lens and PC/104 stack computer. The on-axis star tracker used a PMI-1401 digital camera, manufactured by Qimaging, built around the Kodak 1401 CCD consisting of 6.8-m-square pixels in a 1320×1035 array. The off-axis star trackers used a more recent Retiga-EXi camera which contained a Sony ICX285 progressive-scan interline monochrome CCD with 6.45-m-square pixels in a 1392×1040 array. Both digital cameras were fitted with 180 mm Nikon IF ED lenses that gave a diffraction limited spot size slightly smaller than the pixel size over the CCD wavelength response. The lens focal length and CCD pixel size yielded an approximate pixel sky projection of 2.86×2.24 degrees and 2.86×2.14 degrees for the on-axis and off-axis cameras, respectively. Both cameras were fitted with a B+W 090 filter, which transmits above 600 nm, to improve sensitivity. This filter was optimized to provide the greatest number of stars detected by reducing the background counts by a factor of $\sim$5, while only reducing the source counts by a factor of $\sim$2. More details on the star tracker software can be found in J. Chonko 2006 [3].

The angular separation between the two trackers was measured prior to flight in two configurations, flipped and unflipped. The offsets were measured to be az $= 0.12^\circ \pm 0.005$ and el $= 29.39^\circ \pm 0.005$ when the on-axis tracker was pointed at the horizon.

The two star trackers were the primary absolutely referenced sensors

used to correct the gyros and stabilize the gondola on target. The typical average matching speed for both cameras was ~ 3 seconds. For the off-axis tracker it was slightly faster, since Retiga had a better QE, and for the on-axis slightly slower due to a worse QE and a bright corner, interfering with the matching.

The star trackers could not act alone and required at the very least a GPS to provide a longitude, latitude and time, as well as a sky coordinate which had to be good to about $\pm 4°$.

1.3.3 Magnetometers

HEFT flew two three-axis magnetometers mounted on the side of the frame close to the telescope pivot point. This was far from an ideal position, but we did not have the time to properly mount them on non-conducting material. However, because the magnetometers are relative sensors, and their magnetic to angle conversion is roughly proportional for small angles, their small angle movement is very accurate, and they were used during flight with great success to correct the gyro bias, although their large scale calibration was absolutely rubbish, and highly influenced by the position of the telescope strut.

The magnetometers were not used in the post-flight aspect reconstruction.

1.3.4 Gyros

The gyros were the most important and critical sensor on the gondola and provided the means of stabilizing the platform. The Litton G-2000 two axis gyro is of the 'strap down' type, and instead of measuring the inertial motion, like a classical gimbal mounted gyro, it detects the angular velocity around the gondola's body axis. HEFT flew two of these gyros:

- Gyro1 was mounted on the telescope strut and had one of its axis aligned with the gondola's pitch axis defined by $azimuth \times roll = pitch$, and the other axis in the azimuth-roll plane.

- Gyro2 was mounted onto the platform. It had one of its axis aligned with the platform's azimuthal body axis and the other with the roll axis perpendicular to it.

Since the gyros are of the 'strap down' type they were reference relatively and subject to two types of offsets. One is geometrically dependent and

concerns the mounting of the gyro and proper alignment with the axis. The other is a bias offset, which unfortunately is highly temperature dependent. This meant that during flight we had to continually re-evaluate this bias offset by cross checking with other sensors. In this way the gyros were sampled at a rate of 100 Hz, leaky averaged at 10 Hz, and at the 10 Hz rate the bias was corrected under the assumption that the rate of change registered by the magnetometers should be equal to the gyro.

The gyros are the main controllers of the gondola servos.

1.4 Modes of Operation and Pointing Strategy

The gondola had three main modes of operation: holding, tracking and slewing. When holding it would attempt to remain stationary on the horizontal coordinates (azimuth and elevation), while tracking it would keep the equatorial coordinates (ascension and declination) stationary. When slewing the gondola was moving from one coordinate position to another at a speed of 3 deg a second.

Each mode of operation had connected to it a specific combination of sensors to ensure the best performance and stability of the gondola, such that, for example, during slews some sensors were protected against cross-couplings kicked up by the rapid movement of the gondola.

1.4.1 Slewing

In a slew the gondola's only purpose was moving from one coordinate set to another, and to do so with the least amount of sensor drift. During a slew the gondola ignored the relative sensors - magnetometers and gyros - since these were in danger of drifting for larger slews due to saturation, and in the case of the magnetometers an interfering magnetic field from the surrounding iron. In a slew the elevation of the gondola was controlled by the encoders, while in azimuth it was controlled by the GPS, and in case of no GPS, fall back on the magnetometers.

During a slew both the elevation and azimuthal servos were moving at the same time at a speed of 3 degrees/second, until reaching the capture zone of $\pm 3^{\circ}$ around the destination coordinates, where the normal PID motor stabilization loop took back over and halted the slew.

1.4.2 Tracking/Holding

The tracking and holding modes of operation were very similar and only differed in the type of target coordinates. For tracking a constant Ra/Dec was used, while for holding a constant Az/El was provided.

The tracking/holding mode consisted of three phases. The first phase is the period in which the gondola settles down and the oscillatory motions kicked up by the move/braking of the gondola is dampened. This takes around 30 seconds. Following this phase is one in which the sensor that may have drifted are driven back to convergence with the absolute sensor. This may take up to several minutes and even longer if there are problems with the trackers and the gps, but is usually fast once the trackers kick in. Once convergence has been achieved the main phase is quite undisturbed tracking of stars. If periods of less than ideal tracking was encountered, the gondola would fall back into convergence mode.

During this mode of operation control of the motors was passed dynamically between sensors, as shown in the flowchart in Figure 1.2 for the azimuth. These loops were repeated at 10 hz and following the azimuthal flowchart:

1. Sensors were being read by parallel running threads.

2. If there was a tracker solution then both magnetometers and the gyro were corrected by the tracker.

3. If the trackers had been silent for too long (more than a minute) and there were good gps solutions available, the magnetometers and gyro were corrected by the gps.

4. If both trackers and the gps have been silent for 800 cycle periods (running at 10 hz) then the the gyro was being corrected by the magnetometers.

For the elevation the situation was more simple. We had two encoders and since their reliability was very high, we only used them as correcting sensors. As a precaution we did have the accelerometer included as a back up in case both encoders failed.

All applied corrections were leaky averages and the gyro biases were continually being corrected by the magnetometers regardless of available tracker or gps solutions. A similar scheme was followed by the elevation. More detailed flowcharts of the gondola code and transcripts from the gyro code can be found in the Appendix D.

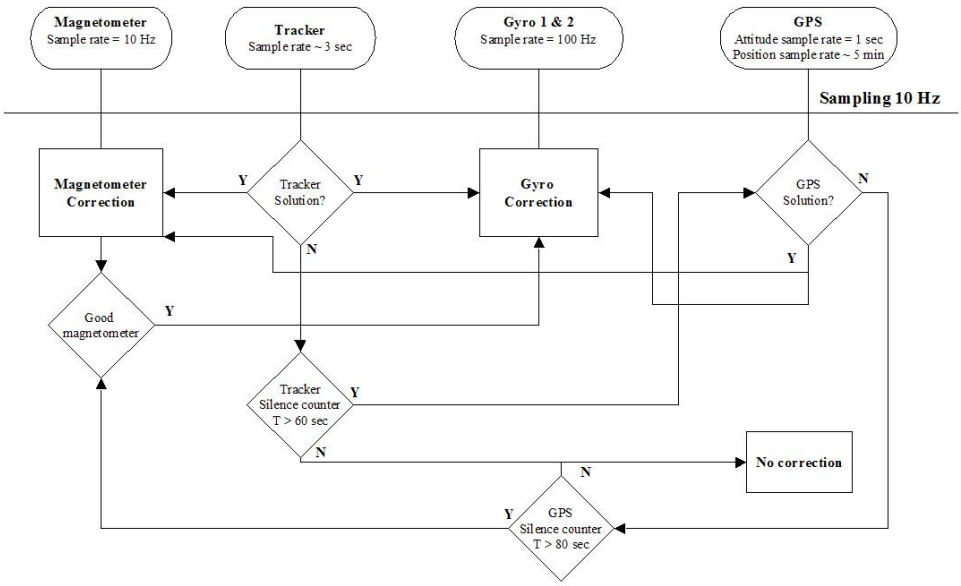

Figure 1.2: Flow diagram describing the azimuthal correction sequence. Magnetormeters and gyros are read at 100 Hz, but only evaluated with leaky averages at 10 Hz, while trackers and gps data are stored upon arrival, then tagged when the value has been used for correction. Old values are not used for corrections. The trackers hold priority over the other sensors, and the code first checks for a tracker solution before falling back on the other sensors. If there are no new values, or good ones, then no correction is performed.

1.4.3 Pointing Strategy

Convergence of the sensor is a vital pre-requisite for successful tracking. Before going to a target we therefore ensured that the sensors were well converged. If there was a bright star in the field of the target that further helped, but if not, as in the case of the crab field, it was necessary to first find a nearby bright rich field on which to zero in the sensors. Only once this had been achieved would we move to the target. If for some reason the sensors during target tracking would not zero or start drifting, going back to a nearby bright rich field became necessary.

Figure 1.3 shows a 40 degree azimuthal slew with a 1.5 degree elevation slew followed by another 1 degree elevation slew. The time axis is in minutes and the displayed sensors are the inflight values, which means they were being continually corrected by the control loop. The black solid line is the inflight calculated azimuth and elevation and the purple stars are the solutions from the on-axis tracker, which for easier viewing have only been plotted on the left side. The right panel shows the values of the various sensors more in detail. For the azimuth the green and blue curves are magnetometer 1 and 2 respectively, and the red curve the GPS azimuth. In the elevation plot the red curve represents the encoder values.

As the slew begins all azimuthal sensors except for the gyro and gps are being ignored. The gyro keeps track of the gondola movement guided by the gps shown here with a 1 degree offset. The capture PID motor control loop kicks in at $\pm 3^\circ$ of the destination coordinate and slows down the movement. There is only a slight oscillation in the azimuth which quickly dies out within 15-20 second. The oscillation is somewhat longer, on the order of 30 seconds, for the elevation because the motor is not quite as powerful as the azimuthal flywheel. Both magnetometers drift during the slew, and as soon as the star tracker kicks in again the two sensors are pulled back in. The second elevation change causes the magnetometers to drift again, since the telescope position unfortunately influenced the magnetometers. Once again as soon as the trackers kick back in the sensors are pulled back in place. All in all smooth tracking can be achieved within 1 minute if the trackers can obtain solutions from the sky.

Difficulties occur when the GPS is not available during longer (less than 10 degrees) slews, or the star field within the tracker's field of view is poor. In the former case, as happened when the GPS was jammed by White Sands, star hopping was done instead. If the slew is less than 10 degrees the magnetometer drift is not so severe that the positional error is less than 2-3 degrees upon arrival at the new coordinate, in which case the star trackers

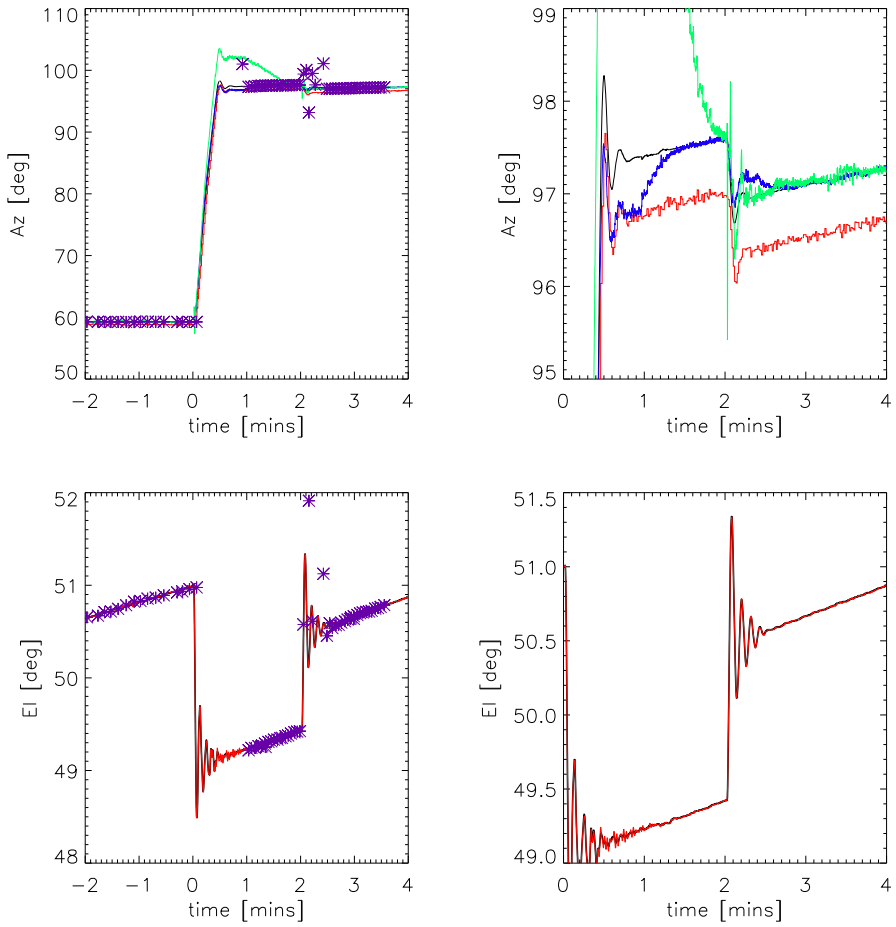

Figure 1.3: Top plots: Azimuthal. Solid black line: in-flight calculated azimuth. Green: magnetometer 1. Blue: magnetometer 2. Red: gps azimuth. Purple stars: star tracker 1 solutions. Bottom plots: Elevation. Solid black line: in-flight calculated elevation. Red: averaged encoder elevation.

should be able to find the field. In this manner one can change position by going from one bright star to another and spending a few minutes on each location to stabilize the sensors. If the star field is poor, then one can zero the sensors on a nearby rich field as needed.

1.4.4 Stability

Because of in-flight corrections, the actual stability on a source could only be evaluated after flight. The next Chapter describes the post-flight pointing reconstruction, but for completeness I will represent the estimated overall stability of on-source tracking here.

Good tracking comes down to the accuracy of the sensors, but also the ability to control the bias drifts of the gyros. Converged sensors keep the gondola on target, but the gondola servos are controlled by the gyros, and even if all sensors are well converged at the start of the tracking, a drift on the gyros will cause the gondola to drift off the target. If the sensor update (tracker rate) and hence the correction of the gyro is fast enough, then the drift can be prevented. However, if the bias is changing faster than it can be corrected, or the drift is larger than the correction speed, the situation can arise where the gondola is "hanging" off target at a distance when the correction speed just cancels the drift.

For the most part we were able to combat this drift and Figure 1.4 shows the rms curves of three Crab observations to be discussed later. These observations were taken at different times during the flight, and in the unflipped orientation, such that we were using the on-axis star tracker. The black curve is the RMS azimuth and the red curve the RMS elevation taken over a running time window of 10 seconds. If disregarding the peaks, which come from the arrival of incorrect tracker values, the standard deviation in all three sections is ~ 36 arcsec.

1.5 Communication

Figure 1.5 shows a schematic of the hardware communication flow between the gondola, its sensors, the science and the ground control. The number on the arrows indicate the communication mode, bit speed and parity. On the gondola side the opto card operated by the Flight Control Computer, provided the main communication hub between science, gondola and ground. There were four separate transmission feeds going down and two communication lines going up. The downlink transmissions were:

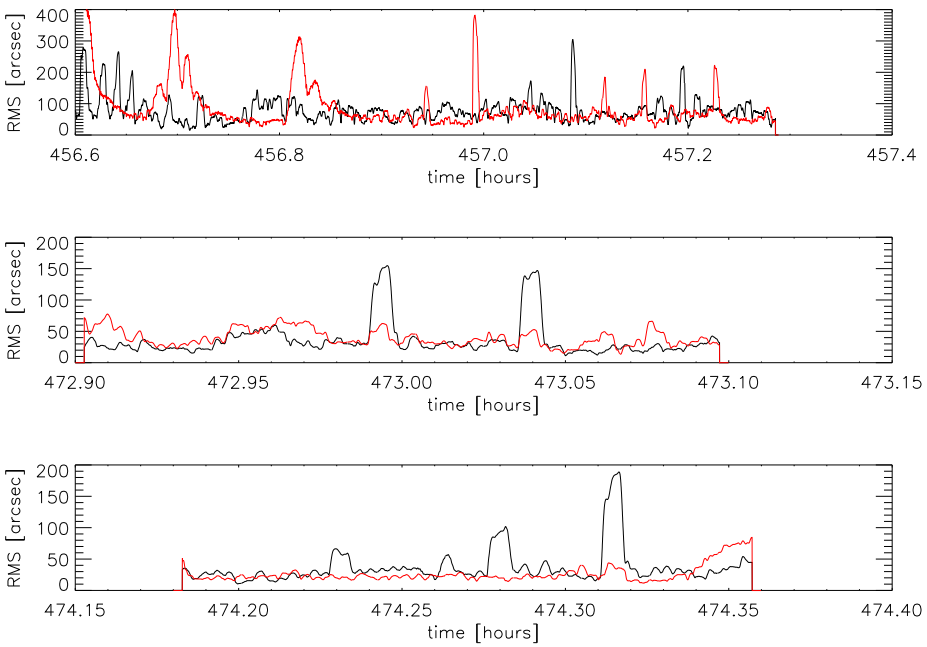

Figure 1.4: RMS curves of a 10 second running window. Black curve: azimuthal rms. Red curve: elevation rms. The gondola launched at time t = 451 and the flight was terminated at t = 475, and so the sections represents periods of good tracking where the average tracker solutions rate $\sim$ 3 seconds (see Table 2.1). During the top series we were doing offsets to find the spot on the detectors and therefore it is more noisy than the other two. The spikes are due to incorrect tracker values which when accepted at good values causes the gondola to respond. On average the gondola had a RMS stability on a source better than 1 arcmin.

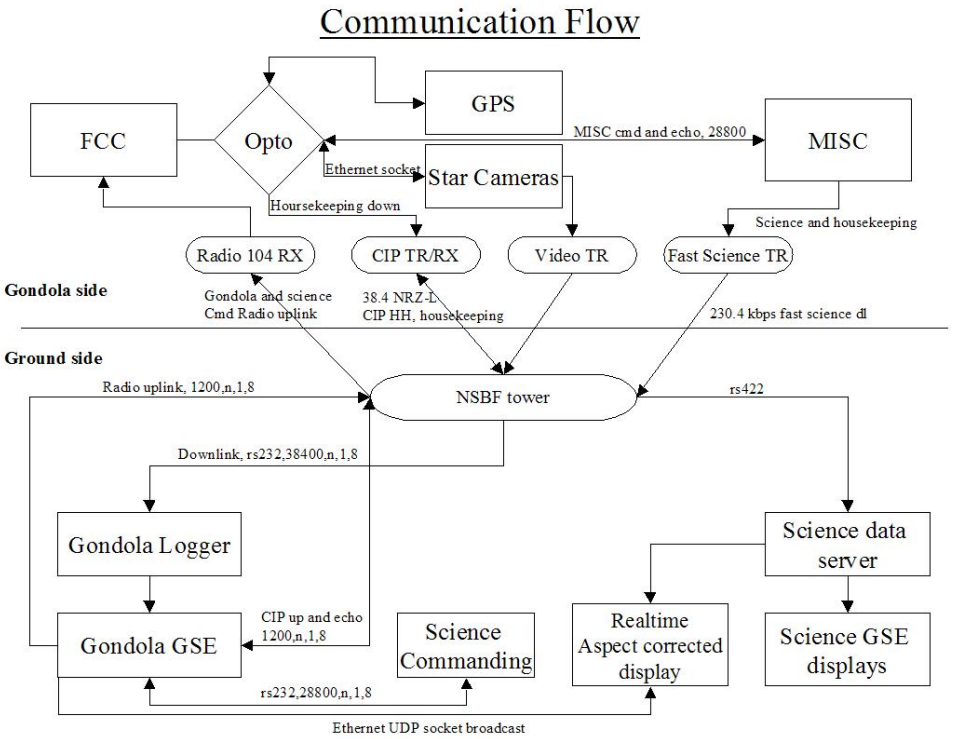

Figure 1.5: Communication flow diagram. The diagram shows the flow of information between onboard systems and the gound systems. Small numbers of connections indicate type of connection, speed and encryption. NSBF = National Space Ballon Facility, GSE = Ground Support Equipment, FCC = Flight Control Computer, MISC = Minimal Instruction Set Computer.

- Science data and housekeeping.
- Gondola housekeeping and command echo.
- Tracker video, which allowed the tracker interface screen to be viewed from the ground.
- CIP (Control Interface Protocol) echo and NSBF gps data.

The two uplink lines were:

- CIP (Control Interface Protocol) commanding.
- Gondola, science and tracker commanding. Uses a 104 radio.

A gondola command was issued through the GSE, such as moving the telescope to a new position, and transmitted with the radio to the FCC

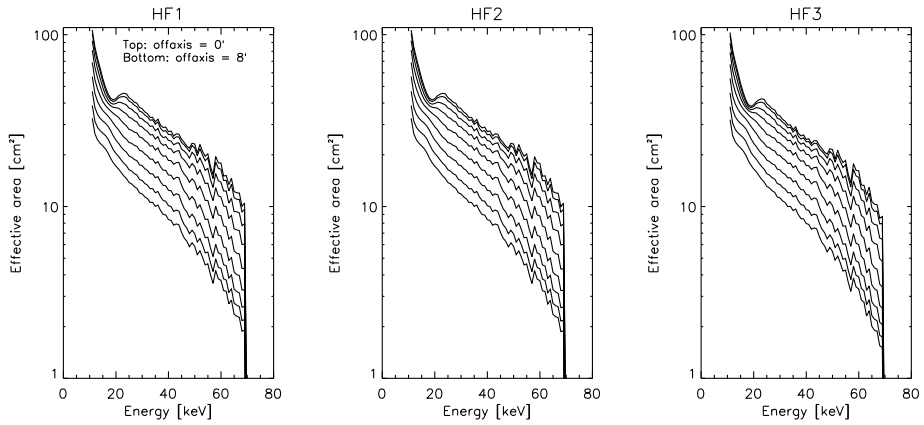

Figure 1.6: Effective area curves for the three optics: HF1, HF2 and HF3. Note that the effective area is lowest for HF3 because it has less geometric area than the other two.

where it was executed. A science command was packaged by the GSE and transmitted with radio to the FCC, which passed the command on to the MISC. An echo was returned down the main housekeeping line in both cases. Gondola housekeeping was first routed through a logger computer saving the raw feed, then passed on to the GSE for parsing. The parsed attitude solutions were transmitted via UDP to a realtime aspect reconstruction programme. The aspect reconstruction programme was also fed the science data from the science server.

1.6 The Science Payload

HEFT flew three conical approximation grazing incidence x-ray telescopes matched with three CdZnTe detectors, arranged in a cloverleaf pattern.

1.6.1 The Optics

The HEFT optics are of a Wolter I conical approximation type, the details of which can be reviewed in Section 4.3.2. Its dimensions are summarized in Table 1.2. The HEFT optics are composed of thermally slumped microsheet glass, 0.2 mm in thickness, originally developed for flat panel displays. The individual glass pieces are 10 cm long and cover a 72° arc, so that 5 are required for a revolution, and 10 are needed for a conical section and 20 for an entire shell, which equals 1440 pieces of glass to make one optic. The individual pieces are mounted on graphite spacers, 3 per piece

of glass for shells 1-22, and 5 for shells 25-72. Layer 23 and 24 are replaced by an intermediate mandrel. Details on the slumping procedure and optic fabrication can be found in J. Koglin et al 2002 [4].

The glass is coated with W/Si multilayers giving it an upper operation energy of 69 keV, where the W absorption edge cuts down the efficiency. The multilayers are deposited at the Danish National Space Center with a magnetron sputtering chamber, and details on the multilayer formula can be found in Section 4.1 and subsequent sections. Fabrication details can be found in C. Jensen et al 2003 [5] and multilayer scattering details in K. K. Madsen 2004 [6].

HEFT flew three of these optics, HF1, HF2 and HF3. HF1 and HF2 are complete optics, while HF3 has had the 12 innermost shells omitted. All three optics have been characterized at 8 keV at the Danish National Space Center using pencil beam scans on the full revolution of a shell, and HF1 also at 40 keV at the European Synchrotron Radiation Facility [7]. The pencil beam scans were performed on selected shells, covering all radii, at intervals of 2.5 degrees in azimuth omitting spacers. The scans were taken at ±6 arcmin around the nominal graze angle of the particular shell. The scans were normalized with the geometric area and projected onto a focal plane. The encircled energy curves for the three optics is shown in Figure 1.7 with the normalized maps. The spoke-like structure comes from the presence of spacers. Table 1.3 lists the HPD at 8 keV and the number of scanned shells that went into the estimates, as well as the HPD of HF1 for 18, 40 and 50 keV measured at the ESRF [7].

Telescope Parameters	
Focal length	6000 mm
Conic section length	200 mm
Substrate thickness	0.3 mm
Min. Aperture radius	40 mm
Max. Aperture radius	120 mm
# Shells	72
# Mirror pieces	1440
Field of View	17’

Table 1.2: HEFT telescope parameters.

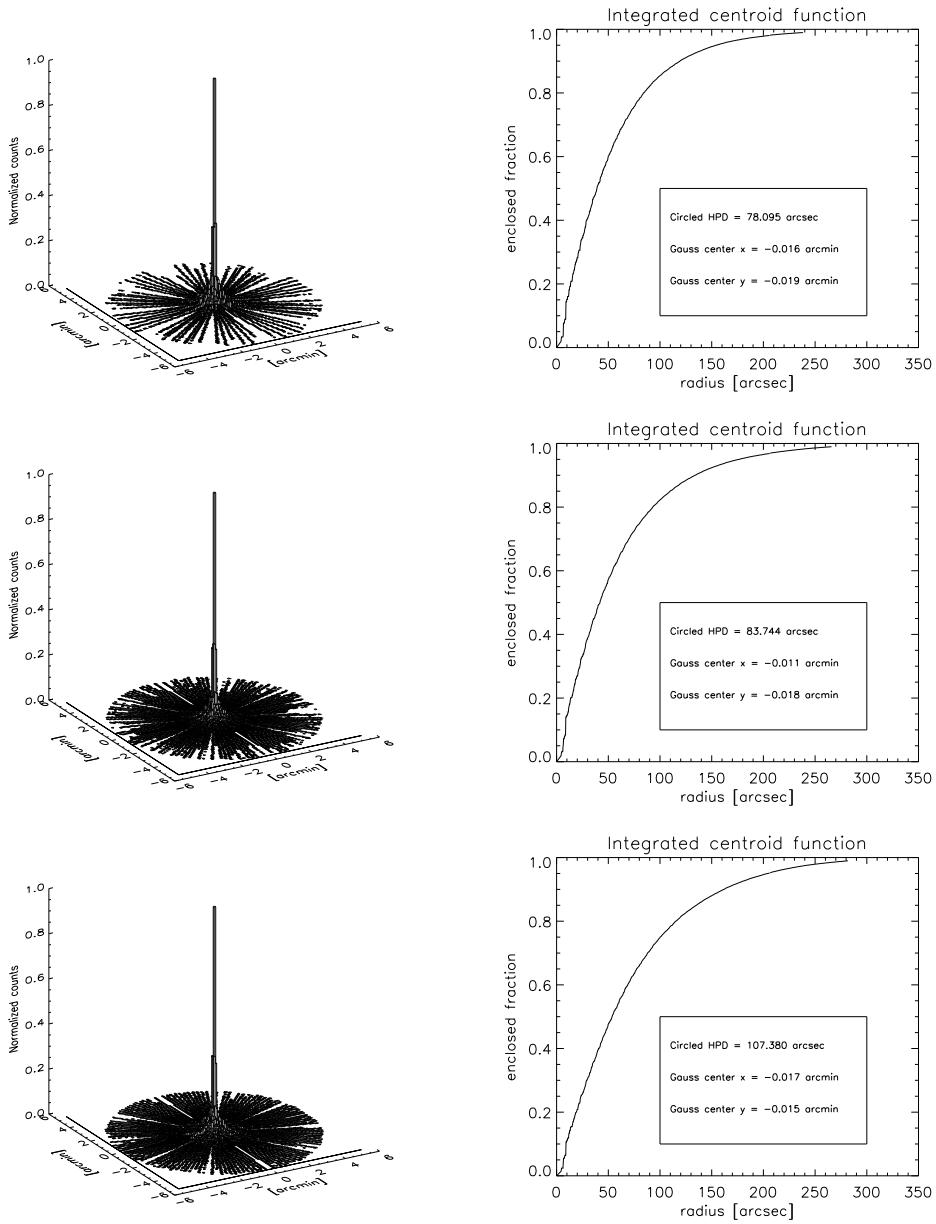

Figure 1.7: Encircled energy curves for the three optics top to bottom: HF1, HF2 and HF3.

Optic	Energy [keV]	HDP [arcsec]	Numbr of Shells
HF1	8	78	39
HF1	18	78	50
HF1	40	72	60
HF1	50	78	60
HF2	8	84	63
HF3	8	107	22

Table 1.3: Half power diameters for the three HEFT optics.

1.6.2 The Detector

The HEFT detector is a large format CdZnTe hybrid pixel detector designed to achieve good resolution with low power over the energy range 5-100 keV. It is composed of two crystals, each an array of 44×22 pixels on a 498 μm pitch. Each pixel is bonded to its own amplifier circuitry on a custom, low-noise application-specific integrated circuit (ASIC) designed at California Institute of Technology [8]. In total one detector has 44×48 pixels, a FoV of 15' and a spatial resolution of 18". The two crystals are slightly shifted on the long side by a few pixels and there is a gap between them approximately one pixel in width.

At $0°C$ the energy FWHM of most one-pixels events was 900 eV. For two-pixel events the FWHM increased to 950 eV. More details on the design and characterization of the detector can be found in H. Chen et al 2004 [8].

HEFT flew 3 of these detectors, one for each optic. The two crystal detectors are named A, B and C, while the individual crystals are numbered 1-6, with 1 and 2 composing detector A, and so on. Table 1.4 summarizes the detector parameters and shows an image of a detector.

The rotational orientation of the detectors are [A, B, C] = [-86.7, 20.3, 66.7], where the zero angle is when the detector is parallel with the horizon, so that for detector A crystal 1 would be at the top.

1.7 Optical Alignment and the γ Offset

The final alignment of the optic and detectors was performed on the fully integrated payload using a portable x-ray generator. Upon assembly rigorous optical alignment of the optics was done using the axial hole of the optics, which is a hole through the center of the optic made during the fabrication of the optic to which the radius of the layers are referenced. This hole defines the revolution axis of the optic and coincides with the optic's boresight.

Detector Characteristics	
Sensor	CdZnTe
Pixel size	498 μm
Thickness	2 mm
Unit dimension	25×25 mm
FoV	15'
Energy range	5 - 100 keV
ΔE	1 keV

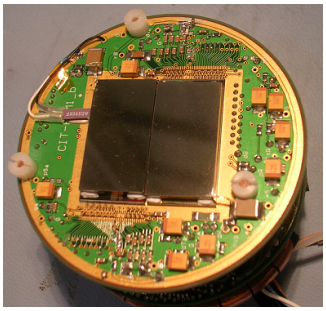

Table 1.4: HEFT CdZnTe detector parameters.

Using a scope on the front side of the optic, the back side and the detector hole at the focal plane were aligned. This method was estimated to be aligned on the arcminute level [9][10][11].

To make sure that we had indeed aligned it properly and to perform a final calibration, we used a portable x-ray generator to flood illuminate the optics. The x-ray generator was placed at 72±0.05 meters and preliminary alignment of the alignment fixture plate was performed using a laser in place of the x-ray source. Pointing it through the optic axial hole, and by noting the occultation pattern of the laser at the focal plane, we were able to align the source to within 2 arcminutes [9][10][11].

The x-ray generator was operated at a current of 0.3 mA and voltage of 35 kV, and at a distance of 72 m the source covered about 1 m^2. The mean energy of the X-ray source at the optic aperture was approximately 25 ±4 keV. A NaI detector with an aperture of 5 cm^2 was used to measure the flux in front of the optic at a monochromatic energy of 25 keV and at the focal plane. The primary error in these measurements was in uniformity of the beam illumination of the optic aperture, and was estimated to be around 20%. The effective area was determined from the ratio of the flux at the detector and the flux density at the optic entrance, taking into account the atmospheric attenuation in between. Table 1.5 lists the result of the throughput measurement and shows that the measured effective area matches within the 20% limit of the simulated effective area. The expected effective area has been calculated [11] using all known geometric obscuration effects, a simple Gaussian scattering model, and the expected throughput estimated from pinpoint x-ray measurements performed at 8 keV.

The X-ray alignment was performed iteratively by acquiring an image, comparing it to a simulated and from that estimating how far, and in which direction, the optic was offset. Two of the three optics were corrected and

Optic	Optic Front Count Rate counts/s	Optic Front Flux counts/cm^2/s	Focal Plane Count Rate counts/s	Focal Plane Flux counts/cm^2/s	Calculated Effective Area cm^2	Expected Effective Area cm^2
HF1	272	13.9	189	275	20	25
HF2	238	12.2	190	277	23	25
HF3	254	12.9	160	233	18	20

Table 1.5: In-field measured calibration values.

the final images of the alignment are shown in the three top images of Figure 1.8. These images clearly show the obscuration pattern of the optic and also reveals dead space in the detectors. the three bottom images of Figure 1.8 shows the simulated images and from these is was estimated that HF1 was off-axis by $\sim 2.0'$ and HF2 by $\sim 1.2'$. Because of the large dead space in detector B it has been difficult to estimate the offset, but it has been estimated that HF3 should be no worse than ~ 2.0 [11]. Table 1.6 summarizes the estimated offsets and the center of the image in detector coordinates, as well as the mapping between detector and optic.

Once the alignment was complete we took a picture with the on-axis star camera of the alignment fixture. The alignment fixture had a hole in it corresponding to the center of the star tracker baffle, and the location of this hole on the tracker CCD relative to the center pixel was taken to be the γ_b offset. The γ_b offset is the amount in azimuth and elevation the gondola is required to move relative to a target coordinate in order to bring the x-ray spot onto the detectors. This offset was estimated to be $\gamma_b(az, el) = (0.08^\circ, -0.015^\circ)$, where the 'b' denotes coordinates in the gondola body frame (details and definitions of the body frame will be given in the next Chapter).

Optic	Detector	Offset	Center pixel [x,y]	Detector id
HF1	Det A	2'	17,1	1
HF2	Det C	2'	23,3	3
HF3	Det B	1.2'	22,2	5

Table 1.6: Offsets and central pixel locations for the three optics. In all cases the brightest pixel was located on the top crystal of the detectors.

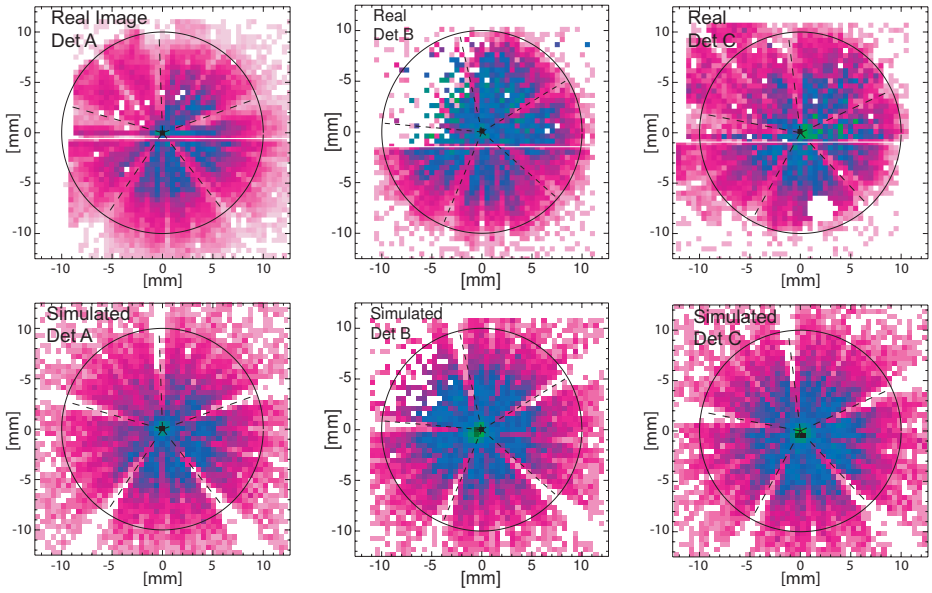

Figure 1.8: Top: The best images taken in field at energy E = 25±4 keV. From left to right the detectors correspond to optics: HF1, HF3 and HF2. Bottom: Simulated images includeing scattering effects and experimentally measured throughputs. Simulations and images were performed by Mike Pivovaroff [11].

1.8 Summary

In this Chapter I have described the major components of the gondola attitude control system build to host the HEFT payload, and explained its modes of operation. The HEFT optics and detectors have been reviewed and their integration with the gondola attitude system described. In the next Chapter the aspect reconstruction of the gondola attitude information will be explained in full detail.

Chapter 2

Aspect Analysis Procedure

2.1 Introduction

In the previous Chapter the components and operation of the gondola attitude system was described. In this Chapter I will show how the flight attitude information gathered by the sensors is used post-flight to recreate the aspect of the flight. Because of the many sensors at our disposal, I decided to approach the aspect reconstruction as a solid body problem. I first will give a brief description of the data structure generated by the onboard flight computer, then outline the gondola geometry and detail the steps of the aspect reconstruction.

2.2 Data Structure

The critical information needed to fly the gondola and to subsequently reconstruct the pointing was transmitted serially at 10 hz. One package has 60 bytes and is divided into a fast and slow part. The fast data part of the package consists of 39 bytes, and this signal stream is always the same and contains for example time as well as gyro information. The slow part has 21 bytes and the signals vary from package to package such that there are 48 different slow packages. The entire down-link telemetry block is thus cycled through once completely in 4.8 seconds. Depending on the sensor and its relevance, the signal information is distributed through out these 48 packages with different cycle periods. The full telemetry documentation can be seen in Appendix C.

2.3 Gondola Geometry

2.3.1 Reference Frames

All sky coordinates are expressed in the local gravitational frame, termed the L-frame, which is just the horizontal azimuth/altitude coordinate system. In this frame the x-axis is pointed to the north, y-axis to the east and z-axis is parallel to the local gravity vector. The azimuth progresses clockwise around the z-axis and when az=0 the vector is aligned with the x-axis. We have and will use elevation for altitude so there is no confusion with atmospheric altitude. The elevation angle is measured from the horizontal such that el=0, az=0 has the vector aligned with the x-axis and el=90, az=0 with the z-axis.

In the B-frame the x-axis is the roll axis, and aligned with the projection of the boresight onto the platform. The axis coincides with the axis of the counter rotation reaction wheel, which dampens out the roll. The yaw axis is the z-axis, and points through the azimuthal reaction flywheel. The y-axis is the pitch axis and is aligned with the pivot axis of the telescope strut.

Getting from one frame to the other requires knowledge of the rotation angles, yaw, pitch and roll, between the B-frame and the L-frame. If these are known one can use the R321 Direction Cosine Matrix (DCM) representation to get from the B-frame to the L-frame. Conversely a R123 DCM brings L-frame coordinates into B-frame coordinates. A R123 DCM is a combination of the following individual rotations:

$$\begin{aligned} \mathbf{R123} &= [\mathbf{R}1][\mathbf{R}2][\mathbf{R}3] \\ &= \begin{bmatrix} 1 & 0 & 0 \\ 0 & \cos\theta & \sin\theta \\ 0 & -\sin\theta & \cos\theta \end{bmatrix} \begin{bmatrix} \cos\theta & 0 & -\sin\theta \\ 0 & 1 & 0 \\ \sin\theta & 0 & \cos\theta \end{bmatrix} \begin{bmatrix} \cos\theta & \sin\theta & 0 \\ -\sin\theta & \cos\theta & 0 \\ 0 & 0 & 1 \end{bmatrix} \end{aligned} \tag{2.1}$$

Where 1 equals rotation about the x-axis, 2 about the y-axis and 3 about the z-axis. Multiplying the matrices together gives the following DCMs for R_{123} and R_{321} respectively, where r = roll, y = yaw, p = pitch and c = cos, s = sin:

$$R_{123} = \begin{bmatrix} cp*cy & cp*sy & sp \\ -sr*sp*cy - cr*sy & -sr*sp*sy + cr*cy & sr*cp \\ -cr*sp*cy + sr*sy & -cr*sp*sy - sr*cy & cr*cp \end{bmatrix} \tag{2.2}$$

$$R_{321} = \begin{bmatrix} cy*cp & -sr*sp*cy - cr*sp & -cr*sp*cy + sr*sy \\ sy*cp & -sr*sp*cy + cr*cy & -cr*sp*sy - sr*cy \\ sp & sr*cp & cr*cp \end{bmatrix} \quad (2.3)$$

These two DCMs are the inverse of the other such that R_{123}*$R_{321} = \mathbf{I}$. In the gondola body frame the coordinate basis is at all times given by a vector representing the position of the on-axis star tracker at an azimuth = 0, no roll and an elevation equal to the value measured by the encoder:

$$\mathbf{b} = \begin{bmatrix} \cos(\text{EncoderElevation}) \\ 0 \\ \sin(\text{EncoderElevation}) \end{bmatrix} \quad (2.4)$$

With a known set of yaw, pitch and roll, this vector is easily converted into the L-frame. Changing the notation for the R_{321} DCM into R_b^l, a vector $\mathbf{b}$ in the B-frame transforms to the L-frame by $\mathbf{l} = R_b^l\mathbf{b}$. A trivial transformation, however, obtaining the proper set of yaw, pitch and roll is far from it and the reason why one flies a plethora of sensors.

2.3.2 Infinitesimal Rotations and DCM rates

If the angles of the DCM by which one frame has moved relative to the other are infinitesimally small, then $\cos\psi \approx 1$ and $\sin\psi \approx \theta$, and the fundamental rotations of Eqn 2.1 reduce to skew-symmetric matrices like

$$R_1 = \begin{bmatrix} 1 & 0 & 0 \\ 0 & 1 & \psi_1 \\ 0 & -\psi_1 & 1 \end{bmatrix} . \quad (2.5)$$

Neglecting second order and higher terms the transformation becomes, $R_{321} = \mathbf{I} - \mathbf{\Psi}$, where $\mathbf{\Psi}$ is the axiator

$$\Psi = \begin{bmatrix} 0 & -\psi_3 & \psi_2 \\ \psi_3 & 0 & -\psi_1 \\ -\psi_2 & \psi_1 & 1 \end{bmatrix} . \quad (2.6)$$

If an approximate DCM, R_{b0}^l, is known and the frame is subsequently rotated by infinitesimal angles then the new DCM, R_b^l, is given by

$$\mathbf{R}_b^l = (\mathbf{I} - \mathbf{\Psi})\mathbf{R}_{b0}^l . \quad (2.7)$$

Inertial sensors register rates of change around the axis of a moving frame, and the derivative of the time dependent DCM R_b^l is important for

solving the equation of motion. The time dependent DCM between arbitrary frames p and q is given by

$$\dot{\mathbf{R}}_p^q = \lim_{\delta t \to 0} \frac{\mathbf{R}_p^q(t_0 + \delta t) - \mathbf{R}_p^q(t_0)}{\delta t} \,. \tag{2.8}$$

Using the expression of Eqn 2.7, $\mathbf{R}_p^q(t_0 + \delta t) = (\mathbf{I} - \mathbf{\Psi})\mathbf{R}_p^q(t_0)$, and substituting back into Eqn 2.11 the differential equation becomes

$$\dot{\mathbf{R}}_p^q = \lim_{\delta t \to 0} \frac{\mathbf{\Psi}}{\delta t} \mathbf{R}_p^q(t_0) = -\Omega_{q/p}^p \mathbf{R}_p^q \,, \tag{2.9}$$

where $\Omega_{q/p}^p$ is the axiator for the axis rates, $(\omega_1, \omega_2, \omega_3)$, around axis 1 = x, 2 = y and 3 = z

$$\Omega_{q/p}^p = \begin{bmatrix} 0 & -\omega_3 & \omega_2 \\ \omega_3 & 0 & -\omega_1 \\ -\omega_2 & \omega_1 & 0 \end{bmatrix} \,. \tag{2.10}$$

In terms of the L,B-frame the attitude equations take the form

$$\dot{\mathbf{R}}_l^b = -\Omega_{b/l}^l \mathbf{R}_l^b = \mathbf{R}_l^b \Omega_{l/b}^b \,. \tag{2.11}$$

The axiator $\Omega_{l/b}^b$ is composed of the angular rates $\omega_{l/b}^b$, which are described in the next section. This equation must be numerically integrated to yield the final attitude solution.

2.3.3 Gyroscope Frame

The 'strap-down' gyroscopes directly measure the change in angular momentum around the gondola's body axis relative to an inertial frame. The navigation frame, however, is the local gravitational L-frame and one must use the intermediate inertial I-frame in order to get from the B-frame to the L-frame.

When operating with angular velocities one can employ the angular velocity addition theorem [12], which states that a velocity $\omega_{a/z}$ given in 'a' coordinates relative to the 'z' frame, can be obtained from velocities in intermediate frames such that

$$\omega_{a/z} = \omega_{a/b} + \omega_{b/c} + ... + \omega_{y/z} \,. \tag{2.12}$$

Expanding the notation for the angular velocities, $\omega_{b/c}^a$ means the rotation of the 'a' frame with respect to the 'b' frame in coordinates of the 'c' frame. The task at hand is to have the angular velocity of the gyro converted to the local L-frame, that is we need the gyro to be on the form $\omega_{l/b}^b$.

However, as already stated the gyro rates are given relative to the inertial frame $\omega^b_{i/b}$. In terms of the angular velocity theorem this means that

$$\omega^b_{l/b} = \omega^b_{l/i} + \omega^b_{i/b} \,, \tag{2.13}$$

where $\omega^b_{l/i}$ is the angular velocity that bridges the gap. This angular velocity describes the rotation of the B-frame to the L-frame in coordinates of the inertial I-frame, and if the coordinate transformation $\mathbf{R}^b_l$ is known then

$$\omega^b_{l/i} = -\mathbf{R}^b_l \omega^l_{i/l} \,, \tag{2.14}$$

where I have used the relation $\omega^b_{l/i} = -\omega^b_{i/l}$. The angular velocity, $\omega^l_{i/l}$, relates the L-frame to the inertial frame and in coordinates of the Earth-Centered, Earth-Fixed frame (ECEF) this is an axial vector composed of surface transport rates and Earth rates,

$$\omega^l_{i/l} = \omega^l_{e/l} + \omega^l_{i/e} \,. \tag{2.15}$$

The first term is the velocity transformation of the ECEF frame to the L-frame due to motion across the earth's surface. The second term is the Earth's movement in the inertial frame. The ECEF frame is described by longitude, ϕ, latitude, λ and if the rate of change of longitude and latitude are given by $\dot{\phi}, \dot{\lambda}$, and the earth's rotation rate by $\omega_{i/e}$ [12] then

$$\omega^g_{e/g} = \begin{bmatrix} \dot{\lambda} \\ -\dot{\phi} \\ -\dot{\lambda}\tan\phi \end{bmatrix} \,, \qquad \omega^g_{i/e} = \begin{bmatrix} \omega_{i/e}\cos\phi \\ 0 \\ \omega_{i/e}\sin\phi \end{bmatrix} \tag{2.16}$$

These two effects combine to what is commonly known as the 'gyro earth drift'. If one has a very slow moving object with a high timing resolution, then the surface transport rate can be safely ignored.

2.3.4 Star Tracker Frame

The star trackers are the most important absolute sensors. They return their coordinates in the L-frame and are used to calibrate and correct the other sensors. One tracker is mounted on-axis and the other off-axis approximately 30 deg apart in elevation. Except for very rare occasions the trackers cannot view the sky at the same time, and to obtain an aspect solution for the off-axis tracker it needs to be transformed into the on-axis trackers coordinates.

The on-axis tracker, T1, is assumed to be co-aligned with the gyroscope reference frame and with the B-frame basis vector **b**. Transformation of **b**

by R_b^l directly yield the coordinates of T1 in the L-frame. The separation angles of the two trackers are only known in the B-frame, and thus if the offset angles in the B-frame are α, then the transformation of the off-axis tracker, T2, into T1 coordinates is given by

$$T1 = \mathbf{R}_b^l(\mathbf{R}_l^b T2 - \alpha) = T2 - \mathbf{R}_b^l \alpha \; . \tag{2.17}$$

2.4 Aspect Reconstruction: Error Sources

At the time of flight we already became aware of three sources of error:

1. An unforseen slow update period, 5 minutes, from the GPS on the longitude/latitude values.

2. For short periods incorrect longitude/latitude values due to GPS jamming by White Sands Missile Range.

3. A high gyro bias drift resulting from insufficient information about the gyros temperature dependence.

We were unable to do anything about either during flight, other than trying to improve the situation for the gyros by manually estimating the correct bias.

The slow longitude/latitude update meant that for a period of 5 minutes at a time the same longitude and latitude values were used in all Ra/Dec to Az/El conversions and vice versa, while in fact the gondola was travelling. This can to some extend be corrected as the gondola path over periods of 5 minutes was for the most part relatively smooth. There is nothing that can be done about the period when we lost the GPS due to jamming, and all observations done during this period are assumed lost.

The gyro bias drift can be reconstructed post flight as will be demonstrated.

2.4.1 GPS: longitude and latitude errors

Correct longitude and latitude values are not only important for the conversion between horizontal and equatorial coordinate frames, but also important for determining the correct earth drift affecting the inertial sensor attitude as shown above. The typical length of an observation during flight was from 10 min to 1 hour and so during an observation there were only 2 to 12 attitude fixes. When in differential mode the position accuracy is 5

meters, if there is a ground station within 500 km. That means that the position is well determined at the time of attitude fix, and that midway between two points the error is the largest.

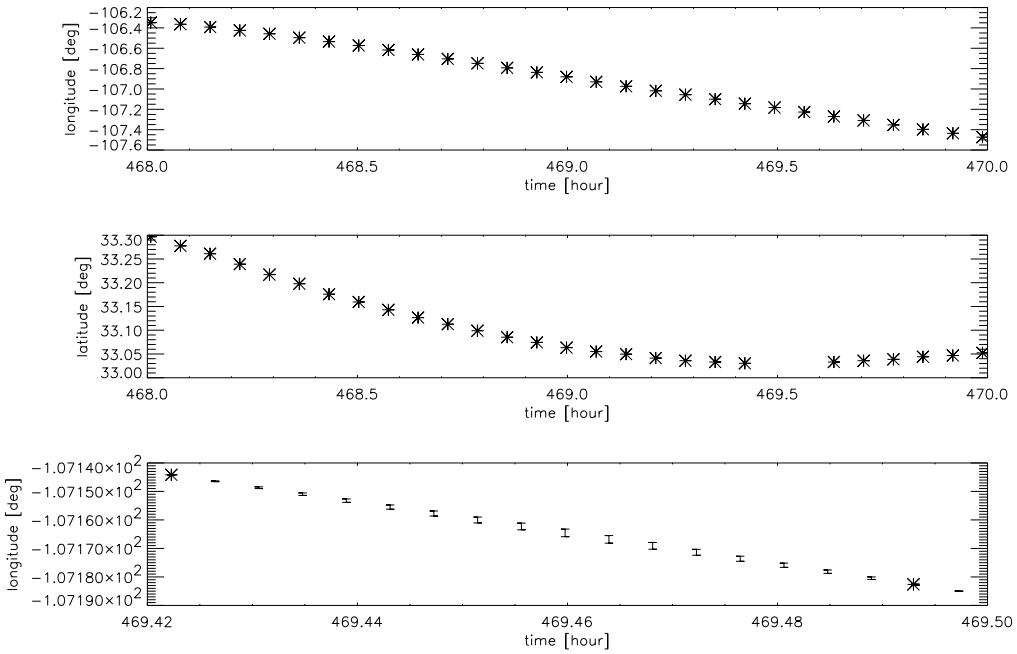

Figure 2.1: Top: section of longitude values. Mid: section of latitude values. Bottom: interpolation errors between attitude fix points. Time axis is in hours since 1st May 2005.

Figure 2.1 shows a section of the longitude and latitude curves against time. The curves are relatively smooth and a linear interpolation is not a bad approximation. The actual flight path between attitude fixes, however, does not necessarily have to be smooth, and with an average ground travelling speed of the gondola, as estimated from the longitude and latitude, of 7.7 $\pm$5.5 m/s, the gondola on average moved 1.1 $\pm$0.8 km in the space of 2.5 minutes. To estimate the error I calculated the velocity dispersion in a window of 50 minutes around the point, and used the standard deviation of the velocity to determine the possible drift from the linear interpolation. The error between two attitude fixes thus scales linearly with time as shown in the lower plot of Figure 2.1. A typical value for the velocity drift is 0.01 mdeg/s and gives a 1.5 mdeg deviation over 2.5 minutes, which corresponds to a positional drift of 150 m.

2.4.2 Aspect Reconstruction: Reconstruction The Gyro

The raw gyro

The gyros are the most important sensors for the gondola stabilization, and also post flight the gyros have the best resolution and least amount of noise. The alternative is using the magnetometers, which are sampled at the same rate, but these are by far much more noisy and heavily bias by onboard changing magnetic fields.

The gyros are sampled at 10 hz and were by the in-flight pointing loop used to determine the gondola position as explained above. The gyros are relative and were continually corrected by the absolute onboard sensors. Gyro 2 mounted on the main platform and measuring azimuth/roll was corrected in azimuth by the star trackers when solutions were available, and gyro 1 mounted on the telescope strut by the star trackers and the encoders.

These in-flight corrections are not good enough to use as is, since the sensors themselves were suffering from drifts and couplings to other sensors. The in-flight corrections ensured that we remained on target, but many higher order corrections had to be omitted, such as the roll, as correction to roll could cause the gondola to start pendulating. The starting point is therefore the raw angular momentum output rates of the gyros.

By an unfortunate accident the raw voltages of the gyros were omitted in the down-link stream, and the raw gyro values have to be derived from the bias and earthdrift corrected gyro rates. This rate is given by

$$\omega_{fx} = G_{fx}(V_x - B_{fx}) - E_{fx} \ , \tag{2.18}$$

where f represents flight value and x either az, el or roll, G is the gain, V is the voltage, B the bias, and E the earth drift. Since the earth drift calculation includes latitude, as can be seen from Eqn 2.16, it was affected by the incorrect latitude, and it is necessary to use the original data streams of B_{fx}, G_{fx}, ω_{fx} and latitude, λ_f to solve for the raw V_x.

Once the raw output voltage has been found, ω_x, can be iteratively reconstructed if the correct values of B_x and E_x are known. The gain value, $G_x = G_{fx}$ is assumed unchanged, and the new earth drift E_x is calculated from Eqn 2.14 including the correctly interpolated latitude. This only leaves the bias, B_x, which will be discussed in the next section.

The final reconstruction of the gyro follows these iterative steps:

- $E_x[i] = \text{earthdrift}(G_x[i-1])$
- $G_x[i] = (\omega_x[i] - B_x[i] * G_x - E_x[i]) * dt[i-1]$

- $$\Omega = \begin{bmatrix} 0 & -\omega_3[i] & \omega_2[i] \\ \omega_3[i] & 0 & -\omega_1[i] \\ -\omega_2[i] & \omega_1[i] & 0 \end{bmatrix} . \tag{2.19}$$

- $R_b^l[i] = R_b^l[i-1]\Omega$

Bias corrections

Gyros are known to drift with temperature, and the Litton gyro is no exception. During flight the magnetometer rate was used to correct the bias, however, the temperature changed more rapidly than the applied correction and equilibrium was never reached.

Determining a bias is in principle simple, but in practice complicated. Sensors are not referenced to the same coordinate frame, and the transformation from one to the other is precisely the problem we would like to answer, yet without referencing the gyro to another sensor we cannot determine the bias. So we are stuck with wanting to transform a sensor with a known set of yaw, pitch and roll, and at the same time having to correct these same yaw, pitch and roll.

A simplified way to approach this problem is to proceed as in Eqn 2.7, and assume that the approximate solution is already known. The infinitesimal addition is then assumed to be due to the bias correction. If we know of a DCM $R_b^{l'}$ that will transform $\mathbf{b}$ to $\mathbf{l}'$, where L'-frame is the intermediate frame, and if the difference between the measured and derived coordinates is $\Delta = \mathbf{l}_{tracker} - \mathbf{l}'$, then

$$R_b^l \mathbf{b} = (\mathbf{I} - \Omega_l^l) R_b^{l'} \mathbf{b} = \mathbf{l}' - \Omega_l^l R_b^{l'} \mathbf{b} = \mathbf{l}' + \Delta \, . \tag{2.20}$$

In practice we first need to determine the approximate DCM, $R_b^{l'}$, which will get us 'close' to the solution. For this one needs an approximate bias, B_x, and it turns out that using the average tracker ra,dec values and transforming them with the in-flight yaw and pitch, excluding roll, gets you close. The roll bias is determined from the GPS roll and once found wont be changed. Instead the gain value, G_{roll}, is adjusted to increase the roll amplitude. This means bias drift due to the roll is now coupled into the yaw and pitch. This is not a problem when we are tracking on-axis, but with the off-axis tracker is does complicate matters.

2.5 Error analysis

2.5.1 System timescales

Since we were dealing with a mechanical system dangling at the end of a long cable, there are some natural time scales and modes imprinted on the system. The time modes can with good reason be separated into two categories, super minute modes and sub minute modes. The best sensor for this temporal study is the gyro, since it is sampled evenly in time and has the best resolution and precision. The gyro is affected by bias, but the bias is a slowly changing function and can be assumed to be relevant only on timescales larger than an hour. The roll gyro is the best axis to study as this gyro is tied to the gondola platform, and is only weakly coupled with the mechanical azimuthal and elevation movements.

The modes were investigated using conventional Fourier analysis, in particular the Power Spectral Density function, which is the fourier transform of the autocorrelation function. Six different time series from the flight were chosen as a sample to study sub minute modes, while only two time series were used for the super minute. The time series were normalized such that the integral of the series was 0, and any slope removed so the end points of the series fulfilled the requirement of periodicity.

Figure 2.2 shows the results of the super minute analysis. The two gyro roll time series of approximately 40 minutes are shown on the left, and the PSD on the right. The shape of the time series over the 40 minutes is quite different, which is attributed to the fact that the lower time series is severely affected by bias drift, which can be confirmed by comparing to the GPS roll, but the presence of the bias is unimportant and can easily be identified in the PSD plot. The first common mode for the two series is found at 10 cycles/hour = 6 minutes. The second appears at around 40 cycles/hour = 1.5 minutes and the third at 50 cycles/hour = 1.2 minutes. Table 2.1 summarizes the series and the modes.

Figure 2.3, 2.4 and 2.5 show the results of the sub-minute analysis. The 6 time sequences are of approximately 12 minutes of length, and two of them are subsets of the super-minute time series. Figure 2.3 shows the gyro roll series to the left and the PSD on the right column, and here the characteristic modes are very apparent. The PSD is shown out to modes 3600/3000 = 1.2 seconds of length, where for all except one curve the PSD flattens out.

Table 2.1 summarizes the time series and the characteristic modes for the roll, pitch and yaw. For the roll the modes are well correlated in all series.

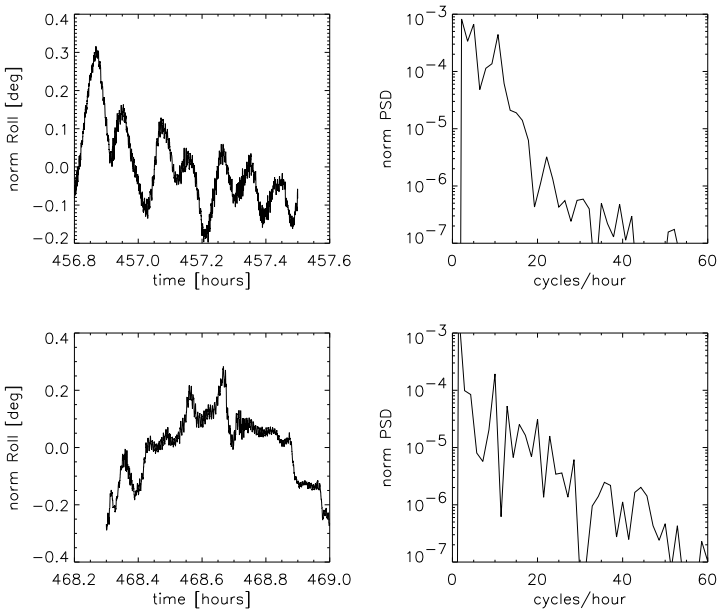

Figure 2.2: Super minute time series. Left panel: the raw roll of the time series. Right panel: PSD transformed in units of cycles/hour.

The same goes for the pitch shown in Figure 2.4, despite the apparently very different shapes of the time series. The yaw is far less correlated, as shown in Figure 2.5, and exhibits a more continuous behavior of modes related to mechanical movements. However, there are a few features that stand out around the 3 second mark - and at half that again which could possibly be some kind of aliasing. Table 2.1 lists the star tracker solution rate for each series, and it can been seen that is it related to the modes found in the azimuth. This is not surprising, and is well illustrated by Figure 2.6, which shows a segment of the in-flight processed azimuth signal. The sharp dips here corresponds to the reception of a star tracker solution, which caused the gondola to correct its azimuthal value. This meant that the gondola was now off-target and consequently had to correct itself (bump). At the same time a bias was causing the gondola to drift off target (slow decline), and thus the cycle repeated itself. Naturally this kicks up oscillations and therefore the strongest sub-minute modes are found around the tracker rate.

This means that ~ 3 seconds is the characteristic timescale of correction. For timescales longer than this, we will have a sampling of the tracker to correct with. Below, however, we must rely on the gyro. An added compli-

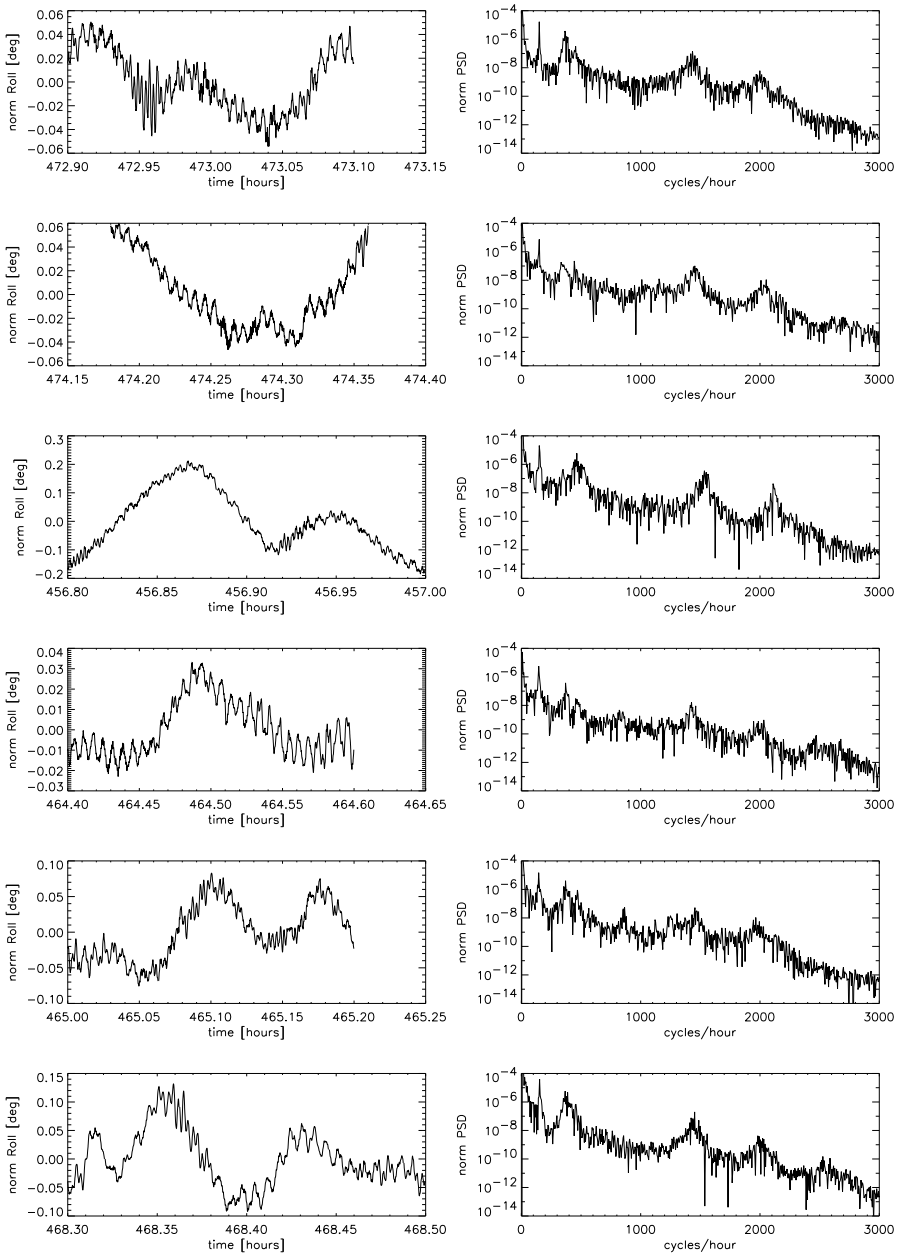

Figure 2.3: Left panel: Gyro roll values. Right panel: PSD transformation of the roll in cycles/hour.

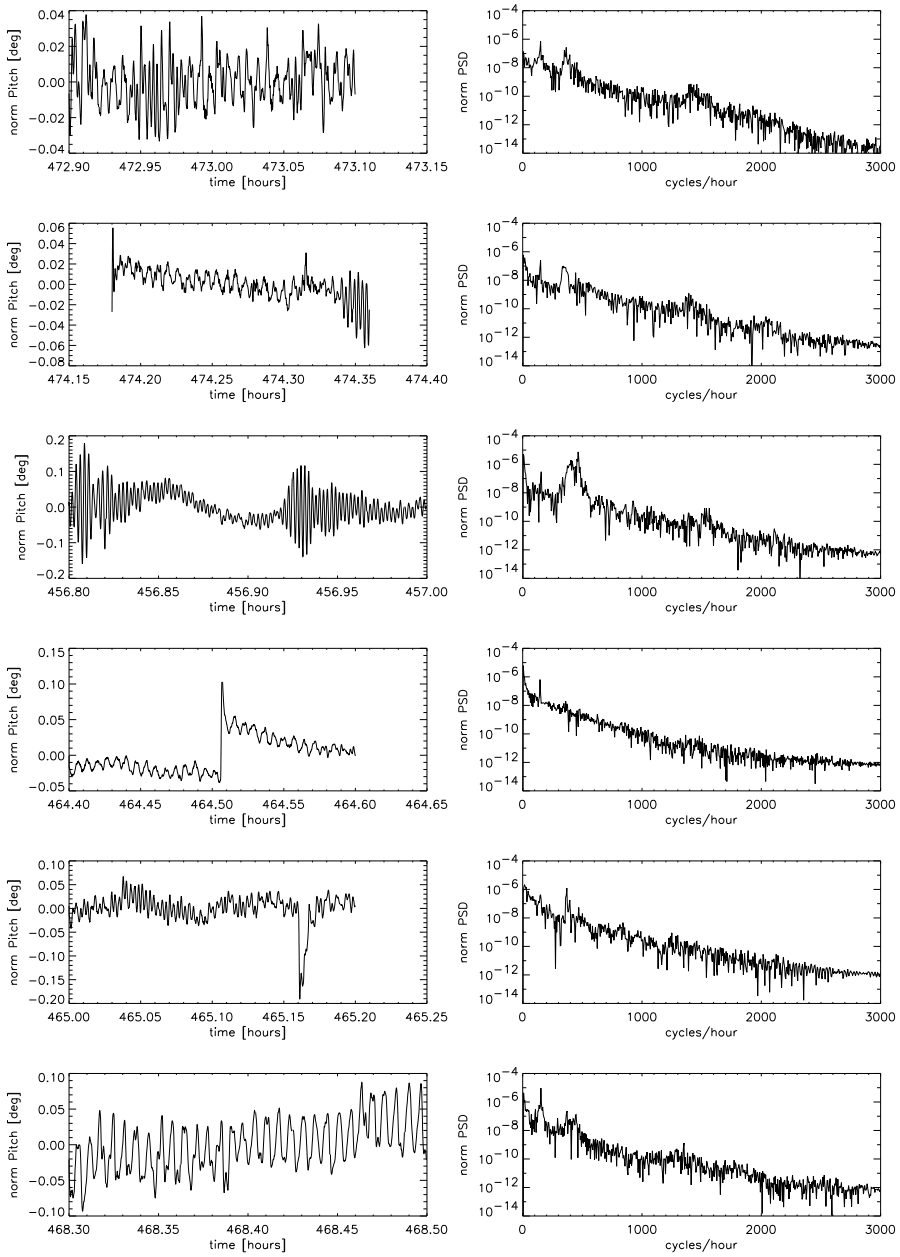

Figure 2.4: Left panel: Gyro pitch values. Right panel: PSD transformation of the pitch in cycles/hour.

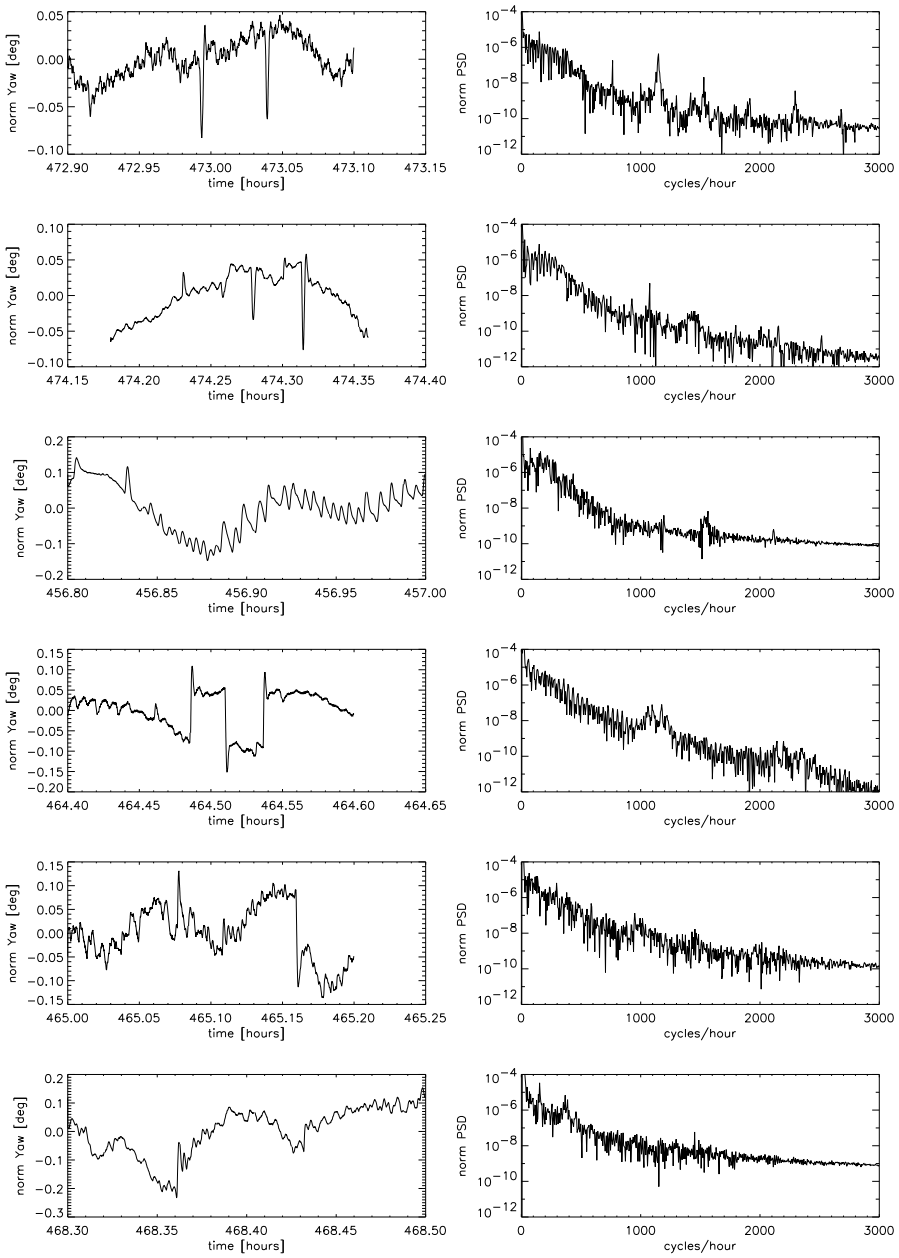

Figure 2.5: Left panel: Gyro yaw values. Right panel: PSD transformation of the yaw in cycles/hour.

Timeserie [hour]	Modes in Roll [sec]	Modes in Pitch [sec]	Modes in Yaw [sec]	Tracker Rate
472.90-473.10	24, 10.2, 8, 2.5, 1.8, 1.3	24, 9, 2.5	3.1, 2.4, 1.9, 1.6, 1.3	3.1 ±1.3
474.18-474.36	24, 10.2, 8, 2.5, 1.8, 1.3	24, 9, 2.5	3.0, 2.3, 1.7	3.3 ±0.5
456.80-457.00	24, 10.2, 8, 2.5, 1.8, 1.3	24, 9, 2.5	3.0, 2.3, 1.7	3.0 ±1.1
464.40-464.65	24, 10.2, 8, 2.5, 1.8, 1.3	24, 9, 2.5	3.1, 1.6	3.1 ±0.5
465.00-465.20	24, 10.2, 8, 2.5, 1.8, 1.3	24, 9, 2.5	3.6, 2.4, 1.8	4.2 ±2.6
468.30-468.50	24, 10.2, 8, 2.5, 1.8, 1.3	24, 9, 2.5	4.5, 2.7	2.9 ±0.9

Table 2.1: Summary of the predominant modes in the PSD of the yaw, pitch and roll respectively. Last column lists the average tracker solution rate for the particular section. The error in the tracker rate is the standard deviation of the average.

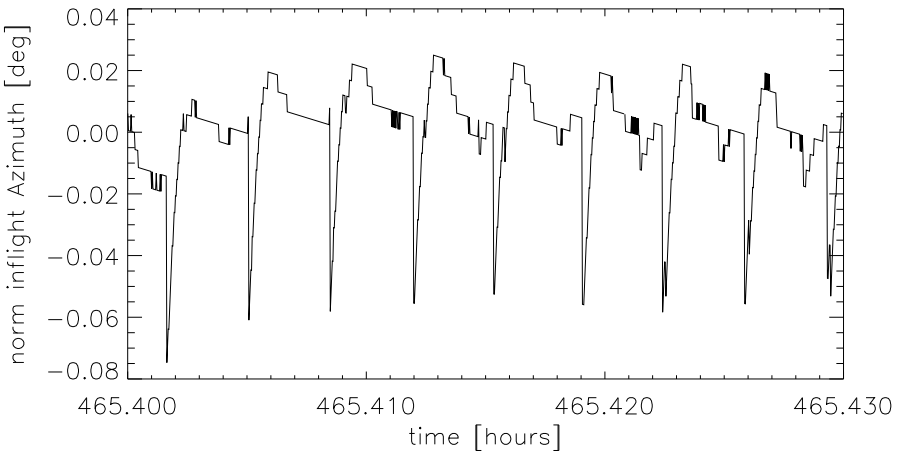

Figure 2.6: In-flight azimuth values. These values are subjected to various on board corrections, but serve to demonstrate how the gyro values were corrected by the tracker.

cation to this, which I will discuss in the next section, is the fact that the trackers suffered from sporadic time delays in their processors, which meant that sometimes the solution was sent belatedly. This delay was found to be between 0-3 seconds, so since we have features on the same timescale, a slight misalignment of the tracker has significance to the aspect solution, and we need to be very careful about applying corrections to the gyro on this timescale.

2.5.2 Tracker Delays

Comparing sets of ra/dec from the trackers to sets of ra/dec received on the gondola, it turned out that the arrival time logged on the gondola flight

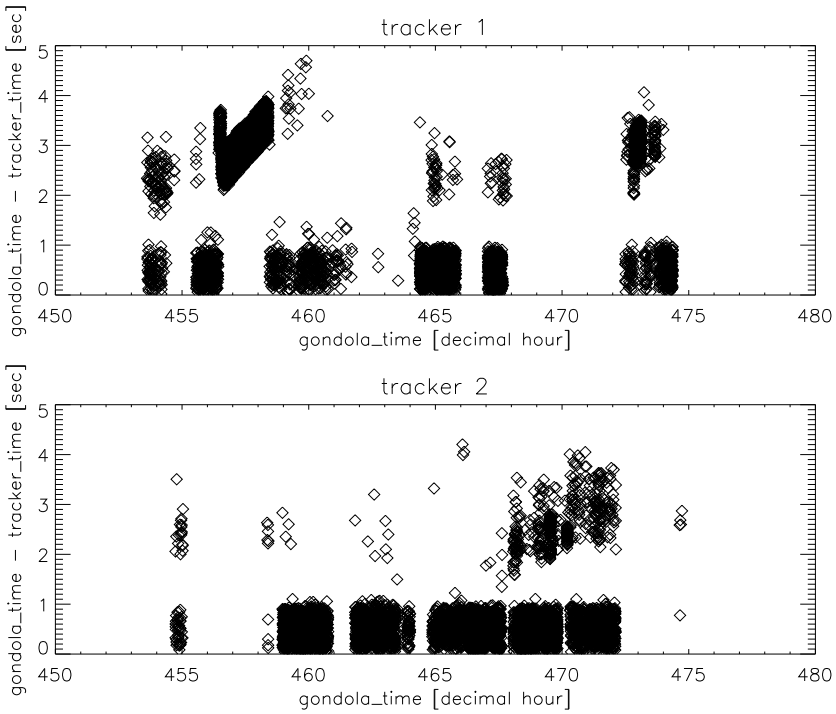

Figure 2.7: Calculated delays for tracker 1 and 2 (on- and off-axis) obtained by comparing the time stamps of tracker solution taken off the tracker and the time stamp recorded on the gondola upon arrival of a new solution.

computer was delayed compared to the time logged on the trackers themselves. The delay is sporadic and worst for tracker 1 as can be seen from Figure 2.7 showing the delay in seconds between the solutions creation time and its registered arrival at the gondola. The band between 0-1 sec is due to the down stream sampling, where some values have been stored longer than others before being sent down. The source of the delay is still not understood, but purported to be related to a process priority conflict on the tracker end.

Initial tests showed that the delay is quite irregular, and the delay is therefore calculated for small segments containing 10 tracker solutions. To obtain the delay I used the elevation axis, which is mostly well-behaved and well correlated to the star tracker elevation. I used a window of 5 seconds with a step size of 0.05 seconds, and shifted the elevation curve of the star tracker against the elevation curve of the gyro, calculating the correlation at every step. The delay was then taken to be at the maximum of the

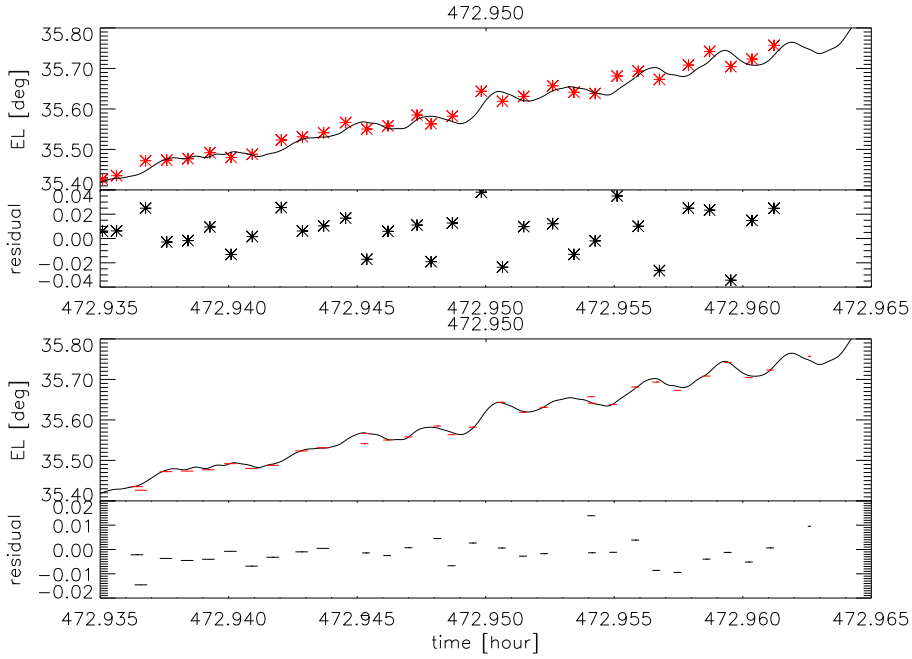

Figure 2.8: Example tracker time delay. Top plot: Red stars are tracker solutions, black solid line the gyro calculated elevation. Bottom plot: Red bars are the time corrected tracker solutions, and the width of the bar is the error in the tracker solution due to the width of the correlation function used to align the curves.

correlation curve.

Figure 2.8 shows a section of an observation affected by the delay. The solid curve is the gyro elevation and the stars tracker solutions from star tracker 1. In the top plot the delay can be clearly observed and is on the order of ~ 3 seconds. In the bottom plot the tracker times have been corrected, and as can be seen from the residuals, the correlation is far better. The width of the red bars in the bottom plot corresponds to a reduction of the correlation function, r, by 0.001, and demonstrates that when the tracker solution lies on a flat section, the determination of the delay becomes more difficult. Also it can be seen that not all tracker solutions appear to have exactly the same delay.

Figure 2.9 shows the standard deviation of the (tracker-gyro) azimuth and elevation residual as a function of the average tracker delay in the six time sequences given in Table 2.1. The tendency of a larger deviation for higher delays is obvious. The delay is also more sporadic for larger delays. Since the azimuth and roll are oscillating with a period of ~ 3 second at an

amplitude of ~ 36", it becomes difficult to improve the solutions with the star trackers much beyond this point, and a measure of trust must be given to the gyro.

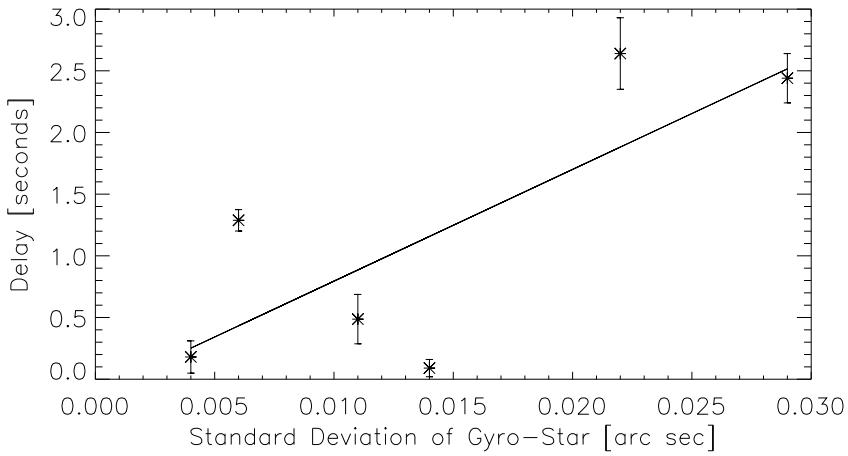

Figure 2.9: The tracker delay as a function of the standard deviation of the residual of the tracker-gyro.

2.5.3 Gyro and Attitude Error

The accuracy of the gyro attitude solution is of course dependent on the gyro error model components. The attitude error in the L frame is given by the dynamical 'psi' error description [12]

$$\dot{\bar{\psi}} = -\omega^l_{i/l}\bar{\psi} - \delta\omega^l_{i/b} \,, \tag{2.21}$$

where the bar notates computed values. The rate $\omega^l_{i/l}$ is the inertial to local level L earth rates, as previously discussed, and $\delta\omega^l_{i/b}$ is the gyro drift coordinated in the L frame.

The gyro drift depends on the gyro error model, which is taken to be

$$\delta\omega^b_{i/b} = \begin{bmatrix} eBias_x \\ eBias_y \\ eBias_z \end{bmatrix} + \begin{bmatrix} eGain_x & M_{xy} & M_{xz} \\ M_{yx} & eGain_y & M_{yz} \\ M_{zx} & M_{zy} & eGain_z \end{bmatrix} \begin{bmatrix} \omega^b_{i/bx} \\ \omega^b_{i/by} \\ \omega^b_{i/bz} \end{bmatrix} + \varepsilon(t) \,. \tag{2.22}$$

The subscripts x, y, z refer to the axis of rotation, *eBias* is the measurement error on the bias, *eGain* the error on the scale factor, and M the misalignment between the gyro axis. $\varepsilon(t)$ refers to any time dependent environmental errors such as temperature changes, or other environmental influences. This error model is for the body referenced B frame and to convert it to the local level L frame we can simply transform it with $\mathbf{R}_b^l$ such that $\delta\omega_{i/b}^l = \mathbf{R}_b^l \delta\omega_{i/b}^b$.

- *eBias*. We already know before hand that during flight the error on the bias was very large, due to the fact that is was constantly being changed by steep temperature gradients. However, we have a way of correcting it as explained above and the error estimate entering into the model above is from the corrected bias. This error is taken to be estimated from the fit to the (tracker-gyro) residuals

- *eGain*. By the manufacturers the non-linear gain error is estimated to be 0.07%.

- M_{xyz}. The misalignments between the axis are given by the manufacturers to be around 2°.

- $\varepsilon(t)$. The time dependent short term error is difficult to estimate. To a large extend this dependence is removed during the bias correction. It is reported by the manufacturer of the Litton G-2000 that the bias has a random component of ∼1 deg/hour, and I have included this term as a way of accounting for any time dependent bias that was not corrected by filtering.

The error on the gyro is in itself actually quite small, and the largest error source comes from the tracker time delay determination.

Table 2.2 gives an overview of the magnitude of the components in the gyro error model.

2.6 Building the event time series

Once the attitude has been determined, and the DCM = R_b^l has been constructed, the detector events can be transformed into sky coordinates. Continuing in the same formalism as above, the body frame oriented detector coordinates are given by

$$D_b = \gamma_b + \mathbf{b} + \Delta D_{b,0} \ , \tag{2.23}$$

Error component	Value
$eBias_x$ (Roll)	∼0.003 deg/hour
$eBias_y$ (Pitch)	∼0.003 deg/hour
$eBias_z$ (Yaw)	∼0.003 deg/hour
$eGain_x$ (Roll)	0.85 deg
$eGain_y$ (Pitch)	0.83 deg
$eGain_z$ (Yaw)	1.34 deg
M_{xyz}	2 deg
$\varepsilon(t)$	1 deg/hour

Table 2.2: Gyro error model components with typical values.

where $\mathbf{b}$ is the gyro basis vector, $\Delta D_{b,0}$ are the platescale corrected event coordinates relative to its own center, and γ_b the offset between on-axis star tracker center position on the sky and the common co-aligned center of the detectors. The target object, O_l, in local level frame horizontal coordinates is obtained by simply using the transformation, R_l^b, so that $O_l = R_l^b(\gamma_b + \mathbf{b})$.

Obtaining the coordinates in this direct method poses some problems, as the accumulation of misalignments shows itself as a coordinate drift, and is the most severe for observations done with the off-axis tracker (T2). A more robust method is to first calculate the track of the object as it appears on the detector in the body frame. If the target has coordinates $\bar{O}_l$ then $\bar{D}_b = R_b^l \bar{O}_l = \mathbf{b} + \bar{\gamma}_b + \Delta D_{b,0}$. The true accumulated offset $\bar{\gamma}_b$ can then be calculated from $\bar{\gamma}_b = D_b - \bar{D}_b$ if $\gamma_b = 0$. Replacing the preflight estimated γ_b with $\bar{\gamma}_b$ ensures that we have removed any lingering drifts that might have accumulated themselves due to angle misalignments, so that D_b can safely be transformed.

2.7 On-axis tracker versus off-axis tracker

On of the main problems encountered during the aspect reconstruction is the degeneracy of yaw and roll. With the available sensor array a few vital feeds were missing, and due to this the yaw and roll axis suffered a degeneracy. The GPS roll can be used to remove the bias and to determine the gain, but the GPS is noisy and its alignment with the gyro frame is not known to better than a few degrees.

When reconstructing with the on-axis star tracker the above procedure will ensure that a very precise transformation matrix, R_b^l, is found using a combination of yaw, pitch and roll, which do not necessarily have to be the exact gyro rates. The principle here is that getting from point p in frame A

to point d in frame B can be done in an infinite number of ways. One could for example completely disregard the roll, as was done during flight, and let the roll movement be included into the azimuth. But once one has to deal with position offsets from point p in frame A, transformed into frame B, the errors start accumulating, since now the transformation R_b^l can no longer be arbitrary. As an example imagine a disk with a spot at the center and one at the edge. The actual movement of the disc is a straight translation, however, spinning the disc by 180° while translating will still get the disc to its correct destination. For the off-axis spot this second translation will bring the point to a wrong location, compared to the direct translation.

Because the gamma-offsets, γ, are small the residual error drifts in the on-axis tracker case are also small. However, for the off-axis tracker the drifts are far more severe. In this case the reconstructed matrix, R_b^l, has been designed to transform between the body frame, B, and the off-axis tracker coordinates, T_2. When it is subsequently transformed into the on-axis star tracker coordinates, $T_1 = T_2 + R_b^l\alpha$, errors due to the degeneracy of yaw and roll, show up as drift errors, $\Delta = (\bar{R}_b^l - R_b^l)\alpha$, where the bar denotes the real transformation. If lucky this is a smooth drift, but when the track on the sky has discontinuous jumps, the drift can be discontinuous as well. It is therefore better to cut down the time series in sections free of sudden jumps. One cannot make these sections to short either as one starts to loose the ability to correct the long term bias drift, and instead become dominated by the delay errors from the trackers.

Sections of length 5 minutes appear to be good, since jumps are frequently associated with the reception of the GPS longitude and latitude.

2.8 Summary

I have in this Chapter described how to construct the aspect transformation matrix, R_b^l, needed to solve the attitude problem, and identified the know error sources: slow GPS updates, bias drifts and tracker delays. I have presented an analysis on the systems typical time modes, and shown that ~ 3 seconds marks a critical time frame below which care should be taken in correcting the gyro. Finally I have described the problematics of the off-axis tracker and how to overcome them.

In the next Chapter I will use the tools developed here on examples from the flight.

Chapter 3

Aspect Solutions

3.1 Flight Time Line

HEFT was launched on the 18'th of May 2005 at 18:00 UTC time and flew a total of 24 hours. The average float altitude was 38,500 m, and out of 20 hours of potential observation time 6-7 hours were spend on actual targets. The gondola flight time is given in hours since 1st of May 2005, and in this time line launch occurred at 451 hours and decent at 475 hours. Table 3.1 lists the targets and the length of the observations in gondola flight time. The numbers behind the Crab and Cygnus X1 labels refer to the quality of the observations with 1 being the best. The observation configuration was either in unflipped or flipped mode, where unflipped means the gondola was tracking with the on-axis star tracker, and flipped means it was tracking with the off-axis star tracker. For observations with detection flag 'yes' we have been able to reconstruct an actual spot on the detector. For the 'maybe' flag we have not actually seen a spot, but the countrate is higher than the background, indicating that the source is at times detected.

In this section I will only discuss the observations for which we have an actual detection and have been able to reconstruct a spot. This does not mean there is nothing to be done about the other observations, but at the moment we do not have good enough data on the detectors to properly subtract all random and systematic effects, that obscure the real source counts. I will go over some of the steps of the aspect reconstruction of selected sections of the Cygnus X1 and the Crab observations, then present the image reconstruction and finally show the extracted spectra. As it turned out detector C performed poorly during flight I will in the following ignore this detector.

Label	time range [hours]	Ra [deg]	Dec [deg]	Mean El [deg]	Configuration	Detection
Crab 3	456.8-457.4	83.642	22.015	33	flipped	yes
Mkn 491	459.8-460.7	166.110	38.209	69	flipped	maybe
Her X1	461.8-462.5	254.460	35.343	63	flipped	no
Cygnus X1 2	465.0-465.6	299.595	35.202	38	unflipped	yes
Cygnus X1 3	466.35-467.0	299.595	35.202	81	flipped	yes
GRS1915+105	467.2-467.6	288.785	10.946	65	flipped	maybe
Cygnus X1 1	468.3-469.0	299.595	35.202	74	flipped	yes
3C454.3	469.4-472.0	242.208	16.147	70	flipped	maybe
Crab 1	472.9-473.12	83.642	22.015	35.6	unflipped	yes
Crab 2	474.18-474.36	83.642	22.015	51.5	unflipped	yes

Table 3.1: HEFT flight time line. The observation times are given in gondola time and is in hours since the 1st of May. The Ra and Dec columns list the sky coordinates of the target taken from the INTEGRAL General Reference Catalog [13]. The configuration refers to the flipped or unflipped observations, where the unflipped means the observation was stabilized by the on-axis star tracker, while the flipped configuration was stabilized by the off-axis tracker. The detection column states whether a detection was made or not ... or maybe.

3.2 Event Extraction

The raw events are transformed from pulse heights to energy through a series of corrections. Figure 3.1 shows an outline of the data reduction, starting with the CRUSH program, translating the compressed flight information and extracting the raw events with the time header information. The photon data is first baseline subtracted. The baseline is a function of pixel electronics and is therefore unique for each pixel. Next the pulse heights are reconstructed and the risetime of the event is calculated. The rise time is the time it takes for the pulse to reach its maximum, after which it starts to decay. The problem here is the finite sampling time makes it difficult to determine the exact height of the pulse, and thus with a proper rise time correction the amount of decay can be calculated such that the pulse height is obtained. The pulse heights, that is the pre-amplifiers, drift with temperature and must therefore be temperature corrected. Once all corrections are made, pulse heights can be converted to energy, and multiple pixel events can then be treated properly for charge sharing.

This constitutes the basic event list containing pulse heights. The events are flagged according to their event type: single pixel event, multiple pixel event, bursting pixel. It turns out that up to 50% of all events are two pixel events [14], and for the event extraction I have therefore included both one and two pixel events. The energy range was chosen to be 10-70 keV.

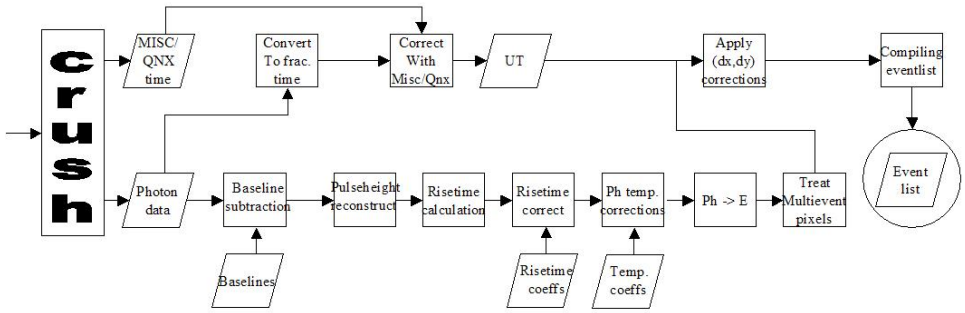

Figure 3.1: Event extraction flow diagram. The individual steps are explained in the text.

3.3 Aspect Reconstruction

3.3.1 The Cygnus X-1 Aspect Reconstruction

The observation of Cygnus X-1 was made on the 19'th of May 12:14 to 13:00 UTC, at an average elevation = 74°, and the time axis in the subsequent plots is in hours since 1 may 2005 unless otherwise stated.

Once the gyro has been reconstructed and the tracker ra/dec transformed into az/el, the first step is to remove the bias drift. Figure 3.2 shows the residual of the star tracker solutions and the gyro. Here the label "gyro" denotes the horizontal azimuth and elevation coordinates derived from the the gyro yaw, pitch and roll, and "star" represents the tracker solutions. The gyro is samples at 10 Hz, while the star tracker has a solution rate of ~ 3 seconds, and thus the plot is binned according to the tracker. The left panel shows the residual before the application of the bias correction, and demonstrates the effect of not having had applied a bias correction. The right panel is after correction, and the 1σ dispersion of the residuals is 0.2" for the azimuth and 0.22" for the elevation.

At time t$\sim$ 468.65 there is a defect of the filtering function. A long time section is desirable when using a lowpass filter since it yields a smooth function, however, at the risk of getting defects due to sudden jumps. The filter will fit a jump with a smooth section, and as a result the step appears as a large amplitude deviation. To avoid these defects I have generally cut the series into smaller sections as dictated by the jumps. This usually corresponds to the time when a longitude latitude fix was received from the GPS, but not always and the reconstructions require some empirical investigations to find just the right cuts. The error bars are due to the uncertainty in the longitude and latitude values as described in Section

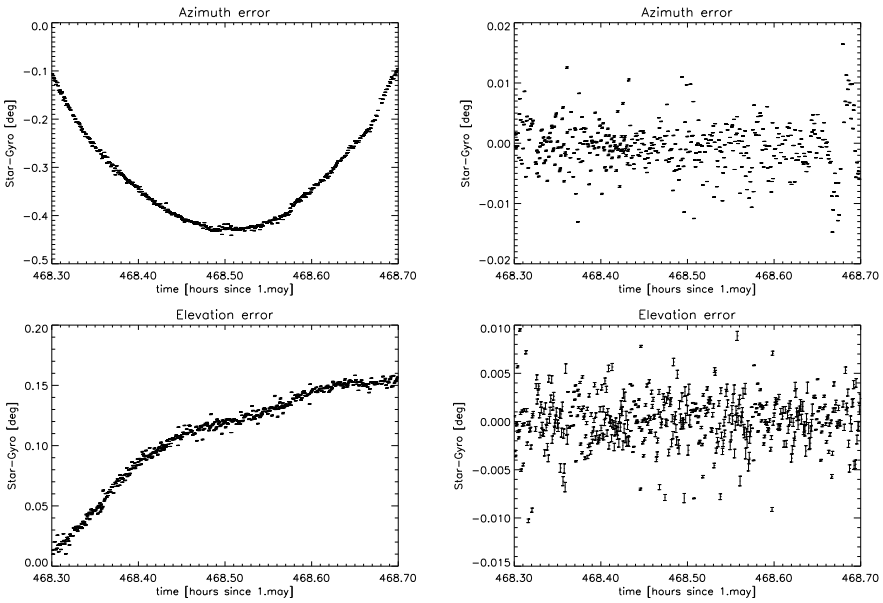

Figure 3.2: Star tracker - gyro residuals for the Cygnus X1 observation. The plots are binned to the tracker solutions. Left panels shows the aspect without bias corrections and the right panel with bias corrections included.

2.4.1, and as can be seen in the lower plot, the time between receiving a new attitude fix from the GPS has the largest positional errors.

Figure 3.3 shows the gondola aspect in the local level frame in the left panel. The elevation values are in excess of 90° because the gondola is in a flipped configuration and thus the telescope arm has travelled through the zenith to the other side. The real elevation is 180°-El. The right panels show the positional offset in arcmin of the source relative to the on-axis position in sky coordinates. The stability in Right Ascencion is controlled by the elevation, which as shown was oscillating at a high frequency. The declination is dominated by the azimuth, and though the small scale oscillations were less than for the ascension, the roll dominates the off-axis movement, since the elevation is high, and the roll couples more strongly than the azimuth. The FOV of the detectors is 15 arcmin so the source remained on the detectors during the entire observation.

Once the aspect DCM, R_b^l, has been obtained the next step is to rebuild the time series of the events. The challenge with Cygnus X-1 is that the observation was stabilized by the off-axis star camera, and thus we know that the difficulty with constraining the roll bias has resulted in the mixing

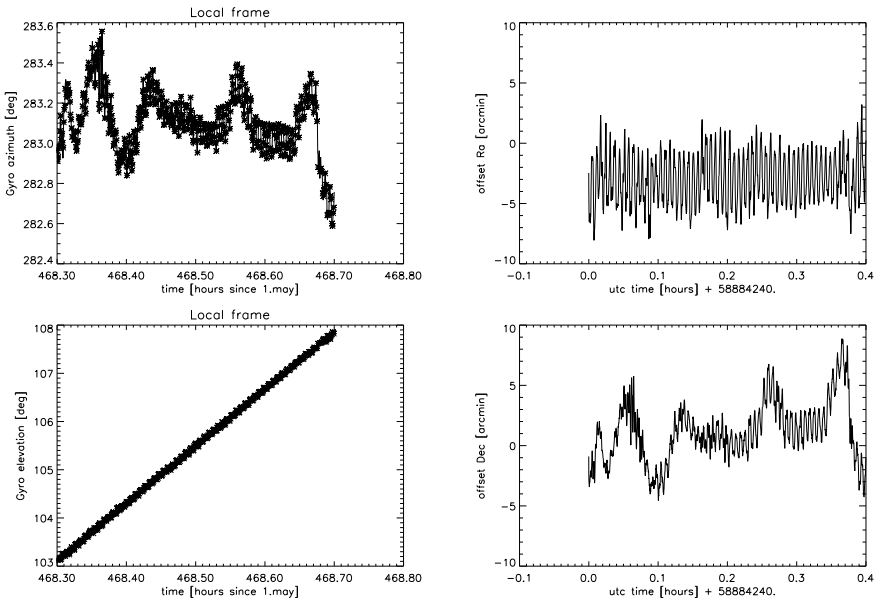

Figure 3.3: Left panel: Final aspect solution binned in gyro space with tracker solutions plotted as stars. Right panel: The source offset from onaxis in arcminutes as a function of UTC time.

of the yaw and roll, and shows up as a coordinate drift when the off-axis star solutions are transformed into the on-axis tracker position.

As explained in Section 2.6 the drift affected gamma offset, $\bar{\gamma}_b$, can be found by $\bar{\gamma}_b = D_b - R_l^b \bar{O}_l$, where $\bar{O}_l$ is the Cygnus sky coordinates and $D_b = \mathbf{b} + \Delta D_{b,0}$ are the detector coordinates in the body frame. Figure 3.4 shows the events taken from detector B, and in the left panel $\bar{\gamma}_b$ is plotted for the azimuth and elevation. It may seem confusing why it is not a constant offset, but the important part to remember is that R_b^l was designed for the off-axis tracker such that $T_2 = R_b^l(\mathbf{b} + \alpha)$, where α is the offset between the off-axis tracker, T_2, and the on-axis tracker, T_1. R_b^l has mixed yaw and roll axis, and although it will precisely yield T_2 when used on the basis $(\mathbf{b} + \alpha)$, that is not the case for $T_1 = R_b^l \mathbf{b}$. However, because the detector track is quite clear, we can correct the misalignment using empirical fits and ensure that $O_l = R_b^l(D_b + \bar{\gamma}_b)$.

The right panel shows the tracks of $D_b + \bar{\gamma}_b$ (black) and $\bar{D}_b$ (red). What can be seen here are events that obviously are not related to the object, and since only an unrealistically large roll could justify those events to be object related, they are background.

Figure 3.5 shows the final product of the aspect reconstruction. The

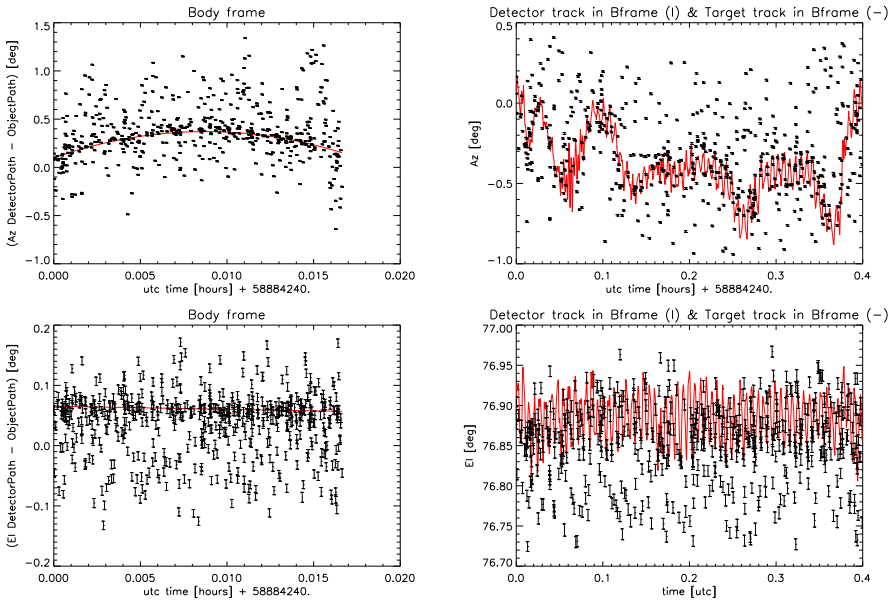

Figure 3.4: Events from detector B. Left panel: $\bar{\gamma}_b$ offset as a function of UTC time. Red curve marks the emperical fit to the drift. Right panel: Source track in the body frame. Black points are detector events and the red curve the track of Cygnus X1 in the body frame.

binning here is as in Figure 3.4 in events from detector B. To the right is plotted the path of the source in horizontal coordinates, and to the left in sky coordinates. The error bars here and in the previous plots are obtained as explained in Section 2.5.3.

3.3.2 The Crab Aspect Reconstruction

The Crab observation were made on the 19'th of May 16:53 to 17:10 UTC at an average elevation = 35.6°.

The Crab was observed in the unflipped configuration, which means the on-axis tracker was used to stabilize the pointing. The aspect reconstruction of the Crab follows the same procedure as Cygnus X-1, but is simplified by being on-axis, such that the constructed rotation matrix is fairly free of misalignments.

Because the observation used the on-axis tracker (T1), there was unfortunately a significant time delay, since this tracker was in particular prone to delays as discussed in Section 2.5.2. Figure 3.6 shows the residuals between the star tracker solutions and the gyro with the same time tag, before (left panel) and after (right panel) the time delay correction. The time delay

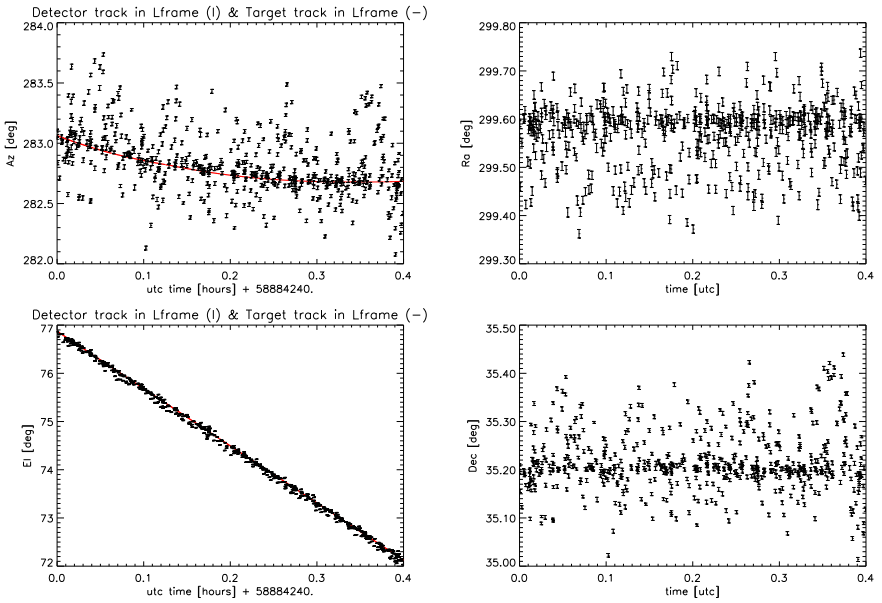

Figure 3.5: Events from detector B. Left panel: Event and source track in the local horizontal frame. Black points are the detector events and the red curve the track of Cygnus X1. Right panel: Events in sky coordinates.

was on the order of ~ 3 seconds and by correctly aligning the time axis the residual dispersion is improved significantly form 0.9" for both azimuth and elevation to 0.36".

Figure 3.7 shows the final aspect to the left, and on the right the gondola offset from the source. The precision is better than for the cygnus observation for two reasons. Firstly because of the lower elevation the roll was less dominant, and secondly use of the on-axis star tracker constrains the drifts. Unfortunately the observation was cut short because the crab field is very poor on bright stars and very difficult to match for extended periods.

The left panel of Figure 3.8 shows $\bar{\gamma}_b$ for the azimuth and elevation. Because we are stabilized by the on-axis tracker the $\bar{\gamma}_b$ drift is much smaller than for Cygnus, but still present since the actual spot is slightly off-axis from the tracker center for which the transformation matrix was designed. This residual drift is the gammaoffset. The right panel shows the tracks of $D_b + \bar{\gamma}$ (black) and $\bar{D}_b$ (red).

Figure 3.9 shows the final product of the aspect reconstruction. The binning here is as in Figure 3.4 in events from detector B. To the right is plotted the path of the source in horizontal coordinates, and to the left in

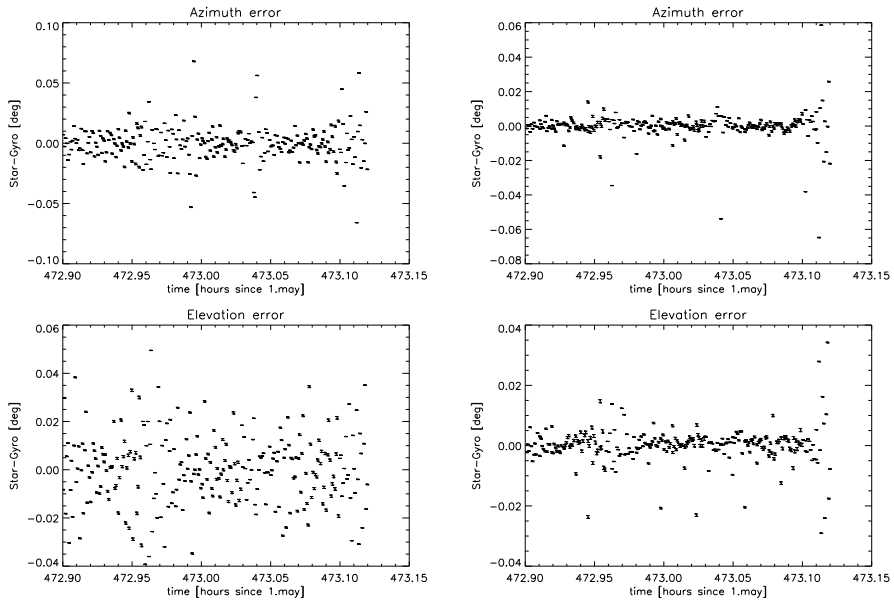

Figure 3.6: Star tracker - gyro residuals for the Crab observation. The plots are binned to the tracker solutions. Left panels shows the aspect without bias corrections and the right panel with bias corrections included.

sky coordinates. The error bars here and in the previous plots are obtained as explained in Section 2.5.3.

3.4 Co-alignment

In the ground calibration, described in Section 1.7, it was estimated that the co-alignment of the x-ray source was good to about 1 arcminute, and that in this configuration HF1 and HF2 were offset with 2' and HF3 with 1.2'. From this alignment the center pixel x,y=[0,0] in each detector was derived.

Using the two on-axis crab observations crab1 = [472.9,473.12] and crab2 = [474.18,474.36], the relative misalignment between HF1 and HF3 can be estimated. The horizontal sky coordinates for the object and center pixel [0,0] were calculated and the coordinates from Detector A and Detector B subtracted. The offset in azimuth and elevation from the crab1 and crab2 observation is shown in Figures 3.10 and 3.11. Assuming that the center pixel of both detectors represents the on-axis position on the sky, and that the object paths on both detectors must coincide, the relative offset between

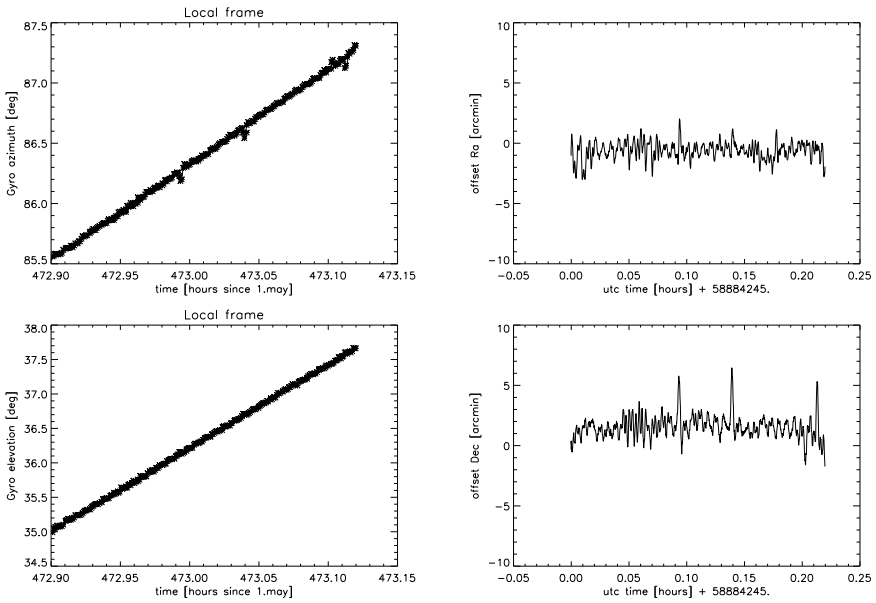

Figure 3.7: Left panel: Final aspect solution binned in gyro space with tracker solutions plotted as stars. Right panel: The source offset from onaxis in arcminutes as a function of UTC time.

the two center pixels is $\Delta = \sqrt{(}\Delta\bar{A}z^2 + \Delta\bar{E}l^2)$, where the bar represents the gaussian center fit of the offset distributions. For the crab1 observation $\Delta = 0.5 \pm 1.2$ and for the crab2 observation $\Delta = 0.2 \pm 1.7$ if a gaussian distribution is assumed. Within the given errors and the error on the ground calibration, the two optics appear to have been well co-aligned during flight.

3.5 Image Reconstruction

Following the convention of most x-rays instruments to date, the images were reconstructed using the instrument response and aspect solution [15]. In this formalism the observed counts, $C(h, \hat{\mathbf{p}})$, as a function of pulseheight h and sky position $\hat{\mathbf{p}}$ is the integral of the exposure map, $E(h, \lambda, \hat{\mathbf{p}})$, and the PSF smeared source surface brightness, $S_f(\lambda, \hat{\mathbf{p}})$:

$$C(h, \hat{\mathbf{p}}) = \tau_{eff} \int d\lambda E(h, \lambda, \hat{\mathbf{p}}) S_f(\lambda, \hat{\mathbf{p}}) \ , \tag{3.1}$$

where τ_{eff} is the exposure time. This integral extends over all wavelengths which contribute to a pulse-height bin h, and assumes that the mirror effective area and point-spread functions are slowly varying, which is a good

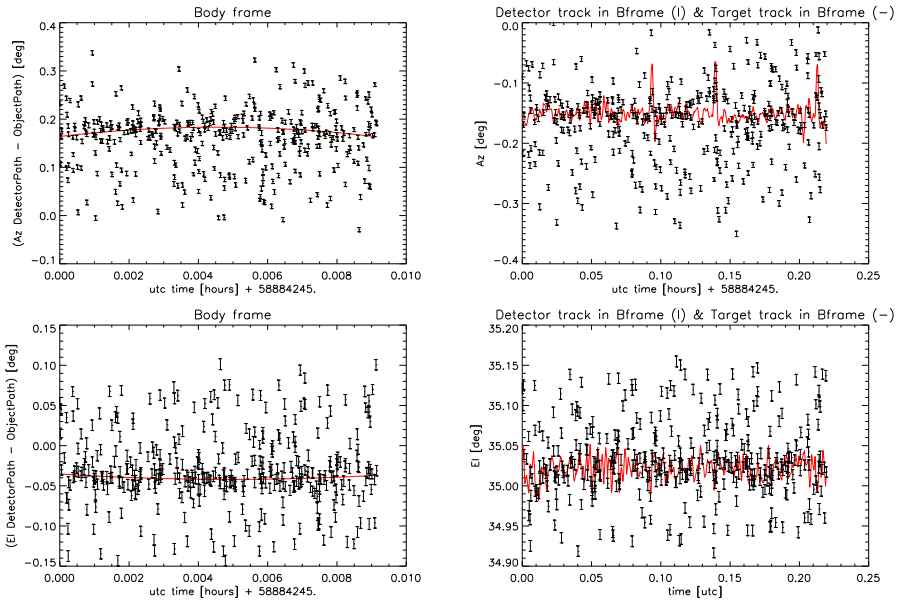

Figure 3.8: Events from detector B. Left panel: $\bar{\gamma}_b$ offset as a function of UTC time. Red curve marks the emperical fit to the drift. Right panel: Source track in the body frame. Black points are detector events and the red curve the track of the Crab in the body frame.

enough approximation for the HEFT effective area. When rebinning to achieve statistically significant numbers of counts per pixel, the integral can be summed over a pulse-height interval Δh instead:

$$C(\Delta h, \hat{\mathbf{p}}) \sim \tau_{eff} E(\Delta h, \lambda_0, \hat{\mathbf{p}}) \int_{\lambda \varepsilon \Delta\lambda} d\lambda S_f(\lambda, \hat{\mathbf{p}}) \, , \tag{3.2}$$

such that $C(\Delta h, \hat{\mathbf{p}}) = \sum_{h \varepsilon \Delta h} C(h, \hat{\mathbf{p}})$, and where $E(\Delta h, \lambda_0, \hat{\mathbf{p}})$ has been moved out of the integral under the assumption that it is relatively constant over $\Delta\lambda$. To obtain the PSF smeared image one simply divides out the sides:

$$\int_{\lambda \varepsilon \Delta\lambda} d\lambda S_f(\lambda, \hat{\mathbf{p}}) = \frac{C(\Delta h, \hat{\mathbf{p}})}{\tau_{eff} E(\Delta h, \lambda_0, \hat{\mathbf{p}})} \, . \tag{3.3}$$

The exposure map $E(\Delta h, \lambda_0, \hat{\mathbf{p}})$ is the instrument map tiled on the sky using the aspect solution. The instrument map is obtained by folding in the positional and energy dependency of the effective area curves shown in Figure 1.6 onto the detector. The resulting instrument map at 40 keV is shown in Figure 3.12 for the 48×48 pixel array in cm^2. These maps are combined with the aspect solution to form the exposure map or Ancilary Response Matrix, the ARF.

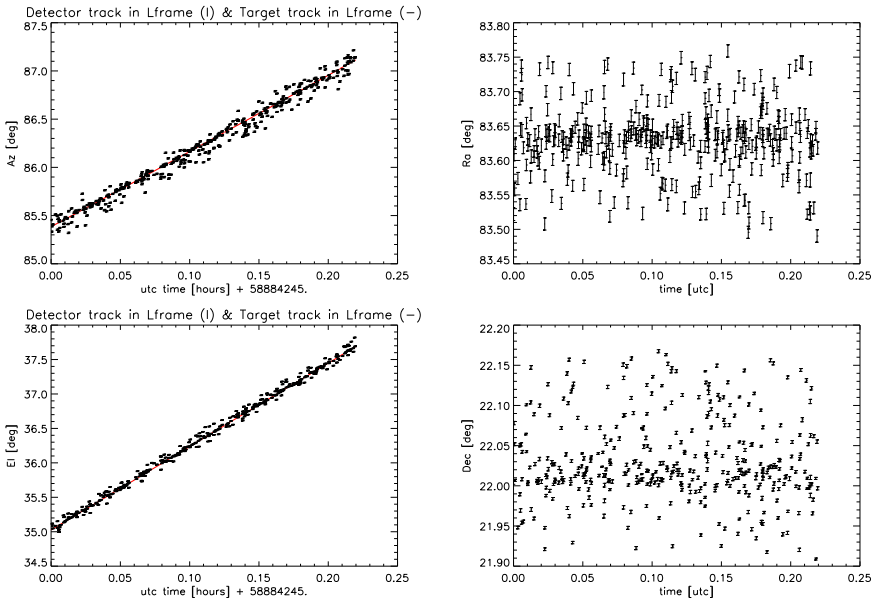

Figure 3.9: Events from detector B. Left panel: Event and source track in the local horizontal frame. Black points are the detector events and the red curve the track of the Crab. Right panel: Events in sky coordinates.

To produce a background subtracted spectrum one first has to determine the background. Due to the size of the detector and the object path on it, which generally took it across 50% of the detector, the background must be extracted from a different observation period. The chosen background period is 47 minutes long and was taken during a time of starhopping at time=[463.5,464.3], with an average elevation of 45°. Using the above, a PSF smeared background image of the detector was obtained and the x and y collapsed profiles are shown in Figure 3.14 for detector A and B for energies E = [10,70] keV. It has been assumed and will further on be assumed, that the detector Response Matrix is a uniform function across the detector. There is strong evidence that this is not the case, but since the analysis is not yet complete, I have assumed a uniform response. Looking at the shape of the background from detector A there is some indication of non-uniformity, which can either be attributed to the non-uniform RMF or the possibility that the boresight is off from its assumed position, in which case its application may be positionally off. With this the average background is 4×10^{-4} ph/counts/cm^2/s/keV.

When applying the background from a different observation, the eleva-

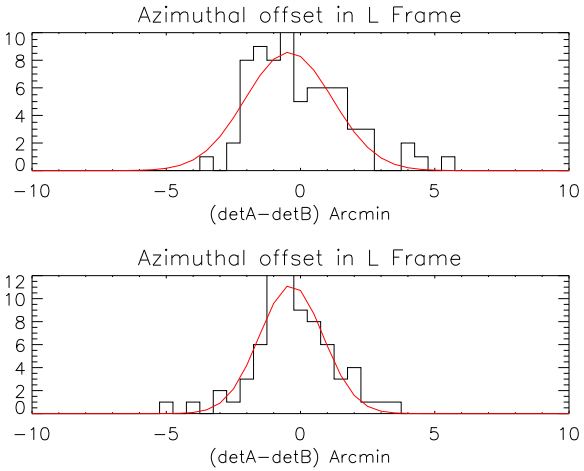

Figure 3.10: Sky coordinate detector offset for Crab 1 observation. The top plot shows the offset in azimuth of (detector A - detector B) where the red line shows the fitted gaussian with mean value -0.4 and $\sigma = 1.6$. The middle plot shows the offset in elevation of (detector A - detector B) and gaussian with center value 0.3 and $\sigma = 1.2$.

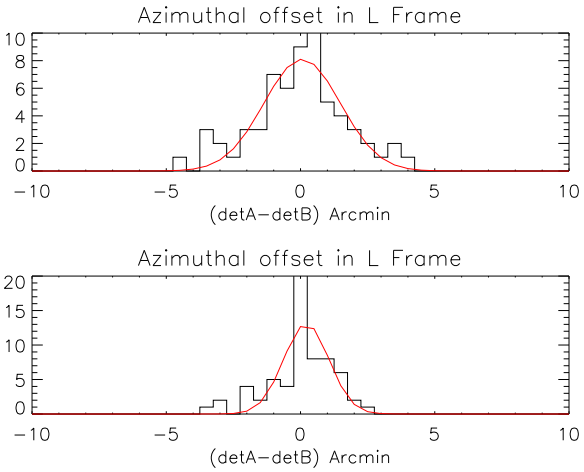

Figure 3.11: Sky coordinate detector offset for Crab 2 observation. The top plot shows the offset in azimuth of (detector A - detector B) where the red line is the gaussian fit with center value 0.06 and $\sigma = 1.4$. The middle plot shows the offset in elevation of (detector A - detector B) and the gaussian with center value 0.2 and $\sigma = 1.2$.

tion of the two observations needs to be taken into account and the count rate scaled with the atmospheric attenuation. Figure 3.13 shows the atmospheric depth in g/cm^2 at the aperture for the entire flight in hours since launch and includes corrections for altitude and viewing angle [16]. Also shown is the atmospheric attenuation as a function of energy at the atmospheric depths of 3, 4 and 5 g/cm^2, calculated from tables found at NIST [17].

Subtracting the backgrounds from the source is formally expressed like:

$$S(h) = \frac{D(h)}{a_D t_D} - \frac{x_D}{x_B}\frac{B(h)}{a_B t_B} \,, \tag{3.4}$$

where D denotes the observation, and B the background observation, $a_{D,B}$ is the extraction area for the observation and the background, and $t_{D,B}$ the respective exposure times. The values x_D/x_B is a scale factor, which in our case includes differences in air attenuation in the two observations.

The ARF and the observation has been binned for ΔE = 2 keV, but the images shown are the summation of energies E = [10,70] keV.

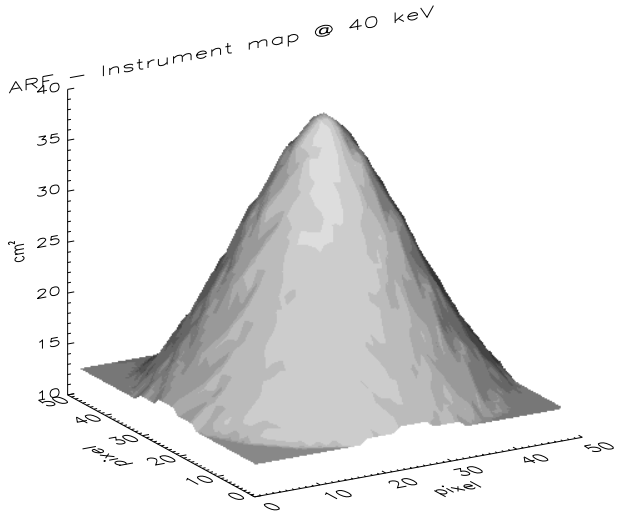

Figure 3.12: Instrument map for the 48 × 48 detector array at 40 keV.

3.5.1 Cygnus-X1 images

Cygnus X-1 is not a primary scientific target for HEFT, but it is of great value as a calibration source, and was during this flight one of the primary

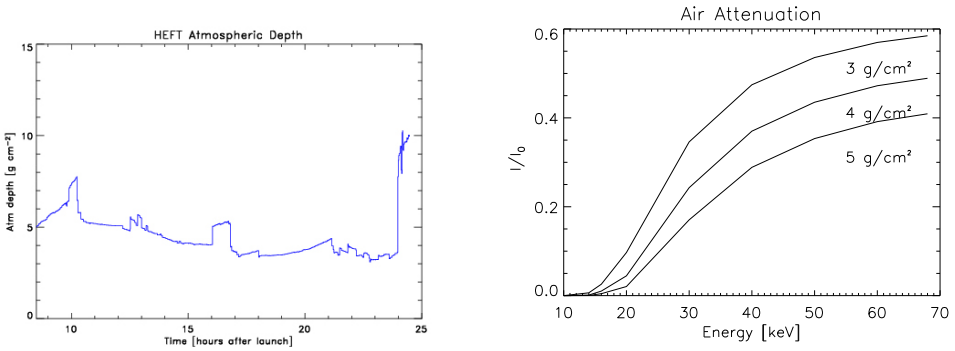

Figure 3.13: Left: Atmospheric depth as a function of gondola flight time in hours since launch. The atmospheric depth includes the altitude and viewing angle made by W. Baumgartner [16]. Right: Attenuation for atmospheric depths of 3,4 and 5 g/cm^2. Mass absorption coefficients have been taken from the National Institute of Standards and Technology, NIST, data base [17].

targets.

Cygnus X-1 is one of the most studies X-ray sources, and is 'the' prototype black hole binary system. The source exhibits two main spectral states, a Low Hard State, LHS, and a High Soft State, HSS, as well as a brief transition period[18]. See Section 5.2.1 for a few details on accretion disk mechanics. It spends about 80% of its time in the LHS and the spectrum can be described by a power law with photon index $\Gamma \sim 1.7$, an exponential cutoff at $\sim$ 150 keV, and a reflection component at 30-50 keV [18] [**?**]. In the HSS the spectra can be well modelled by a standard thermal emission from an accretion disk. The flux at 20-60 keV is for Cygnus X-1 is 2.52×10−8 erg/s/cm^2 as given at the INTEGRAL General Reference Catalog [13] for the LHS.

Following the above procedure Figure 3.15 shows the resulting image for Cygnus-X1 for detector B for energies E=[10,70] keV. The presence of 'hot pixels' at the edge of the detector is an artifact of dividing the observation with the exposure map, but has little significance other than standing out to the eye. Using a 2d gaussian fit the FWHM width and center of the peak is found to be FWHM = 85.38"±0.2 at [Ra,Dec] = [299.60, 35.20]±0.005. The positional error is comparable to the pixel size, and including it as an additional σ_x = 18" the FWHM increases with 2". The encircled energy curve of the Point Spread Function would be wider by a factor of 2 because it is affected by an incomplete detector response, and so has not been calculated here.

The middle panel shows the Ra and Dec collapsed profiles of the image

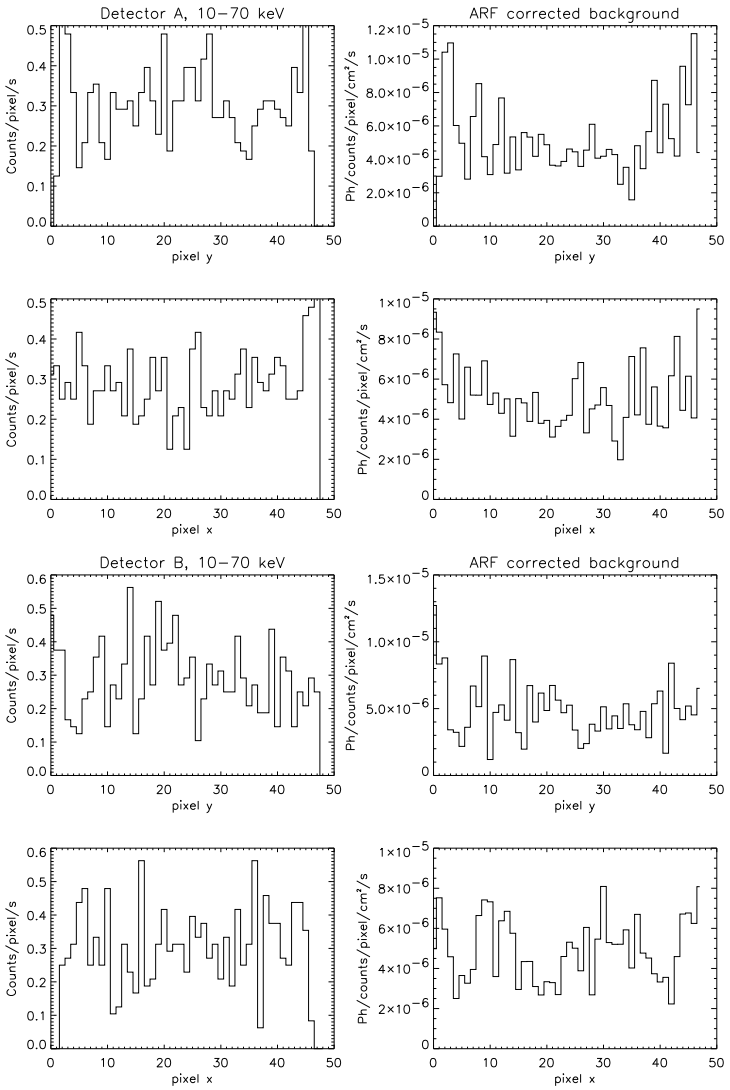

Figure 3.14: Detector A and B backgrounds for the time interval time=[463.5,464.3] in the energy range E=[10,70]. Left panel: The x and y collapsed detector array raw counts/s. Right panel: The ARF corrected background including the effective area vignetting function. The atmospheric depth was during the background observation ~ 5 g/cm^2.

before it has been background subtracted. The solid lines represent the background shown as contours and as a surface in sky coordinates in the bottom panel. The total number of counts in the observation is 995 of which 646 are background counts and 349 source counts.

3.5.2 Crab images

Without fail every single instrument ever flown has pointed its virgin eyes on the Crab and HEFT was, of course, no exception.

The Crab nebula is the remnant of a supernova and contains at its core a central pulsar rotating with a period ∼33 milliseconds. The bulk of the energy of the pulsar as it slows down is carried off in the form of a magnetized, relativistic pulsar wind [19], which emits synchrotron radian. *Chandra* has resolved and mapped a torus and jets in great detail, as shown in the lower plot of Figure 3.19, and it has been found that the power law photon index changes across the pulsar, from a hard index of Γ ∼1.7 to 2.0 in the torus and the central pulsar, to 2.0-3.5 in the outer parts and the jets [19]. The canonical value for the entire nebula has been found to lie around $\Gamma \sim 2.1$. The physical size of the central nebula containing the torus and the jets is about 2.5' to 3' and so it should be possible to resolve the extended emission with HEFT. The flux at 20-60 keV is for the Crab is $1.24\times10-8$ erg/s/cm^2 as given at the INTEGRAL General Reference Catalog [13].

The Crab observations were shorter in length because of the difficulty in stabilizing on the poor Crab star field, and therefore I will show three of the best periods. Figure 3.16 shows the resulting image for the Crab for detector B in the time interval time=[472.9,473.12] (crab1), Figure 3.17 for time=[474.18,474.36] (crab2), and Figure 3.18 for time=[456.8,457.6] (crab3). The presence of 'hot pixels' at the edge of the detector is an artifact of dividing the observation with the exposure map. Using a 2d gaussian fit the FWHM width and center of the peak are given in Table 3.2, and for the 3 observations combined the average FWHM = 95.20" at [Ra,Dec] = [83.63,22.01]±0.01. The bottom panels show the Ra and Dec collapsed profiles of the images before background subtraction. The solid lines represent the background shown as contours. The total exposure time for the 3 observations is 1 hour and the total number of detected counts is 1195, of which 756 are background and 439 source counts. During the crab3 exposure the source was not on the detector at all times, and so the actual source count number could have been higher.

Figure 3.19 shows the three crab images smoothed with a gaussian kernel of width = 36". The axis are in pixels aligned with dec on the y-axis and ra

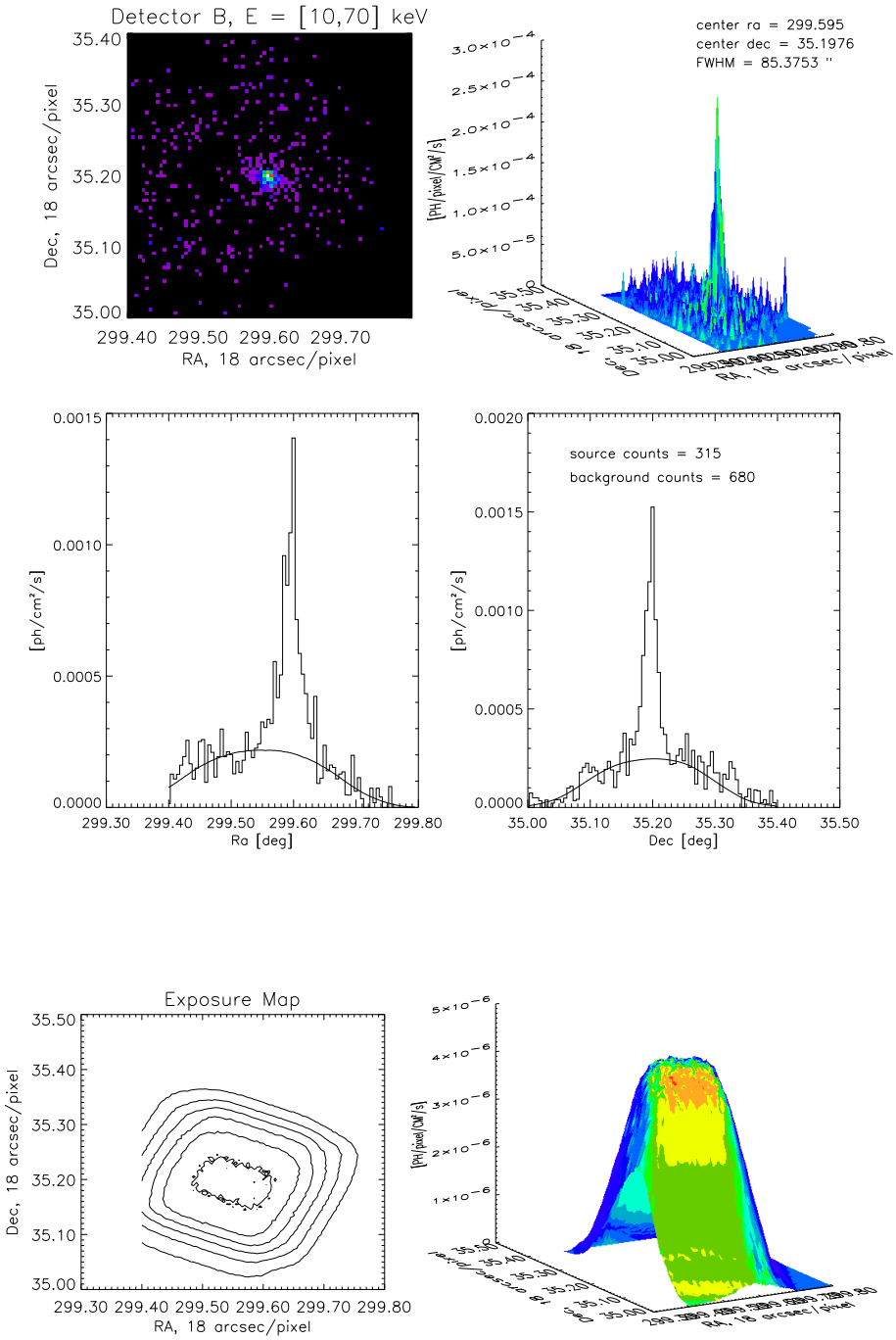

Figure 3.15: Cygnus X1 observation at time=[468.3,469] on Detector B.

on the x-axis and 1 pixel = 18". Comparing with image of the the Crab from *Chandra*, we would expect extended emission on the diagonals. The images are inconclusive, but there does appear to be some elongation present, and the collapsed detector profiles do appear to have some satellite maxima after the background is removed.

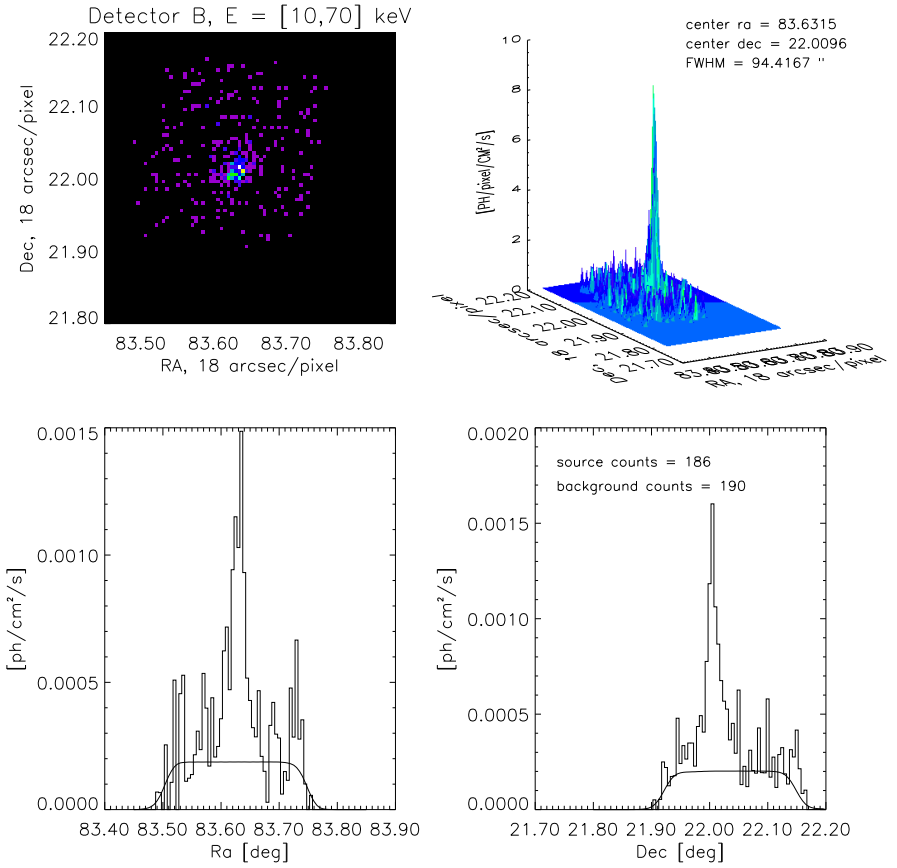

Figure 3.16: Crab observation at time=[472.9,473.12] on Detector B.

3.5.3 Discussion

Table 3.2 summarizes the image properties of the selected observations. It can be seen that in general detector A has a worse performance than detector

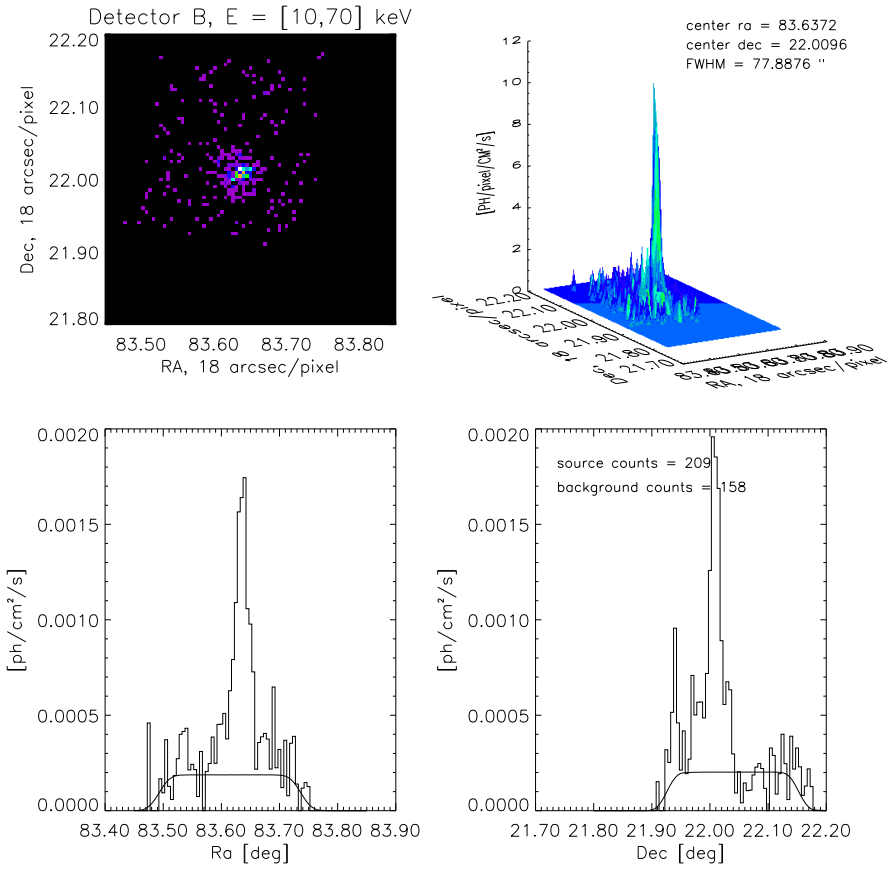

Figure 3.17: Crab observation at time=[456.8,457.6] on Detector B.

B. A probable reason for this is an offset in boresight, which causes the exposure maps to be applied in the wrong position. When the gondola is steady on the source as in observation Crab 1, Crab 2 and Cygnus X1 1 the background is approximately uniform and the exposure map even enough that detector A yeilds a nice image. When the aspect solution is complex so is the background and the exposure map, and any discrepancy in boresight becomes obvious. Deriving the boresight for detector A has unfortunately not yet been done.

The boresight on detector B appears to be well aligned with where we

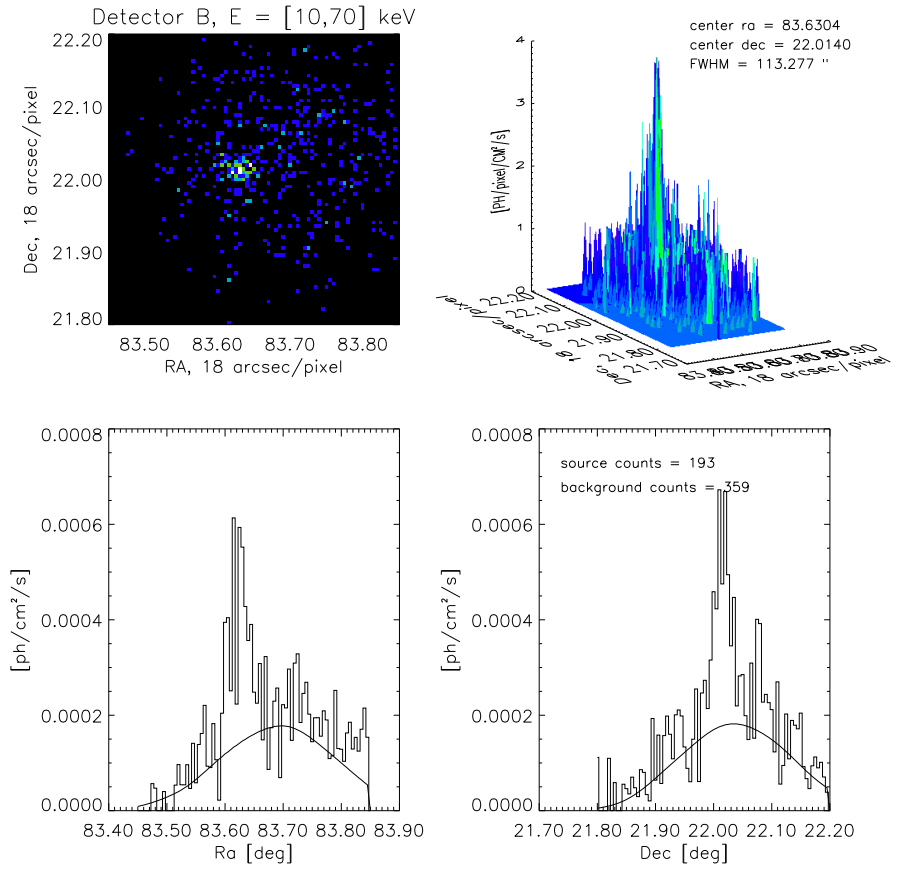

Figure 3.18: Crab observation at time=[474.18,474.36] on Detector B.

expect it to be and most of the detector B images are fairly good. Comparing with the HPD for optic HF3 from before flight, measured at 8 keV to be 107", it can be seen that the FWHM from the point-source Cygnus X-1 is actually smaller. The reason for this could be that the HPD at 8 keV was calculated using the encircled energy function, while the FWHM has been calculated by fitting a gaussian. From the calibration experiments is has been observed that many of the scans deviate slightly from a gaussian and that in general the FWHM does not agree with the HPD. Further the 8 keV calibration only included 22 shells out of 72.

Label	time range [hours]	Ra [deg]	Dec [deg]	FWHM [arcsec]	Total [counts]	Source [counts]	Background [counts]
Crab 1	472.9-473.12						
Detector A		83.625	22.015	94.30±0.3	290	127	163
Detector B		83.632	22.009	94.42±0.3	376	186	190
Crab 2	474.18-474.36						
Detector A		83.636	22.014	81.503±0.2	282	185	97
Detector B		83.637	22.009	77.89±0.2	367	167	200
Crab 3	456.8-457.4						
Detector A		83.629	22.017	100.89±0.2	607	453	154
Detector B		83.630	22.014	113.28±0.3	552	193	359
Cygnus X1 1	468.3-469.0						
Detector A		299.600	35.198	159.27±0.3	1045	347	698
Detector B		299.595	35.197	85.38±0.1	995	349	646
Cygnus X1 2	465.0-465.6						
Detector A		299.638	35.272	150.966±0.3	744	503	241
Detector B		299.632	35.282	65.399±0.2	622	206	416

Table 3.2: Summary of image properties of the selected observations.

Given the errors HF3 appears to perform as expected. The case is harder to make for HF1 until a proper study of the possible boresight offset has been determined.

3.6 Spectral Analysis

I have extracted spectra for the image shown above using a zero order approach. The final pieces needed for a full analysis are only now falling into place, but not yet fully available, so I have chosen to use self written routines in IDL to extract a few zero order corrected spectra and fit them with a simple power law of the form

$$F = NE^{-\Gamma} \,, \tag{3.5}$$

where N is the normalization and Γ the power law index. I have chosen to ignore any photoelectric absorption from the galaxy as the column density, N_H, for both the Crab and Cygnus is of the order 10^{21} cm^{-2} and thus not Compton thick. The model has been folded through the ARF and through the atmospheric attenuation, where I have assumed that the RMF is uniform.

The ARF and the observations have been binned for ΔE = 2 keV, and to improve the stastics the extracted spectrum were further rebinned for ΔE = 4 keV. The spectra were extracted and combined for both detector A and B, from a 2 arcmin circle centered on the source of the observed image

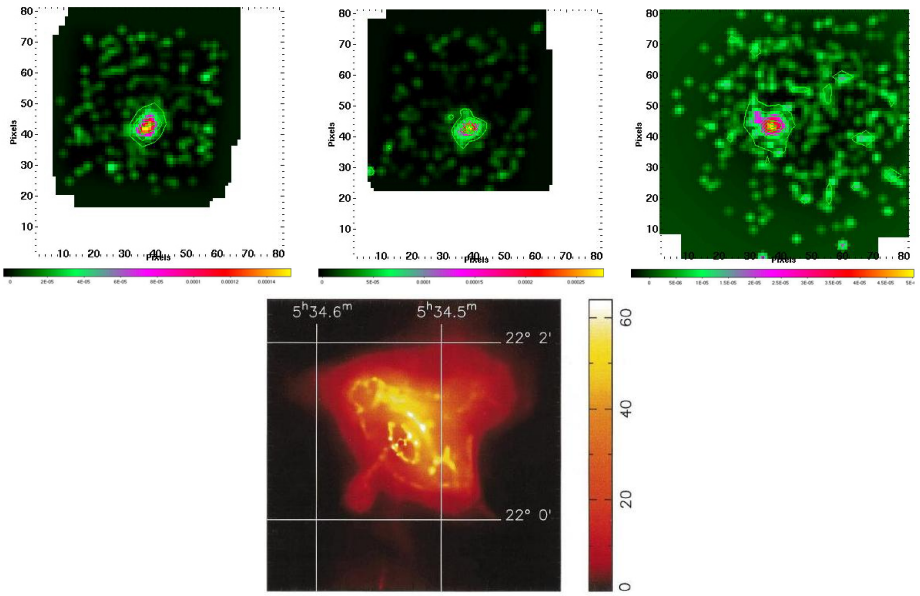

Figure 3.19: Top: Smooth images of crab1, crab2 and crab3. A kernel of width 36" was used. The image is in pixels and 1 pixel=18". Bottom: CHANDRA image of the Crab [19].

and background image. The extracted spectra were converted to physical counts, and poisson errors were calculated. Systematic errors and positional errors have not been included.

3.6.1 Cygnus X-1 spectra

Figure 3.20 shows the spectra and the best fit model of Cygnus X-1. Not too much faith should be put into the estimated errors on the photon index, as it is clear full knowledge of the systematic errors is unknown. We don't know in what state Cygnus X-1 was currently in during the observation, but comparing the countrates of the Crab and Cygnus X-1, the ration should be 2.0 for Cygnus X-1/Crab according to the fluxes, and I get ~ 1. In the high state the flux is about a factor of 10 higher, so since the ratio less than 2 and the fitted photon index at $\Gamma = 2.0 \pm 0.1$, falls close to the known power law index for the Cygnus hard state, I assume that Cygnus X-1 must have been in its Low Hard State. The data is not good enough to determine whether there is a comptonization reflection hump at 30-50 keV.

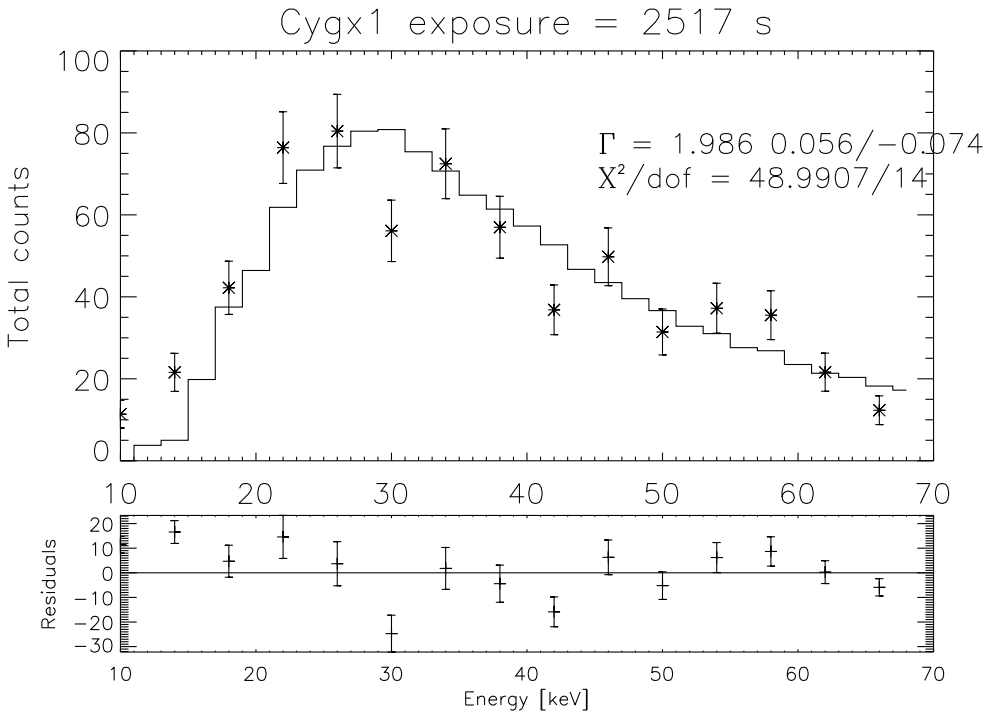

Figure 3.20: Combined spectrum of detector A and B of Cygnus X-1 observation t=[468.3,469], extracted from an annulus of 2 arcmin. The power law was folded with the ARF assuming a uniform RMF and with the atmospheric attenuation assuming an average atmospheric depth of 3.5 g/cm^2.

3.6.2 Crab spectra

Figure 3.21 and 3.22 shows the spectra of the two observations t = [472.9,473.12] and t = [474.18,474.36], and the best fit power law models, $\Gamma = 2.4 \pm 0.3$ for crab 1 and $\Gamma = 2.6 \pm 0.1$ for crab 1. The fits for both are more reasonable than for Cygnus X-1 and agree well with each other accepting the given errors. The photon index also falls within the observed ranges, although a bit on the soft side of the canonical value, $\Gamma \sim 2.10$, for the nebula.

3.6.3 Discussion

I have assumed in the above that the RMF is uniform, and that the boresight coincides with the pixel marked with coordinate [0,0]. I also know this not to be true, and thus the main source of error comes from here. However, the source flux is strongly influenced by the atmospheric attenuation and the effective area of the detector, which are both well known. Also all three observations are fairly steady and the boresight is therefore less importance. The best fits are reasonably close to what has been measured before, but more importantly the relative slope of the Crab and Cygnus observations, 1.99/[(2.59+2.35)/2] = 0.76, do come close to what was expected 1.7/2.1 = 0.81 .

It is obvious what the future work should be for HEFT, now that the aspect has been properly understood, and hopefully soon fits files for the ARF and RMF will be available for better analysis in such spectral analysis programs as **xspec**.

3.7 Concluding Remarks

I have in this Chapter with examples explained the major parts of the data processing for HEFT, from aspect reconstruction to spectral extraction. Not all steps are equally advanced, but a modest estimate is that the aspect reconstruction is 95% done, where the remaining 5% lie in some empirical work identifying good tracking sections from bad, and finally trying to reconstruct the aspect for GRS1915+105 and 3C454-3 for which we think there are detections. The process of the detector characterization has been slowed and complicated due to the fact that all three detectors were destroyed during the landing of the payload, and since not all effects were known prior to flight, some measure of post-flight in-flight data calibration has been necessary. This work is about 70-80% done. Additionally the optics are currently

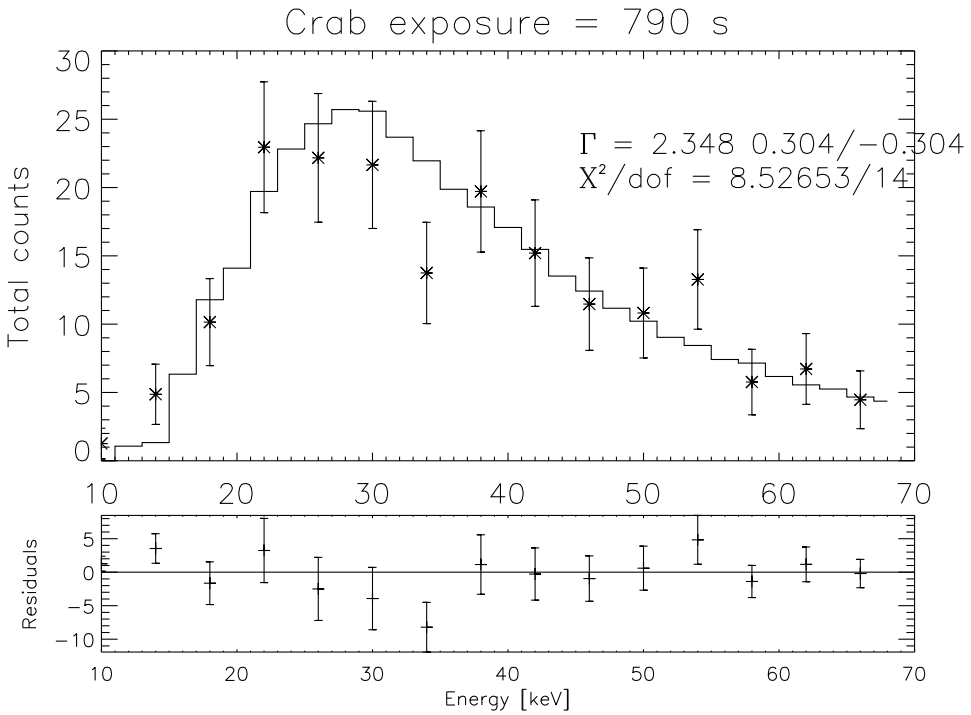

Figure 3.21: Combined spectrum of detector A and B of the Crab observation t = [472.9,473.12], extracted from an annulus of 2 arcmin. The power law was folded with the ARF assuming a uniform RMF and with the atmospheric attenuation assuming an average atmospheric depth of 3.85 g/cm^2.

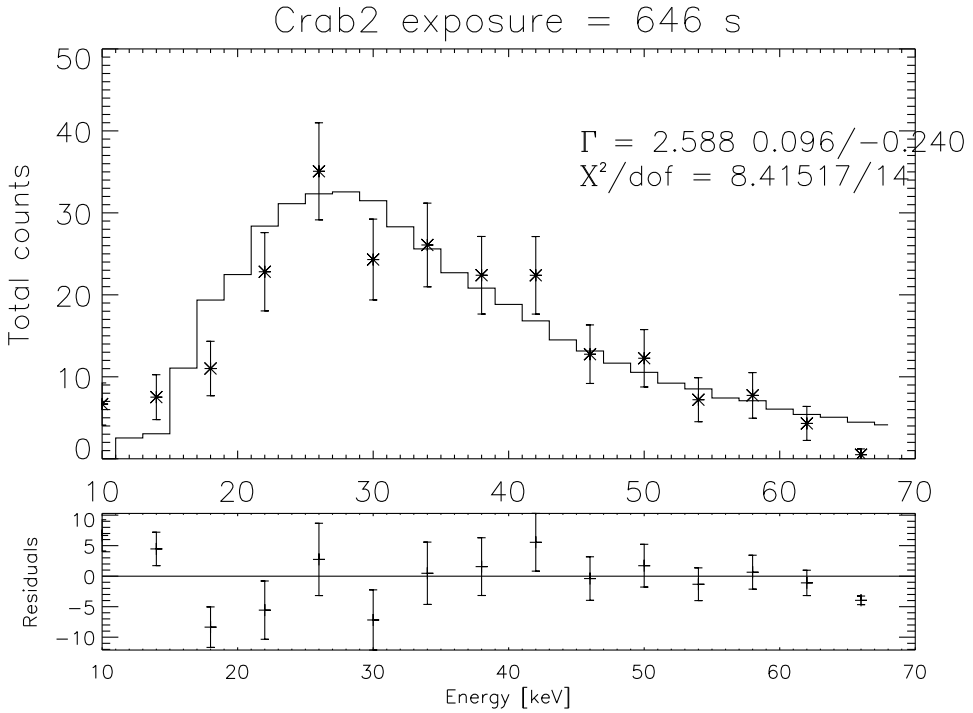

Figure 3.22: Combined spectrum of detector A and B of the Crab observation t = [474.18,474.36], extracted from an annulus of 2 arcmin. The power law was folded with the ARF assuming a uniform RMF and with the atmospheric attenuation assuming an average atmospheric depth of 3.3 g/cm^2.

being tested again at 8 keV to investigate if there is any degradation in performance and hence in effective area.

All in all the payload has performed as expected, both in its ability to track sources and in its scientific acquisition, and hopefully with the knowledge we have obtained, we can significantly improve the instrument's performance for the next flight.

Chapter 4

The XEUS high energy extension

4.1 Introduction

The XEUS mission was originally conceptualized to have a primary mirror of 30 m^2 at 1 keV with a focal length of 50 m, and it was to be launched into a Low Earth Orbing (LEO) as a formation flying unit consisting of a mirrior craft and detector craft. It was also proposed to have the ability to rendevous with the ISS for intital construction, servicing and later upgrading. This was, however, considered impractical and the mission has since been downscaled. The exact configuration is still under debate, but as of writing, the baseline involves a primary mirror of 5 m^2 at 1 keV at a focal length of 35 m, with an upper operational energy of 40 keV, and instead of a LEO it will be sent to L2 still in a free flying formation configuration. This most recent baseline can be reviewed in A. H. Parmar (2006)[20] and the new science case for this baseline in G. Hasinger (2006)[21].

Many astrophysical objects, such as active galaxies, have broad x-ray spectra and combining spectra from different instruments is not a trivial task. An instrument of XEUS size will provide an impressive leap in sensitivity, but also with its main energy band covering 0.1 - 40 keV it will be able to tie together observational bandwidths, which so far have only been accessible using different instruments. Including a high energy extension capable of reaching the soft end of the γ-ray range (around 200 kev), would additionally make it possible to scale observations from γ-ray instruments to the low energy high resolution imaging. Such an high energy extensions would not need to have the same sensitivity nor resolution of the main XEUS

Design	R_{min} [mm]	R_{max} [mm]
Design I	60	265
Design II	60	265
Design III	60	365
Design IV	100	365

Table 4.1: The four different designs investigated.

instrument, but would be capable of imaging on a level previously unseen at those energies.

The work presented here is a study on the design of such a high energy extension using currently available technologies.

4.2 Concept study goals

Space mission design is a balance between achieving cutting edge science at a realistic cost. The objective of the study is therefore to maximize the science output without over-designing and wasting resources. In space cost is proportional to weight, and it is thus one of the primary parameters to control. For example effective area can in principle be obtained by building ever larger optic, but at some point the cost needed to gain another cm^2 will outweigh its scientific value. Finding that balance is the challenge at hand.

The dimensional constraints of the study are given by the main XEUS optic, which must accommodate the high energy extension. The high energy extension must be fitted inside a petal section of the main optic, giving it a maximum outer radius of 36.5 cm, while fabrication constraints limit the inner radius to 6 cm. The focal length is 5000 cm, as it was in the original case since the down-scaling of the focal length has only occurred recently, and the mirror length 40 cm.

As it is not analytically obvious how the effective area depends on the geometry and mirror coating, I decided to look at 4 different sizes of the optic given in Table 4.1. Design I and II have the same dimensions, but use different mirror thicknesses, which will be explained later.

With these four designs I will investigate the following important properties, which give a measure of the scientific merit of each design:

- Effective area and sensitivity.
- Off axis response.

- Uniformity.
- Trade off in effective area versus mass.

The effective area and sensitivity shows how efficient the design is at collecting photons, and for an astronomer this is desired to be as large as possible. The off-axis response is important because objects are rarely perfectly on-axis and often extended. Uniformity is a calculation of the stability of the design against mirror fabrication flaws. Finally what is the trade off between effective area and the mass of the design.

4.3 X-ray Telescopes

This section briefly describes the main elements important for an x-ray telescope. First the physics behind the multilayer reflection of xrays are briefly reviewed. Secondly the material most commonly used for x-ray telescopes are presented and discussed. Finally I will review the geometry of xray telescopes, emphasizing important design parameters which influence the performance of the telescope.

4.3.1 Multilayer Reflection

The reflection of x-rays in the hard end of the spectrum is only really possible because of the existence of the critical angle. The angle, θ_c, marks the grazing incidence angle below which the index of refraction, $n = 1 - \delta + i\beta$, becomes imaginary and hence the ray can no longer be transmitted into the material. The critical angle is energy and material dependent, and is in terms of the material electron density, ρ, and wavenumber, k, given by

$$\theta_c = \sqrt{2\delta} = \frac{\sqrt{4\pi\rho r_0}}{k} \, . \tag{4.1}$$

Most x-ray missions build to date have flown telescopes, which were coated with only a single film, usually of gold, platinum or iridium. The reason these rare metals are particular favored is because of their high electron density, which leading to a high critical angle.

For gold, platinum and iridium with an average graze angle of 0.4 deg, they loose nearly all reflecting power at around 10-15 keV, which is why few of the current x-ray focusing missions can operate efficiently above 15 keV.

The main problem of a monolayer film is that an incident ray only gets a single chance at reflection. Depending on the optical constants, it has

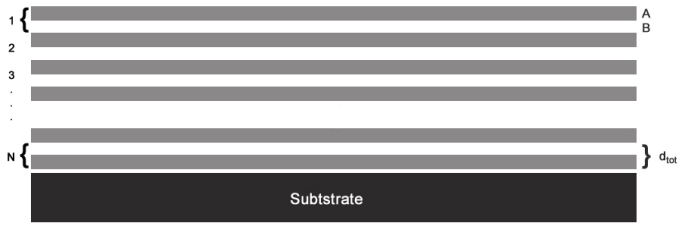

Figure 4.1: Geometry of a multilayer.

a probability of being reflected or transmitted, and once transmitted the photon is of no further use. If one were to put another interface in its path, the photon would be presented with another opportunity of reflection. One such reflected photon might be fortunate to get transmitted back through the first interface, and join the other photons on their way to the detector. Increasing the number of interfaces in this fashion, one effectively increases the chances of reflection and hence the reflection itself.

Such a stack of thin layers of alternating materials is called a multilayer. Figure 4.1 shows the base geometry of a multilayer stack. A pair of material films A and B is called a bi-layer, and the total number of layers refers to the number of layer pairs. They are conventionally numbered from the top down, with bi-layer 1 bordering to air/vacuum, and bi-layer N sitting on top of the substrate. The total thickness of one bi-layer is $d_{\text{tot}} = d_A + d_B$, and the thickness of the individual material components is expressed in fractions of the bilayer thickness,

$$\Gamma_A = \frac{d_A}{d_{\text{tot}}} , \qquad d_B = d_A \frac{\Gamma_A}{1 - \Gamma_A} . \tag{4.2}$$

The reflecting properties of a multilayer stack can be modelled starting from the reflectivity of a thin slab of material and used recursively to build up the stack. This is called Parratt's method, numerically very friendly, and Appendix A describes it in detail.

Multilayer types

Multilayers are extremely versatile and can be found in a wide variety of designs and material combinations. The basic parameters needed to specify

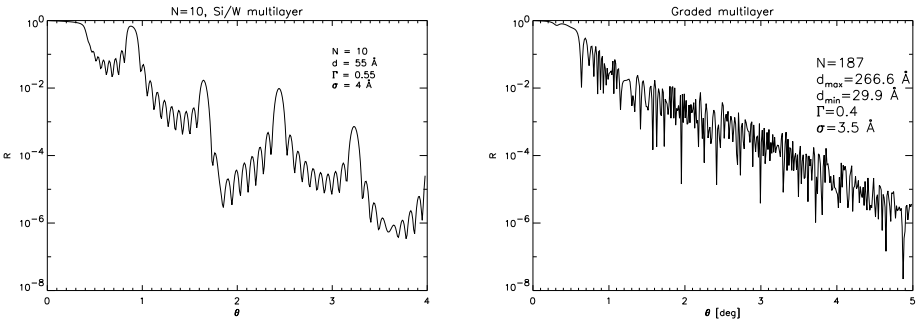

Figure 4.2: Right: A W/Si constant d-spacing coating of N=10 bilayers. Bragg peaks are located at angles 0.9 , 1.625, 2.4 and 3.25 deg. The satellite maxima between the peaks are Kiessig fringes. Left: Theoretical HEFT recipe 2 using power law graded d-spacing.

a multilayer stack are:

- N, the number of layers in the multilayer stack.
- d, the thickness of one bilayer.
- Γ, the fraction of high density material to the bi-layer.

The bilayer thickness may be a function of N, as shall be seen later, but the simplest multilayer is the constant d-spacing, where d and Γ are constant down through the stack. It is in this configuration that one of the multilayers strongest assets can be most clearly observed, for like the periodic latices in crystals, constant d-spacing multilayers also exhibit periodicity in their specular reflection in concordance with the Bragg condition

$$\lambda m = 2d \sin \theta_i \ , \tag{4.3}$$

where λ is the wavelength of the incident wave, θ_i the incidence angle and m the order of the reflection.

Figure 4.2 left panel, shows a theoretical plot of a W/Si multilayer of bi-layer thickness $d = 55$ Å and period N=10. The first, second, third and fourth Bragg order peak are the local maxima at angles 0.9 , 1.625, 2.4 and 3.25 deg. Between the peaks are the smaller Kiessig fringes, which are the cross interactions between the layers, and therefore are of number N-2.

Because of the Bragg condition, mirrors coated with a constant d-spacing will have certain incidence angles were it performs optimally, and angles were it is practically useless. Such a selective performance is not desirable for a astronomical telescope, where a smooth energy response over a continuum is desirable.

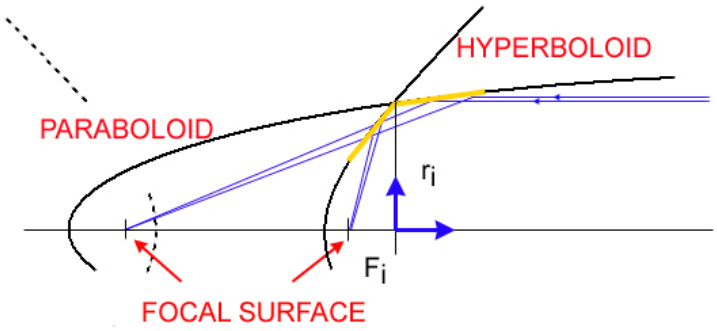

Figure 4.3: Wolter-I. The hyperbolic and parabolic surfaces are rotationally symmetric and confocal such that the focal point of the parabolic coincides with the secondary hyperbolic focal point.

The trick to achieving smooth responses lies in the variations of the bilayer thickness, and Figure 4.2 right panel, shows a theoretical curve of a W/Si multilayer that has been thickness graded down through the stack according to the power-law profile [22]

$$d_i = \frac{a}{(b+i)^c} \ . \tag{4.4}$$

The values a, b and c are constants, and d_i the bilayer thickness of layer i. The constants a and b are uniquely determined for given values of c, d_{min} and d_{max}. The effect of grading the bilayer thickness results in the fractional shifting of Bragg peaks and Kiessig fringes so that the low reflectance region between the Bragg peaks are filled. This type of grading is called a power law coating, and is the grading formula that was used for the HEFT mirrors.

4.3.2 Telescope Geometry

Wolter Telescopes

Two of the main difficulties with xray reflecting telescopes is the nearly parallel orientation of the reflecting surface to the incident ray, which invariably leads to a long focal length. Ground based telescopes with long focal lengths are not a problem, but since the atmosphere, fortunately for humans, is opaque to x-rays, x-ray telescopes can only be mounted on flying platforms, where focal lengths of tens of meters becomes very problematic.

The simplest focussing system widely in use is the parabolic mirror. It is easy to construct, but suffers from severe coma effects at all points away from the apex where it fails to meet the Abbe sine condition. This means all off-axis rays will be imaged into a circle around the focus. The Abbe sine condition dictates that to obtain a coma free image, the surface where the incoming axis parallel ray and an outgoing ray from the focal point intersects, must obey

$$r = \frac{h_1}{\sin \alpha_1} = \frac{h_2}{\sin \alpha_2} \ , \tag{4.5}$$

where h_1, h_2 is the distance from the axis parallel ray to the axis, and r corresponds to a circle around the focal point. Where the circle intersects the reflecting surface of the mirror any off- and on-axis will be coma free. For this reason parabolic mirrors have a very large curvature so only the Abbe sine approximate part reflects. This immediately excludes a parabolic mirror, as x-ray reflection requires shallow angles. Fortunately in 1952, motivated by a desire to build an x-ray microscope for the study of biological material, the German scientist Hans Wolter worked out the basic geometry of a grazing incidence x-ray telescope [23][24], by using a hyperboloid as a secondary mirror. This design is known as a Wolter-I, and as shown in Figure 4.3 it consist of a coaxial paraboloid followed by a hyperboloid, which must be confocal with the paraboloid. The focal point of such a telescope is

$$\frac{r_i}{F_i} = \tan(4\theta) \ , \tag{4.6}$$

where r_i is the distance from the axis to the point where the two surfaces intersect, and F_i the distance along the axis from the focal point to the intersection plane of the two surfaces. The angle θ is the sum of grazing incidence angles θ_p, θ_h, which are respectively the angles of the parabolic and hyperbolic mirror surfaces an infinitesimal distance from their intersection. The Wolter-I geometry does not perfectly obey the Abbe sine condition, and Wolter subsequently proceeded to solve the mirror systems to exactly obey the Abbe sine, but the improvements in image production are small and only good very near the axis [24].

All past space-borne focusing x-ray missions have flown stacked Wolter-I telescopes.

Conical Approximation

Replacing the upper paraboloid and the lower hyperboloid with conical sections, produces a telescope design type called "a conical approximation".

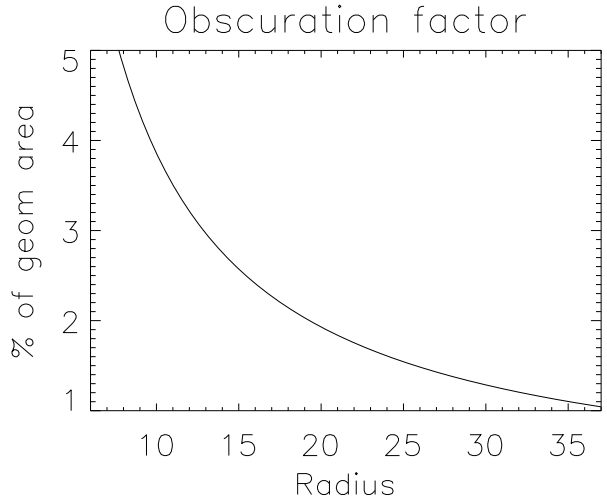

Figure 4.4: Obscuration v. Radius: length of the shell is 400 mm, the glass thickness 0.2 mm and the focal length 5000 cm

There are several advantages gained from using a conical approximation. First and foremost is the high filling factor obtained by more efficient nesting of conical surfaces [25]. The reason is that substrates used for a Wolter-I, usually will have a substantial greater thickness compared to the thin foils which can easily be formed into a conical section. A higher nesting in turn means a higher utilization of aperture and a higher effective area, which sums to a better sensitivity. The drawback is that unlike a Wolter-I the conical optic will not focus rays at a geometric focus. This is in part compensated by the fact that the resolution is approximately invariant across the field of view unlike a true Wolter-I [25].

But blurring is unavoidable, and going from a Wolter-I to a conic approximation results in an on-axis blurring, which given in the geometric half energy width, HEW, is of the order [25]

$$HEW \propto \frac{LR^2}{F^2} \, , \tag{4.7}$$

where R is the aperture width, L the length of the primary mirror, and F the focal length.

For a design with a focal length of 5000 cm, maximum outer radius 36.5 cm and primary mirror length 40 cm, the worst case blurring is of the order ~ 2 mrad.

4.4 Design Parameters

4.4.1 Shell spacing, Substrate and Substrate thickness

The number of shells that can be packed into the space reserved for the telescope is dependent on the thickness of the substrate, and the spacing between shells. The thickness of the substrate also determines the weight of the telescope, and is thus a very important parameter.

The radial spacing between the shells is a tradeoff between on- and off-axis collecting area. The on-axis area is maximized when the inner radius of the $(i+1)$'st shell lies on the same coaxial cylinder as the outer edge of the ith primary shell. This is also known as 'close packing'. Widening the radial gap will improve the off-axis collecting area, as there well be less shadowing of the off-axis angles from neighboring shells. This however means that fewer shells can be nested inside the specified radius, and therefore a wider gap costs on-axis area. Another concern when the gap becomes to large is stray light, which only undergoes one or no reflection at all.

It was found that an additional spacing of 33 % of the close packing yielded the best balance between on- and off-axis area **??**.

The thickness of the substrate is important for the stability of the telescope, and obviously a thicker substrate gives a better stability. In this way the XMM telescope had shells, which became progressively thicker with increasing radius. Something similar might be envisioned for these high energy extensions as they are of roughly the same size. Unfortunately the code does not currently support this option, and as glass pieces of thickness 0.2 mm have been successfully mounted and there is work in progress on mounting even thinner sheets, I will chose an average substrate thickness of 0.2 mm.

With the above spacing and substrate thickness Table 4.2 lists the number of shells and the total glass mass of the telescope, where a glass density, $\rho_{glass} = 2.67\text{g/cm}^3$ of the AF45 used for HEFT [4] has been used. The mass estimate has assumed that each shell is solid of revolution, and has not included any mounting spacers.

4.4.2 Multilayer design

The optimization procedure optimizes over the 3 parameters: the number of bi-layers N, c, and $\Gamma = d_{\text{highZ}}/d_{\text{tot}}$. Before an optimization can begin a range of d_{min}, d_{max}, and thus E_{min} and E_{max} must be made. These can be inferred by using the Bragg formula (4.3) on a desired range of energies and choice of graze angles. The calculation of half opening angle α is for a

Design	R_{min} [mm]	R_{max} [mm]	T [mm]	Total mass [kg]	# shells
Design I	60	265	0.2	124	347
Design II	60	265	0.3	161	294
Design III	60	365	0.2	198	443
Design IV	100	365	0.2	180	346

Table 4.2: Masses, substrate thickness and number of shells for the four designs.

conical approximation given by the ratio of radius to focal length

$$\frac{r}{F} = \tan(4\alpha) \simeq 4\alpha \; . \tag{4.8}$$

The range of $d_{\min},\ d_{\max}$, and $E_{\min}$, $E_{\max}$ are not made for the individual shells but for the groups. Ideally each shell should be optimized individually, but this would take far too long. Instead shells are divided into groups. This division is a tradeoff between optimization time and utilization of the shells. The minimum and maximum thicknesses can be calculated using the first order Bragg Eqn (4.3), m=1, with $\lambda = hc/E$ which solved for d looks like

$$d = \frac{hc}{2E\sin\theta} \; . \tag{4.9}$$

Since $\sin\theta$ is an increasing function for the range of grazing incidence angles, a fixed energy will cause the bilayer thickness to decrease as one moves outwards through the shells. Or equivalently the same will happen if the angle is fixed and the energy increased. This means that in order to have all mirrors within one group reflect in the chosen energy band $E_{\min} - E_{\max}$, $d_{\min}$ is determined by the $(E_{\max}, \theta_{\max})$ and $d_{\max}$ by $(E_{\min}, \theta_{\min})$ [26]

$$d_{\min} = \frac{hc}{2E_{\max}\sin(\theta_{\max})} \tag{4.10}$$

$$d_{\max} = \frac{hc}{2E_{m\min}\sin(\theta_{\min})} \; . \tag{4.11}$$

The choice of $\theta_{\min},\ \theta_{\max}$ can be inferred from considering the off-axis angles. For a conical approximation with primary mirrors of half-angle α, and field of view half-angle ϕ, the minimum and maximum reflection angles are

$$\theta_{\min} = \begin{cases} \alpha - \phi & \alpha - \phi > \theta_{\text{crit}} \\ \theta_{\text{crit}} & \alpha - \phi < \theta_{\text{crit}} \end{cases} \tag{4.12}$$

$$\theta_{\max} = \begin{cases} \alpha + \phi & \phi > \alpha \\ 2\alpha & \phi < \alpha \end{cases} \tag{4.13}$$

Here θ_{crit} is the critical angle for total external reflection. When angles are less than θ_{min} the photon will either be out of view ($\theta < \alpha - \phi$) or be in an angular range where it will reflect by total external reflection ($\theta < \theta_{\text{crit}}$). At angles greater than θ_{max} the photon is either out of the field of view ($\theta > \alpha + \phi$) or striking the primary mirror at an angle where it will not reflect off the secondary mirror ($\theta > 2\alpha$).

These equations are used to build tables relating energy to bi-layer thickness. From these the optimal choices of minimum and maximum d-spacing for each mirror group is found, taking into account the location of the critical angle and the presence of absorption edges.

The choices of minimum and maximum d-spacing for each design can be seen in Tables 4.6, 4.7, 4.8 and 4.9 columns 5 and 6. A table of angle versus radius can be found in Appendix B.

4.4.3 Material Selection

The reflectance of a multilayer is proportional to the optical contrast between its two materials. This means one would like the difference in refractive index, Δn, to be as large as possible. This is equivalent to having a highly absorbing material called the *absorber* next to a much less absorbing material, called the *spacer*. The best absorber-spacer combination consists in a tradeoff between maximizing the optical contrast while minimizing the overall absorbtion in the stack, as well as making sure the chemical properties of the materials do not clash, and the physical properties match the purpose of the mirror.

A typical example of the latter requirement is the presence of absorbtion edges in the middle of the energy range one is trying to design a mirror for. If the surface is too rough the reflectance is reduced by scattering [27]. Among problematic chemical properties are material reactions to air, high inter-diffusion of the materials, low stability over time, as well as temperature sensitivity. The construction and final implementation of a multilayer telescope may be as high as 10 years and if a coating degrades significantly over this time then there is obviously a problem. Ideally one would like a stable material, which is insensitive to the temperature fluctuations it might be exposed to during construction and later in a space environment.

Well known tried and tested material combinations are: W/Si, Pt/C, Mo/Si, Ni/Si, Ni/Ti. The Ni combinations are used by neutron supermirrors, and the the W, Pt and Mo combinations are applicable at different energy ranges, due to their absorbtion edges, which are listed in Table 4.3.

HEFT has flown the W/Si solution because it covers the required energy

Material	Absorbtion edge [keV]
Pt	(K-edge) 78.39
W	(K-edge) 69.53
Mo	(K-edge) 19.99

Table 4.3: High density materials and their K absorption edges.

range of 20-70 keV, and has an acceptable low interfacial roughness, $\sigma = 0.4 \pm 0.05$ nm. The W/Si coating is very stabile over time, and only has shown a slight degradation when submitted to high environmental temperatures. Additionally the materials are cheap, simple to obtain, and easy to deposit. Mo/Si has been used for extreme ultraviolet and soft x-ray [28], but because the optical contrast is not very high it is of no use to a high energy extension. Pt/C has been used on the Japanese hard x-ray mission Astro-E [29], and of the above probably has the best coverage. However, Pt/C is both expensive to produce and slow to deposit. Also it has a considerable worse interfacial roughness than W/Si, $\sigma = 0.5 \pm 0.05$ nm, as measured under the same conditions at the Danish National Space Center [30].

Recent developments in the search of multilayer combinations have come up with compounds to solve the interfacial roughness problem and to create smooth transitions across absorbtion edges. The compounds WC/Si, WC/SiC and W/SiC, have been extensively tested in relation to future x-ray mission and also in connection to XEUS [31]. Experiments have shown that the SiC as spacer with W reduces the interfacial roughness from 0.35-0.4 nm to 0.2-0.25 nm, and in combination with WC it becomes possible to create very thin layers. Conventional W/Si can only be made as thin as 1.5 nm, while WC/SiC can be sputtered as thinly as 1.0 nm [32]. The advantage of being able to make thin layers can be seen from Eqn. (4.10), where a thinner layer increases the maximal energy that can be reflected off the mirror.

Unfortunately both W/SiC and WC/SiC have a slightly lower theoretical reflectance than W/Si, even when taking into account the lower interfacial roughness. The problem with the compounds SiC and WC are the fact that their optical constants are not well known. Sputtered SiC and WC optical constants have only been experimentally measured in the range 35-130 keV [33] and when comparing with the theoretical, there is a noticeable discrepancy.

Yet, even if the reflectance is lower the ability to make thinner layers still make WC/SiC and W/SiC better choices for use above 78 keV, and therefore

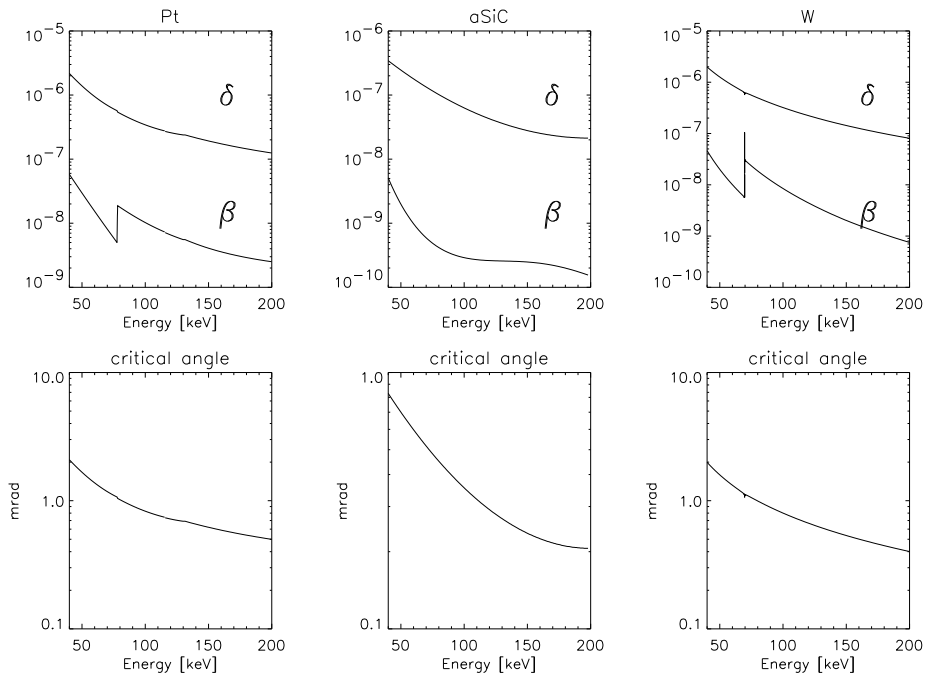

Figure 4.5: Optical constants, $n = 1 - \delta + \beta$, for W, aSiC and Pt. Bottom panel shows the critical angle, $\alpha_C = \sqrt{2\delta}$.

I have chosen to use W/SiC for energies above 78 keV. For energies below 78 keV I have chosen to use Pt/SiC because of its coverage of the W absorbtion edge. Measurements have shown that W/SiC deposited on a glass substrate has an interfacial roughness of 0.3-0.4 nm, so for these optimizations the interfacial roughness has been set to 0.35 nm. For Pt/SiC the roughness is slightly higher, 0.4-0.5 nm, and I have chosen 0.45 nm to represent the interfacial roughness for this material combination. Figure 4.5 shows the optical constants for the three materials, W, aSiC and Pt, as well as the critical angle for each material. The optical constants are a combination of measured values [33], 40-130 keV, and theoretical, 130-180 keV, which were taken tables calculated by Center for X-Ray Optics, CXRO.

For completeness I will mention that the art of sandwiching two multilayer structures together to overcome the absorbtion edges are being studied, and that preliminary results show great promise [34][35]. In this approach the bottom part of the stack is coated with W/SiC for high reflectance, and when one reaches the depth of the stack equivalent to the energy of the absorbtion edge, the materials are switched to NiV/SiC. Extensive tests of the

stability over time still needs to be made, but once it has been established that they can indeed survive unchanged for years, it is very probably that this sort of coating will be used in the future. However, for the concept study at hand, it is the overall reflectance level that is important, and the currently best coatings of W/SiC and Pt/SiC will be enough to answer the questions. If later the coating should be replaced with a sandwiched structure, I don't predict the important answers of the concept study to change by much.

4.4.4 Additional design parameters: Obscuration

Obscuration is a real and large source of throughput extinction. Thousands of pieces of glass must be mounted in a secure way and the finite thickness of the glass itself fills out the aperture with dead space. The XEUS high energy extension will be similar to the HEFT optic and scaling the HEFT optic obscuration is therefore a close approximation.

In the HEFT optic there are 5 graphite spacers per octant. Additionally there is a 1 mm space between the mounted octant where there is no glass. The spacers themselves are attached with epoxy that has a squish-out, and spacer plus epoxy approximately blots out 1 mm. So in one complete shell of 8 octants there is a total obscuration of the glass surface of $5 \times 1\text{mm} \times 8 + 8 \times 1\text{mm} = 48\text{mm}$.

The projected surface of this is $1/2 \times \text{length} \times \sin(\alpha)$, where α is the grazing incidence angle. Figure 4.4 shows the obscuration factor in percent of the geometric area, which is the area of full revolution shell, as a function of radius. In this plot the length of the shell is 400 mm, the glass thickness 0.2 mm and the focal length 5000 cm.

4.4.5 Summary of design parameters

Because the high energy extension is a relatively small optic, and something of that size has already been build, we know the constraints on rigidity are less than for the main XEUS, and as current developments allow a substrate thickness of 0.2 mm, the designs have been optimized with a Si substrate of 0.2 mm. Measurements of the 0.2 mm substrates show an average roughness of 0.25 nm. A conical approximation optic geometry has been chosen as this has the greatest flexibility in construction. The length of the primary and secondary mirror are 400 mm. A generic square detector of length 5 cm has been assumed, and a Field of View of 1 mrad compatible with the detector size.

In the hard x-ray to soft gamma ray range scattering effects of the multilayers become very important. A very smooth multilayer material is therefore needed, and since SiC combinations have shown great promise, we have chosen to use Pt/SiC and W/SiC. With these materials, and a focal length of 5000 cm, an energy range of 40-180 keV can comfortably be covered. Table 4.4 summarizes the general design parameters described above.

Baseline	
Focal length	50 m
Energy	40 - 180 keV
Mirror thickness	0.2 mm
Primary mirror lenght	400 mm
Coating materials	Pt/SiC, W/SiC
Interface roughness W/SiC	0.35 nm
Interface roughness Pt/SiC	0.45 nm
Detector size	50 x 50 mm
FOV	1 mrad

Table 4.4: General high energy extension design parameters.

4.5 Optimization Procedure

The program set for the optimization of multilayers was originally developed by Peter Mao [26] as a general tool for the design of multilayers in mission designs. Its two most powerful features is the extensive ray tracing of the telescope and the calculation of an energy and off-axis angle dependent reflectivity matrix $R[E, \alpha]$.

Because off-axis performance is strongly affected by vignetting, which is the decrease of the effective area as a function of the increase in off-axis angle, the on-axis collecting area must be balanced by the off-axis vignetting. The uniform distribution of off-axis angles has been chosen to lie between 0 and 1 mrad. Both on-axis and off-axis response are ray traced by a Monte Carlo routine with an input of about 10^9 events.

The calculation of the reflectivity matrix $R[E, \alpha]$ is quite CPU intensive and is run on 2 parallel processors on the Danish Center for Scientific Computing, DCSC, using the Message Passing Interface Library. The program uses the `amoeba` algorithm from *Numerical Recipes* [36] based on the downhill simplex method to maximize the Figure of Merit.

4.5.1 FOM, Figure of Merit

At the heart of the optimization lies the evaluation of the Figure of Merit, FOM, which is the weighted energy integral of the field-of-view averaged effective area for each mirror shell, summed over all mirrors

$$\mathrm{FOM} = \frac{\sum_{i=1}^{N} \int_{E_{\min}}^{E_{\max}} \mathrm{d}E A_{\mathrm{wolter}}(E) W_E(E)}{(E_{\max} - E_{\min})\langle W_E \rangle} \ . \tag{4.14}$$

$A_i(E)$, Effective Area

The on-axis effective area of a Wolter-I is given by the product of the projected collecting area and the reflectivity of the mirrors. The area of the i'th shell at radius r_i with half-opening angle α_i and parabola length l, is thus

$$A_i(E) = 2\pi r_i \alpha_i l \times [R(E, \alpha_i)]^2 \ . \tag{4.15}$$

$R(E, \alpha_i)$ is a matrix of reflectivity as a function of energies and angles, and it is calculated using the Névot-Croce formalism explained in Appendix A.

For an off-axis photon the incidence angle on the secondary mirror is different for the primary, and so in order to correctly calculate the effective area an incidence angle distribution of the two mirrors is needed. If the photon arrives at off-axis angle ψ the incidence angles on the primary and secondary mirrors are $\theta_1 = \alpha + \psi_1$ and $\theta_2 = \alpha + \psi_2$. The ray trace explicitly keeps track of the correlation between ψ_1 and ψ_2, and if the 2-dimensional incidence angle distribution is given by $W_{inc}(\alpha_i, \psi_1, \psi_2)$ then the effective area becomes

$$A_i(E) = \int_{-\psi}^{\psi} d\psi_1 \int_{-\psi}^{\psi} d\psi_2 W_{inc}(\alpha_i, \psi_1, \psi_2)[R(E, \alpha_i + \psi_1) R(E, \alpha_i + \psi_2)] \tag{4.16}$$

This equation is entirely general and is easily modified to include more reflections. The angular weighting function $W_{inc}(\alpha_i, \psi, \psi_2)$ is generated by uniform illumination of the telescope aperture and tracing the rays through the telescope.

For the optimization though, $W_{\mathrm{inc}}(\alpha_i, \psi_1, \psi_2)$ is approximated by $W(\alpha, \psi_1)$. The grazing incidence angle for the given shell plus the off-axis angle which is $\alpha = 1$ mrad, is plotted as a function of the angular weighting function. The functions are peaked for the on axis graze angle thus favoring the on-axis performance.

W_E, Energy Weighting Function

The energy weighting function sets the desired spectral response. $\langle W_E \rangle$ is the average value of the weighting response over the energy range $E_{\min} - E_{\max}$, and including it in the denominator of eqn (4.14) ensures that the Figure of Merit is independent of the normalization of W_E. For this optimization the energy weighting function is the same as used for HEFT

$$W_E = \frac{E(\text{keV}) + 70}{100} \, . \tag{4.17}$$

The reason for this shape is because the optimization might otherwise favor lower energies if a given material combination yields a very high area at low energies. The energy weighting thus enforces the optimization to favor higher energies.

4.5.2 Optimization technique

Given the power law parameterizations of the bilayer thickness distribution from Eqn. (4.4), the number of parameters necessary to define a graded multilayer is 5. For values of power index c and number of bi-layers N, the constants a and b from the power law can be uniquely determined by $d_{\min}$ and $d_{\max}$. The fifth parameter, the high density material fractional thickness Γ, is assumed to be a constant down through the multilayer stack. The time to calculate a reflectivity matrix for one parameter is proportional to N, and therefore although optimizing over $d_{\min}$ and $d_{\max}$ would be more correct, given the limited time available on the super computing facilities, the phase space has been reduced to the three parameters: c, Γ and N.

With $d_{\min}$ and $d_{\max}$ constrained, the total thickness of one layer is largely determined by the total number of bi-layers N, and only weakly dependent on the choice of c and Γ. Also since more bi-layers will increase the reflectivity until at some point absorption starts to dominate in the stack and no more reflectivity is gained from adding more layers. Γ and c behave similarly but the relationship between the reflectivity performance is somewhat less transparent. The optimization is therefore run by choosing a value of N that from experience is known to be less than optimum. The values of Γ and c are then optimized until the FOM peaks, after which N is incremented by 25 % and the process is repeated until the FOM decreases following successive values of N.

4.6 Derived Properties

4.6.1 Sensitivity

The sensitivity calculation follows from the definition of the signal to noise ratio, S/N. This ratio is given by the expression

$$\frac{S}{N} = \frac{S(E)A_{eff}\Delta E\, T}{\sqrt{S(E)A_{eff}\Delta E\, T + BA_{foc}\Delta E\, T}}\,, \tag{4.18}$$

where the list below describes the meaning of each parameter.

- S(E) = continuums sensitivity
- A_{eff} = Effective area = Geometric area * Reflectivity
- A_{foc} = focal spot size on the detector
- T = integration time
- B = background flux
- ΔE = fractional energy resolution

Solving this for the sensitivity, S(E), yields a quadratic equation, and the positive solution in units of $A_{eff}\Delta E\, T$ is

$$S(E)[A_{eff}\Delta E\, T] = \frac{-(\frac{S}{N})^2 + \sqrt{(\frac{S}{N})^2((\frac{S}{N})^2 - 4BA_{foc}\Delta E\, T)}}{2}\,. \tag{4.19}$$

The effective area is obtained as described above. Integration time, T, fractional energy resolution ΔE and the signal to noise ratio $\frac{S}{N}$ are set parameters. The background flux is based on experimentally determined background from other space flights and knowledge about the background of the detector. The focal spot size is an elastic size scaled to the size of the expected HPD. For example if the expected HPD is 20" then 50% of the counts are expected to fall within this circle. However, the focal spot size might be defined as being the circle at which 75 % of all counts fall.

Table 4.5 lists the values used for the sensitive calculations, which are quite general for such sensitivity calculations, and the background is a general for these energies.

Sensitiviy Params	
T	10^6 sec
A_{foc}	75% of HPD
ΔE/E	0.5
B	10^{-4}ph/cm^2/s/keV

Table 4.5: Parameters used in the sensitivity calculation.

4.6.2 Off-axis response

The off-axis effective area calculation uses the same ray-trace code as described previously. The group reflectivity files obtained from the optimization are fed into the program, and the ray-trace simulates a point source moved from on-axis to off-axis positions. The number of counts accumulated at the focal plane at the off-axis position relative to the number of counts at the on-axis position, gives the decrease in effective area.

4.6.3 Uniformity

The repeated deposition of multilayers is not exact, but a function of time dependent fabrication parameters connected to the sputtering chamber, such as magnetic field strength and lifetime of the sputtering target. This effects the expected d-spacing thickness of a multilayer, and although much of it can be calibrated out, it is not all which can be removed and one has to expect a d-spacing variation of about 5%.

I simulate the effect of this on the effective area, by varying the minimum and maximum d-spacing by 5 % and calculating the new effective area. I study four cases: $d_{min} \pm 5\%$ when d_{max} is unchanged, and $d_{max} \pm 5\%$ when d_{min} is unchanged.

4.7 Optimization Results

4.7.1 Design I : R = [6,26.5]

Table 4.6 and Figure 4.6 show the optimization results of design I. As can be seen in the Table most of the designs cover a similar parameter space c = 0.15 - 0.40 and $\Gamma = 0.4 - 0.7$, but there are a few exceptions most notibly at the extreme ends of an energy range. Group 1 thus has a $\Gamma = 0.91$, which is very large and in principle means that there is a thick slab of absorber

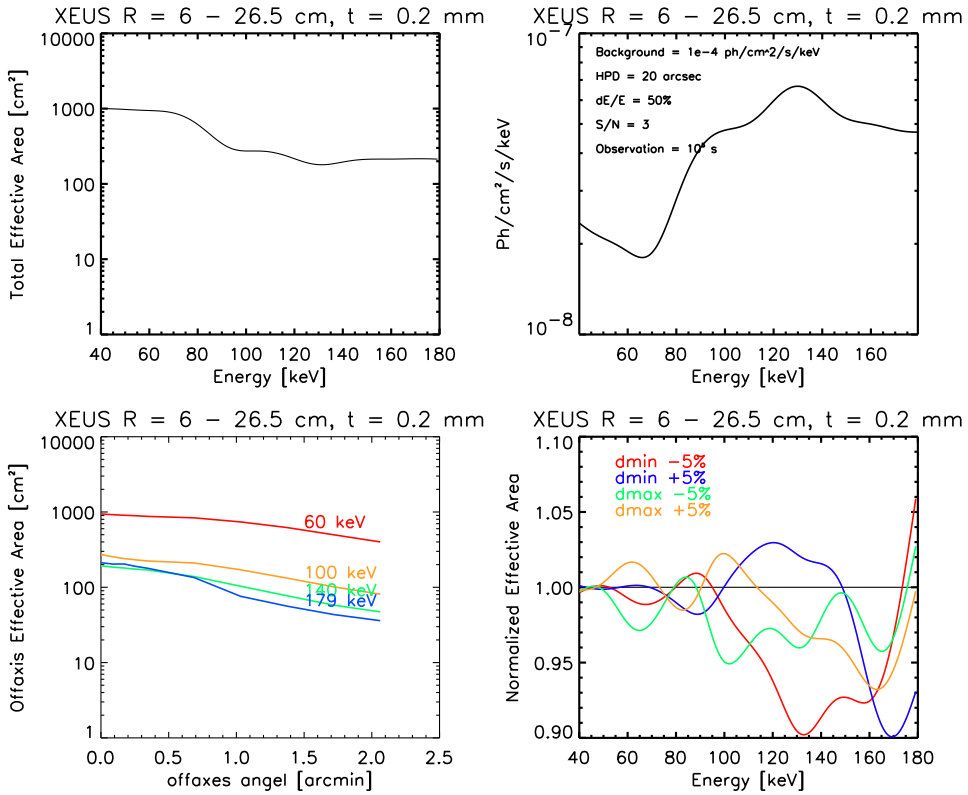

Figure 4.6: Top left: Effective Area. Top right: Sensitivity calculated using the parameters summarized in Table 4.5. Bottom left: Off-axis effective area as a function of off-axis angle. Bottom right: Uniformity simulations perturbing the minimum and maximum d-spacing. Curves are normalized against the on-axis effective area from the plot top left.

material, W, and very little spacer. At these innermost shells this does not cause a problem, since we are well within the critical angle as can be seen from Figure 4.5, and replacing the multilayer with a monolayer of W would probably not change the reflectivity by much. Groups 15 and 16 have a similar problem as here we are once again well within the critical angle at 78 kev. Study of the FOM optimization files also reveals that at these angles the FOM is very insensitive to Γ.

The off-axis response can be seen in the bottom left panel of Figure 4.6, and shows that for an off-axis angle of 2 arcmin, the effective area has dropped by a factor of $\sim$2 for 60 keV to a factor of $\sim$6 for 180 keV. The bottom right plot shows how the effective area varies when one of the d-

Grp	1/2	Emin	Emax	dmin	dmax	N	c	Gamma	Thick	FOM
1	aSiC/W	70	200	95.925	295.201	50	0.358	0.908	0.683	1.204
2	aSiC/W	70	200	89.059	274.071	77	0.366	0.544	0.978	1.504
3	aSiC/W	70	200	82.684	254.453	58	0.366	0.494	0.686	1.902
4	aSiC/W	70	200	76.766	236.240	47	0.398	0.438	0.525	2.208
5	aSiC/W	70	200	71.271	219.330	47	0.398	0.438	0.488	2.697
6	aSiC/W	70	200	66.169	203.631	18	0.158	0.613	0.150	3.361
7	aSiC/W	70	200	61.433	189.055	15	0.205	0.592	0.122	4.062
8	aSiC/W	70	200	57.036	175.583	15	0.230	0.597	0.115	4.477
9	aSiC/W	70	200	52.953	162.959	22	0.217	0.621	0.153	5.157
10	aSiC/W	70	200	49.163	151.295	25	0.227	0.592	0.162	5.524
11	aSiC/W	60	200	45.644	163.877	30	0.222	0.539	0.181	6.718
12	aSiC/W	60	200	42.377	152.147	40	0.235	0.538	0.225	7.121
13	aSiC/W	60	200	39.344	141.256	40	0.260	0.525	0.213	7.452
14	aSiC/W	60	200	36.527	131.145	50	0.265	0.527	0.247	8.100
15	aSiC/Pt	50	78	86.956	146.110	12	0.395	0.822	0.130	28.135
16	aSiC/Pt	50	78	80.732	135.651	15	0.394	0.829	0.151	31.422
17	aSiC/Pt	40	78	74.953	157.427	15	0.301	0.772	0.147	36.714
18	aSiC/Pt	40	78	69.588	146.159	15	0.369	0.720	0.139	42.393
19	aSiC/Pt	40	78	64.607	135.697	15	0.460	0.688	0.132	45.630
20	aSiC/Pt	40	78	59.983	125.984	15	0.533	0.679	0.124	52.380

Table 4.6: Optimization results for design I, R = 6 - 26.5 cm, t = 0.2 mm.

spacings is changed by ± 5%. The curves have been normalized with the ideal effective area from the top left plot, and here the most significant change comes from the variation of the minimum d-spacing. The minimum d-spacing controls the upper energy limit, which is why it affects the high energies. Because of the power law shape of the d-spacing grading, there are many more layers with small d-spacings stacked at the bottom, than the few large at the top, and thus the impact is more pronounced from the small layers.

4.7.2 Design II : R = [6,26.5], t = 0.3

Table 4.7 and Figure 4.7 show the optimization results of design II. The off-axis in the bottom left panel behaves like that from design 1 with a similar progressive reduction of the effective area towards higher energies. The bottom right plot shows how the effective area varies when one of the d-spacings is changed by ± 5%, and again here the most notable variation comes from the change of the minimum d-spacing.

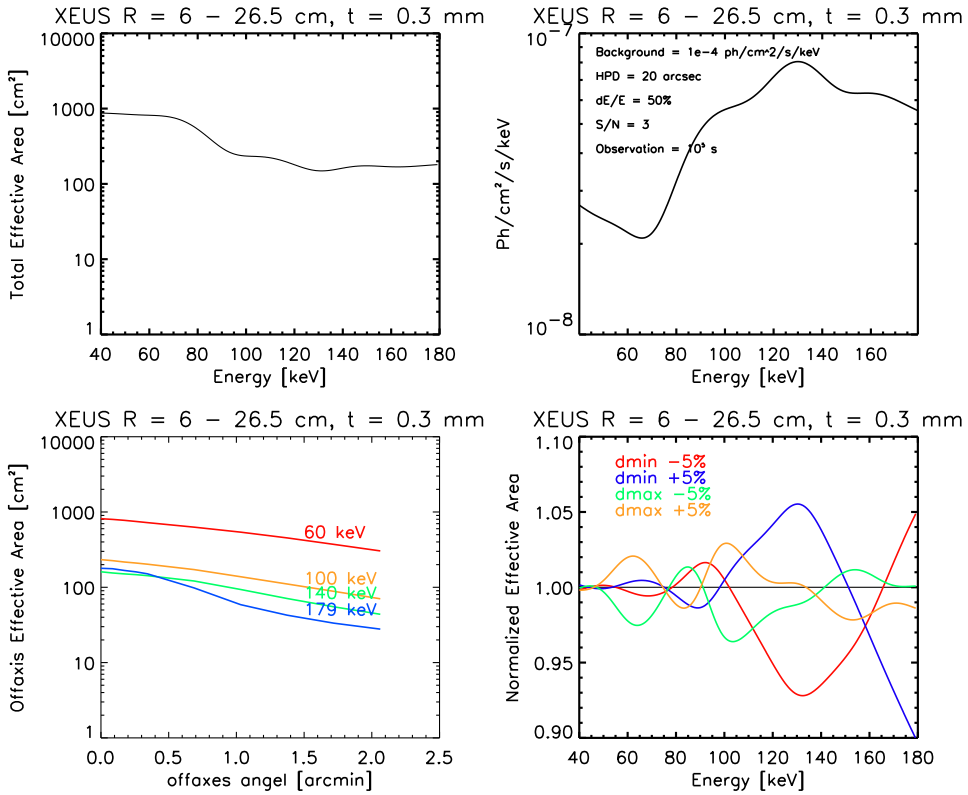

Figure 4.7: Top left: Effective Area. Top right: Sensitivity calculated using the parameters summarized in Table 4.5. Bottom left: Off-axis effective area as a function of off-axis angle. Borrom right: Uniformity simulations perturbing the minimum and maximum d-spacing. Curves are normalized against the on-axis effective area from the plot top left.

4.7.3 Design III : R = [6,36.5]

Table 4.8 and Figure 4.8 show the optimization results of design III. One thing to note with this design is the increase of the power law index, c, for groups 19 and 20 to $c > 1$. The effect of increasing c is to make the power law progressively more linear. Large angles and few layers tend to favor a linear grading instead of a power law, as as shall be seen in later sections there is a strong indication that these layers are no longer efficient.

The off-axis behavior follows the same trend as design I and II, but although the d-spacing variation still exhibits the strongest deviation for high energies, when the minimum d-spacing is changes, there is now also devia-

Grp	1/2	Emin	Emax	dmin	dmax	N	c	Gamma	Thick	FOM
1	aSiC/W	70	200	95.925	295.201	15	0.160	0.825	0.184	2.468
2	aSiC/W	70	200	89.059	274.071	15	0.085	0.688	0.162	3.290
3	aSiC/W	70	200	82.684	254.453	15	0.100	0.660	0.152	3.546
4	aSiC/W	70	200	76.766	236.24	12	0.135	0.638	0.118	5.022
5	aSiC/W	70	200	71.271	219.33	12	0.191	0.644	0.114	5.890
6	aSiC/W	70	200	66.169	203.631	12	0.198	0.600	0.106	6.791
7	aSiC/W	70	200	61.433	189.055	20	0.185	0.650	0.157	8.321
8	aSiC/W	70	200	57.036	175.583	20	0.198	0.600	0.148	9.231
9	aSiC/W	70	200	52.953	162.959	30	0.180	0.609	0.199	10.769
10	aSiC/W	70	200	49.163	151.295	30	0.223	0.594	0.192	12.463
11	aSiC/W	60	200	45.644	163.877	30	0.235	0.550	0.183	14.476
12	aSiC/W	60	200	42.377	152.147	40	0.235	0.550	0.225	15.398
13	aSiC/W	60	200	39.344	141.256	50	0.248	0.531	0.262	17.237
14	aSiC/W	60	200	36.527	131.145	62	0.243	0.518	0.299	18.966
15	aSiC/Pt	50	78	86.956	146.11	12	0.354	0.806	0.130	66.467
16	aSiC/Pt	50	78	80.732	135.651	12	0.354	0.806	0.120	74.719
17	aSiC/Pt	40	78	74.953	157.427	12	0.316	0.744	0.118	95.034
18	aSiC/Pt	40	78	69.588	146.159	12	0.366	0.694	0.112	105.826
19	aSiC/Pt	40	78	64.607	135.697	12	0.624	0.700	0.108	121.617
20	aSiC/Pt	40	78	59.983	125.984	12	0.849	0.642	0.102	135.729

Table 4.7: Optimization results for design II, R = 6 - 26.5 cm, t = 0.3 mm.

tions from the maximum d-spacing for low energies. This can be explained by the fact that for this design we have a larger low energy geometric area than the two previous designs, and changing the maximum d-spacing now effects a larger geometric area.

4.7.4 Design IV : R = [10,36.5]

Table 4.9 and Figure 4.9 show the optimization results of design IV. Again here we see $c > 1$ for the outer groups, which tends towards a linear grading.

4.8 Comparison

Figure 4.10 is a summary of the calculated effective areas and sensitivity. Design III has the highest low energy effective area, since it also has the highest geometric area, while Design II has the lowest effective area for low energy, since its shells are less tightly packed. Design IV has the lowest effective area for the high energy, since its innermost shells only go down to 10 cm, and Design I has the highest effective area at high energies.

It is not evident from these effective area curves which design is the more efficient. All they report is the effective area without any indication at what cost they are achieved. So instead of looking at the Effective area

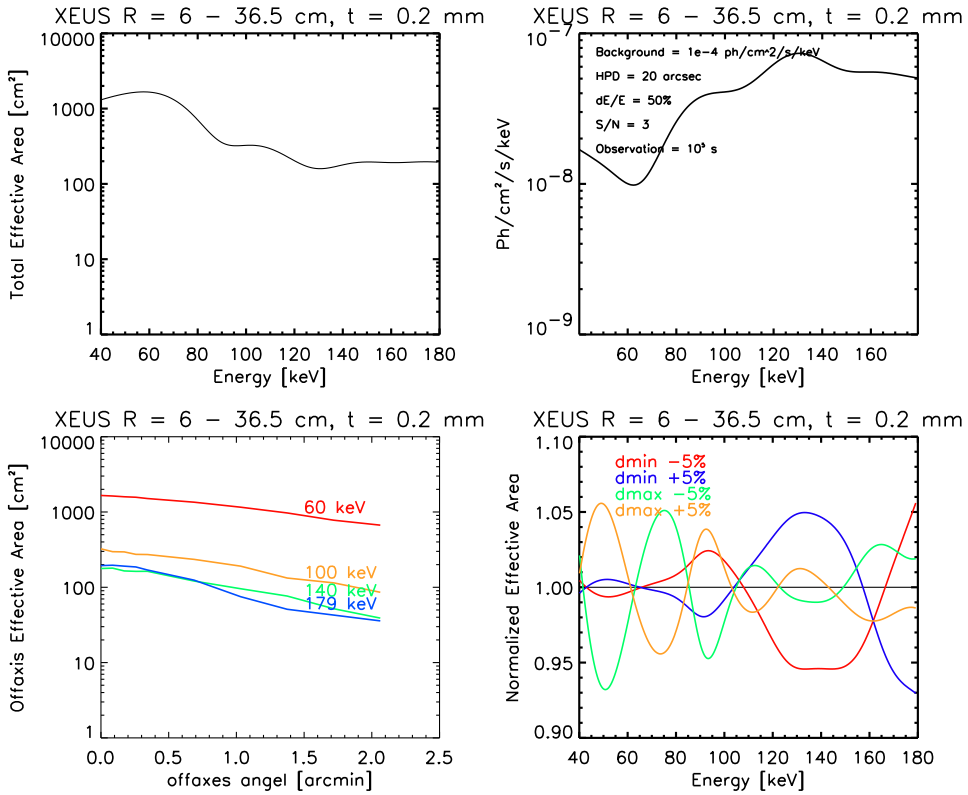

Figure 4.8: Top left: Effective Area. Top right: Sensitivity calculated using the parameters summarized in Table 4.5. Bottom left: Off-axis effective area as a function of off-axis angle. Borrom right: Uniformity simulations perturbing the minimum and maximum d-spacing. Curves are normalized against the on-axis effective area from the plot top left.

as a function of energy, it is more useful to study it as a function of group and normalize with the glass mass. The radii for the groups do not match up for the four designs, but by normalizing with the mass it allows one to better compare the designs group by group. I have extracted the effective area for the energies: E = 40 keV, 80 keV, 120 kev and 160 keV.

Figure 4.11 shows the evolution of the group dependent effective area for the selected energies, and immediately reveals that for Design III and IV, which have $R_{max} = 36.5$ cm, the effective area drops off for groups 19 and 20 already at 40 keV. The reason for this is that already at 40 keV the critical angle is $\alpha_c \sim 1.9$ mrad and since $\alpha(R = 36.5) = 1.825 < 1.9$ mrad, taking the outer radius to be that large is thus not efficient for 40 keV and above.

Grp	1/2/S	Emin	Emax	dmin	dmax	N	c	Gamma	Thick	FOM
1	aSiC/W	70	200	94.401	295.201	37	0.510	0.875	0.537	1.546
2	aSiC/W	70	200	86.252	269.718	37	0.429	0.481	0.475	2.093
3	aSiC/W	70	200	78.807	246.435	30	0.532	0.466	0.367	2.543
4	aSiC/W	70	200	72.004	225.162	46	0.392	0.438	0.483	2.988
5	aSiC/W	70	200	65.788	205.726	12	0.218	0.623	0.108	4.260
6	aSiC/W	70	200	60.109	187.967	18	0.201	0.605	0.142	4.932
7	aSiC/W	70	200	54.921	171.741	18	0.216	0.575	0.131	5.799
8	aSiC/W	70	200	50.180	156.916	25	0.230	0.595	0.166	6.315
9	aSiC/W	60	200	45.848	167.266	33	0.209	0.532	0.197	8.055
10	aSiC/W	60	200	41.890	152.827	38	0.249	0.517	0.214	8.641
11	aSiC/W	60	200	38.274	139.635	47	0.258	0.521	0.243	9.449
12	aSiC/Pt	60	78	89.668	127.581	10	0.368	0.684	0.106	29.332
13	aSiC/Pt	60	78	81.927	116.568	10	0.368	0.684	0.097	34.139
14	aSiC/Pt	40	78	74.855	159.758	12	0.419	0.778	0.122	45.553
15	aSiC/Pt	40	78	68.393	145.968	12	0.548	0.706	0.114	51.071
16	aSiC/Pt	40	78	62.109	133.367	12	0.873	0.671	0.107	57.395
17	aSiC/Pt	40	78	57.167	121.855	12	1.198	0.636	0.099	59.057
18	aSiC/Pt	40	78	52.167	111.336	15	1.378	0.615	0.114	60.487
19	aSiC/Pt	40	78	47.664	101.725	18	3.693	0.534	0.127	59.585
20	aSiC/Pt	40	78	43.549	92.944	22	10.022	0.468	0.143	58.707

Table 4.8: Optimization results for design III, R = 6 - 36.5 cm, t = 0.2 mm.

At 80 keV the critical angle has moved to $\alpha_c \sim 1.1$ mrad and consequently the effective area is essentially dead above groups 14-15.

For Design I and II the interesting feature is around group 10 at energies 120 keV and 160 keV, which corresponds to a change in minimum optimization energy from 70 keV to 60 keV. The trough at group 14 at 80 keV comes from the transition to Pt/SiC from W/SiC. It is not straightforward to remove these troughs as modifying them at one energy will cause them to appear at other energies. In this it is therefore important to set specific scientific energy requirements before the final multilayer design is worked out.

Looking at the area pr mass for the designs, Design I and II are the same geometry but with different glass thickness, which results in Design II having an overall worse area to mass ratio. Design III and IV are more difficult to compare. The radius at group 7 is $\sim$ 10 cm for Design II and corresponds to group 1 of Design IV. The area/mass of these two groups are the same when starting at group 7 for Design III, and so only real difference between the two Designs is the extra gain in effective area at the cost of mass.

Design II clearly looses in every test against Design I, and thus thinner glass with closer packing is the way to go. So between Designs I, III and IV, besides the fact that R=36.5 cm is too large a radius for this energy

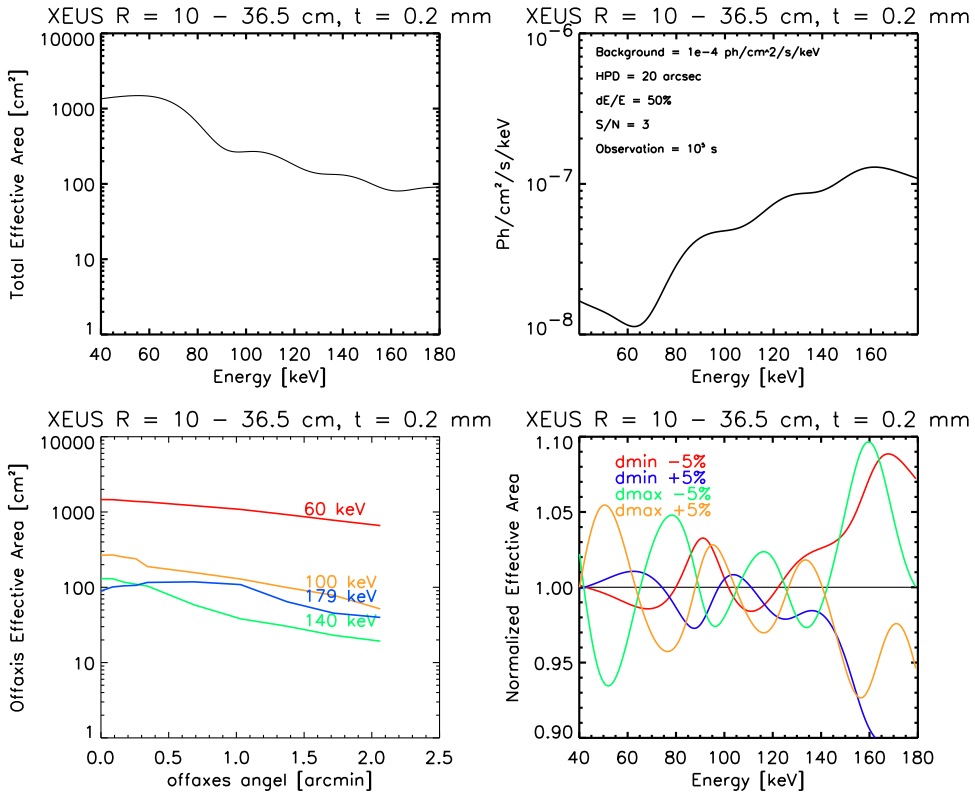

Figure 4.9: Top left: Effective Area. Top right: Sensitivity calculated using the parameters summarized in Table 4.5. Bottom left: Off-axis effective area as a function of off-axis angle. Borrom right: Uniformity simulations perturbing the minimum and maximum d-spacing. Curves are normalized against the on-axis effective area from the plot top left.

range, choosing one design above another seems to be a matter of purpose. If one desires to have a high energy response with less care about the low end then Design I. If one desires a more even response with emphasis on the low energy then Design III is right choice, and if the high energy is of little interest at all then Design IV would be the right choice, but since this study concerns high energy extensions, Design VI is a poor design for these energies.

Grp	1/2/S	Emin	Emax	dmin	dmax	N	c	Gamma	Thick	FOM
1	aSiC/W	70	200	58.106	177.120	37	0.376	0.797	0.310	1.445
2	aSiC/W	70	200	54.464	166.017	30	0.388	0.734	0.238	1.886
3	aSiC/W	70	200	51.050	155.611	30	0.423	0.713	0.226	2.097
4	aSiC/W	70	200	47.850	145.856	37	0.348	0.667	0.251	2.810
5	aSiC/W	70	200	44.850	136.713	15	2.230	0.672	0.119	3.008
6	aSiC/W	50	200	42.039	179.400	15	0.669	0.670	0.114	3.834
7	aSiC/W	50	200	39.403	168.155	15	0.919	0.660	0.114	4.244
8	aSiC/W	50	200	36.933	157.614	58	0.273	0.594	0.295	5.309
9	aSiC/W	50	200	34.618	147.734	97	0.245	0.570	0.446	5.834
10	aSiC/W	50	120	57.697	138.473	31	0.362	0.792	0.244	9.218
11	aSiC/W	40	120	54.080	162.241	20	0.348	0.667	0.155	11.379
12	aSiC/W	40	120	50.690	152.071	15	0.650	0.652	0.121	12.607
13	aSiC/W	40	120	47.513	142.538	12	0.946	0.642	0.095	13.600
14	aSiC/Pt	40	78	66.802	133.603	10	0.368	0.684	0.090	23.255
15	aSiC/Pt	40	78	62.614	125.228	10	0.368	0.648	0.085	27.962
16	aSiC/Pt	40	78	58.689	117.378	10	0.368	0.648	0.079	31.034
17	aSiC/Pt	40	78	55.010	110.020	10	0.368	0.684	0.074	33.199
18	aSiC/Pt	40	78	51.562	103.123	15	4.262	0.614	0.111	56.996
19	aSiC/Pt	40	78	48.330	96.659	18	3.767	0.543	0.125	57.430
20	aSiC/Pt	40	78	45.300	90.600	22	5.749	0.483	0.143	57.702

Table 4.9: Optimization results for design IV, R = 10 - 36.5 cm, t = 0.2 mm.

4.9 Conclusion

This study is purely conceptual, but based on experiments and considerations learned from the HEFT mission. The study shows that by comparing different designs, it becomes easier to pin down specific design parameters, that may not be intuitively known beforehand. For example, it is not evident from the effective area curves that R=36.5 cm over-designs the optic at the selected energy range.

The time consumption on these simulations is not staggering, and as an average taking into account reruns and corrections, simulating one design takes about 2 weeks. These types of simulations are thus a fast and easy way of testing different geometries, and from measurements from the actual HEFT optics, for which this tool was originally developed, we also know that the simulations are quite accurate.

The future of x-ray optics has just begun to flourish, and the use of such a tool as this will undoubtedly be much needed.

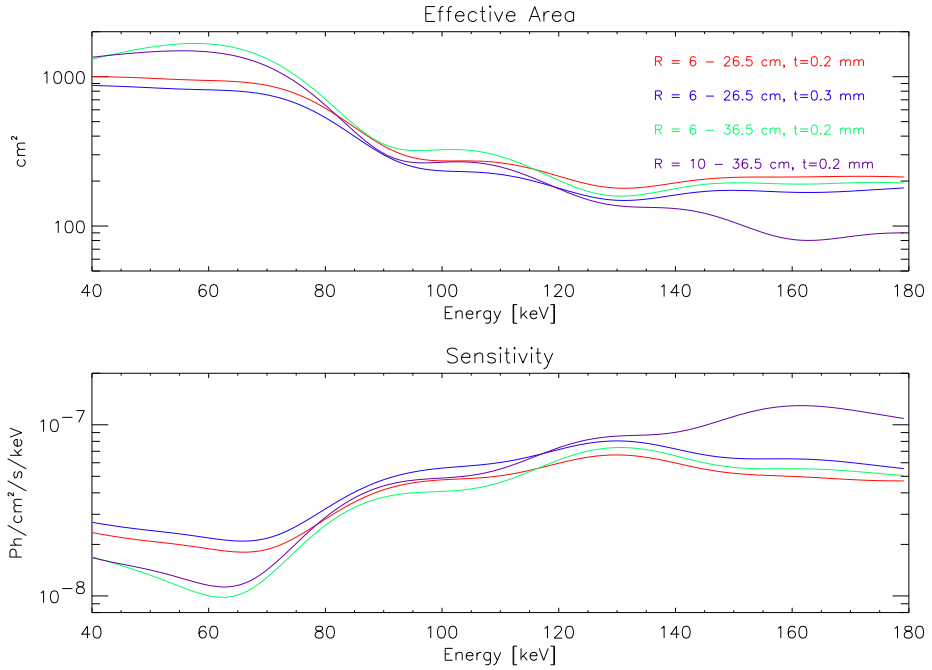

Figure 4.10: Summary of the effective area. Red = Design I. Blue = Design II. Green = Design II. Violet = Design IV.

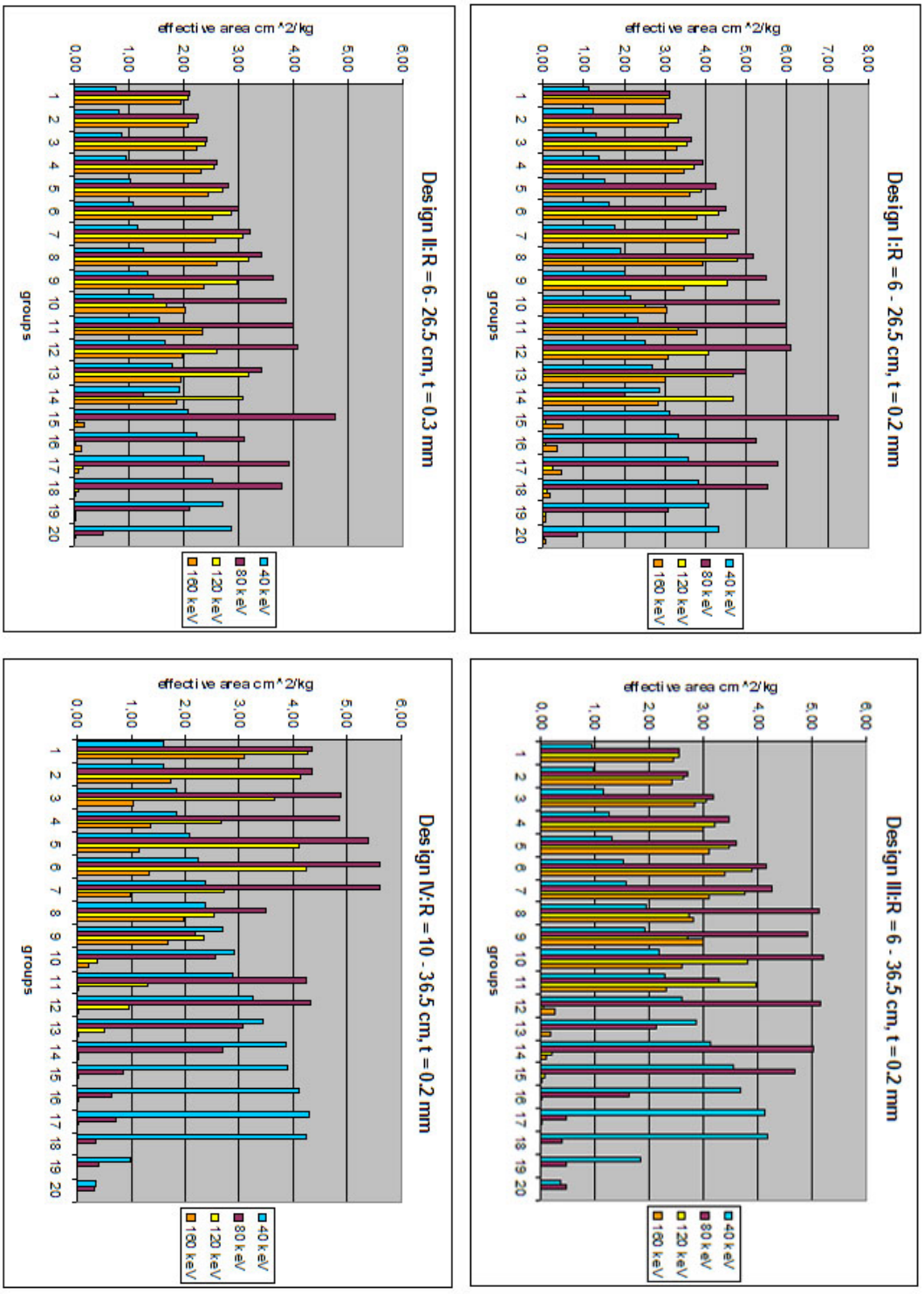

Figure 4.11: Effective Area/Mass as a function of groups and the energies 40,80,120 and 160 keV.

Chapter 5

Chandra observtion of B1152+199

5.1 Introduction

5.2 Overview: AGN Unification

Active Galactic Nuclei, AGN, go by a long list of names: quasars, QSO (quasi-steller object), blazars, BL Lac objects, Seyfert galaxies, FR1 (Fanaroff-Riley type1), FR2, and so on. The names describe observational differences long thought to be exclusive and intrinsic to that particular type of object, such as spectral features or lack thereof, broad/narrow lines and high/low luminosities. However, to a large extend in the frame work of AGN unification, all these observationally apparently different objects are in principle aspects of the same general object.

Covering 20 years of detailed investigations of AGN, the condensed list of the unification paradigm covers the fundamental ingredients:

- Supermassive central black hole, $10^6 - 10^{10} M_\odot$.
- Accretion disc and corona.
- Broad-line region. High velocity gas.
- Narrow-line region. Low velocity gas.
- Obscuring torus.
- Relativistic Jet.

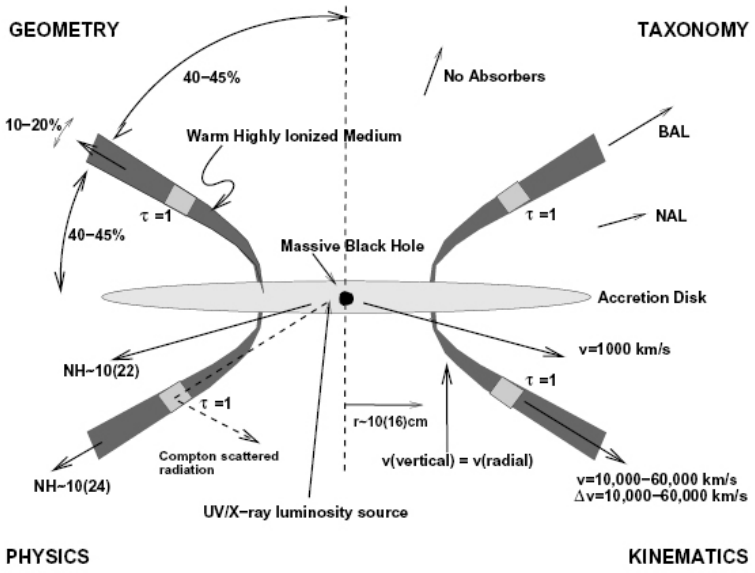

Figure 5.1: Schematic of an archetype AGN.

Except for the last item, the list appears to hold for all AGN, with variations, of course, in black hole mass, ionization parameter, luminosity etc. Relativistic jets are found in most radio loud AGN, but are rarely seen in radio quiet AGN, and so there is still some debate whether Radio Loud and Radio Quiet should be treated as separate objects. However allowing for a wide parameter space both RQ and RL can be fitted into the above list.

In the unification scheme the basic geometry of an AGN is believe to appear as detailed in Figure 5.1. Surrounding the central black hole is an optically thick, geometrically thin accretion disc stretching out to several hundred $r_g = GM/c^2$. Above and below is a hot hard X-ray corona responsible for the continuum, which can be redirected, as illustrated, to the observer by reflection off the colder accretion disc. Surrounding the disc is a thick obscuring torus of cold optically thick gas, which when the AGN is viewed close to edge on, blocks out the direct source from the observer.

In unification the angle of the observer to the plane of the torus deter-

mines what part of the object is seen, and what shape the spectrum takes. For example, an observer located in the plane of the torus will see emission like that of a Seyfert 2 galaxy, where the direct source flux has been obscured by the torus, allowing the observer to see the narrow forbidden lines created in the torus. If the inclination is high enough to allow the observer to see the direct source, the object is a Seyfert 1 galaxy, dominated by broad lines and reflection components scattered off the accretion disc, while facing the disc and looking straight down the funnel of a jet produces a blazar.

An AGN emits in an extraordinary wide energy range covering nearly 13 orders of magnitude in frequency, and the nucleus emission completely overwhelms the light from the host galaxy. In the radio region the spectrum is dominated by polarized synchrotron emission from the jet. The optical and UV is dominated by a feature termed the Big Blue Bump, which is the thermal radiation from an accretion disc of T $< 10^5$ K peaking in the UV [37]. The high energy tail of this BBB is visible in the soft end of the X-ray band as the 'soft excess'. The spectrum in the X-ray is represented by a power law, which extends up to a few hundred keV, where it is abruptly cut off. The source of the X-ray continuum comes from the inner parts of the accretion disc close to the black hole.

Since I am using data acquired with the *Chandra* observatory, I will hereafter focus on the important processes occurring in the 0.1 - 15 keV range.

5.2.1 X-ray continuum: Reflection Components, Warm Absorbers and Soft Excess

The source of X-rays is thought to be in the form of a hot coronal gas located above and below the disc [38]. The geometric shape and extend of the gas is still unknown, and most models include the possibility of a halo as well as a point source or lamp post model where the source is located in a point above the disc. The emitted continuum spectrum can be fitted by a simple power law, $F_\nu \propto \nu^{-\alpha}$, which is a good approximation to most AGN spectra in the energy range 0.3 - 10 keV. The index falls in a narrow range $\Gamma = 1.8$ to $\Gamma = 2.1$ [39][40] and includes all types of AGN. Layered on this continuum are processes arising from reflection of the X-ray flux, and soft X-ray features produced by the radiation passing thought highly ionized clouds, termed warm absorbers.

The reflection component is the most dominant of the two. It is caused by the high energy photons of the source impinging on the cool accretion disc [41]. If the disc is optically thick and neutral the incoming radiation will

suffer compton scattering as well as photoionizing the neutral medium. The component rises sharply, if present, at 10 keV, since a column density of such a disc is suspected of the order 10^{24} cm^2, and the optical depth for photons below 10 keV will be larger than unity, and so essentially absorbed. Compton recoil down scatterers the energetic photons, and few reflected photons of energies above 100 keV can emerge. The effective reflected continuum therefore looks like a hump between 10-50 keV, peaking at around $\sim$ 30 keV. A major part of the opacity in the disc is the Fe K-edge, and since it is abundant compared to other high-Z elements, the resulting photoionization and fluorescence produces a strong Kα line.

The location of the "warm absorber" relative to the source is still unknown. The telltale signature of the absorber are K-shell absorption edges of warm oxygen (O VII and O VIII) characteristic of an optically thin, photoionized cloud [40]. Based on the Equivalent Widths of the oxygen absorption lines the level of ionization can be calculated, and since the warm absorber appears to be correlated to UV line absorption, features in the UV can aid in determining the level of ionization of the absorber.

The final major deviation from a power law comes from the 'soft excess' which appears in many AGN below $\sim$ 1 keV. The source of the 'soft excess' is believed to be the high end tail of the thermal emission from the accretion disc. There is some problems with fitting termal models to the Big Blue Bump, especially towards the extreme UV where the observations and models diverge, and the excess has been attributed to inversely compton scattered synchrothon radiation.

5.3 Line Distortions and Hot Spots

The vicinity of the Black Hole is perhaps the most important region in the AGN, and fortunately it is not as elusive as one might have feared.

There is little dispute over the rough geometry and general scenario that is played out close to the Black Hole. Most agree that the Black Hole can be described by a Kerr metric and fully characterized by only three quantities: mass M, angular momentum J and electric charge Q, which is assumed to be negligible for astrophysically relevant Black Holes and thus $Q = 0$. Since General Relativity is scale invariant, it is convenient to use the angular momentum per unit mass or 'spin', $a = Jc/GM^2$, and the distance in units of the gravitational radius, $r_g = GM/c^2$. The a-dimensional spin can be $0 < a < 1$. When $a = 0$ the metric reduces to the well known static Schwarzchild solution, and from potential energy calculations the last

stable orbit for this metric is at $6r_g$. A maximally rotating black hole can have $a \sim 0.988$ as calculated by Thorne (1974) on the basis of counteracting torques, and for this metric the last stable orbit for matter moving prograde is $r_{LSO} \sim 1.23r_g$.

In-falling gas on the Black Hole forms into an accretion disc, which is assumed thin compared to its radial extend, and optically thick. Despite being exposed to an intense flux of hard radiation, it has been shown [41] that the accretion disc can remain 'cold' at $T < 10^5 K$, provided the disc is sufficiently dense. Such a disc is in thermal equilibrium and essentially neutral to the incoming external X-ray flux, although it is possible that the top layers of the disc become ionized [42]. The incoming hard X-ray photon is subject to a number of possible interactions: Compton scattering, photoelectric absorption leading to fluorescent line emission, or photoelectric absorption followed by Auger de-excitation. The emerging photons are thus either compton scattered or in the form of fluorescent line emission, the former of which results in the reflection hump described above. The fluorescent iron line is produced when one of the two K-shell electrons or the iron atom is ejected following photoelectric absorption of a X-ray. There are other fluorescence lines produced in this manner like Ni and Cr, but since Fe is the most abundant heavy-Z element it is also the most prominent.

By nature the Fe $K\alpha$ line is narrow, and any broadening can be assumed to be due to Doppler shifts and gravitational redshifting. The line from a non-relativistic disc of accreting matter is double horned and symmetric about the rest energy. The blue shifted horn corresponds to matter moving towards us at maximal speed, and the red horn from matter moving away at the maximal speed. However, environments around Black Holes are not newtonian and the lines are consequently skewed by relativistic effects. Broad skewed iron lines are common in AGN of Seyfert 1 type, examples of which are MCG -6-30-15 [43][44] and NGC 3516 [45]. Both have a Fe line with a narrow core and an extended red wing consistent with GR effects, suggesting that the emission originated in the inner parts of the accretion disc.

How the incoming non-thermal corona forms, responsible for the hard X-ray flux is far from understood, but the basic concept is believed to involve transfer processes, which inversely Compton scatterers the thermal optical/UV disc photons, thereby dissipating the accretion power into a corona situated above the disc in the inner most parts. If the corona is emitting isotropically then half of its flux will be reprocessed by the disc, and reflection features are thus tightly tied to the coronal flux. Below 10 keV the reflected component will essentially respond instantly to a change in the in-

coming flux since the cold gas thermal inertia is very small, while above 10 keV the Compton scattering will produce a time lag of the reflection component to the direct flux on a timescale on the order of the Thomson length [41].

The X-ray lightcurves of AGN have been found to be very similar to X-ray binary systems (XRB's), which are often dominated by strong aperiodic flickering variability (ref McHardy, Van der Klis Vaughan). Because of the similarities of the AGN lightcurves to XRBs and black hole XRBs, the mechanism behind the flux variability is suspected to be of a similar origin, in which powerful magnetic reconnection causes part of the disc and corona to flare. A method of quantifying this variability is through the power-spectral density function of the lightcurve, which is a well understood function and a common tool for temporal analysis. However, the PSD can only yield a mathematical model, which then must be related to physical processes. Interpretation of the PSD is therefore strongly biased by the model and complicated by the fact that many models can account for the same power-spectral density. PSDs of AGN can to a first approximation be represented by broken or gently bending power laws. They are found to be slightly "red", which means that the stochastic process underlying the curve is slightly non-stationary, and that the mean and variance changes with time [46]. Also there is some evidence that the lightcurves are non-linear, where the AGN appear to have a linear rms-flux relation, so brighter objects are more variable [46].

In the simplest "shot-noise" models [47] the lightcurve is produced by a sum of random flares of different amplitudes, with decay times given by a power law distribution, where the breaks in the PSD give the maximum and minimum decay timescale. Such a model is linear and the timescales unrelated, and can't produce a linear rms-flux relation. Instead the physical processes giving rise to the variability are thought to be multiplicative, such that power on different timescales are related. Models that realize this allow for an evolution of the flares or hot spots produced on the disc surface, which can co-rotate with the disc and/or merge with other spots.

Regardless of the exact physics, such flares are anisotropic events which result in an uneven illumination of the disc. Since the iron line is a reflection component, it must react to the sporadic flaring and exhibit temporal skewed behavior. In particular if a hot spot was localized and co-rotating, very distinct shapes of the iron line would be seen. This has been modelled by Dovciak (2004)[48] and Goosmann (2006)[49], and the spots location on the disc relative to the observer, as well as its lifetime, decides the shape of the line. Figure 5.2 shows theoretical neutral iron line curves viewed under

different conditions, generated by the **kyr1line** code. When a large portion of the disc is fluorescent with Fe Kα, the line exhibits a wide red wing. An emitting annulus close to the black hole will be double peaked, where the weaker peak is redshifted, and the blue peak (still redshifted relative to the rest energy) is stronger due to beaming. Increasing the viewing angle, increases the distance between the peaks until at $\theta = 90°$, the red wing has vanished and there is only one narrow core. A flare in orbit will exhibit the strongest redshift at $\phi = 90°$ as the matter moves away at maximum speed, and it will have the highest flux at $\phi = 270°$ when the matter moves towards the observer at the maximal orbital velocity.

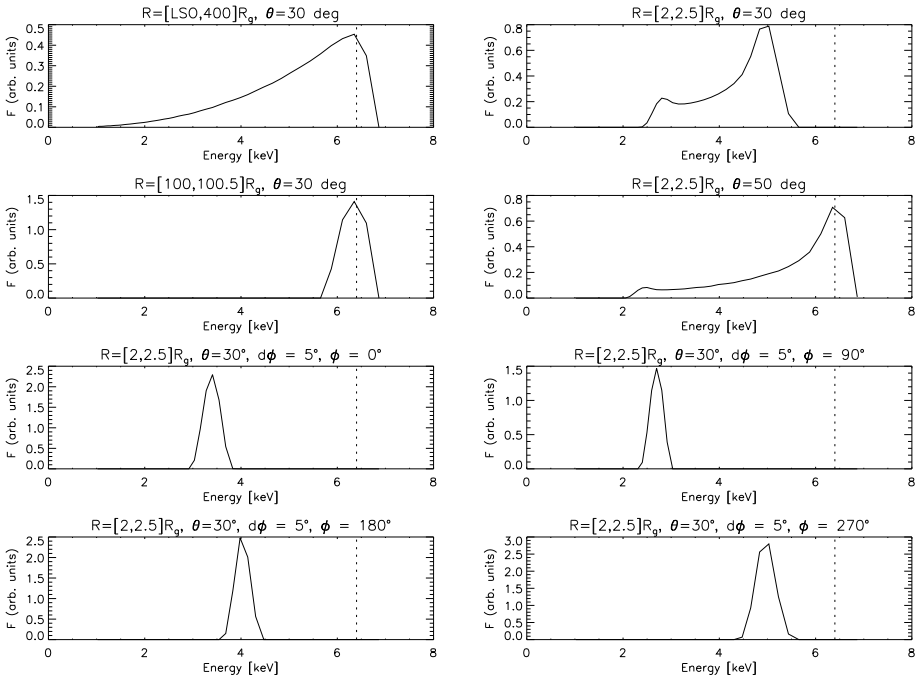

Figure 5.2: Neutral iron line shapes in strong gravity. The radius is in units of the gravitational radius, $R_g = GM/c^2$, and LSO = last stable orbit. The black hole is assumed spinning at maximal speed, a = 0.998, θ is the observational angle to the disc plane, ϕ is the azimuthal angle with $\phi = 0$ being the point on the disc closest to the observer. In the top four plots $d\phi = 360^o$ including the whole disc. The lower four plots shows the redshifted movement of the line as a small subsection of the disc, $[d\phi = 5^o, dR = 0.5R_g]$, is viewed at different azimuthal positions.

Temporally skewed behavior of the iron line has been observed in several cases such as NGC 3516 [50] [51], NGC 7314 [52] and Mkn 766 [53]. NCG 3516 is among the best studied Seyfert 1 galaxies, and has a broad variable

iron line. It has been observed with about every X-ray observatory, but the best data are of course from XMM-*Newton* and *Chandra* observations which were partly overlapping. The spectrum exhibits a core with broad wings, red- and blue wards. The core appears to be responding to the continuum changes [50] and the wings appear to be correlated to the core. It is possible that the wings are unrelated to the core, but regardless of origin, all proposed models indicate variable emission from close to the central black hole [50] [51].

NGC 7314 is known for its high variability, and high resolution HETGS *Chandra* observations found narrow line neutral and ionized components responding differently to the continuum variability. The low state was found to be dominated by reflection from optically-thick matter, and the high state dominated by reflection from more highly ionized matter. The former might be associated with distant matter and so would not respond to variability in the direct continuum. The reflection from ionized matter is likely present at all time, and responds to continuum variability, dominating the spectrum in the high state [52].

Mkn 766 has been observed by ASCA [45], ROSAT [54], BeppoSAX [55] and twice by XMM-*Newton* in 2001 [53] and 2005 [56], with some confusing results. The ASCA observations reported a relativistic broad iron line, while the ROSAT data only found a narrow line. The XMM-*newton* observations were far longer than the previous, and with the better sensitivity it was determined that Mkn 766 is variable, thereby explaining the differences in previous observations. The spectrum exhibits a relatively weak and narrow neutral Fe $K\alpha$ line, as well as He-like emission, which is found to be correlated to the continuum variability, but without exhibiting gravitational redshift. This is interpreted as originating from highly ionized matter in the line of sight at some distance from the central black hole[53][56].

From the above it is clear that the iron line provides a powerful tool of probing the properties of the inner accretion disc, the central Black Hole, and the surrounding geometry. The line shape, redshift and strength of the Fe $K\alpha$ can reveal degrees of disc ionization, orientation, and spin of the black hole. If additionally a radial location of an emission is know the mass of the Black Hole may be derived.

5.4 B1152+199

The gravitational lens B1152+199 was discovered during VLA observations in 1998 as part of the Cosmic Lens All-Sky Survey [57]. The lens produces

two images of the background quasar separated by 1.56", which have a flux ratio at 8.46 GHz of 3.03 ± 0.03. We follow the convention of the previous authors S. T. Meyers [57] and S. Toft [58], naming the brighter of the two components 'A' and the fainter component 'B'. The quasar is located at redshift $z = 1.019$ and the lensing galaxy at $z = 0.439$ [57]. Rusin et al [59] observed the lens with the Hubble Space Telescope, HST, and found optical counterparts to the lensed object and determined a flux ration of $\sim 70 : 1$ in the V band and $\sim 20 : 1$ in the I band, confirming strong extinction of the B component, previously reported by Toft [58], as it passes through the lens. Rusin et al [59] also obtained high resolution VLBI observations of the object and resolved two jets. They found that the jet from component A is quite straight, while the jet from component B shows a bend, interpreted by Metcalf [60] possibly to be caused by substructure of the lensing mass. Component B is closest to the lensing mass and the light of B is thus ahead of component A. A simple dark halo lens model made by Toft [58] suggests the time delay between the images to be on the order of 60 days using $\Omega = 0.2, \Omega_\Lambda = 0, H_0 = 65\,\mathrm{kms}^{-1}\mathrm{Mpc}^{-1}$, which is consistent with what Rusin [59] finds using a singular power law ellipsoid, that has time delay to be $\sim 39h^{-1}$ days assuming a flat $\Omega_\Lambda = 0.7, H_0 = 100h\,\mathrm{kms}^{-1}\mathrm{Mpc}^{-1}$ cosmology.

5.5 Observations and Data Reduction

Chandra observed the lensed QSO B1152+199 with the Advanced CCD Imaging Spectrometer on 22 February 2005 (OBS ID 6249) for a duration of 16.4 ks and later on 26 February 2005 (OBS ID 5909) for 8.3 ks. B1152+199 was positioned on the back-illuminated S3 chip in 1/8 sub array mode. All data were obtained in Very Faint mode, and no periods of high background occurred during the observations. The Level 1 data were reduced using the Chandra Interactive Analysis of Observations (CIAO) version 3.3.0.1 software package. The data were reprocessed with the *acis_process_events* procedure screening out bad pixels, and excluding the pixel randomization to prevent smearing as the angular extend of the objects is on the arcsec level. Only the standard ASCA grades 0,2,3,4 and 6 were used in the analysis, and the calibration files CALDB version 3.2.2.

5.6 Photometry

The separation between component A and B is 1.56", and to investigate how much contamination there might be from one image in the other, we simulated the 0.3-8 keV PSF at the A and B image positions with the Chandra Ray Tracer, ChaRT [61]. The Chandra Ray Tracer is a tool, which simulates a PSF based on an input spectrum, sky coordinates and location on the ACIS chip. As input source spectra I used 0.3-8 keV spectra obtained from a 1.0" circle centered on each component, judged to include negligible contamination from the other component. The simulated images were normalized to the measured count rate of the *Chandra* images extracted from the 1.0" circles. For all simulated images we evaluated the amount of contamination from the other image as a function of the extraction circle radius. Figure 5.3 shows the accumulation of counts from the simulated PSFs as a function of radius for component A and B respectively. The left panel counts are normalized with respect to the total amount of counts in A, and the right panel has been normalized with respect to the total amount of counts in component B. In the left panel the extraction annuli have their common center on component A, and as the radius increases counts from component B gradually enters into the extraction circle. In the right panel the common center is on component B. The horizontal dashed line is the 90% mark.

For image A at 90% there is little contamination, and we moved the threshold to 95%, yielding a contamination level of 2.5% by image B at an extraction radii of 1.26". At this radius the total number of counts for observation 6249 and 5909 combined is 3299. For image B at 90% the contamination by image A is 7% at 0.95". From this point on the contamination rises steeply and was thus held at 0.95". The total number of counts combined from both observations in image B is 815.

X-ray spectra and lightcurves were generated from events in the 0.3-8 keV range within the circular regions described above, centered on the A and B components of B1152+199. The energy bounds were chosen so as to leave out the lowest energies where the spectral calibration is poor, and to disregard the highest energies dominated by background. Background spectra were generated from circular regions devoid of sources and not overlapping any source regions.

Unless otherwise stated the extracted spectra were binned with a minimum of 20 counts per bin, and uncertainties are presented at the 90% limit.

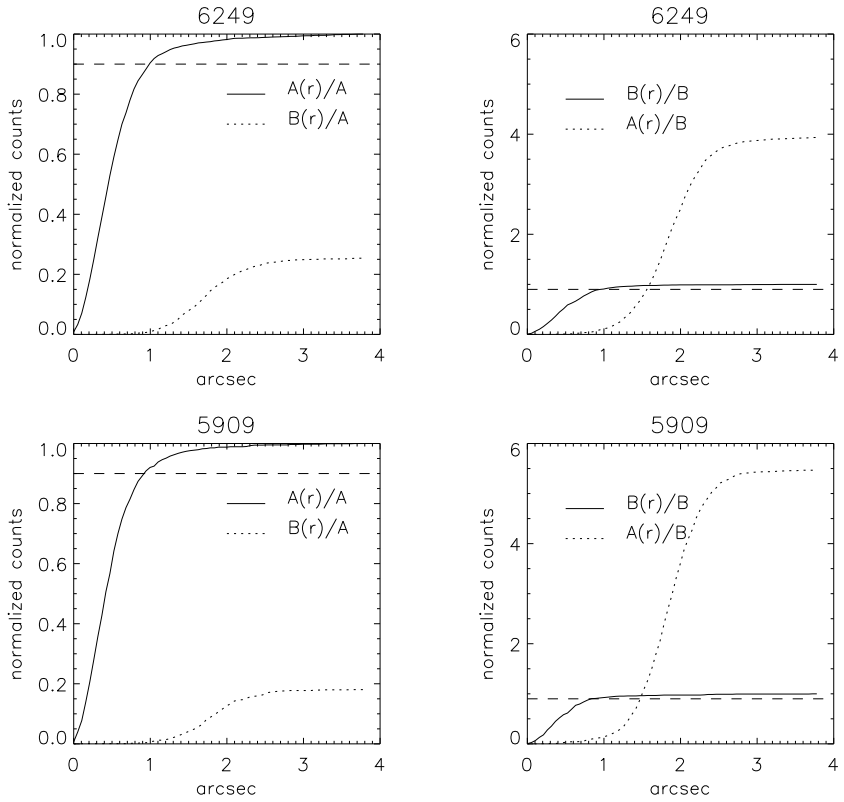

Figure 5.3: Left panel: Accumulated counts as a function of extraction radius. Center of the extraction circle is on component A, and all curves are normalized with the total number of counts in component A. Right panel: Center of the extraction circle is on component B, and all curves are normalized with the total number of counts in component B. The horizontal dashed line is the 90% mark.

5.7 Spectral Analysis

5.7.1 Lightcurves

Lightcurves for the two observations and two components were generated for the energy range 0.3-8.0 keV. Figure 5.4 shows the four lightcurves in units of count rate using a binning of 1ks, and with errors calculated using standard poisson statistics. A simple sinusoidal function of the type f = $A_1 + A_2 * \sin(A_3 * t + A_4)$ was fitted to the light curves, the results of which are summarized in Table 5.1. Only component A of the 6249 observation has all four parameters free and for this the sinusoidal function provides a

Object	A_1 Scale [c/s]	A_2 Amplitude [c/s]	A_3 Period [h^{-1}]	A_4 Phase	χ^2/dof
6249 A	$0.139^{\pm 0.002}$	$0.011^{\pm 0.003}$	$2.891^{\pm 0.005}$	$-2.477^{\pm 0.368}$	0.604
5909 A	$0.147^{\pm 0.004}$	$0.011^{\pm 0.006}$	2.891^{b}	$-0.042^{\pm 0.533}$	0.799
5909 A	$0.148^{\pm 0.004}$	0.011^{a}	$4.059^{\pm 0.676}$	$-3.712^{\pm 1.078}$	1.014
6249 B	$0.037^{\pm 0.001}$	0.011^{a}	2.891^{b}	$2.917^{\pm 0.154}$	2.206
6249 B	$0.038^{\pm 0.001}$	0.011^{a}	$2.883^{\pm 0.003}$	$-1.880^{\pm 0.189}$	2.240
5909 B	$0.035^{\pm 0.002}$	0.011^{a}	2.891^{b}	$2.435^{\pm 0.244}$	1.184
5909 B	$0.037^{\pm 0.002}$	0.011^{a}	$4.075^{\pm 0.326}$	$-4.408^{\pm 0.484}$	2.399

Table 5.1: ^{a} This parameter has been frozen to the value of A_2 of 6249 A.^{b} This parameter has been frozen to the value of A_3 of 6249 A.

good fit to the data. The solid curve in observation 5909 image A represents the fit where the period A_3, obtained from the 6249 A fit, has been frozen, while for 6249 B and 5909 B the solid line represents a fit where both A_2 and A_3 parameters were kept frozen, since letting all parameters range freely produces a flat fit. The black dotted line in those same three plots are fits where only the amplitude, A_2, found in 6249 A was kept frozen. The red dotted curves in the observation 5909 plots are the time extrapolated solid line fits from 6249 A and B.

6249 A is clearly variable and the best fit finds it to be periodic with a period of $T = 2.89 \pm 0.005$ hours. For 5909 A, B and 6249 B the evidence for periodic variability is less obvious, and the simple sine function does not provide a very good fit. This is not surprising given that the variability in many AGN has been observed to be of a spurious nature as explained before. Also the time extrapolated fits from 6249 A and B, are out of phase with the best fit for the B images. The most likely interpretation of this, comparing to results from far longer observations of well known AGN, is that the variability is probably aperiodic, and the periodicity observed in 6249 A is a special case, where a particular bright flare manages to outshine the other components as it orbits.

5.7.2 Continuum

The two observations are separated by ∼4 days and the time delay between images A and B is estimated to be around 60 days, with image B leading image A. Hence, in principle there are observations of four intrinsic different time series of B1152+199. Significant X-ray absorption [62] and extinction in UV for image B has been found by Eliasdottir [63] and Toft [58], and we have placed a photoelectric absorber with column density nH = 0.2*10^{22} cm^2

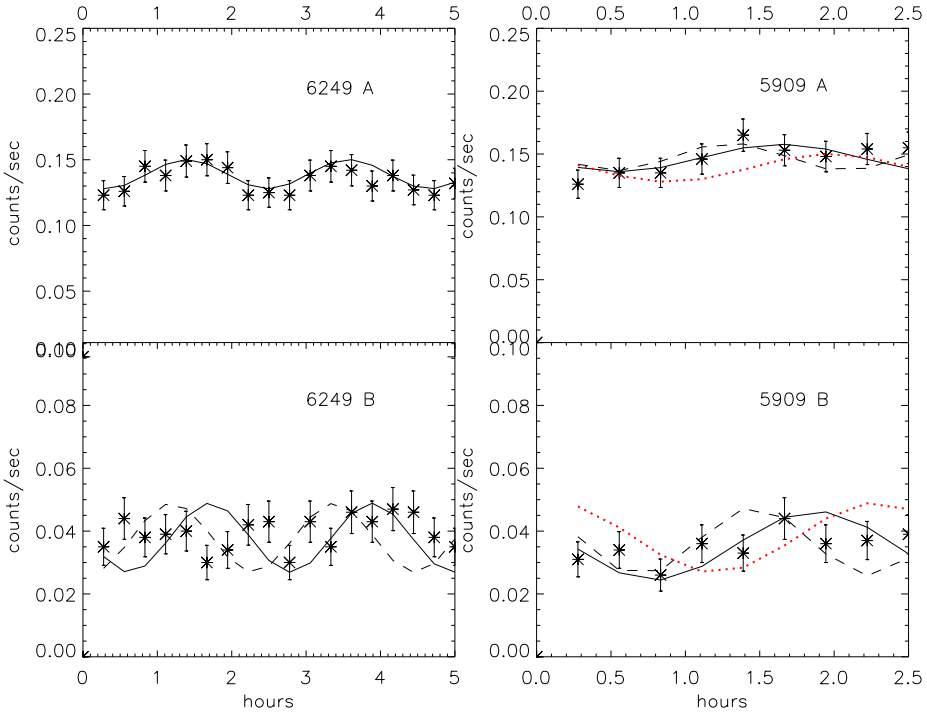

Figure 5.4: The lightcurves of both components have been binned with 1 ks. Solid lines and dashed lines are best fits using different parametric constraints, summarized in Table 5.1, and dotted red lines are the time extrapolation of the 6249 solid fits. Error bars are 1 σ.

at the location of the lensing galaxy at redshift z=0.439 for this component. Ignoring the 2.2-3.0 keV region containing the redshifted Fe Kα line, which can bias the continuum fit, the continuum in the four images was fitted with an absorbed power law with galactic column depth nH = 2.89*10^{20} cm^2[64]. Table 5.2 lists the best fit parameters for the continuum of each component. For the A component we find an average slope of $\Gamma = 2.10 \pm 0.08$, which is at the softer end of the typical power law index range, $\Gamma = 1.7 - 2.1$ found by Nandra and Pounds [39] and other surveys [40][65]. For component B the average spectral index is $\Gamma = 1.81 \pm 0.35$, which is somewhat harder than A, but may be explained by worse statistics.

To investigate the possible correlation between temporal and spectral variation, observation 6249 component A was divided into two sections as dictated by the lightcurve fit shown in Figure 5.4. Time cuts were made at the best fit count rate 0.134 c/s at times: t=(0.80,2.97,1.99,4.17) hours.

Object	Zhabs Z.nH [10^{22} cm^2]	Zpowerlw Γ	norm [10^4]	χ^2/dof
6249 A		$2.11^{+0.07}_{-0.06}$	$7.31^{+0.45}_{-0.44}$	83/81
5909 A		$2.09^{+0.09}_{-0.08}$	$8.08^{+0.69}_{-0.68}$	69/62
6249 B	$0.26^{+0.16}_{-0.11}$	$1.86^{+0.22}_{-0.18}$	$2.54^{+1.1}_{-0.6}$	28/37
5909 B	$0.18^{+0.33}_{-0.18}$	$1.77^{+0.48}_{-0.35}$	$1.9^{+22}_{-0.7}$	12/16
6249 A low		$2.12^{+0.09}_{-0.09}$	$7.46^{+6.18}_{-5.99}$	36/51
6249 A high		$2.06^{+0.09}_{-0.09}$	$7.62^{+0.74}_{-0.72}$	37/41
A combined		$2.07^{+0.05}_{-0.05}$	$22.77^{+1.1}_{-1.1}$	120/118
B combined	$0.23\ ^{+0.11}_{-0.11}$	$1.79^{+0.16}_{-0.16}$	$6.83^{+2.0}_{-1.59}$	25/42

Table 5.2: All continuum were fitted with a photoelectric absorbing galactic component of nH = 2.89*10^{20} cm^2.

The separated series were added together to form two spectra: a 'low' rate of length 8.4 ks, and 'high' rate of length 7.5 ks. For the 'low' state the slope is $\Gamma = 2.12 \pm 0.1$ and $\Gamma = 2.06 \pm 0.1$ for the 'high', and may therefore hint at a hardening of the spectra in the high flux state.

Compton reflection of the direct source off the cold neutral accretion disc has been predicted and observed in several AGN [66][67][68], and we attempted to include a compton reflection component using the XSPEC **pexrav** model. Unfortunately the softness of the spectra means there are very few counts above 5 keV of the observed frame, and except for the iron line region itself, which possibly biases the fit, there were too few counts to constrain the model.

5.7.3 Variability Study

To better quantify the variability in observation 6249 in a model independent way, Figure 5.5 shows the high/low flux fraction of the 'high' and 'low' spectra as a function of energy. The figure shows that the 'high' flux rises up in excess at around 1 keV, peaks at 2 keV and falls back down at 3.5 keV. This is indicative of the spectral hardening of the power law, and the spectral fits of the 'high' and 'low' spectra also shows the tendency of a hardening of the 'high' spectrum. At 4.4 keV rest frame *Chandra's* gold absorption edge (2.2 keV) cuts the effective area down abruptly, which is why the bin size is doubled, but even then it is clear that the flux rises for the 'high' spectra at the iron line region. The vertical dotted line is the

location of the center of the gaussian fit of 6249 A 'high' (see Table 5.4) at 5.3 keV. The transition edge at 4.4 keV is ambiguous since it includes the gold absorption edge, where the calibration files are known to be unreliable, and it is thus not entirely clear where the rise of the excess occurs.

To further investigate the variability of the lightcurve of 6249 B we follow the approach by Edelson (2002) [69] and calculated the Fractional Excess Variability Amplitude. The fractional excess amplitude is the noise subtracted variance fraction of the mean:

$$F_{var} = \sqrt{\frac{S^2 - < \sigma_{err}^2 >}{< X >^2}} \, , \tag{5.1}$$

where S is the variance, X the mean count rate of the lightcurve, and $< \sigma_{err}^2 >$ the average instrumental statistical noise of the lightcurve. The lightcurve was divided into 6 energy bins 600 eV wide from 0.3 - 3.9 keV in the observed frame. The six lightcurves are shown in Figure 5.6 with their 1σ error, calculated from standard poisson statistics. The Fractional Excess Variability Amplitude was calculated for these six bins, and the result is shown in Figure 5.7 as a function of the rest frame energy. The 1σ error is given by

$$\sigma_{F_{var}} = \frac{1}{2F_{var}} \sqrt{\frac{1}{N}} \frac{S^2}{< X >^2} \, , \tag{5.2}$$

and assumes that the variance due to systematic errors is small compared to the total variance. It can be seen that the curve supports the tendency of Figure 5.5, showing the variability to be the greatest around the iron line emitting region. However, there is a word of caution since the above assumes that the processes underlying the variability are governed by gaussian statistics, which is not strictly the case for AGN found to be "weakly non-stationary" [46]. The error cannot account for fluctuations in F_{var} which are a function of time [69]. A more robust method would be to calculate the Power Spectral Distribution used for variability studies of pulsars, but our lightcurves are less than 20 ks long, and any analysis would consequently be severely biased by the window function of the lightcurve[47]. I have therefore not attempted to calculate the PSD of the lightcurves.

5.7.4 Iron Line

To model the iron line I have used two different models: a gaussian and the gaussian relativistic line models **kyrline** or **kyr1line** [70]. The **xspec**

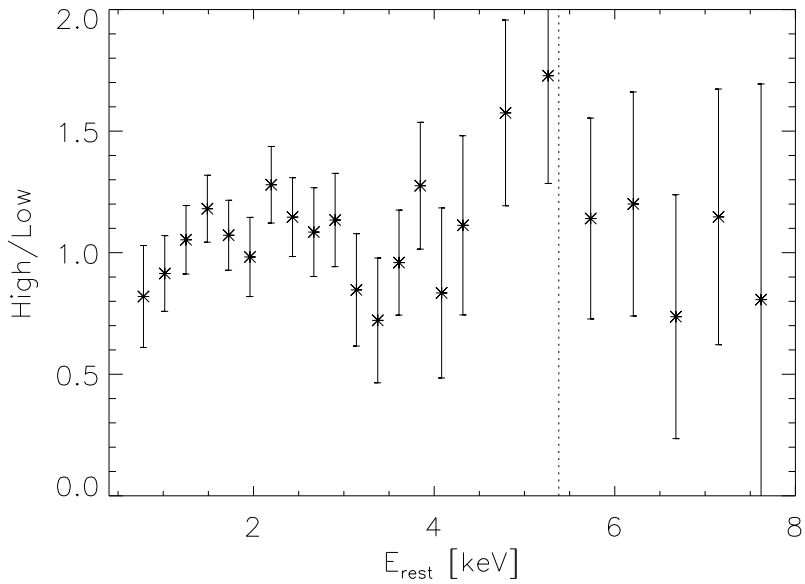

Figure 5.5: Flux fraction of the 'high' and 'low' states, where the 'high' state has a count rate greater than 0.134 c/s. The vertical dotted line is the location of the center of the gaussian fit of 6249 A 'high' at 5.3 keV (see Table 5.4). Error bars are given in 1σ.

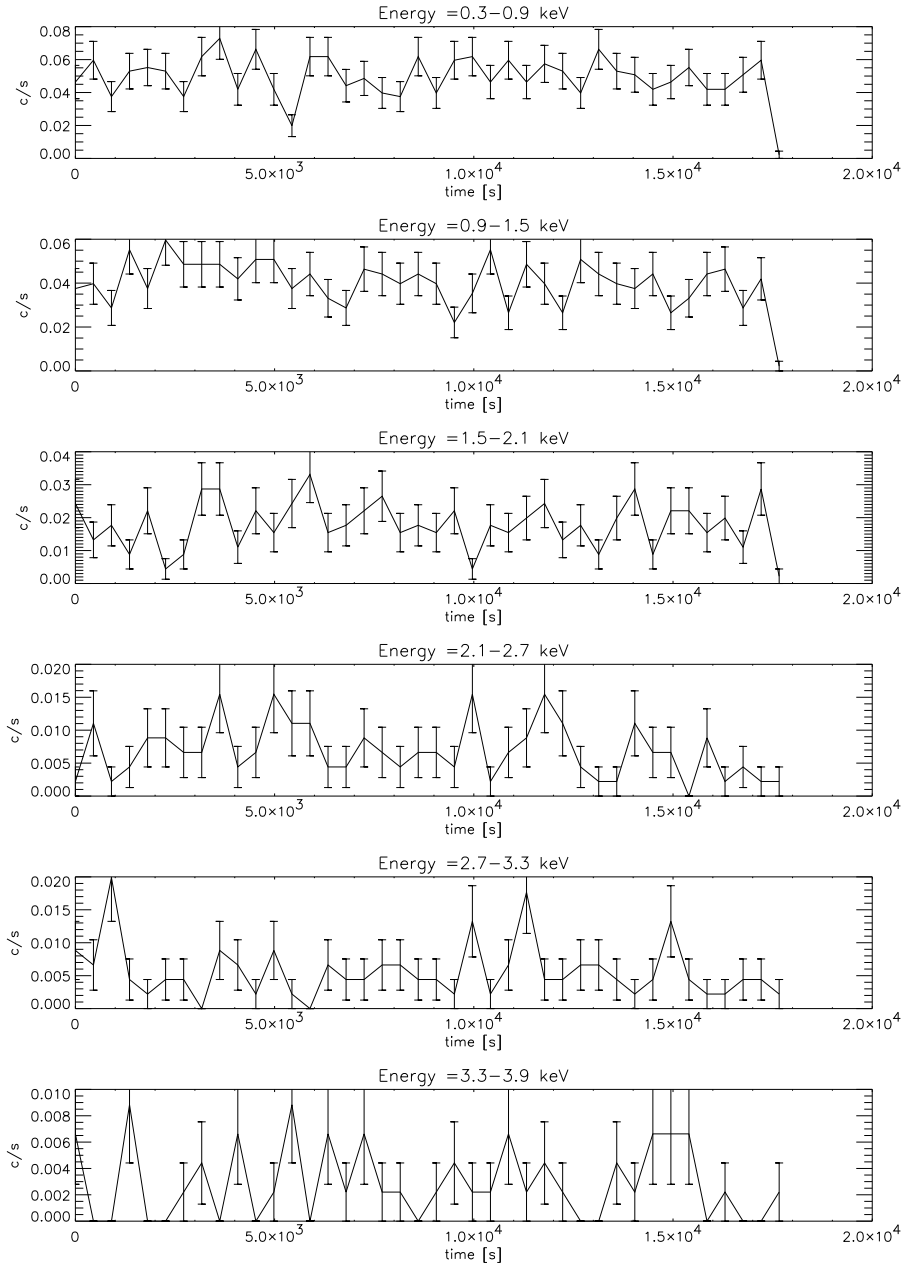

Figure 5.6: Energy dependent light curves. Energy bins are given in the observational frame. Error bars are given in 1σ.

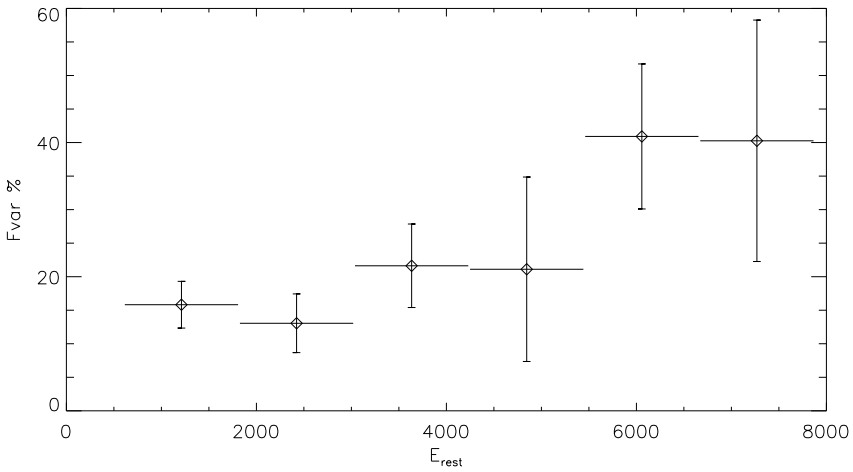

Figure 5.7: Fractional excess amplitude variability. Energy bins are given in rest frame. Error bars are 1 σ.

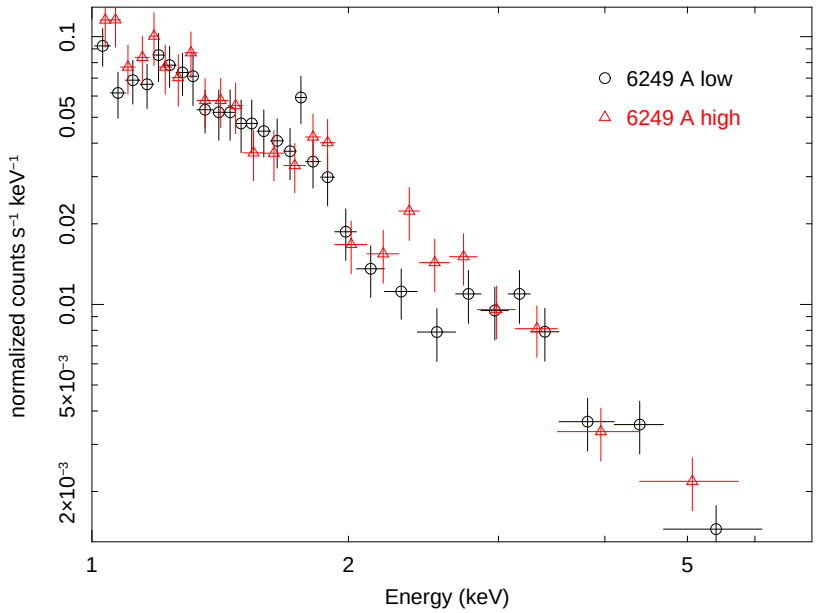

Figure 5.8: Black circle is the low state and red triangle the high state.

Energy range keV	Mean count rate $< X^2 >$[c/s]	Total variance S^2 $[10^{-5}]$	systematic error $< \sigma_{err}^2 >$ $[10^{-5}]$	Fractional Variability F_{var} [%]
0.3 - 0.9	0.049	17.01	10.91	$15.82^{\pm 3.48}$
0.9 - 1.5	0.040	11.54	8.82	$13.05^{\pm 4.38}$
1.5 - 2.1	0.018	5.44	3.95	$21.63^{\pm 6.22}$
2.1 - 2.7	0.007	1.72	1.51	$21.11^{\pm 13.75}$
2.7 - 3.3	0.006	1.77	1.24	$40.91^{\pm 10.81}$
3.3 - 3.9	0.003	0.78	0.65	$40.26^{\pm 18.00}$

Table 5.3: Fractional Variability for binned energy ranges in the observational band. Errors are given as 1σ.

kyrline models use the thin disk approximation, where the accretion disk is assumed to be an optically thick, geometrically thin disk in thermal equilibrium, as calculated by Laor [71][72], and includes all known general relativistic effects. The disc's dimensions are given by R_{in}, the inner orbit, and R_{out}, the outer orbit, where these are in units relative to the Last Stable Orbit, R_{LSO}, determined by the dimensionless spin parameter, a, of the central Black Hole. The **kyrline** model is axisymmetric while **kyr1line** is the non-axisymmetric version, allowing one to integrate the emission over a fraction of the azimuthal angle of the disc. The emissivity of the disc is given by the radial power law $\propto R^{-\alpha}$ for the axisymmetric **kyrline** model, but as a broken power law for **kyr1line**, α and β, which are switched at a border radius, R_b.

In lack of any indication of ionization I have assumed that for the **kyrline** models the emitted line is the neutral Fe Kα, $E_{K\alpha} = 6.40$ keV. Also because of a high degree of degeneracy, I have frozen the radial power law $\alpha = 3$, and for the **kyr1line** model placed $R_b = 0 = R_{LSO}$, such that for this model I also only have one radial power law index, α, describing the outer parts. Since the lines are unresolved the Black Hole spin, a, is throughout all the fits a poorly constrained value and was fixed at $a = 0.9982$, although for every fit I did test for $a = 0$ to investigate if there was better fit, which there never was. The Last Stable Orbit for the Kerr geometry is in this case $R = 1.23 r_g$.

The gaussian was used used to find the location of a peak and determining if it was relativistically broadened. The probable physical situation was then fitted using the **kyrline** models. Table 5.4 lists the best fit parameters of the models used.

Image 6249 A

Observation 6249 A is the component that is the most clearly periodically variable. Its period is T=2.89±0.005 hours suggesting that a hot spot might be co-rotating with the accretion disc. We first fitted the iron line region with a gaussian (model *a*), and obtained a broad line $\sigma = 0.49 \pm 0.43$ keV centered on $E_{rest} = 5.91 \pm 0.52$ keV, which is redshifted assuming it is the Fe $K\alpha$ line. We proceeded to fit with the relativistic **kyrline**, and discovered that one of these alone (model *b*) was not enough to cover the width of the line. We then added a second **kyrline** component under the assumption that part of the line's broadness could be attributed to a co-rotating hot spot, or a narrow annular emission. Model component *c1* is the iron line produced by the accretion disk stretching from the last stable orbit out to 400 r_g, and model component *c2* is the emission from an annular region of $R_{in} = 2.11 \pm 6r_g$ to $R_{out} = 2.22 \pm 6r_g$. The disk inclination settled around $45° \pm 6$, but the combination of R_{in}, R_{out} and disc inclination is degenerate for unresolved lines and offers a series of similar solutions with an upper bound of 50°. However, since we have failed to find any significant absorbtion of the object and AGN viewed edge on are predicted to have their source blocked by the putative dust torus, we can rule out inclination angles of less than 30°. Figure 5.10 a) shows the spectrum fitted with the best fit model *c*.

Following this complexity in the spectrum, we thought to investigate the 'high' and 'low' spectral part separately. Figure 5.8 shows the two spectra over the energy 1-7 keV, and demonstrates the 'excess' of the 'high' state (triangles) over the 'low' state (circles) in the observed energy range 2-3 keV.

The 6240 A 'low' spectra can be fitted with a broad gaussian centered on $E_{rest} = 6.44 \pm 0.42$ with $\sigma = 0.32 \pm 0.38$ (model *a*). This feature has a hint of an dip at the core, and when fitting with a **kyrline** one obtains a best fit presented by model *b*, which corresponds to an emitting annulus at 35-36r_g at disc inclination $39° \pm 16$. The line profile produced by this model is double peaked and is a good fit at any radius, as long as the emitting region is narrow $\sim 1r_g$, and the disc inclination is adjusted accordingly, since the distance between the peaks is controlled by the inclination and emitting radius [38] [70]. A similar quality fit (model *c*) can also be obtained by including the entire disc from a few tens of r_g out to $999r_g$. Figure 5.10 b) shows the 'low' spectrum fitted with the best fit model *b*.

The 'high' spectra is more curious. It requires a component around the center of the iron line at E_{rest} ∼6.4 keV, but also has additional emission

around $E_{rest} \sim 5.3$ keV. We fitted first a gaussian (model *a*) and found a broad line at $E_{rest} = 5.24 \pm 0.57$ with $\sigma = 0.51 \pm 0.42$. We then fitted model *b*, which consists of a **kyrline** model, *b1*, and the non-axisymmetric **kyr1line** model, *b2*. The integration of the non-axisymmetric **kyr1line** model was performed over $\Delta\phi = 180°$ staring at $\phi = -90°$, which is the point in orbit farthest from the observer. Figure 5.10 c) shows the 'high' spectrum fitted with the best fit model *b*.

The object has a 'high' and 'low' state, with the low state appearing to be the more common. In the low state there is a line consistent with neutral Fe Kα with broadened wings, whereas in the high state the neutral line is still present, but a redshifted components also appears consistent with emission from an annulus at $\sim 2.5R_g$.

Image 5909 A, 6249 B and 5909 B

Image 5909 A can be fitted by a single gaussian centered on $E_{rest} = 6.36 \pm 0.42$ and width $\sigma = 0.32 \pm 0.52$ keV. This is a broad line and only marginally shifted from its rest energy. If a binning with lesser than 20 counts is used, two peaks begin to appear around the center line much like in the 'low' state of 6249 A. Figure 5.10 d) shows the 'high' spectrum fitted with the best fit gaussian.

Observation 6249 image B has a well defined narrow line centered at $E_{rest} = 6.33 \pm 0.33$ keV. This line is only marginally redshifted, quite narrow and might therefore originate far from the black hole.

Observation 5909 has very poor statistics and the best fit yields a gaussian of center energy $E_{rest} = 6.48 \pm 0.7$ keV and width $\sigma = 0.65 \pm 0.5$ keV. Based on the location and width of the gaussian this spectrum also appears to be similar to 6249 A 'low' and 5909 A.

5.7.5 Combined Spectra

For the purpose of enhancing the line features, I have combined the spectrum of component A into one spectra and the same for component B. The line feature of component A was fitted with a gaussian of width $\sigma = 0.44 \pm 0.2$ keV and centroid $E_{rest} = 6.04 \pm 0.3$ keV, summarized in Table 5.4. The line feature of component A was fitted with a gaussian of width $\sigma = 0.32 \pm 0.43$ keV and centroid $E_{rest} = 6.32 \pm 0.38$ keV. Figure 5.11 shows these best fits. These was little indication of a 'high' state for component B, and I find the that the gaussian is close to the neutral Fe Kα line. Component A, on the other hand, includes the high state and as a result the gaussian fit is

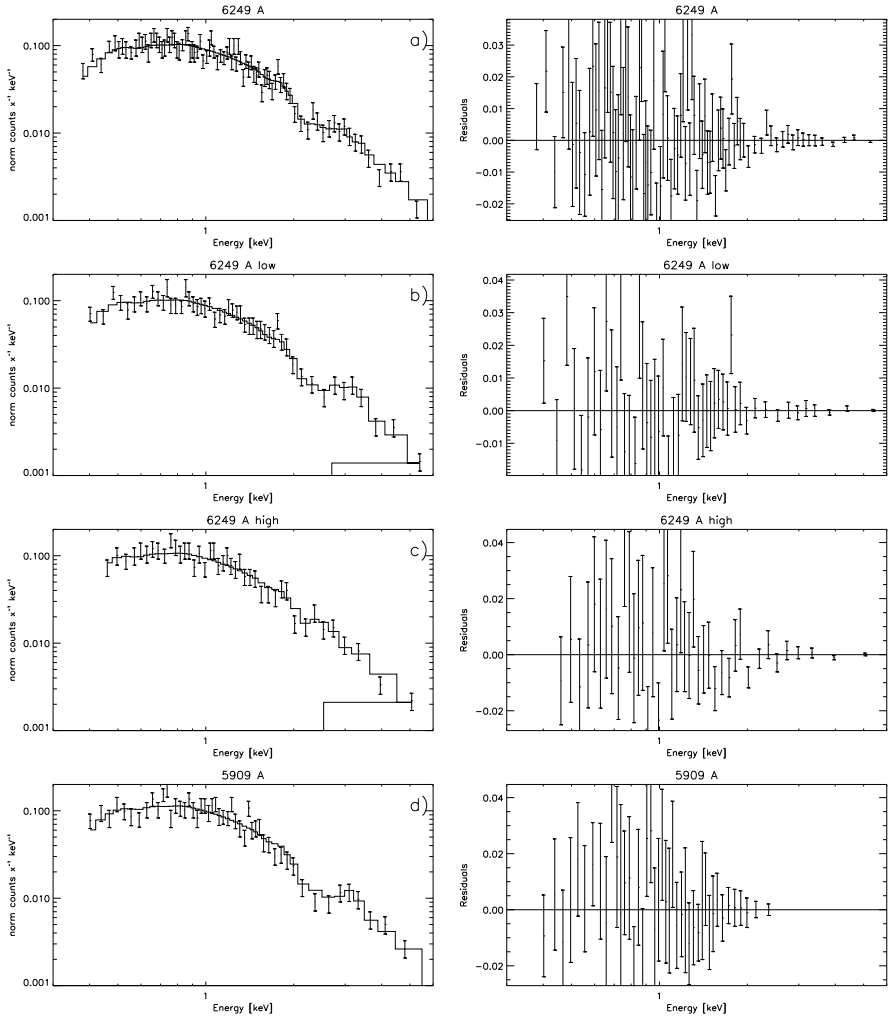

Figure 5.9: Best fit and residuals for component A given in Table 5.4. a) Model c1 and c2. b) Model b1 and b2. c) Model b1 and b2. d) Model a.

Object	Model	Zgauss			Kyrline/Kyr1line			χ^2/dof
		E_{rest} [keV]	σ [keV]	EW [keV]	Incl [deg]	R_{in} [r_g]	R_{out} [r_g]	
6249 A	a	$5.91^{+0.49}_{-0.55}$	$0.49^{+0.55}_{-0.30}$	$0.29^{+0.17}$				79/84
	b				39^{+12}_{-39}	0^f	400^f	75/79
	c1			$0.25^{+0.58}$	45^{+9}_{-5}	0^f	400^f	
	c2			$0.17^{+0.27}$	45^{+9}_{-5}	2.11^{+6}	2.22^{+6}	79/84
6249 A low	a	$6.44^{+0.35}_{-0.49}$	$0.32^{+0.43}_{-0.32}$	$0.30^{+0.48}$				30/46
	b1			$0.49^{+0.57}$	39^{+17}_{-15}	35^{+35}	36^{+36}	28/49
	b2			$0.46^{+0.46}$	39^{+17}_{-15}	25.77^{+85}_{-25}	999^a	28/49
6249 A high	a	$5.24^{+0.62}_{-0.52}$	$0.51^{+0.51}_{-0.32}$	$0.40^{+0.54}$				30/40
	b1			$0.16^{+0.66}$	37^{+6}_{-6}	7.02^{+20}	999^a	
	b2[b]			$0.39^{+0.42}$	37^{+6}_{-6}	1.35^{+1}_{-1}	2.36^{+1}_{-1}	27/39
5909 A	a	$6.36^{+0.45}_{-0.39}$	$0.32^{+0.71}_{-0.32}$	$0.30^{+0.6}$				48/49
6249 B	a	$6.33^{+0.43}_{-0.24}$	$\sim 0^{+0.46}$	$0.24^{+0.58}$				20/28
5909 B	a	$6.48^{+0.5}_{-1}$	$0.65^{+0.5}_{-0.5}$	...				12/16
A combined	a	$6.04^{+0.39}_{-0.28}$	$0.50^{+0.24}_{-0.12}$	$0.28^{+0.32}$				120/118
B combined	a	$6.32^{+0.38}_{-0.38}$	$0.32^{+0.43}_{-0.43}$	$0.137^{+0.32}$				120/118

Table 5.4: Iron line fits. The 'Model' column refers to the number of models that were fitted, eg. 'a' is a single model, while 'c1' and 'c2' are two components of the same model. [a] The kyrline model has a hard limit at 999. [b] Because the high spectra is interpreted as originating from a blob of matter in movement, we have fitted a non-axisymmetric **kyr1line** model, and apart from the listed parameters default values of the model were maintained. The integration ran over $\Delta\phi = 180$ and $\phi = -90$. [f] Parameter has been frozen.

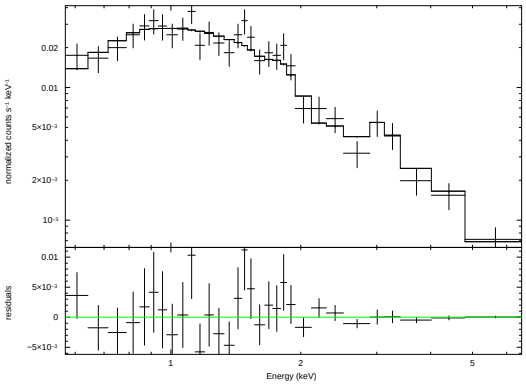

Figure 5.10: Best fit model a and residuals for component 6249 B given in Table 5.4.

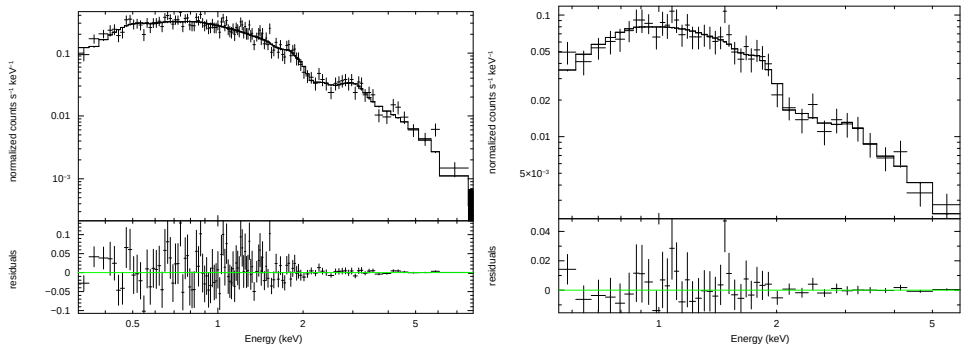

Figure 5.11: Left: Best fit model a and residuals for the combined spectrum of component A observations 5909 and 6249, given in Table 5.4. Right: Best fit for the combined spectrum of component B observation 5909 and 6249, given in Table 5.4.

redshifted from the neutral line and broad.

5.8 Discussion

Spectrum 5909 A, B and 6249 B all have similar fits with an average gaussian centroid of $E_{rest} = 6.39 \pm 0.8$ and width $\sigma = 0.28 \pm 0.83$. This is within the errors consistent with the neutral Fe Kα line. The line is appears broadened, but the resolution is insufficient to distinguish gravitational broadening from doppler broadening by fast moving material. The state also appears to be 'typical' of the object, contrary to the period 6249 A, which has an additional redshifted component. This component has a centroid of $E_{rest} = 5.91 \pm 0.52$ and width $\sigma = 0.49 \pm 0.23$, and can be represented by a gravitationally

redshifted line emitted at a radius of 2-3 r_g. Fits find a disc inclination of 35-45°, and although the parameter space allows for disc inclinations of less than 30°, these are unlikely since no significant absorbtion of the spectrum was discovered. Inclinations larger than 50° were not favored by any of the models.

Only period 6249 and component A was investigated for variability, since the other 3 periods had measurement errors that were larger than the variance. For 6249 excess fractional variability was discovered, with a statistically significant increase around the iron line. The fraction of 'high' to 'low' flux also shows a difference in flux level that is the strongest around the iron line region, but also for the continuum, leading to a slight hardening of the spectra in the 'high' flux state.

Combining the variability with the spectral study, a 'flare' scenario seems attractive. The spectrum responds as predicted by hardening the photon index during the 'flare'. Also the movement of the iron line is accompanied by a flux increase of the continuum.

If the period of the 6249 A observation is interpreted as a 'hot spot' on the accretion disk, then the orbital period is T_{orb}=2.89±0.005 hours. Upper limits on the mass of the central black hole can be estimated using the formula [73], which describes the trajectory of a circular orbit in the equatorial plane of the black hole

$$T_{orb} = 310(r^{3/2} + a)\frac{M_{BH}}{10^7 M_\odot} \, . \tag{5.3}$$

Assuming that the spot is orbiting on the last stable orbit, then for a maximally rotating Kerr black hole, $a = 0.998$, $r = 1.23\ r_g$, the mass is $M_{BH} = 1.44 * 10^8 M_\odot$, where a is the dimensionless angular spin of a Kerr black hole and $r_g = GM/c^2$ is the gravitational radius. For a Schwarzschild geometry, $a = 0$, $r = 6\ r_g$ the upper mass limit is $M_{BH} = 2.33 * 10^7 M_\odot$.

Finally a common interpretation of variability in gravitational lenses has been attributed to microlensing [74], [75] and [76]. The evidence for microlensing comes the observation that the increase in flux has been limited to the iron line alone, not the continuum, and that the additional flux has failed to be detected in the other images of the lenses [74], [75] and [76]. The time delay between images A and B have been estimated to be 60 days, while the gap between our observations is only 4 days. This means we can't test whether the variability in B shows up in image A. However, both line and continuum shows an increase in flux, which is inconsistent with the magnification of a microlensing caustic [76], which would only magnify part of the spectrum. Also the strong evidence of the fast periodicy in the

lightcurve of 6249 A seems inconsistent with the passing of a microlensing event, as well as the fact that the line is strongly redshifted by the event. I therefore conclude that the source of the variability in this QSO is more likely to be due to flaring than to microlensing.

Despite the relatively short observations, there is clear evidence that this object may be very interesting, and warrants further attention.

Appendix A

Parratt's Recursive Method

The exact expression of reflectivity from a homogenous slab can be extended to describe a multilayer stack. This was done by Parratt [77] and in this picture the multilayer is considered to be composed of N layers sitting on top of an infinitely thick substrate. The N'th layer is directly on the substrate and layer j in the stack of thickness Δ_j has refractive index, $n_j = 1-\delta_j+i\beta_j$. The wave vector $\mathbf{k}$ becomes $\mathrm{k}_j = n_j\mathbf{k}$ in the j'th layer and decomposes into $\mathrm{k}_{x,j}$ and $\mathrm{k}_{z,j}$. The x component is conserved through the stack so that $\mathrm{k}_{x,j}$=k_x and the z component can be calculated

$$\mathrm{k}_{z,j}^2 = (n_j\mathrm{k})^2 - \mathrm{k}_x^2 = (1-\delta_j+i\beta_j)^2\mathrm{k}^2 - \mathrm{k}_x^2 \cong \mathrm{k}_z^2 - 2\delta_j\mathrm{k}^2 + i2\beta_j\mathrm{k}^2 \ . \quad \text{(A.1)}$$

In terms of the momentum transfer vector, q_j this becomes

$$\mathrm{q}_j = \sqrt{\mathrm{q}^2 - 8\mathrm{k}^2\delta_j + i8\mathrm{k}^2\beta_j} \ . \quad \text{(A.2)}$$

Now the reflection from an interface, without taking into account multiple reflections, can be inferred from the Fresnel equations which recast in q becomes

$$r'_{j,j+1} = \frac{\mathrm{q}_j - \mathrm{q}_{j+1}}{\mathrm{q}_j + \mathrm{q}_{j+1}} \ , \quad \text{(A.3)}$$

and gives the reflectivity from interface j, $j+1$.

Beginning at the bottom the N'th layer on top of the substrate is not subject to any multiple scattering from lower levels and therefore the reflectivity from this surface can be calculated using the Fresnel reflectivity from (A.3)

$$r'_{N,\,\infty} = \frac{\mathrm{q}_N - \mathrm{q}_\infty}{\mathrm{q}_N + \mathrm{q}_\infty} \ . \quad \text{(A.4)}$$

The layer N-1 just atop the N'th must include both multiple reflection and refraction and for this the Fresnel equations are not enough. Using the expression of reflectivity from a single slab [78] the combined reflectivity is

$$r_{N-1,N} = \frac{r'_{N-1,N} + r'_{N,\infty} \mathrm{e}^{iq_N \Delta_N}}{1 + r'_{N-1,N} r'_{N,\infty} \mathrm{e}^{iq_N \Delta_N}} \ , \tag{A.5}$$

where the Fresnel reflectivity is denoted with a prime and so for an arbitrary layer j this equation becomes

$$r_{j,j-1} = \frac{r'_{j-1,j} + r'_{j,\infty} \mathrm{e}^{iq_j \Delta_j}}{1 + r'_{j-1,j} r'_{j,\infty} \mathrm{e}^{iq_j \Delta_j}} \ . \tag{A.6}$$

This is a recursive formula which can be used up through the stack or in the case of transmissivity downwards. It is an extension of the exact expression for a homogeneous slab which accurately models specular reflectivity from an ideal surface, and it is well adapted for use in programs.

Appendix B

Graze angle and Radius Tables

Group	Design I & II		Design III		Design IV	
	Radius	Angle	Radius	Angle	Radius	Angle
1	6.000	0.300	6.000	0.300	10.000	0.500
2	6.463	0.323	6.567	0.328	10.669	0.533
3	6.961	0.348	7.187	0.359	11.382	0.569
4	7.497	0.375	7.866	0.393	12.144	0.607
5	8.076	0.404	8.610	0.430	12.956	0.648
6	8.698	0.435	9.423	0.471	13.822	0.691
7	9.369	0.468	10.313	0.516	14.746	0.737
8	10.091	0.505	11.288	0.564	15.733	0.787
9	10.869	0.543	12.354	0.618	16.785	0.839
10	11.707	0.585	13.521	0.676	17.907	0.895
11	12.610	0.630	14.799	0.740	19.105	0.955
12	13.582	0.679	16.197	0.810	20.383	1.019
13	14.629	0.731	17.727	0.886	21.746	1.087
14	15.757	0.788	19.402	0.970	23.200	1.160
15	16.971	0.849	21.235	1.062	24.752	1.283
16	18.280	0.914	23.241	1.162	26.407	1.320
17	19.689	0.984	25.437	1.272	28.173	1.409
18	21.207	1.060	27.840	1.392	30.057	1.503
19	22.842	1.142	30.470	1.524	32.067	1.603
20	24.603-26.500	1.230-1.325	33.349-36.500	1.667-1.825	34.212-36.500	1.711-1.825

Table B.1: The angle and radius for each group is for the inner most shell in each group.

Appendix C

Telemetry Documentation

C.1 Telemetry Packet Format

The HEFT control loop is managed by an AMP Tiny786 computer. It monitors data from a variety of sensors to determine attitude, and drives the control motors accordingly. The most critical data that can be used for reconstructing the gondola's attitude during flight will be transmitted to the ground serially in the control loop telemetry packets.

A single, fixed-size, control loop telemetry packet will be transmitted at the loop cycle rate (10 Hz nominal). Some of the contents of that packet will vary from packet to packet. The packet size, including framing bytes, is 60 bytes.

A packet consists of two constant framing bytes (DLE and ETX), a single byte ID code, and two blocks of data. The data blocks are labeled "FAST" and "SLOW" as an indication of the frequency at which their constituent signals are transmitted. The packet structure looks like:

[DLE][ID code][- - - Fast data - - -][- - - Slow data - - -][- - - Checksum - - -][ETX]

The framing bytes are: DLE = 0x10 ETX = 0x03 The ID code range is 0xd0 - 0xff (48 total) The checksum value is a total of all bytes (of 61 bytes total) within the packet except: DLE ETX Checksum Therefore: 0 < CHECKSUM < 255*60 = 15300

The fast data block always contains 39 bytes. The constituent signals are transmitted in every packet (at the loop period, a.k.a. sample rate, which is the highest frequency at which meaningful data can be transmitted), so the fast data block contents are therefore independent of the ID code.

The slow data block always contains 19 bytes. The constituent signals

of the slow block vary from packet to packet. The ID code indicates the contents of the slow data block. The slow data block contents are listed in Tables C.1-C.3.

Since there are 48 different slow packets, the longest period for which a particular signal can be transmitted is 48 loop period = 4.8 seconds, nominally. The shortest period is the loop period, 0.1 seconds, nominally.

C.2 Telemetry Parsing Format

The format:

ID,startbyte,endbyte,name,VB param, name,operation,signed/unsigned,0,operator,unit,multibleframes[,#bytes, number] [] only if multibleframes = yes

```
;Fast, 21, 1, 38
0, 1, 4,QNX Time,self,QNX Time,mult,U,0,1.39698e-8,mins,no
0, 5, 2,Az Err,self,Az Err,mult,S,0,2.777778e-4,deg,no
0, 7, 2,El Err,self,El Err,mult,S,0,2.777778e-4,deg,no
0, 9, 2,Roll,self,Roll,mult,S,0,2.777778e-4,deg,no
0, 11, 2,Plat El,self,Plat El,mult,S,0,2.777778e-4,deg,no
0, 13, 2,Pointing RA,self,Pointing RA,mult,U,0,3.662109375e-4,hours,no
0, 15, 2,Pointing DEC,self,Pointing DEC,mult90off,U,0,2.746582031E-03,deg,no
0, 17, 2,Pointing Az,self,Pointing Az,mult,U,0,5.4931640625E-03,deg,no
0, 19, 2,Pointing El,self,Pointing El,mult,U,0,2.746582031E-03,deg,no
0, 21, 2,Gyro az rate,self,Gyro az rate,mult,S,0,3.0517578E-04,deg/s,no
0, 23, 2,Gyro el rate,self,Gyro el rate,mult,S,0,3.0517578E-04,deg/s,no
0, 25, 2,Gyro roll rate, self,Gyro roll rate,mult,S,0,3.0517578E-04,deg/s,no
0, 27, 2,QNX hour, self, QNX hour,mult,U,0,03.662109375e-4, hour, no
0, 29, 2,Tans Az,self,Tans Az,mult,U,0,5.4931640625E-03,deg,no
0, 31, 2,Mag 1 Az,self,Mag 1 Az,mult,U,0,5.4931640625E-03,deg,no
0, 33, 2,Mag 2 Az,self,Mag 2 Az,mult,U,0,5.4931640625E-03,deg,no
0, 35, 2,Acc El,self,Acc El,mult,U,0,2.746582031E-03,deg,no
0, 37, 3,Enc MSB,self,Enc El,encOp,L,0,0.005493205838223,deg,yes,3,0
0,39,1,Enc LSb,self,Enc EL lsb,encOp,L,0,0.005493205838223,deg,yes,3,2
0,39,1,Count LSB,self,Count LSB,bitBlankOp,U,0,63, ,no
0,39,1,Slewing,self,Slewing,fastStatOp,B,6,0, ,no
;Slow 1, 50, 40, 41
1,40,2,Keg Temp,self,Keg Temp,mult,S,0,3.0517578E-03,C,no
2,40,2,Outside Keg,self,Outside Keg,mult,S,0,3.0517578E-03,C,no
3,40,2,Enc2 Temp,self,Enc2 Temp,mult,S,0,3.0517578E-03,C,no
4,40,2,Enc1 Temp,self,Enc1 Temp,mult,S,0,3.0517578E-03,C,no
5,40,2,R3 Temp,self,R3 Temp,mult,S,0,3.0517578E-03,C,no
6,40,2,Optic 1,self,Optic 1,mult,S,0,3.0517578E-03,C,no
7,40,2,Optic 2,self,Optic 2,mult,S,0,3.0517578E-03,C,no
8,40,2,Optic 3,self,Optic 3,mult,S,0,3.0517578E-03,C,no
9,40,2,Gyro1/Acc1,self,Gyro1/Acc1,mult,S,0,3.0517578E-03,C,no
10,40,2,Gyro2,self,Gyro2,mult,S,0,3.0517578E-03,C,no
11,40,2,Magnetometer1,self,Magnetometer1,mult,S,0,3.0517578E-03,C,no
12,40,2,Magnetometer2,self,Magnetometer2,mult,S,0,3.0517578E-03,C,no
13,40,2,Star1 Temp,self,Star1 Temp,mult,S,0,3.0517578E-03,C,no
14,40,2,Star2 Temp,self,Star2 Temp,mult,S,0,3.0517578E-03,C,no
15,40,2,H-bar,self,H-bar,mult,S,0,3.0517578E-03,C,no
```

LABEL	BYTE	0xd0	0xd1	0xd2	0xd3	0xd4
SLOW 1	40-41	Keg Temp	Outside Keg	Enc2 Temp	Enc1 Temp	R3 Temp
GPS	42-43	GPS AZ	GPS Pitch	GPS Roll	packet stat	LatMSBs
MAGS 1	44-45	Mag bias rate cap	Mag bias clamp	Mag bias weight	Tans point wt	Tans tracker cnt
SERVO	46-47	AZ trq set	AZ I	AZ tach	El trq set	Gain ref rpm
INCLIN/ENC	48-49	Tracker 1 az	Tans offset Az	ENC1	Tracker 1 el	Gammaoffset hor
STATUS	50	S1	S2	S3	S4	S5
BYTES 1	51	Last Cmd	ENC1 OE	ENC2 OE	Latch Cmd	Lat LSB
TRACK 1	52-53	RA 1 MSBs	DEC 1 MSBs	Roll 1 MSBs	RA 2 MSBs	DEC 2 MSBs
TRACK 2	54	MSB t1	t1	LSB t1	MSB t2	t2
GAINS	55	EL P MSB	EL P LSB	EL I MSB	EL I LSB	EL D MSB
TRACK3	56	CCD1 gain MSB	CCD1 gain	CCD1 gain	CCD1 gain LSB	CCD1 int t MSB
TRACK4	57	RA 1 LSB	DEC 1 LSB	Roll 1 LSB	RA 2 LSB	DEC 2 LSB
NEW 1	58	Servo60 V MSB	Servo60 I MSB	FCC30 V MSB	FCC30 I MSB	Criss30 V MSB
NEW 2	59	Servo60 V LSB	Servo60 I LSB	FCC30 V LSB	FCC30 I LSB	Criss30 V LSB

LABEL	BYTE	0xd5	0xd6	0xd7	0xd8	0xd9
SLOW 1	40-41	Optic 1	Optic 2	Optic 3	Gyro1/Acc1	Gyro2
GPS	42-43	LongMSBs	error code	packet stat	GPS AZ	GPS Pitch
MAGS 1	44-45	Mag tans count	mag1 X	mag1 Y	mag1 Z	mag2 X
SERVO	46-47	R3 trq set	R3 I	Criss trq set	Criss I	Criss tach
INCLIN/ENC	48-49	ENC2	Tracker 2 az	Bore-sight X	ENC1	Tracker 2 el
STATUS	50	S6	S7	S8	S9	S10
BYTES 1	51	Long LSB	Servo reset	File time	Update time	Uplink time
TRACK 1	52-53	Roll 2 MSBs	Nstar1	Nstar2	RA 1 MSBs	DEC 1 MSBs
TRACK 2	54	LSB t2	Ncmd1	Ncmd2	MSB t1	t1
GAINS	55	EL D LSB	AZ P MSB	AZ P LSB	AZ I MSB	AZ I LSB
TRACK3	56	CCD1 int t	CCD1 int t	CCD1 int t LSB	Ap size1 MSB	Ap size 1
TRACK4	57	Roll 2 LSB	X box 1 MSB	X box 1 LSB	RA 1 LSB	DEC 1 LSB
NEW 1	58	Criss30 I MSB	Digital30 V MSB	Digital30 I MSB	Gyr AZ bias msb (3)	Gyr AZ bias (1)
NEW 2	59	Criss30 I LSB	Digital30 V LSB	Digital30 I LSB	Gyr AZ bias (2)	Gyr AZ bias (0)

LABEL	BYTE	0xda	0xdb	0xdc	0xdd	0xde	0xdf
SLOW 1	40-41	Magnetometer1	Magnetometer 2	Star1 Temp	Star2 Temp	H-bar	Up Top
GPS	42-43	GPS Roll	packet stat	Alt MSBs	GPS week	Sec MSBs	packet stat
MAGS 1	44-45	mag2 Y	mag2 Z	mag1 X	mag1 Y	mag1 Z	mag2 X
SERVO	46-47	AZ trq set	R3 Dump V	AZ tach	El trq set	El I	R3 trq set
INCLIN/ENC	48-49	Bore-sight Y	ENC2	Tracker 1 az	Bore-sight Z	ENC1	Tracker 1 el
STATUS	50	S11	S12	S13	S14	S15	S16
BYTES 1	51	Dnlink time	TANS time	Alt LSB	File t max	GPS sec	Time used
TRACK 1	52-53	Roll 1 MSBs	RA 2 MSBs	DEC 2 MSBs	Roll 2 MSBs	Nstar1	Nstar2
TRACK 2	54	LSB t1	MSB t2	t2	LSB t2	GPS sec lsB	Mag lim 1
GAINS	55	AZ D MSB	AZ D LSB	AZ V MSB	AZ V LSB	Roll P MSB	Roll P LSB
TRACK3	56	Ap size 1	Ap size 1 LSB	Img thresh 1 MSB	Img thresh 1	Img thresh 1	Img thresh 1 LSB
TRACK4	57	Roll 1 LSB	RA 2 LSB	DEC 2 LSB	Roll 2 LSB	Y box 1 MSB	Y box 1 LSB
NEW 1	58	Gyr EL bias (3)	Gyr EL bias (1)	Gyr roll bias (3)	Gyr roll bias (1)	Gyr hyb bias (3)	Gyr hyb bias (1)
NEW 2	59	Gyr EL bias (2)	Gyr EL bias (0)	Gyr roll bias (2)	Gyr roll bias (0)	Gyr hyb bias (2)	Gyr hyb bias (0)

Table C.1: Slow data block contents. See Table 3 for the signal key and format.

LABEL	BYTE	0xe0	0xe1	0xe2	0xe3	0xe4
SLOW 1	40-41	Cross	Battery 2	Battery 1	Optics frame 1	Optics frame 2
GPS	42-43	GPS AZ	GPS Pitch	GPS Roll	packet stat	LatMSBs
MAGS 1	44-45	mag2 Y	mag2 Z	mag1 X	mag1 Y	mag1 Z
SERVO	46-47	R3 I	Criss trq set	Criss I	Criss tach	AZ trq set
INCLIN/ENC	48-49	Gammaoffset Az	ENC2	Tracker 2 az	Gammaoffset El	ENC1
STATUS	50	S1	S2	S3	S4	S5
BYTES 1	51	Uplink t max	Dnlink t max	Update t max	TANS t max	Lat LSB
TRACK 1	52-53	RA 1 MSBs	DEC 1 MSBs	Roll 1 MSBs	RA 2 MSBs	DEC 2 MSBs
TRACK 2	54	MSB t1	T1	LSB t1	MSB t2	t2
GAINS	55	Roll D MSB	Roll D LSB	+AZ slew V MSB	+AZ slew V LSB	-AZ slew V MSB
TRACK3	56	CCD2	gain MSB	CCD2 gain	CCD2 gain LSB	CCD2 int t MSB
TRACK4	57	DEC 1 LSB	Roll 1 LSB	RA 2 LSB	DEC 2 LSB	Roll 2 LSB
NEW 1	58	Time on Target msb	Time to next target msb	Target Ra msb	Target Dec msb	Target Az msb
NEW 2	59	Time on Target lsb	Time to next target lsb	Target Ra lsb	Target Dec lsb	Target Az msb

LABEL	BYTE	0xe5	0xe6	0xe7	0xe8	0xe9
SLOW 1	40-41	Keg Pressure	El Pressure	Star 1 Press.	Star 2 Press.	+58V
GPS	42-43	LongMSBs	GPS Pitch	GPS Roll	GPS AZ	GPS Pitch
MAGS 1	44-45	mag2 X	mag2 Y	mag2 Z	mag1 X	mag1 Y
SERVO	46-47	AZ I	AZ tach	El trq set	El I	R3 trq set
INCLIN/ENC	48-49	Tracker 2 el	Bore-sight X	ENC2	Tracker 1 az	Bore-sight Y
STATUS	50	S6	S7	S8	S9	S10
BYTES 1	51	Long LSB	Loop prd. I	Loop prd. II	Samp / loop	Trk1 in t
TRACK 1	52-53	Roll 2 MSBs	Nstar1	Nstar2	RA 1 MSBs	DEC 1 MSBs
TRACK 2	54	LSB t2	Ncmd1	Ncmd2	MSB t1	t1
GAINS	55	-AZ slew V LSB	+EL slew V MSB	+EL slew V LSB	-EL slew V MSB	-EL slew V LSB
TRACK3	56	CCD2 int t	CCD2 int t	CCD2 int t LSB	Ap size2 MSB	Ap size 2
TRACK4	57	RA 1 LSB	X box 2 MSB	X box 2 LSB	RA 1 LSB	DEC 1 LSB
NEW 1	58	Target El msb	Gyr AZ bias msb (3)	Gyr AZ bias (1)	Tracker1 time of fix, msb	Tracker1 time of fix, msb
NEW 2	59	Target El msb	Gyr AZ bias (2)	Gyr AZ bias (0)	Tracker1 time of fix, lsb	Tracker1 time of fix, lsb

LABEL	BYTE	0xea	0xeb	0xec	0xed	0xee	0xef
SLOW 1	40-41	+28V	Gyro1 (acc)	Tans att fix	Tans lla fix	SMag 1 Az	sMag2 Az
GPS	42-43	GPS Roll	packet stat	Alt MSBs	GPS week	Sec MSBs	packet stat
MAGS 1	44-45	mag1 Z	mag2 X	mag2 Y	mag2 Z	mag1 X	mag1 Y
SERVO	46-47	R3 I	Criss trq set	Criss I	Criss tach	AZ trq set	AZ I
INCLIN/ENC	48-49	ENC1	Tracker 1 el	Bore-sight Z	ENC2	Tracker 2 az	Tans offset Az
STATUS	50	S11	S12	S13	S14	S15	S16
BYTES 1	51	Trk1 out t	Trk2 in t	Alt LSB	Trk2 out t	GPS sec	Time used
TRACK 1	52-53	Roll 1 MSBs	RA 2 MSBs	DEC 2 MSBs	Roll 2 MSBs	Nstar1	Nstar2
TRACK 2	54	LSB t1	MSB t2	T2	LSB t2	GPS sec lsB	Mag lim 2
GAINS	55	EL trq lim MSB	EL trq lim LSB	AZ trq lim MSB	AZ trq lim LSB	EL I lim MSB	EL I lim LSB
TRACK3	56	Ap size 2	Ap size 2 LSB	Img thresh 2 MSB	Img thresh 2	Img thresh 2	Img thresh 2 LSB
TRACK4	57	Roll 1 LSB	RA 2 LSB	DEC 2 LSB	Roll 2 LSB	Y box 2 MSB	Y box 2 LSB
NEW 1	58	Gyr EL bias (3)	Gyr EL bias (1)	Gyr roll bias (3)	Gyr roll bias (1)	Gyr hyb bias (3)	Gyr hyb bias (1)
NEW 2	59	Gyr EL bias (2)	Gyr EL bias (0)	Gyr roll bias (2)	Gyr roll bias (0)	Gyr hyb bias (2)	Gyr hyb bias (0)

Table C.2: Slow data block contents. See Table 3 for the signal key and format.

LABEL	BYTE	0xf0	0xf1	0xf2	0xf3	0xf4
SLOW 1	40-41	Bytes svd I	Bytes svd II	Bytes svd III	Bytes svd IV	Cycle cnt I
GPS	42-43	GPS AZ	GPS Pitch	GPS Roll	packet stat	LatMSBs
MAGS 1	44-45	mag1 Z	mag1 offset	mag2 offset	Next Az	Next El
SERVO	46-47	AZ tach	El trq set	El I	R3 trq set	R3 I
INCLIN/ENC	48-49	ENC1	Tracker 2 el	Gammaoffset hor	ENC2	Tracker 1 az
STATUS	50	S1	S2	S3	S4	S5
BYTES 1	51	Trk1 in tmax	Trk1 out tmax	Trk2 in tmax	Trk2 out tmax	Lat LSB
TRACK 1	52-53	RA 1 MSBs	DEC 1 MSBs	Roll 1 MSBs	RA 2 MSBs	DEC 2 MSBs
TRACK2	54	MSB t1	T1	LSB t1	MSB t2	t2
GAINS	55	I AZ lim MSB	I AZ lim LSB	AZ slew lm MSB	AZ slew lm LSB	EL slew lm MSB
TRACK3	56	Port1 MSB	Port1 LSB	Port2 MSB	Port2 LSB	Nsent1 MSB
TRACK4	57	RA 1 LSB	DEC 1 LSB	Roll 1 LSB	RA 2 LSB	DEC 2 LSB
NEW 1	58	Time on Target msb	Time to next target msb	Enc bias rate cap msb	Enc bias weight msb	Enc bias clampmsb
NEW 2	59	Time on Target lsb	Time to next target lsb	Enc bias rate cap lsb	Enc bias weight lsb	Enc bias clamp lsb

LABEL	BYTE	0xf5	0xf6	0xf7	0xf8	0xf9
SLOW 1	40-41	Cycle cnt II	Cycle cnt III	Cycle cnt IV	Desired RA msB	Desired d msB
GPS	42-43	LongMSBs	error code	Packet stat	GPS AZ	GPS Pitch
MAGS 1	44-45	Next Ra	Next Dec	El s. angle zone	El s.angle Diff	El rate limit
SERVO	46-47	Criss trq set	Criss I	Criss tach	AZ trq set	AZ I
INCLIN/ENC	48-49	Star offset Az	ENC1	Tracker 1 el	Star offset El	ENC2
STATUS	50	S6	S7	S8	S9	S10
BYTES 1	51	Long LSB	NTargets MSB	N targets LSB	Desired RA lsB	Desired d lsB
TRACK 1	52-53	Roll 2 MSBs	Nstar1	Nstar2	RA 1 MSBs	DEC 1 MSBs
TRACK2	54	LSB t2	Ncmd1	Ncmd2	MSB t1	t1
GAINS	55	EL slew lm LSB	R3 slew V, msb	R3 slew V, lsb	R3 Trq lim, msb	R3 Trq limit, lsb
TRACK3	56	Nsent 1 LSB	Nsent2 MSB	Nsent2 LSB	Nrec1 MSB	Nrec1 LSB
TRACK4	57	Roll 2 LSB	Tracker 1 point weight.msb	Tracker 1 point weight,lsb	RA 1 LSB	DEC 1 LSB
NEW 1	58	Enc point weight msb	Enc 1 offsetmsb	Enc 2 offsetmsb	Gyr AZ bias msb (3)	Gyr AZ bias (1)
NEW 2	59	Enc point weight lsb	Enc 1 offset lsb	Enc 2 offset lsb	Gyr AZ bias (2)	Gyr AZ bias (0)

LABEL	BYTE	0xfa	0xfb	0xfc	0xfd	0xfe	0xff
SLOW 1	40-41	Desired Az	Desired El	Sensor Az	Sensor El	QNX hr/day	QNX mo/yr
GPS	42-43	GPS Roll	Packet stat	Alt MSBs	GPS week	GPS sec MSBs	packet stat
MAGS 1	44-45	mag1 X	mag1 Y	mag1 Z	mag2 X	mag2 Y	mag2 Z
SERVO	46-47	AZ tach	El trq set	El I	Criss trq set	Criss I	Criss tach
INCLIN/ENC	48-49	Tracker 2 az	Gammaoffset Az	ENC1	Tracker 2 el	Gamma offset El	ENC2
STATUS	50	S11	S12	S13	S14	S15	S16
BYTES 1	51	Current targetnum MSB	Current targetnum LSB	Alt LSB	Max Senor point corr	GPS sec	Time used
TRACK 1	52-53	Roll 1 MSBs	RA 2 MSBs	DEC 2 MSBs	Roll 2 MSBs	Nstar1	Nstar2
TRACK2	54	LSB t1	MSB t2	t2	LSB t2	GPS sec LSB	—
GAINS	55	Sci nRX MSB	Sci nRX	Sci nRX	Sci nRX LSB	Sci nRX new MSB	Sci nrx new LSB
TRACK3	56	Nrec2 MSB	Nrec2 LSB	Srv port MSB	Srv port LSB	—	—
TRACK4	57	Roll 1 LSB	RA 2 LSB	DEC 2 LSB	Roll 2 LSB	Tracker 2 point weight.msb	Tracker 2 point weight,lsb
NEW 1	58	Gyr EL bias (3)	Gyr EL bias (1)	Gyr roll bias (3)	Gyr roll bias (1)	Gyr hyb bias (3)	Gyr hyb bias (1)
NEW 2	59	Gyr EL bias (2)	Gyr EL bias (0)	Gyr roll bias (2)	Gyr roll bias (0)	Gyr hyb bias (2)	Gyr hyb bias (0)

Table C.3: Slow data block contents. See Table 3 for the signal key and format.

```
16,40,2,Up Top,self,Up Top,mult,S,0,3.0517578E-03,C,no
17,40,2,Cross,self,Cross,mult,S,0,3.0517578E-03,C,no
18,40,2,Battery 2,self,Battery 2,mult,S,0,3.0517578E-03,C,no
19,40,2,Battery 1,self,Battery 1,mult,S,0,3.0517578E-03,C,no
20,40,2,Optics frame 1,self,Optics frame 1,mult,S,0,3.0517578E-03,C,no
21,40,2,Optics frame 2,self,Optics frame 2,mult,S,0,3.0517578E-03,C,no
22,40,2,Keg Pressure,self,Keg Pressure,mult,S,0,3.0517578E-01,Torr,no
23,40,2,El Pressure,self,El Pressure,mult,S,0,3.0517578E-01,Torr,no
24,40,2,Star 1 Press.,self,Star 1 Press.,mult,S,0,3.0517578E-01,Torr,no
25,40,2,Star 2 Press.,self,Star 2 Press.,mult,S,0,3.0517578E-01,Torr,no
26,40,2,+58V,self,+58V,mult,S,0,3.0517578E-03,V,no
27,40,2,+28V,self,+28V,mult,S,0,3.0517578E-03,V,no
28,40,2,Gyro1 (Acc),self,Gyro1 (acc),mult,S,0,3.0517578E-03,C,no
29,40,2,Tans att fix,self,Tans att fix,mult,S,0,3.0517578E-04,C,no
30,40,2,Tans lla fix,self,Tans lla fix,mult,S,0,3.0517578E-04,V,no
31,40,2,Mag 1 Az,self,sMag 1 Az,mult,U,0,5.493164062E-3,deg,no
32,40,2,Mag 2 Az,self,sMag 2 Az,mult,U,0,5.493164062E-3,deg,no
33,40,2,Bytes svd I,self,Bytes svd I,noOp,U,0,0,Unset,yes,8,0
34,40,2,Bytes svd II,self,Bytes svd I,noOp,U,0,0,Unset,yes,8,2
35,40,2,Bytes svd III,self,Bytes svd I,noOp,U,0,0,Unset,yes,8,4
36,40,2,Bytes svd IV,self,Bytes svd I,noOp,U,0,0,Unset,yes,8,6
37,40,2,Cycle cnt I,self,Cycle cnt I,noOp,U,0,0,Unset,yes,8,0
38,40,2,Cycle cnt II,self,Cycle cnt I,noOp,U,0,0,Unset,yes,8,2
39,40,2,Cycle cnt III,self,Cycle cnt I,noOp,U,0,0,Unset,yes,8,4
40,40,2,Cycle cnt IV,self,Cycle cnt I,noOp,U,0,0,Unset,yes,8,6
41,40,2,Desired RA msB,self,Desired RA,mult,U,0,1.430511E-06,hours,yes,3,0
42,40,2,Desired Dec msB,self,Desired Dec,mult90off,U,0,2.746582031e-03,deg,no
43,40,2,Desired Az,self,Desired Az,mult,U,0,5.493164062E-3,deg,no
44,40,2,Desired El,self,Desired El,mult,U,0,2.746582031E-3,deg,no
45,40,2,Sensor Az,self,Sensor Az,mult,U,0,5.493164062E-03,deg,no
46,40,2,Sensor El,self,Sensor El,mult,U,0,2.746582031E-3,deg,no
47,40,1,QNX hr,self,QNX hr,noOp,U,0,0, ,no
47,41,1,QNX Day,self,QNX Day,noOp,U,0,0, ,no
48,40,1,QNX Mo,self,QNX Mo,noOp,U,0,0, ,no
48,41,1,QNX yr,self,QNX yr,noOp,U,0,0, ,no
;GPS, 48, 42, 43
1,42,2,AZ,self,GPS AZ,mult,U,0,5.4931641E-03,deg,no
2,42,2,Pitch,self,GPS Pitch,mult,S,0,5.4931641E-03,deg,no
3,42,2,Roll,self,GPS Roll,mult,S,0,5.4931641E-03,deg,no
4,42,2,Status code,self,Status code,noOp,U,0,0, ,no
5,42,2,Lat,self,Lat,mult,S,0,2.746582E-03,deg N ,no
6,42,2,Long,self,Long,mult,S,0,5.4931641E-03,deg W ,no
7,42,2,Error code,self,Error code,noOp,U,0,0, ,no
8,42,2,Status code,self,Status code,noOp,U,0,0, ,no
9,42,2,AZ,self,GPS AZ,mult,U,0,5.4931641E-03,deg,no
10,42,2,Pitch,self,GPS Pitch,mult,S,0,5.4931641E-03,deg,no
11,42,2,Roll,self,GPS Roll,mult,S,0,5.4931641E-03,deg,no
12,42,2,Status code,self,Status code,noOp,U,0,0, ,no
13,42,2,Alt MSB's,self,Alt,noOp,U,0,0,meter,yes,3,0
14,42,2,week,self,week,noOp,U,0,0, ,no
15,42,2,sec MSB's,self,GPS sec,noOp,U,0,0,sec,yes,4,0
16,42,2,Status code,self,Status code,noOp,U,0,0, ,no
17,42,2,AZ,self,GPS AZ,mult,U,0,5.4931641E-03,deg,no
18,42,2,Pitch,self,GPS Pitch,mult,S,0,5.4931641E-03,deg,no
19,42,2,Roll,self,GPS Roll,mult,S,0,5.4931641E-03,deg,no
20,42,2,Status code,self,Status code,noOp,U,0,0, ,no
```

```
21,42,2,Lat,self,Lat,mult,S,0,2.746582E-03,deg N,no
22,42,2,Long,self,Long,mult,S,0,5.4931641E-03,deg W,no
23,42,2,Error code,self,Error code,noOp,U,0,0, ,no
24,42,2,Status code,self,Status code,noOp,S,0,0, ,no
25,42,2,AZ,self,GPS AZ,mult,U,0,5.4931641E-03,deg,no
26,42,2,Pitch,self,GPS Pitch,mult,S,0,5.4931641E-03,deg,no
27,42,2,Roll,self,GPS Roll,mult,S,0,5.4931641E-03,deg,no
28,42,2,Status code,self,Status code,noOp,U,0,0,deg,no
29,42,2,Alt MSB's,self,Alt,noOp,U,0,0,meter,yes,3,0
30,42,2,week,self,week,noOp,U,0,0, ,no
31,42,2,sec MSB's,self,GPS sec,noOp,U,0,0,sec,yes,4,0
32,42,2,Status code,self,Status code,noOp,U,0,0, ,no
33,42,2,AZ,self,GPS AZ,mult,U,0,5.4931641E-03,deg,no
34,42,2,Pitch,self,GPS Pitch,mult,S,0,5.4931641E-03,deg,no
35,42,2,Roll,self,GPS Roll,mult,S,0,5.4931641E-03,deg,no
36,42,2,Status code,self,Status code,noOp,U,0,0, ,no
37,42,2,Lat,self,Lat,mult,S,0,2.746582E-03,deg N ,no
38,42,2,Long,self,Long,mult,S,0,5.4931641E-03,deg W,no
39,42,2,Error code,self,Error code,noOp,U,0,0, ,no
40,42,2,Status code,self,Status code,noOp,U,0,0, ,no
41,42,2,AZ,self,GPS AZ,mult,U,0,5.4931641E-03,deg,no
42,42,2,Pitch,self,GPS Pitch,mult,S,0,5.4931641E-03,deg,no
43,42,2,Roll,self,GPS Roll,mult,S,0,5.4931641E-03,deg,no
44,42,2,Status code,self,Status code,noOp,U,0,0, ,no
45,42,2,Alt MSB's,self,Alt,noOp,U,0,0,meter,yes,3,0
46,42,2,week,self,week,noOp,U,0,0, ,no
47,42,2,sec MSB's,self,GPS sec,noOp,U,0,0,sec,yes,4,0
48,42,2,Status code,self,Status code,noOp,U,0,0, ,no
;MAGS 1, 48, 44, 45
1,44,2,Mag bias rate cap,self,Mag bias rate cap,mult,S,0,3.0517578E-04,V,no
2,44,2,Mag bias clamp,self,Mag bias clamp,mult,S,0,3.0517578E-04,V,no
3,44,2,Mag bias weight,self,Mag bias weight,mult,S,0,1.508789e-3,mV,no
4,44,2,Tans point wt,self,Tans point wt,mult,S,0,3.0517578E-04,V,no
5,44,2,Tans tracker cnt,self,Tans tracker cnt,mult,S,0,3.0517578E-04,V,no
6,44,2,Mag tans count,self,Mag tans count,mult,S,0,3.0517578E-04,V,no
7,44,2,\#1 X,self,\#1 X,mult,S,0,3.0517578E-04,V,no
8,44,2,\#1 Y,self,\#1 Y,mult,S,0,3.0517578E-04,V,no
9,44,2,\#1 Z,self,\#1 Z,mult,S,0,3.0517578E-04,V,no
10,44,2,\#2 X,self,\#2 X,mult,S,0,3.0517578E-04,V,no
11,44,2,\#2 Y,self,\#2 Y,mult,S,0,3.0517578E-04,V,no
12,44,2,\#2 Z,self,\#2 Z,mult,S,0,3.0517578E-04,V,no
13,44,2,\#1 X,self,\#1 X,mult,S,0,3.0517578E-04,V,no
14,44,2,\#1 Y,self,\#1 Y,mult,S,0,3.0517578E-04,V,no
15,44,2,\#1 Z,self,\#1 Z,mult,S,0,3.0517578E-04,V,no
16,44,2,\#2 X,self,\#2 X,mult,S,0,3.0517578E-04,V,no
17,44,2,\#2 Y,self,\#2 Y,mult,S,0,3.0517578E-04,V,no
18,44,2,\#2 Z,self,\#2 Z,mult,S,0,3.0517578E-04,V,no
19,44,2,\#1 X,self,\#1 X,mult,S,0,3.0517578E-04,V,no
20,44,2,\#1 Y,self,\#1 Y,mult,S,0,3.0517578E-04,V,no
21,44,2,\#1 Z,self,\#1 Z,mult,S,0,3.0517578E-04,V,no
22,44,2,\#2 X,self,\#2 X,mult,S,0,3.0517578E-04,V,no
23,44,2,\#2 Y,self,\#2 Y,mult,S,0,3.0517578E-04,V,no
24,44,2,\#2 Z,self,\#2 Z,mult,S,0,3.0517578E-04,V,no
25,44,2,\#1 X,self,\#1 X,mult,S,0,3.0517578E-04,V,no
26,44,2,\#1 Y,self,\#1 Y,mult,S,0,3.0517578E-04,V,no
27,44,2,\#1 Z,self,\#1 Z,mult,S,0,3.0517578E-04,V,no
```

```
28,44,2,\#2 X,self,\#2 X,mult,S,0,3.0517578E-04,V,no
29,44,2,\#2 Y,self,\#2 Y,mult,S,0,3.0517578E-04,V,no
30,44,2,\#2 Z,self,\#2 Z,mult,S,0,3.0517578E-04,V,no
31,44,2,\#1 X,self,\#1 X,mult,S,0,3.0517578E-04,V,no
32,44,2,\#1 Y,self,\#1 Y,mult,S,0,3.0517578E-04,V,no
33,44,2,\#1 Z,self,\#1 Z,mult,S,0,3.0517578E-04,V,no
34,44,2,mag1 offset,self,mag1 offset,mult,S,0,5.4931641E-03,deg,no
35,44,2,mag2 offset,self,mag2 offset,mult,S,0,5.4931641E-03,deg,no
36,44,2,Next Az,self,Next Az,mult,U,0,0.005493164,deg,no
37,44,2,Next El,self,Next El,mult,U,0,0.002746582,deg,no
38,44,2,Next Ra,self,Next Ra,mult,U,0,0.000366211,hr,no
39,44,2,Next Dec,self,Next Dec,mult90off,U,0,0.002746582,deg,no
40,44,2,El s.angle zone,self,El s.angle zone,mult,S,0,3.0517578E-04,deg,no
41,44,2,El s.angle Diff,self,El s.angle Diff,mult,S,0,3.0517578E-04,V,no
42,44,2,El rate limit,self,El rate limit,mult,S,0,3.0517578E-04,V,no
43,44,2,\#1 X,self,\#1 X,mult,S,0,3.0517578E-04,V,no
44,44,2,\#1 Y,self,\#1 Y,mult,S,0,3.0517578E-04,V,no
45,44,2,\#1 Z,self,\#1 Z,mult,S,0,3.0517578E-04,V,no
46,44,2,\#2 X,self,\#2 X,mult,S,0,3.0517578E-04,V,no
47,44,2,\#2 Y,self,\#2 Y,mult,S,0,3.0517578E-04,V,no
48,44,2,\#2 Z,self,\#2 Z,mult,S,0,3.0517578E-04,V,no
;SERVO, 47, 46, 47
1,46,2,AZ trq set,self,AZ trq set,mult,S,0,3.051757812E-4,V,no
2,46,2,AZ I,self,AZ I,mult,S,0,3.051757812E-4,V,no
3,46,2,Az tach,self,Az tach,mult,S,0,3.051757812E-4,V,no
4,46,2,El trq set,self,El trq set,mult,S,0,3.051757812E-4,V,no
5,46,2,Gain ref rpm,self,Gain ref rpm,mult,S,0,3.051757812E-4,V,no
6,46,2,R3 trq set,self,R3 trq set,mult,S,0,3.051757812E-4,V,no
7,46,2,R3 I,self,R3 I,mult,S,0,3.051757812E-4,V,no
8,46,2,Criss trq set,self,Criss trq set,mult,S,0,3.051757812E-4,V,no
9,46,2,Criss I,self,Criss I,mult,S,0,3.051757812E-4,V,no
10,46,2,Criss tach,self,Criss tach,mult,S,0,3.051757812E-4,V,no
11,46,2,Az trq set,self,Az trq set,mult,S,0,3.051757812E-4,V,no
12,46,2,R3 dumper V,self,R3 dumper V,mult,S,0,3.051757812E-4,V,no
13,46,2,Az tach,self,Az tach,noOp,S,0,0,V,no
14,46,2,El trq set,self,El trq set,mult,S,0,3.051757812E-4,V,no
15,46,2,El I,self,El I,mult,S,0,3.051757812E-4,V,no
16,46,2,R3 trq set,self,R3 trq set,mult,S,0,3.051757812E-4,V,no
17,46,2,R3 I,self,R3 I,mult,S,0,3.051757812E-4,V,no
18,46,2,Criss trq set,self,Criss trq set,mult,S,0,3.051757812E-4,V,no
19,46,2,Criss I,self,Criss I,mult,S,0,3.051757812E-4,V,no
20,46,2,Criss tach,self,Criss tach,noOp,S,0,0,V,no
21,46,2,AZ trq set,self,AZ trq set,mult,S,0,3.051757812E-4,V,no
22,46,2,AZ I,self,AZ I,mult,S,0,3.051757812E-4,V,no
23,46,2,AZ tach,self,AZ tach,noOp,S,0,0,V,no
24,46,2,El trq set,self,El trq set,mult,S,0,3.051757812E-4,V,no
25,46,2,El I,self,El I,mult,S,0,3.051757812E-4,V,no
26,46,2,R3 trq set,self,R3 trq set,mult,S,0,3.051757812E-4,V,no
27,46,2,R3 I,self,R3 I,mult,S,0,3.051757812E-4,V,no
28,46,2,Criss trq set,self,Criss trq set,mult,S,0,3.051757812E-4,V,no
30,46,2,Criss tach,self,Criss tach,mult,S,0,3.051757812E-4,V,no
31,46,2,AZ trq set,self,AZ trq set,mult,S,0,3.051757812E-4,V,no
32,46,2,AZ I,self,AZ I,mult,S,0,3.051757812E-4,V,no
33,46,2,AZ tach,self,AZ tach,noOp,S,0,0,V,no
34,46,2,El trq set,self,El trq set,mult,S,0,3.051757812E-4,V,no
35,46,2,El I,self,El I,mult,S,0,3.051757812E-4,V,no
```

```
36,46,2,R3 trq set,self,R3 trq set,mult,S,0,3.051757812E-4,V,no
37,46,2,R3 I,self,R3 I,mult,S,0,3.051757812E-4,V,no
38,46,2,Criss trq set,self,Criss trq set,mult,S,0,3.051757812E-4,V,no
39,46,2,Criss I,self,Criss I,mult,S,0,3.051757812E-4,V,no
40,46,2,Criss tach,self,Criss tach,noOp,S,0,0,V,no
41,46,2,AZ trq set,self,AZ trq set,mult,S,0,3.051757812E-4,V,no
42,46,2,AZ I,self,AZ I,mult,S,0,3.051757812E-4,V,no
43,46,2,AZ tach,self,AZ tach,noOp,S,0,0,V,no
44,46,2,El trq set,self,El trq set,mult,S,0,3.051757812E-4,V,no
45,46,2,El I,self,El I,mult,S,0,3.051757812E-4,V,no
46,46,2,Criss trq set,self,Criss trq set,mult,S,0,3.051757812E-4,V,no
47,46,2,Criss I,self,Criss I,mult,S,0,3.051757812E-4,V,no
48,46,2,Criss tach,self,Criss tach,mult,S,0,3.051757812E-4,V,no
;INCLIN/ENC,48,48,49
1,48,2,Tracker 1 Az,self,Tracker 1 Az,mult,U,0,5.493164062e-3,deg,no
2,48,2,Tans offset Az,self,Tans offset Az,mult,S,0,5.493164062e-3,deg,no
3,48,2,ENC 1,self,ENC 1,mult,U,0,2.746582031e-3,deg,no
4,48,2,Tracker 1 El,self,Tracker 1 El,mult,U,0,2.746582031e-3,deg,no
5,48,2,Gammaoffset hor, self, Gammaoffset hor,mult,S,0,1.5258789e-4,deg,no
6,48,2,ENC 2,self,ENC 2,mult,U,0,2.746582031e-3,deg,no
7,48,2,Tracker 2 Az,self,Tracker 2 Az,mult,U,0,5.493164062e-3,deg,no
8,48,2,Boresight X,self,Boresight X,mult,S,0,3.051757812e-4,X,no
9,48,2,ENC 1,self,ENC 1,mult,U,0,2.746582031e-3,deg,no
10,48,2,Tracker 2 El,self,Tracker 2 El,mult,U,0,2.746582031e-3,deg,no
11,48,2,Boresight Y,self,Boresight Y,mult,S,0,3.051757812e-4,Y,no
12,48,2,ENC 2,self,ENC 2,mult,U,0,2.746582031e-3,deg,no
13,48,2,Tracker 1 Az ,self,Tracker 1 Az,mult,U,0,5.493164062e-3,deg,no
14,48,2,Boresight Z,self,Boresight Z,mult,S,0,3.051757812e-4,Z,no
15,48,2,ENC 1,self,ENC 1,mult,U,0,2.746582031e-3,deg,no
16,48,2,Tracker 1 El ,self,Tracker 1 El,mult,U,0,2.746582031e-3,deg,no
17,48,2,Gammaoffset Az, self, Gammaoffset Az,mult,S,0,1.5258789e-4,deg,no
18,48,2,ENC 2,self,ENC 2,mult,U,0,2.746582031e-3,deg,no
19,48,2,Tracker 2 Az ,self,Tracker 2 Az,mult,U,0,5.493164062e-3,deg,no
20,48,2,Gammaoffset El, self, Gammaoffset El,mult,S,0,1.5258789e-4,deg,no
21,48,2,ENC 1,self,ENC 1,mult,U,0,2.746582031e-3,deg,no
22,48,2,Tracker 2 El ,self,Tracker 2 El,mult,U,0,2.746582031e-3,deg,no
23,48,2,Boresight X,self,Boresight X,mult,S,0,3.051757812e-4,X,no
24,48,2,ENC 2,self,ENC 2,mult,U,0,2.746582031e-3,deg,no
25,48,2,Tracker 1 Az ,self,Tracker 1 Az,mult,U,0,5.493164062e-3,deg,no
26,48,2,Boresight Y,self,Boresight Y,mult,S,0,3.051757812e-4,Y,no
27,48,2,ENC 1,self,ENC 1,mult,U,0,2.746582031e-3,deg,no
28,48,2,Tracker 1 El ,self,Tracker 1 El,mult,U,0,2.746582031e-3,deg,no
29,48,2,Boresight Z,self,Boresight Z,mult,S,0,3.051757812e-4,Z,no
30,48,2,ENC 2,self,ENC 2,mult,U,0,2.746582031e-3,deg,no
31,48,2,Tracker 2 Az ,self,Tracker 2 Az,mult,U,0,5.493164062e-3,deg,no
32,48,2,Tans offset Az,self,Tans offset Az,mult,S,0,5.493164062e-3,deg,no
33,48,2,ENC 1,self,ENC 1,mult,U,0,2.746582031e-3,deg,no
34,48,2,Tracker 2 El ,self,Tracker 2 El,mult,U,0,2.746582031e-3,deg,no
35,48,2,Gammaoffset hor, self, Gammaoffset hor,mult,S,0,1.5258789e-4,deg,no
36,48,2,ENC 2,self,ENC 2,mult,U,0,2.746582031e-3,deg,no
37,48,2,Tracker 1 Az ,self,Tracker 1 Az,mult,U,0,5.493164062e-3,deg,no
38,48,2,Star offset Az, self,Star offset Az,mult,S,0,5.493164062e-3,deg,no
39,48,2,ENC 1,self,ENC 1,mult,U,0,2.746582031e-3,deg,no
40,48,2,Tracker 1 El ,self,Tracker 1 El,mult,U,0,2.746582031e-3,deg,no
41,48,2,Star offset El, self,Star offset El,mult,U,0,2.746582031e-3,deg,no
42,48,2,ENC 2,self,ENC 2,mult,U,0,2.746582031e-3,deg,no
```

```
43,48,2,Tracker 2 Az ,self,Tracker 2 Az,mult,U,0,5.493164062e-3,deg,no
44,48,2,Gammaoffset Az, self, Gammaoffset Az,mult,S,0,1.5258789e-4,deg,no
45,48,2,ENC 1,self,ENC 1,mult,U,0,2.746582031e-3,deg,no
46,48,2,Tracker 2 El ,self,Tracker 2 El,mult,U,0,2.746582031e-3,deg,no
47,48,2,Gammaoffset El, self, Gammaoffset El,mult,S,0,1.5258789e-4,deg,no
48,48,2,ENC 2,self,ENC 2,mult,U,0,2.746582031e-3,deg,no
;Display Status,57,0,50
5,50,1,Slewing,self,Slewing,BitOp,B,0,0,Unset,no
10,50,1,S10,self,Flipped EL Orient,BitOp,B,5,0,Unset,no
5,50,1,Tracking,self,Tracking,BitOp,B,2,0,Unset,no
5,50,1,Holding,self,Holding,BitOp,B,3,0,Unset,no
14,50,1,S14,self,Wait For Targ 1,BitOp,B,1,0,Unset,no
14,50,1,S14,self,Target Prog Active,BitOp,B,2,0,Unset,no
14,50,1,S14,self,Target Prog OvrRd,BitOp,B,3,0,Unset,no
3,50,1,Do Mag bias,self,Do Mag bias,BitOp,B,5,0,Unset,no
9,50,1,Doing Mag corr,self,Doing Mag corr,BitOp,B,5,0,Unset,no
2,50,1,Tans point corr,self,Tans point corr,BitOp,B,2,0,Unset,no
2,50,1,Encoder point corr,self,Encoder point corr,BitOp,B,3,0,Unset,no
3,50,1,Tracker1 point corr ,self,Tracker1 point corr,BitOp,B,6,0,Unset,no
3,50,1,Tracker2 point corr,self,Tracker2 point corr,BitOp,B,7,0,Unset,no
19,50,1,TANS new LLA,self,Tans new LLA,BitOp,B,3,0,Unset,no
5,50,1,Bad TANS Att,self,Bad TANS Att,BitOp,B,1,0,Unset,no
3,50,1,TANS Comm,self,Tans Comm,BitOp,B,3,0,Unset,no
9,50,1,TANS timeout,self,TANS timeout,BitOp,B,2,0,Unset,no
5,50,1,Tracker 1 timeout,self,Tracker 1 timeout,BitOp,B,4,0,Unset,no
5,50,1,Tracker 2 timeout,self,Tracker 2 timeout,BitOp,B,5,0,Unset,no
4,50,1,Elev. Enabled,self,Elev. Enabled,BitOp,B,4,0,Unset,no
4,50,1,Az Enabled,self,Az Enabled,BitOp,B,5,0,Unset,no
4,50,1,R3 Enabled,self,R3 Enabled,BitOp,B,6,0,Unset,no
4,50,1,Criss Enabled,self,Criss Enabled,BitOp,B,7,0,Unset,no
21,50,1,Slewing,self,Slewing,BitOp,B,0,0,Unset,no
21,50,1,Tracking,self,Tracking,BitOp,B,2,0,Unset,no
21,50,1,Holding,self,Holding,BitOp,B,3,0,Unset,no
30,50,1,S14,self,Wait For Targ 1,BitOp,B,1,0,Unset,no
30,50,1,S14,self,Target Prog Active,BitOp,B,2,0,Unset,no
30,50,1,S14,self,Target Prog OvrRd,BitOp,B,3,0,Unset,no
25,50,1,TANS timeout,self,TANS timeout,BitOp,B,2,0,Unset,no
18,50,1,Tans point corr,self,Tans point corr,BitOp,B,2,0,Unset,no
18,50,1,Encoder point corr,self,Encoder point corr,BitOp,B,3,0,Unset,no
19,50,1,Tracker1 point corr,self,Tracker1 point corr,BitOp,B,6,0,Unset,no
19,50,1,Tracker2 point corr,self,Tracker2 point corr,BitOp,B,7,0,Unset,no
37,50,1,Tracker 1 timeout,self,Tracker 1 timeout,BitOp,B,4,0,Unset,no
37,50,1,Tracker 2 timeout,self,Tracker 2 timeout,BitOp,B,5,0,Unset,no
20,50,1,Elev. Enabled,self,Elev. Enabled,BitOp,B,4,0,Unset,no
20,50,1,Az Enabled,self,Az Enabled,BitOp,B,5,0,Unset,no
20,50,1,R3 Enabled,self,R3 Enabled,BitOp,B,6,0,Unset,no
20,50,1,Criss Enabled,self,Criss Enabled,BitOp,B,7,0,Unset,no
37,50,1,Slewing,self,Slewing,BitOp,B,0,0,Unset,no
37,50,1,Tracking,self,Tracking,BitOp,B,2,0,Unset,no
37,50,1,Holding,self,Holding,BitOp,B,3,0,Unset,no
46,50,1,S14,self,Wait For Targ 1,BitOp,B,1,0,Unset,no
46,50,1,S14,self,Target Prog Active,BitOp,B,2,0,Unset,no
46,50,1,S14,self,Target Prog OvrRd,BitOp,B,3,0,Unset,no
41,50,1,TANS timeout,self,TANS timeout,BitOp,B,2,0,Unset,no
34,50,1,Tans point corr,self,Tans point corr,BitOp,B,2,0,Unset,no
34,50,1,Encoder point corr,self,Encoder point corr,BitOp,B,3,0,Unset,no
```

```
35,50,1,Tracker1 point corr,self,Tracker1 point corr,BitOp,B,6,0,Unset,no
35,50,1,Tracker2 point corr,self,Tracker2 point corr,BitOp,B,7,0,Unset,no
21,50,1,Tracker 1 timeout,self,Tracker 1 timeout,BitOp,B,4,0,Unset,no
21,50,1,Tracker 2 timeout,self,Tracker 2 timeout,BitOp,B,5,0,Unset,no
36,50,1,Elev. Enabled,self,Elev. Enabled,BitOp,B,4,0,Unset,no
36,50,1,Az Enabled,self,Az Enabled,BitOp,B,5,0,Unset,no
36,50,1,R3 Enabled,self,R3 Enabled,BitOp,B,6,0,Unset,no
36,50,1,Criss Enabled,self,Criss Enabled,BitOp,B,7,0,Unset,no
;STATUS,275,50,50
1,50,1,Using Gyro 1,self,Using Gyro 1,BitOp,B,0,0,Unset,no
1,50,1,Using Gyro 2,self,Using Gyro 2,BitOp,B,1,0,Unset,no
1,50,1,Using Accel 1,self,Using Accel 1,BitOp,B,2,0,Unset,no
1,50,1,Bad Uplink Packet,self,Bad UpLink Pack,BitOp,B,3,0,Unset,no
1,50,1,Using Mag 1,self,Using Mag 1,BitOp,B,4,0,Unset,no
1,50,1,Using Mag 2,self,Using Mag 2,BitOp,B,5,0,Unset,no
1,50,1,Using TANS,self,Using TANS,BitOp,B,7,0,Unset,no
2,50,1,Using Enc 1,self,Using Enc 1,BitOp,B,0,0,Unset,no
2,50,1,Using Enc 2,self,Using Enc 2,BitOp,B,1,0,Unset,no
2,50,1,Good Gyro 1,self,Good Gyro 1,BitOp,B,4,0,Unset,no
2,50,1,Good Gyro 2,self,Good Gyro 2,BitOp,B,5,0,Unset,no
2,50,1,Good Mag 1,self,Good Mag 1,BitOp,B,6,0,Unset,no
2,50,1,Good Mag 2,self,Good Mag 2,BitOp,B,7,0,Unset,no
3,50,1,Good Enc 1,self,Good Enc 1,BitOp,B,1,0,Unset,no
3,50,1,Good Enc 2,self,Good Enc 2,BitOp,B,2,0,Unset,no
3,50,1,Good Accel 1,self,Good Accel 1,BitOp,B,4,0,Unset,no
4,50,1,Latch Open,self,Latch Open,BitOp,B,0,0,Unset,no
4,50,1,Latch Closed,self,Latch Closed,BitOp,B,1,0,Unset,no
4,50,1,Latch Locked,self,Latch Locked,BitOp,B,2,0,Unset,no
4,50,1,Latch Unlocked,self,Latch Unlocked,BitOp,B,3,0,Unset,no
5,50,1,DIO mode: B1-CH,self,DIO mode: B1-CH,BitOp,B,6,0,Unset,no
5,50,1,DIO mode: B1-CL,self,DIO mode: B1-CL,BitOp,B,7,0,Unset,no
6,50,1,DIO mode: B2-A,self,DIO mode: B2-A,BitOp,B,0,0,Unset,no
6,50,1,DIO mode: B2-B,self,DIO mode: B2-B,BitOp,B,1,0,Unset,no
6,50,1,DIO mode: B2-CH,self,DIO mode: B2-CH,BitOp,B,2,0,Unset,no
6,50,1,DIO mode: B2-CL,self,DIO mode: B2-CL,BitOp,B,3,0,Unset,no
6,50,1,DIO mode: B3-A,self,DIO mode: B3-A,BitOp,B,4,0,Unset,no
6,50,1,DIO mode: B3-B,self,DIO mode: B3-B,BitOp,B,5,0,Unset,no
6,50,1,DIO mode: B3-CH,self,DIO mode: B3-CH,BitOp,B,6,0,Unset,no
6,50,1,DIO mode: B3-CL,self,DIO mode: B3-CL,BitOp,B,7,0,Unset,no
7,50,1,Awake,self,Awake,BitOp,B,0,0,Unset,no
7,50,1,TM on,self,TM on,BitOp,B,1,0,Unset,no
7,50,1,New Command,self,New Command,BitOp,B,2,0,Unset,no
7,50,1,Writting to File,self,Writting to File,BitOp,B,3,0,Unset,no
7,50,1,DAC mode: B1-0,self,DAC mode B1-0,BitOp,B,4,0,Unset,no
7,50,1,DAC mode: B1-1,self,DAC mode B1-1,BitOp,B,5,0,Unset,no
7,50,1,DAC mode: B1-2,self,DAC mode B1-2,BitOp,B,6,0,Unset,no
7,50,1,DAC mode: B1-3,self,DAC mode B1-3,BitOp,B,7,0,Unset,no
8,50,1,DAC mode: B2-0,self,DAC mode B2-0,BitOp,B,0,0,Unset,no
8,50,1,DAC mode: B2-1,self,DAC mode B2-1,BitOp,B,1,0,Unset,no
8,50,1,DAC mode: B2-2,self,DAC mode B2-2,BitOp,B,2,0,Unset,no
8,50,1,DAC mode: B2-3,self,DAC mode B2-3,BitOp,B,3,0,Unset,no
8,50,1,DAC mode: B3-0,self,DAC mode B3-0,BitOp,B,4,0,Unset,no
8,50,1,DAC mode: B3-1,self,DAC mode B3-1,BitOp,B,5,0,Unset,no
8,50,1,DAC mode: B3-2,self,DAC mode B3-2,BitOp,B,6,0,Unset,no
8,50,1,DAC mode: B3-3,self,DAC mode B3-3,BitOp,B,7,0,Unset,no
9,50,1,Bad Update Period,self,Bad Update Period,BitOp,B,0,0,Unset,no
```

```
9,50,1,Bad Filewrite Period,self,Bad Filewrite Period,BitOp,B,1,0,Unset,no
9,50,1,Bad Downlink Period,self,Bad Downlink Period,BitOp,B,3,0,Unset,no
9,50,1,Bad Uplink Period,self,Bad Uplink Period,BitOp,B,4,0,Unset,no
9,50,1,El Tracking,self,El Tracking,BitOp,B,6,0,Unset,no
9,50,1,Criss Tracking,self,Criss Tracking,BitOp,B,7,0,Unset,no
10,50,1,S10,self,R3 Tracking,BitOp,B,0,0,Unset,no
10,50,1,S10,self,Az Servo Fault,BitOp,B,1,0,Unset,no
10,50,1,S10,self,R3 Servo Fault,BitOp,B,2,0,Unset,no
10,50,1,S10,self,Criss Servo Fault,BitOp,B,3,0,Unset,no
10,50,1,S10,self,EL Servo Fault,BitOp,B,4,0,Unset,no
10,50,1,S10,self,Bad Uplink Pack,BitOp,B,6,0,Unset,no
11,50,1,S11,self,Tracker Fctn On,BitOp,B,0,0,Unset,no
11,50,1,S11,self,Serving,BitOp,B,1,0,Unset,no
11,50,1,S11,self,Sckt Created,BitOp,B,2,0,Unset,no
11,50,1,S11,self,Sckt Bound,BitOp,B,3,0,Unset,no
11,50,1,S11,self,Listen Conn,BitOp,B,4,0,Unset,no
11,50,1,S11,self,Cont Accpt Conn,BitOp,B,5,0,Unset,no
11,50,1,S11,self,New Conn Rqs,BitOp,B,6,0,Unset,no
12,50,1,S12,self,Trckr 1 est,BitOp,B,0,0,Unset,no
12,50,1,S12,self,Trckr 1 est inv,BitOp,B,1,0,Unset,no
12,50,1,S12,self,Trckr 1 CL to Comm,BitOp,B,2,0,Unset,no
12,50,1,S12,self,Trckr 1 Comm to CL,BitOp,B,3,0,Unset,no
12,50,1,s12,self,Trckr 1 Req Resp,BitOp,B,4,0,Unset,no
12,50,1,s12,self,Trckr 1 New Data,BitOp,B,5,0,Unset,no
12,50,1,S12,self,Trckr 1 Last Pckt OK,BitOp,B,6,0,Unset,no
13,50,1,S13,self,Trckr 2 est,BitOp,B,0,0,Unset,no
13,50,1,S13,self,Trckr 2 est inv,BitOp,B,1,0,Unset,no
13,50,1,S13,self,Trckr 2 CL to Comm,BitOp,B,2,0,Unset,no
13,50,1,S13,self,Trckr 2 Comm to CL,BitOp,B,3,0,Unset,no
13,50,1,s13,self,Trckr 2 Req Resp,BitOp,B,4,0,Unset,no
13,50,1,s13,self,Trckr 2 New Data,BitOp,B,5,0,Unset,no
13,50,1,S13,self,Trckr 2 Last Pckt OK,BitOp,B,6,0,Unset,no
14,50,1,S14,self,Good Target Prog,BitOp,B,0,0,Unset,no
15,50,1,using Star 1,self,Using Star 1,BitOp,B,1,0,Unset,no
15,50,1,using Star 2,self,Using Star 2,BitOp,B,2,0,Unset,no
15,50,1,using Gyros,self,Using Gyros,BitOp,B,3,0,Unset,no
15,50,1,LLNL file ok, self,LLNL file ok,BitOp,B,4,0,Unset,no
16,50,1,Serial input,self,Serial input,BitOp,B,0,0,Unset,no
16,50,1,Serial output,self,Serial output,BitOp,B,1,0,Unset,no
16,50,1,Science File ok,self,Science file ok,BitOp,B,2,0,Unset,no
16,50,1,Rx thread ok,self,Rx thread ok,BitOp,B,3,0,Unset,no
16,50,1,Tx thread ok,self,Tx thread ok,BitOp,B,4,0,Unset,no
16,50,1,Write thread ok,self,Write thread ok,BitOp,B,5,0,Unset,no
17,50,1,Using Gyro 1,self,Using Gyro 1,BitOp,B,0,0,Unset,no
17,50,1,Using Gyro 2,self,Using Gyro 2,BitOp,B,1,0,Unset,no
17,50,1,Using Accel 1,self,Using Accel 1,BitOp,B,2,0,Unset,no
17,50,1,Using Accel 2,self,Using Accel 2,BitOp,B,3,0,Unset,no
17,50,1,Using Mag 1,self,Using Mag 1,BitOp,B,4,0,Unset,no
17,50,1,Using Mag 2,self,Using Mag 2,BitOp,B,5,0,Unset,no
17,50,1,Using TANS,self,Using TANS,BitOp,B,7,0,Unset,no
18,50,1,Using Enc 1,self,Using Enc 1,BitOp,B,0,0,Unset,no
18,50,1,Using Enc 2,self,Using Enc 2,BitOp,B,1,0,Unset,no
18,50,1,Good Gyro 1,self,Good Gyro 1,BitOp,B,4,0,Unset,no
18,50,1,Good Gyro 2,self,Good Gyro 2,BitOp,B,5,0,Unset,no
18,50,1,Good Mag 1,self,Good Mag 1,BitOp,B,6,0,Unset,no
18,50,1,Good Mag 2,self,Good Mag 2,BitOp,B,7,0,Unset,no
```

```
19,50,1,Good Enc 1,self,Good Enc 1,BitOp,B,1,0,Unset,no
19,50,1,Good Enc 2,self,Good Enc 2,BitOp,B,2,0,Unset,no
19,50,1,Good Accel 1,self,Good Accel 1,BitOp,B,4,0,Unset,no
20,50,1,Latch Open,self,Latch Open,BitOp,B,0,0,Unset,no
20,50,1,Latch Closed,self,Latch Closed,BitOp,B,1,0,Unset,no
20,50,1,Latch Locked,self,Latch Locked,BitOp,B,2,0,Unset,no
20,50,1,Latch Unlocked,self,Latch Unlocked,BitOp,B,3,0,Unset,no
21,50,1,Encoders gyro1 bias,self,Encoders gyro1 bias,BitOp,B,1,0,Unset,no
21,50,1,DIO mode: B1-CH,self,DIO mode: B1-CH,BitOp,B,6,0,Unset,no
21,50,1,DIO mode: B1-CL,self,DIO mode: B1-CL,BitOp,B,7,0,Unset,no
22,50,1,DIO mode: B2-A,self,DIO mode: B2-A,BitOp,B,0,0,Unset,no
22,50,1,DIO mode: B2-B,self,DIO mode: B2-B,BitOp,B,1,0,Unset,no
22,50,1,DIO mode: B2-CH,self,DIO mode: B2-CH,BitOp,B,2,0,Unset,no
22,50,1,DIO mode: B2-CL,self,DIO mode: B2-CL,BitOp,B,3,0,Unset,no
22,50,1,DIO mode: B3-A,self,DIO mode: B3-A,BitOp,B,4,0,Unset,no
22,50,1,DIO mode: B3-B,self,DIO mode: B3-B,BitOp,B,5,0,Unset,no
22,50,1,DIO mode: B3-CH,self,DIO mode: B3-CH,BitOp,B,6,0,Unset,no
22,50,1,DIO mode: B3-CL,self,DIO mode: B3-CL,BitOp,B,7,0,Unset,no
23,50,1,Awake,self,Awake,BitOp,B,0,0,Unset,no
23,50,1,TM on,self,TM on,BitOp,B,1,0,Unset,no
23,50,1,New Command,self,New Command,BitOp,B,2,0,Unset,no
23,50,1,Writting to File,self,Writting to File,BitOp,B,3,0,Unset,no
23,50,1,DAC mode: B1-0,self,DAC mode B1-0,BitOp,B,4,0,Unset,no
23,50,1,DAC mode: B1-1,self,DAC mode B1-1,BitOp,B,5,0,Unset,no
23,50,1,DAC mode: B1-2,self,DAC mode B1-2,BitOp,B,6,0,Unset,no
23,50,1,DAC mode: B1-3,self,DAC mode B1-3,BitOp,B,7,0,Unset,no
24,50,1,DAC mode: B2-0,self,DAC mode B2-0,BitOp,B,0,0,Unset,no
24,50,1,DAC mode: B2-1,self,DAC mode B2-1,BitOp,B,1,0,Unset,no
24,50,1,DAC mode: B2-2,self,DAC mode B2-2,BitOp,B,2,0,Unset,no
24,50,1,DAC mode: B2-3,self,DAC mode B2-3,BitOp,B,3,0,Unset,no
24,50,1,DAC mode: B3-0,self,DAC mode B3-0,BitOp,B,4,0,Unset,no
24,50,1,DAC mode: B3-1,self,DAC mode B3-1,BitOp,B,5,0,Unset,no
24,50,1,DAC mode: B3-2,self,DAC mode B3-2,BitOp,B,6,0,Unset,no
24,50,1,DAC mode: B3-3,self,DAC mode B3-3,BitOp,B,7,0,Unset,no
25,50,1,Bad Update Period,self,Bad Update Period,BitOp,B,0,0,Unset,no
25,50,1,Bad Filewrite Period,self,Bad Filewrite Period,BitOp,B,1,0,Unset,no
25,50,1,Bad Downlink Period,self,Bad Downlink Period,BitOp,B,3,0,Unset,no
25,50,1,Bad Uplink Period,self,Bad Uplink Period,BitOp,B,4,0,Unset,no
25,50,1,Az Tracking,self,Az Tracking,BitOp,B,5,0,Unset,no
25,50,1,El Tracking,self,El Tracking,BitOp,B,6,0,Unset,no
25,50,1,Criss Tracking,self,Criss Tracking,BitOp,B,7,0,Unset,no
26,50,1,S10,self,R3 Tracking,BitOp,B,0,0,Unset,no
26,50,1,S10,self,Az Servo Fault,BitOp,B,1,0,Unset,no
26,50,1,S10,self,R3 Servo Fault,BitOp,B,2,0,Unset,no
26,50,1,S10,self,Criss Servo Fault,BitOp,B,3,0,Unset,no
26,50,1,S10,self,EL Servo Fault,BitOp,B,4,0,Unset,no
26,50,1,S10,self,Flipped EL Orient,BitOp,B,5,0,Unset,no
26,50,1,S10,self,Bad Uplink Pack,BitOp,B,6,0,Unset,no
27,50,1,S11,self,Tracker Fctn On,BitOp,B,0,0,Unset,no
27,50,1,S11,self,Serving,BitOp,B,1,0,Unset,no
27,50,1,S11,self,Sckt Created,BitOp,B,2,0,Unset,no
27,50,1,S11,self,Sckt Bound,BitOp,B,3,0,Unset,no
27,50,1,S11,self,Listen Conn,BitOp,B,4,0,Unset,no
27,50,1,S11,self,Cont Accpt Conn,BitOp,B,5,0,Unset,no
27,50,1,S11,self,New Conn Rqs,BitOp,B,6,0,Unset,no
28,50,1,S12,self,Trckr 1 est,BitOp,B,0,0,Unset,no
```

```
28,50,1,S12,self,Trckr 1 est inv,BitOp,B,1,0,Unset,no
28,50,1,S12,self,Trckr 1 CL to Comm,BitOp,B,2,0,Unset,no
28,50,1,S12,self,Trckr 1 Comm to CL,BitOp,B,3,0,Unset,no
28,50,1,s12,self,Trckr 1 Req Resp,BitOp,B,4,0,Unset,no
28,50,1,s12,self,Trckr 1 New Data,BitOp,B,5,0,Unset,no
28,50,1,S12,self,Trckr 1 Last Pckt OK,BitOp,B,6,0,Unset,no
29,50,1,S13,self,Trckr 2 est,BitOp,B,0,0,Unset,no
29,50,1,S13,self,Trckr 2 est inv,BitOp,B,1,0,Unset,no
29,50,1,S13,self,Trckr 2 CL to Comm,BitOp,B,2,0,Unset,no
29,50,1,S13,self,Trckr 2 Comm to CL,BitOp,B,3,0,Unset,no
29,50,1,s13,self,Trckr 2 Req Resp,BitOp,B,4,0,Unset,no
29,50,1,s13,self,Trckr 2 New Data,BitOp,B,5,0,Unset,no
29,50,1,S13,self,Trckr 2 Last Pckt OK,BitOp,B,6,0,Unset,no
30,50,1,S14,self,Good Target Prog,BitOp,B,0,0,Unset,no
31,50,1,using Star 1,self,Using Star 1,BitOp,B,1,0,Unset,no
31,50,1,using Star 2,self,Using Star 2,BitOp,B,2,0,Unset,no
31,50,1,using Gyros,self,Using Gyros,BitOp,B,3,0,Unset,no
31,50,1,LLNL file ok, self,LLNL file ok,BitOp,B,4,0,Unset,no
32,50,1,Serial input,self,Serial input,BitOp,B,0,0,Unset,no
32,50,1,Serial output,self,Serial output,BitOp,B,1,0,Unset,no
32,50,1,Science File ok,self,Science file ok,BitOp,B,2,0,Unset,no
32,50,1,Rx thread ok,self,Rx thread ok,BitOp,B,3,0,Unset,no
32,50,1,Tx thread ok,self,Tx thread ok,BitOp,B,4,0,Unset,no
32,50,1,Write thread ok,self,Write thread ok,BitOp,B,5,0,Unset,no
33,50,1,Using Gyro 1,self,Using Gyro 1,BitOp,B,0,0,Unset,no
33,50,1,Using Gyro 2,self,Using Gyro 2,BitOp,B,1,0,Unset,no
33,50,1,Using Accel 1,self,Using Accel 1,BitOp,B,2,0,Unset,no
33,50,1,Using Mag 1,self,Using Mag 1,BitOp,B,4,0,Unset,no
33,50,1,Using Mag 2,self,Using Mag 2,BitOp,B,5,0,Unset,no
33,50,1,Using TANS,self,Using TANS,BitOp,B,7,0,Unset,no
34,50,1,Using Enc 1,self,Using Enc 1,BitOp,B,0,0,Unset,no
34,50,1,Using Enc 2,self,Using Enc 2,BitOp,B,1,0,Unset,no
34,50,1,Good Gyro 1,self,Good Gyro 1,BitOp,B,4,0,Unset,no
34,50,1,Good Gyro 2,self,Good Gyro 2,BitOp,B,5,0,Unset,no
34,50,1,Good Mag 1,self,Good Mag 1,BitOp,B,6,0,Unset,no
34,50,1,Good Mag 2,self,Good Mag 2,BitOp,B,7,0,Unset,no
35,50,1,Good Enc 1,self,Good Enc 1,BitOp,B,1,0,Unset,no
35,50,1,Good Enc 2,self,Good Enc 2,BitOp,B,2,0,Unset,no
35,50,1,New TANS Att,self,New Tans Att,BitOp,B,3,0,Unset,no
35,50,1,Good Accel 1,self,Good Accel 1,BitOp,B,4,0,Unset,no
35,50,1,Good Accel 2,self,Good Accel 2,BitOp,B,5,0,Unset,no
36,50,1,Latch Open,self,Latch Open,BitOp,B,0,0,Unset,no
36,50,1,Latch Closed,self,Latch Closed,BitOp,B,1,0,Unset,no
36,50,1,Latch Locked,self,Latch Locked,BitOp,B,2,0,Unset,no
36,50,1,Latch Unlocked,self,Latch Unlocked,BitOp,B,3,0,Unset,no
37,50,1,Trackers gyro1 bias,self,Trackers gyro1 bias,BitOp,B,1,0,Unset,no
37,50,1,DIO mode: B1-CH,self,DIO mode: B1-CH,BitOp,B,6,0,Unset,no
37,50,1,DIO mode: B1-CL,self,DIO mode: B1-CL,BitOp,B,7,0,Unset,no
38,50,1,DIO mode: B2-A,self,DIO mode: B2-A,BitOp,B,0,0,Unset,no
38,50,1,DIO mode: B2-B,self,DIO mode: B2-B,BitOp,B,1,0,Unset,no
38,50,1,DIO mode: B2-CH,self,DIO mode: B2-CH,BitOp,B,2,0,Unset,no
38,50,1,DIO mode: B2-CL,self,DIO mode: B2-CL,BitOp,B,3,0,Unset,no
38,50,1,DIO mode: B3-A,self,DIO mode: B3-A,BitOp,B,4,0,Unset,no
38,50,1,DIO mode: B3-B,self,DIO mode: B3-B,BitOp,B,5,0,Unset,no
38,50,1,DIO mode: B3-CH,self,DIO mode: B3-CH,BitOp,B,6,0,Unset,no
38,50,1,DIO mode: B3-CL,self,DIO mode: B3-CL,BitOp,B,7,0,Unset,no
```

```
38,50,1,Awake,self,Awake,BitOp,B,0,0,Unset,no
38,50,1,TM on,self,TM on,BitOp,B,1,0,Unset,no
39,50,1,New Command,self,New Command,BitOp,B,2,0,Unset,no
39,50,1,Writting to File,self,Writting to File,BitOp,B,3,0,Unset,no
39,50,1,DAC mode: B1-0,self,DAC mode B1-0,BitOp,B,4,0,Unset,no
39,50,1,DAC mode: B1-1,self,DAC mode B1-1,BitOp,B,5,0,Unset,no
39,50,1,DAC mode: B1-2,self,DAC mode B1-2,BitOp,B,6,0,Unset,no
39,50,1,DAC mode: B1-3,self,DAC mode B1-3,BitOp,B,7,0,Unset,no
40,50,1,DAC mode: B2-0,self,DAC mode B2-0,BitOp,B,0,0,Unset,no
40,50,1,DAC mode: B2-1,self,DAC mode B2-1,BitOp,B,1,0,Unset,no
40,50,1,DAC mode: B2-2,self,DAC mode B2-2,BitOp,B,2,0,Unset,no
40,50,1,DAC mode: B2-3,self,DAC mode B2-3,BitOp,B,3,0,Unset,no
40,50,1,DAC mode: B3-0,self,DAC mode B3-0,BitOp,B,4,0,Unset,no
40,50,1,DAC mode: B3-1,self,DAC mode B3-1,BitOp,B,5,0,Unset,no
40,50,1,DAC mode: B3-2,self,DAC mode B3-2,BitOp,B,6,0,Unset,no
40,50,1,DAC mode: B3-3,self,DAC mode B3-3,BitOp,B,7,0,Unset,no
41,50,1,Bad Update Period,self,Bad Update Period,BitOp,B,0,0,Unset,no
41,50,1,Bad Filewrite Period,self,Bad Filewrite Period,BitOp,B,1,0,Unset,no
41,50,1,Bad Downlink Period,self,Bad Downlink Period,BitOp,B,3,0,Unset,no
41,50,1,Bad Uplink Period,self,Bad Uplink Period,BitOp,B,4,0,Unset,no
41,50,1,Az Tracking,self,Az Tracking,BitOp,B,5,0,Unset,no
41,50,1,El Tracking,self,El Tracking,BitOp,B,6,0,Unset,no
41,50,1,Criss Tracking,self,Criss Tracking,BitOp,B,7,0,Unset,no
42,50,1,S10,self,R3 Tracking,BitOp,B,0,0,Unset,no
42,50,1,S10,self,Az Servo Fault,BitOp,B,1,0,Unset,no
42,50,1,S10,self,R3 Servo Fault,BitOp,B,2,0,Unset,no
42,50,1,S10,self,Criss Servo Fault,BitOp,B,3,0,Unset,no
42,50,1,S10,self,EL Servo Fault,BitOp,B,4,0,Unset,no
42,50,1,S10,self,Flipped EL Orient,BitOp,B,5,0,Unset,no
42,50,1,S10,self,Bad Uplink Pack,BitOp,B,6,0,Unset,no
43,50,1,S11,self,Tracker Fctn On,BitOp,B,0,0,Unset,no
43,50,1,S11,self,Serving,BitOp,B,1,0,Unset,no
43,50,1,S11,self,Sckt Created,BitOp,B,2,0,Unset,no
43,50,1,S11,self,Sckt Bound,BitOp,B,3,0,Unset,no
43,50,1,S11,self,Listen Conn,BitOp,B,4,0,Unset,no
43,50,1,S11,self,Cont Accpt Conn,BitOp,B,5,0,Unset,no
43,50,1,S11,self,New Conn Rqs,BitOp,B,6,0,Unset,no
44,50,1,S12,self,Trckr 1 est,BitOp,B,0,0,Unset,no
44,50,1,S12,self,Trckr 1 est inv,BitOp,B,1,0,Unset,no
44,50,1,S12,self,Trckr 1 CL to Comm,BitOp,B,2,0,Unset,no
44,50,1,S12,self,Trckr 1 Comm to CL,BitOp,B,3,0,Unset,no
44,50,1,s12,self,Trckr 1 Req Resp,BitOp,B,4,0,Unset,no
44,50,1,s12,self,Trckr 1 New Data,BitOp,B,5,0,Unset,no
44,50,1,S12,self,Trckr 1 Last Pckt OK,BitOp,B,6,0,Unset,no
45,50,1,S13,self,Trckr 2 est,BitOp,B,0,0,Unset,no
45,50,1,S13,self,Trckr 2 est inv,BitOp,B,1,0,Unset,no
45,50,1,S13,self,Trckr 2 CL to Comm,BitOp,B,2,0,Unset,no
45,50,1,S13,self,Trckr 2 Comm to CL,BitOp,B,3,0,Unset,no
45,50,1,s13,self,Trckr 2 Req Resp,BitOp,B,4,0,Unset,no
45,50,1,s13,self,Trckr 2 New Data,BitOp,B,5,0,Unset,no
45,50,1,S13,self,Trckr 2 Last Pckt OK,BitOp,B,6,0,Unset,no
46,50,1,S14,self,Good Target Prog,BitOp,B,0,0,Unset,no
47,50,1,using Star 1,self,Using Star 1,BitOp,B,1,0,Unset,no
47,50,1,using Star 2,self,Using Star 2,BitOp,B,2,0,Unset,no
47,50,1,using Gyros,self,Using Gyros,BitOp,B,3,0,Unset,no
47,50,1,LLNL file ok, self,LLNL file ok,BitOp,B,4,0,Unset,no
```

```
48,50,1,Serial input,self,Serial input,BitOp,B,0,0,Unset,no
48,50,1,Serial output,self,Serial output,BitOp,B,1,0,Unset,no
48,50,1,Science File ok,self,Science file ok,BitOp,B,2,0,Unset,no
48,50,1,Rx thread ok,self,Rx thread ok,BitOp,B,3,0,Unset,no
48,50,1,Tx thread ok,self,Tx thread ok,BitOp,B,4,0,Unset,no
48,50,1,Write thread ok,self,Write thread ok,BitOp,B,5,0,Unset,no
;BYTES 1,45,51,51
1,51,1,Last Cmd,self,Last Cmd,noOp,U,0,0,Unset,no
2,51,1,ENC 1 OE,self,ENC 1 OE,noOp,U,0,0,Unset,no
3,51,1,ENC 2 OE,self,ENC 2 OE,noOp,U,0,0,Unset,no
4,51,1,Latch Cmd,self,Latch Cmd,noOp,U,0,0,Unset,no
;5,51,1,Lat LSB,GPS,GPS Lat,noOp,U,0,0,Unset,yes,3,2
;6,51,1,Long LSB,GPS,Long,noOp,U,0,0,Unset,yes,3,2
7,51,1,Servo Reset,self,Servo Reset,noOp,U,0,0,Unset,no
8,51,1,File Time,self,File Time,mult,U,0,.5,ms,no
9,51,1,Update Time,self,Update Time,mult,U,0,.5,ms,no
10,51,1,Uplink Time,self,Uplink Time,mult,U,0,.5,ms,no
11,51,1,Dnlink Time,self,Dnlink Time,mult,U,0,.5,ms,no
12,51,1,TANS Time,self,TANS Time,mult,U,0,.5,ms,no
13,51,1,Alt LSB,GPS,Alt,noOp,U,0,0,m,yes,3,2
14,51,1,File t max,self,File t max,mult,U,0,2,ms,no
15,51,1,GPS sec,GPS,GPS sec,noOp,U,0,0,s,yes,4,2
16,51,1,Time used,self,Time used,mult,U,0,.5,ms,no
17,51,1,Uplink t max,self,Uplink t max,mult,U,0,2,ms,no
18,51,1,Dnlink t max,self,Dnlink t max,mult,U,0,2,ms,no
19,51,1,Update t max,self,Update t max,mult,U,0,2,ms,no
20,51,1,TANS t max,self,TANS t max,mult,U,0,2,ms,no
;21,51,1,Lat LSB,GPS,GPS Lat,noOp,U,0,0,Unset,yes,3,2
;22,51,1,Long LSB,GPS,Long,noOp,U,0,0,Unset,yes,3,2
23,51,1,Loop prd MSB,self,Loop prd,mult,U,0,.1,ms,yes,2,0
24,51,1,Loop prd LSB,self,Loop prd,mult,U,0,.1,ms,yes,2,1
25,51,1,Samp/Loop,self,Samp/Loop,noOp,U,0,0, ,no
26,51,1,Trk 1 in t,self,Trk 1 in t,mult,U,0,.5,ms,no
27,51,1,Trk 1 out t,self,Trk 1 out t,mult,U,0,.5,ms,no
28,51,1,Trk 2 in t,self,Trk 2 in t,mult,U,0,.5,ms,no
29,51,1,Alt LSB,GPS,Alt,noOp,U,0,0,m,yes,3,2
39,51,1,Trk 2 out t,self,Trk 2 out t,mult,U,0,.5,ms,no
31,51,1,GPS sec,GPS,GPS sec,noOp,U,0,0,s,yes,4,2
32,51,1,Time used,self,Time used,mult,U,0,.5,ms,no
33,51,1,Trk 1 in tmax,self,Trk 1 in tmax,mult,U,0,2,ms,no
34,51,1,Trk 1 out tmax,self,Trk 1 out tmax,mult,U,0,2,ms,no
;37,51,1,Lat LSB,GPS,Lat,noOp,U,0,0,Unset,yes,3,2
;38,51,1,Long LSB,GPS,Long,noOp,U,0,0,Unset,yes,3,2
39,51,1,N Targets MSB,self,N Targets,noOp,U,0,0, ,yes,2,0
40,51,1,N Targets LSB,self,N Targets,noOp,U,0,0, ,yes,2,1
41,51,1,Desired RA LSB, Slow 1,Desired RA,mult,U,0,1.430511E-06,hours,yes,3,2
42,51,1,Desired DEC LSB, Slow 1,Desired DEC,mult90Off,U,0,1.072883E-05,degrees,yes,3,2
43,51,1,Current Target MSB,self,Current Target,noOp,U,0,0, ,yes,2,0
44,51,1,Current Target LSB,self,Current Target,noOp,U,0,0, ,yes,2,1
45,51,1,Alt LSB,GPS,Alt,noOp,U,0,0,Unset,yes,3,2
47,51,1,GPS sec LSB,GPS,GPS sec,noOp,U,0,0,s,yes,4,2
48,51,1,Time used,self,Time used,mult,U,0,.5,ms,no
;TRACK 1, 60, 52, 53
1,52,2,RA 1 MSBs,self,RA 1,mult,U,0,2.145767212E-5,hours,yes,3,0
2,52,2,DEC 1 MSBs,self,DEC 1,mult,U,0,1.072883606E-5,deg,yes,3,0
3,52,2,Roll 1 MSBs,self,Roll 1,mult,U,0,2.145767212E-5,deg,yes,3,0
```

```
4,52,2,RA 2 MSBs,self,RA 2,mult,U,0,2.145767212E-5,hours,yes,3,0
5,52,2,DEC 2 MSBs,self,DEC 2,mult,U,0,1.072883606E-5,deg,yes,3,0
6,52,2,Roll 2 MSBs,self,Roll 2,mult,U,0,2.145767212E-5,deg,yes,3,0
7,52,1,N star 1,self,N Star 1,noOp,U,0,0, ,no
7,53,1,N star Fit 1,self,N Star Fit 1,noOp,U,0,0, ,no
8,52,1,N star 2,self,N Star 2,noOp,U,0,0, ,no
8,53,1,N star Fit 2,self,N Star Fit 2,noOp,U,0,0, ,no
9,52,2,RA 1 MSBs,self,RA 1,mult,U,0,2.145767212E-5,hours,yes,3,0
10,52,2,DEC 1 MSBs,self,DEC 1,mult,U,0,1.072883606E-5,deg,yes,3,0
11,52,2,Roll 1 MSBs,self,Roll 1,mult,U,0,2.145767212E-5,deg,yes,3,0
12,52,2,RA 2 MSBs,self,RA 2,mult,U,0,2.145767212E-5,hours,yes,3,0
13,52,2,DEC 2 MSBs,self,DEC 2,mult,U,0,1.072883606E-5,deg,yes,3,0
14,52,2,Roll 2 MSBs,self,Roll 2,mult,U,0,2.145767212E-5,deg,yes,3,0
15,52,1,N star 1,self,N Star 1,noOp,U,0,0, ,no
15,53,1,N star Fit 1,self,N Star Fit 1,noOp,U,0,0, ,no
16,52,1,N star 2,self,N Star 2,noOp,U,0,0, ,no
16,53,1,N star Fit 2,self,N Star Fit 2,noOp,U,0,0, ,no
17,52,2,RA 1 MSBs,self,RA 1,mult,U,0,2.145767212E-5,hours,yes,3,0
18,52,2,DEC 1 MSBs,self,DEC 1,mult,U,0,1.072883606E-5,deg,yes,3,0
19,52,2,Roll 1 MSBs,self,Roll 1,mult,U,0,2.145767212E-5,deg,yes,3,0
20,52,2,RA 2 MSBs,self,RA 2,mult,U,0,2.145767212E-5,hours,yes,3,0
21,52,2,DEC 2 MSBs,self,DEC 2,mult,U,0,1.072883606E-5,deg,yes,3,0
22,52,2,Roll 2 MSBs,self,Roll 2,mult,U,0,2.145767212E-5,deg,yes,3,0
23,52,1,N star 1,self,N Star 1,noOp,U,0,0, ,no
23,53,1,N star Fit 1,self,N Star Fit 1,noOp,U,0,0, ,no
24,52,1,N star 2,self,N Star 2,noOp,U,0,0, ,no
24,53,1,N star Fit 2,self,N Star Fit 2,noOp,U,0,0, ,no
25,52,2,RA 1 MSBs,self,RA 1,mult,U,0,2.145767212E-5,hours,yes,3,0
26,52,2,DEC 1 MSBs,self,DEC 1,mult,U,0,1.072883606E-5,deg,yes,3,0
27,52,2,Roll 1 MSBs,self,Roll 1,mult,U,0,2.145767212E-5,deg,yes,3,0
28,52,2,RA 2 MSBs,self,RA 2,mult,U,0,2.145767212E-5,hours,yes,3,0
29,52,2,DEC 2 MSBs,self,DEC 2,mult,U,0,1.072883606E-5,deg,yes,3,0
30,52,2,Roll 2 MSBs,self,Roll 2,mult,U,0,2.145767212E-5,deg,yes,3,0
31,52,1,N star 1,self,N Star 1,noOp,U,0,0, ,no
31,53,1,N star Fit 1,self,N Star Fit 1,noOp,U,0,0, ,no
32,52,1,N star 2,self,N Star 2,noOp,U,0,0, ,no
32,53,1,N star Fit 2,self,N Star Fit 2,noOp,U,0,0, ,no
33,52,2,RA 1 MSBs,self,RA 1,mult,U,0,2.145767212E-5,hours,yes,3,0
34,52,2,DEC 1 MSBs,self,DEC 1,mult,U,0,1.072883606E-5,deg,yes,3,0
35,52,2,Roll 1 MSBs,self,Roll 1,mult,U,0,2.145767212E-5,deg,yes,3,0
36,52,2,RA 2 MSBs,self,RA 2,mult,U,0,2.145767212E-5,hours,yes,3,0
37,52,2,DEC 2 MSBs,self,DEC 2,mult,U,0,1.072883606E-5,deg,yes,3,0
38,52,2,Roll 2 MSBs,self,Roll 2,mult,U,0,2.145767212E-5,deg,yes,3,0
39,52,1,N star 1,self,N Star 1,noOp,U,0,0, ,no
39,53,1,N star Fit 1,self,N Star Fit 1,noOp,U,0,0, ,no
40,52,1,N star 2,self,N Star 2,noOp,U,0,0, ,no
40,53,1,N star Fit 2,self,N Star Fit 2,noOp,U,0,0, ,no
41,52,2,RA 1 MSBs,self,RA 1,mult,U,0,2.145767212E-5,hours,yes,3,0
42,52,2,DEC 1 MSBs,self,DEC 1,mult,U,0,1.072883606E-5,deg,yes,3,0
43,52,2,Roll 1 MSBs,self,Roll 1,mult,U,0,2.145767212E-5,deg,yes,3,0
44,52,2,RA 2 MSBs,self,RA 2,mult,U,0,2.145767212E-5,hours,yes,3,0
45,52,2,DEC 2 MSBs,self,DEC 2,mult,U,0,1.072883606E-5,deg,yes,3,0
46,52,2,Roll 2 MSBs,self,Roll 2,mult,U,0,2.145767212E-5,deg,yes,3,0
47,52,1,N star 1,self,N Star 1,noOp,U,0,0, ,no
47,53,1,N star Fit 1,self,N Star Fit 1,noOp,U,0,0, ,no
48,52,1,N star 2,self,N Star 2,noOp,U,0,0, ,no
```

```
48,53,1,N star Fit 2,self,N Star Fit 2,noOp,U,0,0, ,no
;TRACK 2,45,54,54
1,54,1,MSB t1,self,t1,mult,U,0,5.960464478e-8,sec,yes,3,0
2,54,1,t1,self,t1,mult,U,0,5.960464478e-8,sec,yes,3,1
3,54,1,LSB t1,self,t1,mult,U,0,5.960464478e-8,sec,yes,3,2
4,54,1,MSB t2,self,t2,mult,U,0,5.960464478e-8,sec,yes,3,0
5,54,1,t2,self,t2,mult,U,0,5.960464478e-8,sec,yes,3,1
6,54,1,LSB t2,self,t2,mult,U,0,5.960464478e-8,sec,yes,3,2
7,54,1,N Cmd 1,self,N Cmd 1,noOp,U,0,0,  ,no
8,54,1,N Cmd 2,self,N Cmd 2,noOp,U,0,0,  ,no
9,54,1,MSB t1,self,t1,mult,U,0,5.960464478e-8,sec,yes,3,0
10,54,1,t1,self,t1,mult,U,0,5.960464478e-8,sec,yes,3,1
11,54,1,LSB t1,self,t1,mult,U,0,5.960464478e-8,sec,yes,3,2
12,54,1,MSB t2,self,t2,mult,U,0,5.960464478e-8,sec,yes,3,0
13,54,1,t2,self,t2,mult,U,0,5.960464478e-8,sec,yes,3,1
14,54,1,LSB t2,self,t2,mult,U,0,5.960464478e-8,sec,yes,3,2
15,54,1,GPS sec LSB,GPS,GPS sec,noOp,U,0,0,Unset,yes,4,3
17,54,1,MSB t1,self,t1,mult,U,0,5.960464478e-8,sec,yes,3,0
18,54,1,t1,self,t1,mult,U,0,5.960464478e-8,sec,yes,3,1
19,54,1,LSB t1,self,t1,mult,U,0,5.960464478e-8,sec,yes,3,2
20,54,1,MSB t2,self,t2,mult,U,0,5.960464478e-8,sec,yes,3,0
21,54,1,t2,self,t2,mult,U,0,5.960464478e-8,sec,yes,3,1
22,54,1,LSB t2,self,t2,mult,U,0,5.960464478e-8,sec,yes,3,2
23,54,1,N Cmd 1,self,N Cmd 1,noOp,U,0,0, ,no
24,54,1,N Cmd 2,self,N Cmd 2,noOp,U,0,0, ,no
25,54,1,MSB t1,self,t1,mult,U,0,5.960464478e-8,sec,yes,3,0
26,54,1,t1,self,t1,mult,U,0,5.960464478e-8,sec,yes,3,1
27,54,1,LSB t1,self,t1,mult,U,0,5.960464478e-8,sec,yes,3,2
28,54,1,MSB t2,self,t2,mult,U,0,5.960464478e-8,sec,yes,3,0
29,54,1,t2,self,t2,mult,U,0,5.960464478e-8,sec,yes,3,1
30,54,1,LSB t2,self,t2,mult,U,0,5.960464478e-8,sec,yes,3,2
31,54,1,GPS sec LSB,GPS,GPS sec,noOp,U,0,0,Unset,yes,4,3
33,54,1,MSB t1,self,t1,mult,U,0,5.960464478e-8,sec,yes,3,0
34,54,1,t1,self,t1,mult,U,0,5.960464478e-8,sec,yes,3,1
35,54,1,LSB t1,self,t1,mult,U,0,5.960464478e-8,sec,yes,3,2
36,54,1,MSB t2,self,t2,mult,U,0,5.960464478e-8,sec,yes,3,0
37,54,1,t2,self,t2,mult,U,0,5.960464478e-8,sec,yes,3,1
38,54,1,LSB t2,self,t2,mult,U,0,5.960464478e-8,sec,yes,3,2
39,54,1,N Cmd 1,self,N Cmd 1,noOp,U,0,0, ,no
40,54,1,N Cmd 2,self,N Cmd 2,noOp,U,0,0, ,no
41,54,1,MSB t1,self,t1,mult,U,0,5.960464478e-8,sec,yes,3,0
42,54,1,t1,self,t1,mult,U,0,5.960464478e-8,sec,yes,3,1
43,54,1,LSB t1,self,t1,mult,U,0,5.960464478e-8,sec,yes,3,2
44,54,1,MSB t2,self,t2,mult,U,0,5.960464478e-8,sec,yes,3,0
45,54,1,t2,self,t2,mult,U,0,5.960464478e-8,sec,yes,3,1
46,54,1,LSB t2,self,t2,mult,U,0,5.960464478e-8,sec,yes,3,2
47,54,1,GPS sec LSB,GPS,GPS sec,noOp,U,0,0,Unset,yes,4,3
;GAINS,42,55,55
1,55,1,El P MSB,self,El P,mult,S,0,6.103516E-4, ,yes,2,0
2,55,1,El P LSB,self,El P,mult,S,0,6.103516E-4, ,yes,2,1
3,55,1,El In MSB,self,El In,mult,S,0,6.103516E-4, ,yes,2,0
4,55,1,El In LSB,self,El In,mult,S,0,6.103516E-4, ,yes,2,1
5,55,1,El D MSB,self,El D,mult,S,0,6.103516E-4, ,yes,2,0
6,55,1,El D LSB,self,El D,mult,S,0,6.103516E-4, ,yes,2,1
7,55,1,AZ P MSB,self,AZ P,mult,S,0,6.103516E-4, ,yes,2,0
8,55,1,AZ P LSB,self,AZ P,mult,S,0,6.103516E-4, ,yes,2,1
```

```
9,55,1,AZ In MSB,self,AZ In,mult,S,0,6.103516E-4, ,yes,2,0
10,55,1,AZ In LSB,self,AZ In,mult,S,0,6.103516E-4, ,yes,2,1
11,55,1,AZ D MSB,self,AZ D,mult,S,0,6.103516E-4, ,yes,2,0
12,55,1,AZ D LSB,self,AZ D,mult,S,0,6.103516E-4, ,yes,2,1
13,55,1,AZ V MSB,self,AZ V,mult,S,0,6.103516E-4, ,yes,2,0
14,55,1,AZ V LSB,self,AZ V,mult,S,0,6.103516E-4, ,yes,2,1
15,55,1,Roll P MSB,self,Roll P,mult,S,0,6.103516E-4, ,yes,2,0
16,55,1,Roll P LSB,self,Roll P,mult,S,0,6.103516E-4, ,yes,2,1
17,55,1,Roll D MSB,self,Roll D,mult,S,0,6.103516E-4, ,yes,2,0
18,55,1,Roll D LSB,self,Roll D,mult,S,0,6.103516E-4, ,yes,2,1
19,55,1,pAZ Slew V MSB,self,pAZ Slew V,mult,S,0,3.0518e-4,V,yes,2,0
20,55,1,pAZ Slew V LSB,self,pAZ Slew V,mult,S,0,3.0518e-4,V,yes,2,1
21,55,1,nAZ Slew V MSB,self,nAZ Slew V,mult,S,0,3.0518e-4,V,yes,2,0
22,55,1,nAZ Slew V LSB,self,nAZ Slew V,mult,S,0,3.0518e-4,V,yes,2,1
23,55,1,pEL Slew V MSB,self,pEL Slew V,mult,S,0,3.0518e-4,V,yes,2,0
24,55,1,pEL Slew V LSB,self,pEL Slew V,mult,S,0,3.0518e-4,V,yes,2,1
25,55,1,nEL Slew V MSB,self,nEL Slew V,mult,S,0,3.0518e-4,V,yes,2,0
26,55,1,nEL Slew V LSB,self,nEL Slew V,mult,S,0,3.0518e-4,V,yes,2,1
27,55,1,EL trq lim MSB,self,EL trq lim,mult,S,0,3.0518e-4,V,yes,2,0
28,55,1,EL trq lim LSB,self,EL trq lim,mult,S,0,3.0518e-4,V,yes,2,1
29,55,1,AZ trq lim MSB,self,AZ trq lim,mult,S,0,3.0518e-4,V,yes,2,0
30,55,1,AZ trq lim LSB,self,AZ trq lim,mult,S,0,3.0518e-4,V,yes,2,1
31,55,1,EL I lim MSB,self,EL I lim,mult,S,0,3.0518e-4,V,yes,2,0
32,55,1,EL I lim LSB,self,EL I lim,mult,S,0,3.0518e-4,V,yes,2,1
33,55,1,I AZ lim MSB,self,I AZ lim,mult,S,0,3.0518e-4,V,yes,2,0
34,55,1,I AZ lim LSB,self,I AZ lim,mult,S,0,3.0518e-4,V,yes,2,1
35,55,1,AZ Slew lim MSB,self,AZ Slew lim,mult,S,0,6.103516E-4,deg,yes,2,0
36,55,1,AZ Slew lim LSB,self,AZ Slew lim,mult,S,0,6.103516E-4,deg,yes,2,1
37,55,1,EL Slew lim MSB,self,EL Slew lim,mult,S,0,6.103516E-4,deg,yes,2,0
38,55,1,EL Slew lim LSB,self,EL Slew lim,mult,S,0,6.103516E-4,deg,yes,2,1
39,55,1,R3 slew msb,self,R3 slew lim,mult,S,0,6.103516E-4,deg,yes,2,0
40,55,1,R3 slew lsb,self,R3 slew lim,mult,S,0,6.103516E-4,deg,yes,2,1
41,55,1,R3 Trq lim msb,self,R3 Trq lim,mult,S,0,6.103516E-4,deg,yes,2,0
42,55,1,R3 Trq lim lsb,self,R3 Trq lim,mult,S,0,6.103516E-4,deg,yes,2,1
;TRACK 3,46,56,56
1,56,1,CCD 1 Gain MSB,self,CCD 1 Gain,noOp,F,0,0, ,yes,4,0
2,56,1,CCD 1 Gain Upper,self,CCD 1 Gain,noOp,F,0,0, ,yes,4,1
3,56,1,CCD 1 Gain Lower,self,CCD 1 Gain,noOp,F,0,0, ,yes,4,2
4,56,1,CCD 1 Gain LSB,self,CCD 1 Gain,noOp,F,0,0, ,yes,4,3
5,56,1,CCD 1 Int t MSB,self,CCD 1 Int t,noOp,F,0,0, ,yes,4,0
6,56,1,CCD 1 Int t Upper,self,CCD 1 Int t,noOp,F,0,0, ,yes,4,1
7,56,1,CCD 1 Int t Lower,self,CCD 1 Int t,noOp,F,0,0, ,yes,4,2
8,56,1,CCD 1 Int t LSB,self,CCD 1 Int t,noOp,F,0,0, ,yes,4,3
9,56,1,CCD 1 Ap Size MSB,self,CCD 1 Ap Size,noOp,F,0,0, ,yes,4,0
10,56,1,CCD 1 Ap Size Upper,self,CCD 1 Ap Size,noOp,F,0,0, ,yes,4,1
11,56,1,CCD 1 Ap Size Lower,self,CCD 1 Ap Size,noOp,F,0,0, ,yes,4,2
12,56,1,CCD 1 Ap Size LSB,self,CCD 1 Ap Size,noOp,F,0,0, ,yes,4,3
13,56,1,Img Thrs 1 MSB,self,Img Thrs 1,noOp,F,0,0, ,yes,4,0
14,56,1,Img Thrs 1 Upper,self,Img Thrs 1,noOp,F,0,0, ,yes,4,1
15,56,1,Img Thrs 1 Lower,self,Img Thrs 1,noOp,F,0,0, ,yes,4,2
16,56,1,Img Thrs 1 LSB,self,Img Thrs 1,noOp,F,0,0, ,yes,4,3
17,56,1,CCD 2 Gain MSB,self,CCD 2 Gain,noOp,F,0,0, ,yes,4,0
18,56,1,CCD 2 Gain Upper,self,CCD 2 Gain,noOp,F,0,0, ,yes,4,1
19,56,1,CCD 2 Gain Lower,self,CCD 2 Gain,noOp,F,0,0, ,yes,4,2
20,56,1,CCD 2 Gain LSB,self,CCD 2 Gain,noOp,F,0,0, ,yes,4,3
21,56,1,CCD 2 Int t MSB,self,CCD 2 Int t,noOp,F,0,0, ,yes,4,0
```

```
22,56,1,CCD 2 Int t Upper,self,CCD 2 Int t,noOp,F,0,0, ,yes,4,1
23,56,1,CCD 2 Int t Lower,self,CCD 2 Int t,noOp,F,0,0, ,yes,4,2
24,56,1,CCD 2 Int t LSB,self,CCD 2 Int t,noOp,F,0,0, ,yes,4,3
25,56,1,CCD 2 Ap Size MSB,self,CCD 2 Ap Size,noOp,F,0,0, ,yes,4,0
26,56,1,CCD 2 Ap Size Upper,self,CCD 2 Ap Size,noOp,F,0,0, ,yes,4,1
27,56,1,CCD 2 Ap Size Lower,self,CCD 2 Ap Size,noOp,F,0,0, ,yes,4,2
28,56,1,CCD 2 Ap Size LSB,self,CCD 2 Ap Size,noOp,F,0,0, ,yes,4,3
29,56,1,Img Thrs 2 MSB,self,Img Thrs 2,noOp,F,0,0, ,yes,4,0
30,56,1,Img Thrs 2 Upper,self,Img Thrs 2,noOp,F,0,0, ,yes,4,1
31,56,1,Img Thrs 2 Lower,self,Img Thrs 2,noOp,F,0,0, ,yes,4,2
32,56,1,Img Thrs 2 LSB,self,Img Thrs 2,noOp,F,0,0, ,yes,4,3
33,56,1,Port 1 MSB,self,Port 1,noOp,U,0,0, ,yes,2,0
34,56,1,Port 1 LSB,self,Port 1,noOp,U,0,0, ,yes,2,1
35,56,1,Port 2 MSB,self,Port 2,noOp,U,0,0, ,yes,2,0
36,56,1,Port 2 LSB,self,Port 2,noOp,U,0,0, ,yes,2,1
37,56,1,N Sent 1 MSB,self,N Sent 1,noOp,U,0,0, ,yes,2,0
38,56,1,N Sent 1 LSB,self,N Sent 1,noOp,U,0,0, ,yes,2,1
39,56,1,N Sent 2 MSB,self,N Sent 2,noOp,U,0,0, ,yes,2,0
40,56,1,N Sent 2 LSB,self,N Sent 2,noOp,U,0,0, ,yes,2,1
41,56,1,N rec 1 MSB,self,N rec 1,noOp,U,0,0, ,yes,2,0
42,56,1,N rec 1 LSB,self,N rec 1,noOp,U,0,0, ,yes,2,1
43,56,1,N rec 2 MSB,self,N rec 2,noOp,U,0,0, ,yes,2,0
44,56,1,N rec 2 LSB,self,N rec 2,noOp,U,0,0, ,yes,2,1
45,56,1,Srv Port MSB,self,Srv Port,noOp,U,0,0, ,yes,2,0
46,56,1,Srv Port LSB,self,Srv Port,noOp,U,0,0, ,yes,2,1
;TRACK 4,40,57,57
1,57,1,RA 1 LSB,TRACK 1,RA 1,mult,U,0,2.145767212E-5,hours,yes,3,2
2,57,1,DEC 1 LSB,TRACK 1,DEC 1,mult,U,0,1.072883606E-5,deg,yes,3,2
3,57,1,Roll 1 LSB,TRACK 1,Roll 1,mult,U,0,2.145767212E-5,Deg,yes,3,2
4,57,1,RA 2 LSB,TRACK 1,RA 2,mult,U,0,2.145767212E-5,hours,yes,3,2
5,57,1,DEC 2 LSB,TRACK 1,DEC 2,mult,U,0,1.072883606E-5,deg,yes,3,2
6,57,1,Roll 2 LSB,TRACK 1,Roll 2,mult,U,0,2.145767212E-5,Deg,yes,3,2
9,57,1,RA 1 LSB,TRACK 1,RA 1,mult,U,0,2.145767212E-5,hours,yes,3,2
10,57,1,DEC 1 LSB,TRACK 1,DEC 1,mult,U,0,1.072883606E-5,deg,yes,3,2
11,57,1,Roll 1 LSB,TRACK 1,Roll 1,mult,U,0,2.145767212E-5,Deg,yes,3,2
12,57,1,RA 2 LSB,TRACK 1,RA 2,mult,U,0,2.145767212E-5,hours,yes,3,2
13,57,1,DEC 2 LSB,TRACK 1,DEC 2,mult,U,0,1.072883606E-5,deg,yes,3,2
14,57,1,Roll 2 LSB,TRACK 1,Roll 2,mult,U,0,2.145767212E-5,Deg,yes,3,2
17,57,1,RA 1 LSB,TRACK 1,RA 1,mult,U,0,2.145767212E-5,hours,yes,3,2
18,57,1,DEC 1 LSB,TRACK 1,DEC 1,mult,U,0,1.072883606E-5,deg,yes,3,2
19,57,1,Roll 1 LSB,TRACK 1,Roll 1,mult,U,0,2.145767212E-5,Deg,yes,3,2
20,57,1,RA 2 LSB,TRACK 1,RA 2,mult,U,0,2.145767212E-5,hours,yes,3,2
21,57,1,DEC 2 LSB,TRACK 1,DEC 2,mult,U,0,1.072883606E-5,deg,yes,3,2
22,57,1,Roll 2 LSB,TRACK 1,Roll 2,mult,U,0,2.145767212E-5,Deg,yes,3,2
25,57,1,RA 1 LSB,TRACK 1,RA 1,mult,U,0,2.145767212E-5,hours,yes,3,2
26,57,1,DEC 1 LSB,TRACK 1,DEC 1,mult,U,0,1.072883606E-5,deg,yes,3,2
27,57,1,Roll 1 LSB,TRACK 1,Roll 1,mult,U,0,2.145767212E-5,Deg,yes,3,2
28,57,1,RA 2 LSB,TRACK 1,RA 2,mult,U,0,2.145767212E-5,hours,yes,3,2
29,57,1,DEC 2 LSB,TRACK 1,DEC 2,mult,U,0,1.072883606E-5,deg,yes,3,2
30,57,1,Roll 2 LSB,TRACK 1,Roll 2,mult,U,0,2.145767212E-5,Deg,yes,3,2
33,57,1,RA 1 LSB,TRACK 1,RA 1,mult,U,0,2.145767212E-5,hours,yes,3,2
34,57,1,DEC 1 LSB,TRACK 1,DEC 1,mult,U,0,1.072883606E-5,deg,yes,3,2
35,57,1,Roll 1 LSB,TRACK 1,Roll 1,mult,U,0,2.145767212E-5,Deg,yes,3,2
36,57,1,RA 2 LSB,TRACK 1,RA 2,mult,U,0,2.145767212E-5,hours,yes,3,2
37,57,1,DEC 2 LSB,TRACK 1,DEC 2,mult,U,0,1.072883606E-5,deg,yes,3,2
38,57,1,Roll 2 LSB,TRACK 1,Roll 2,mult,U,0,2.145767212E-5,Deg,yes,3,2
```

```
39,57,1,Tracker 1 p.W msb, self,Tracker 1 p.w,mult,S,0,3.051757812e-4, ,yes,2,0
40,57,1,Tracker 1 p.W lsb, self,Tracker 1 p.w,mult,S,0,3.051757812e-4, ,yes,2,1
41,57,1,RA 1 LSB,TRACK 1,RA 1,mult,U,0,2.145767212E-5,hours,yes,3,2
42,57,1,DEC 1 LSB,TRACK 1,DEC 1,mult,U,0,1.072883606E-5,deg,yes,3,2
43,57,1,Roll 1 LSB,TRACK 1,Roll 1,mult,U,0,2.145767212E-5,Deg,yes,3,2
44,57,1,RA 2 LSB,TRACK 1,RA 2,mult,U,0,2.145767212E-5,hours,yes,3,2
45,57,1,DEC 2 LSB,TRACK 1,DEC 2,mult,U,0,1.072883606E-5,deg,yes,3,2
46,57,1,Roll 2 LSB,TRACK 1,Roll 2,mult,U,0,2.145767212E-5,Deg,yes,3,2
47,57,1,Tracker 2 p.W msb, self,Tracker 2 p.w,mult,S,0,3.051757812e-4, ,yes,2,0
48,57,1,Tracker 2 p.W lsb, self,Tracker 2 p.w,mult,S,0,3.051757812e-4, ,yes,2,1
;New 1, 48, 58,58
1,58,1,Servo60V MSB,self,Servo60 V,mult,S,0,.0030517578125,V,yes,2,0
2,58,1,Servo60V I MSB,self,Servo60 I,mult,S,0,0.030517578125,I,yes,2,0
3,58,1,FCC30V MSB,self,FCC30 V,mult,S,0,0.0030517578125,V,yes,2,0
4,58,1,FCC30I MSB,self,FCC30 I,mult,S,0,0.030517578125,I,yes,2,0
5,58,1,Criss30V MSB,self,Criss30 V,mult,S,0,0.0030517578125,V,yes,2,0
6,58,1,Criss30I MSB,self,Criss30 I,mult,S,0,0.030517578125,I,yes,2,0
7,58,1,Digital30V MSB,self,Digital30 V,mult,S,0,0.0030517578125,V,yes,2,0
8,58,1,Digtal30 I MSB,self,Digital30 I,mult,S,0,0.030517578125,I,yes,2,0
9,58,1,Gyro AZ Bias MSB,self,Gyro AZ Bias,noOp,F,0,0,V,yes,4,0
10,58,1,Gyro AZ Bias LSB2,self,Gyro AZ Bias,noOp,F,0,0,V,yes,4,2
11,58,1,Gyro EL Bias MSB,self,Gyro EL Bias,noOp,F,0,0,V,yes,4,0
12,58,1,Gyro EL Bias LSB2,self,Gyro EL Bias,noOp,F,0,0,V,yes,4,2
13,58,1,Gyro ROLL Bias MSB,self,Gyro ROLL Bias,noOp,F,0,0,V,yes,4,0
14,58,1,Gyro ROLL Bias LSB2,self,Gyro ROLL Bias,noOp,F,0,0,V,yes,4,2
15,58,1,Gyro HYB Bias MSB,self,Gyro HYB Bias,noOp,F,0,0,V,yes,4,0
16,58,1,Gyro HYB Bias LSB2,self,Gyro HYB Bias,noOp,F,0,0,V,yes,4,2
17,58,1,Time on target msb,self,Time on target,mult,S,0,4.39331244e-1,min,yes,2,0
18,58,1,Time to next trg msb,self,Time to next trg,mult,S,0,4.39331244e-1,min,yes,2,0
19,58,1,Target Ra lsb,self,Target Ra,mult,S,0,7.32421875e-3,hours,yes,2,0
20,58,1,Target Dec lsb,self,Target Dec,mult,S,0,5.493164062e-2,deg,yes,2,0
21,58,1,Target Az lsb,self,Target Az,mult,S,0,0.109863281,deg,yes,2,0
22,58,1,Target El lsb,self,Target El,mult,S,0,2.746582031e-2,deg,yes,2,0
23,58,1,Tracker1 fix t. msb,self,Tracker1 fix time,mult,S,0,3.051757812e-4,hours,yes,2,0
24,58,1,Tracker2 fix t. msb,self,Tracker2 fix time,mult,S,0,3.051757812e-4,hours,yes,2,0
25,58,1,Gyro AZ Bias MSB,self,Gyro AZ Bias,noOp,F,0,0,V,yes,4,0
26,58,1,Gyro AZ Bias LSB2,self,Gyro AZ Bias,noOp,F,0,0,V,yes,4,2
27,58,1,Gyro EL Bias MSB,self,Gyro EL Bias,noOp,F,0,0,V,yes,4,0
28,58,1,Gyro EL Bias LSB2,self,Gyro EL Bias,noOp,F,0,0,V,yes,4,2
29,58,1,Gyro ROLL Bias MSB,self,Gyro ROLL Bias,noOp,F,0,0,V,yes,4,0
30,58,1,Gyro ROLL Bias LSB2,self,Gyro ROLL Bias,noOp,F,0,0,V,yes,4,2
31,58,1,Gyro HYB Bias MSB,self,Gyro HYB Bias,noOp,F,0,0,V,yes,4,0
32,58,1,Gyro HYB Bias LSB2,self,Gyro HYB Bias,noOp,F,0,0,V,yes,4,2
33,58,1,Time on target msb,self,Time on target,mult,S,0,4.39331244e-1,min,yes,2,0
34,58,1,Time to next trg msb,self,Time to next trg,mult,S,0,4.39331244e-1,min,yes,2,0
35,58,1,Enc bias rate cap,self,Enc bias rate cap,mult,S,0,3.051757812e-4,V,yes,2,0
36,58,1,Enc bias clamp,self,Enc bias clamp,mult,S,0,3.051757812e-4,V,yes,2,0
37,58,1,Enc bias weight,self,Enc bias weight,mult,S,0,1.508789e-3,mV,yes,2,0
38,58,1,Enc point weight,self,Enc point weight,mult,S,0,3.051757812e-4,V,yes,2,0
39,58,1,Enc 1 offset,self,Enc 1 offset,mult,S,0,6.103515625e-3,deg,yes,2,0
40,58,1,Enc 2 offset,self,Enc 2 offset,mult,S,0,6.103515625e-3,deg,yes,2,0
41,58,1,Gyro AZ Bias MSB,self,Gyro AZ Bias,noOp,F,0,0,V,yes,4,0
42,58,1,Gyro AZ Bias LSB2,self,Gyro AZ Bias,noOp,F,0,0,V,yes,4,2
43,58,1,Gyro EL Bias MSB,self,Gyro EL Bias,noOp,F,0,0,V,yes,4,0
44,58,1,Gyro EL Bias LSB2,self,Gyro EL Bias,noOp,F,0,0,V,yes,4,2
45,58,1,Gyro ROLL Bias MSB,self,Gyro ROLL Bias,noOp,F,0,0,V,yes,4,0
```

```
46,58,1,Gyro ROLL Bias LSB2,self,Gyro ROLL Bias,noOp,F,0,0,V,yes,4,2
47,58,1,Gyro HYB Bias MSB,self,Gyro HYB Bias,noOp,F,0,0,V,yes,4,0
48,58,1,Gyro HYB Bias LSB2,self,Gyro HYB Bias,noOp,F,0,0,V,yes,4,2
;New 2,48,59,59
1,59,1,Servo60V LSB,New 1,Servo60 V,mult,S,0,.0030517578125,V,yes,2,1
2,59,1,Servo60I LSB,New 1,Servo60 I,mult,S,0,0.030517578125,V,yes,2,1
3,59,1,FCC30V LSB,New 1,FCC30 V,mult,S,0,0.0030517578125,V,yes,2,1
4,59,1,FCC30I LSB,New 1,FCC30 I,mult,S,0,0.030517578125,V,yes,2,1
5,59,1,Criss30V LSB,New 1,Criss30 V,mult,S,0,0.0030517578125,V,yes,2,1
6,59,1,Criss30I LSB,New 1,Criss30 I,mult,S,0,0.030517578125,V,yes,2,1
7,59,1,Digital30V LSB,New 1,Digital30 V,mult,S,0,0.0030517578125,V,yes,2,1
8,59,1,Digital30I LSB,New 1,Digital30 I,mult,S,0,0.030517578125,V,yes,2,1
9,59,1,Gyro AZ Bias msb2,New 1,Gyro AZ Bias,noOp,F,0,0,V,yes,4,1
10,59,1,Gyro AZ Bias LSB,New 1,Gyro AZ Bias,noOp,F,0,0,V,yes,4,3
11,59,1,Gyro EL Bias msb2,New 1,Gyro EL Bias,noOp,F,0,0,V,yes,4,1
12,59,1,Gyro EL Bias LSB,New 1,Gyro EL Bias,noOp,F,0,0,V,yes,4,3
13,59,1,Gyro ROLL Bias msb2,New 1,Gyro ROLL Bias,noOp,F,0,0,V,yes,4,1
14,59,1,Gyro ROLL Bias LSB,New 1,Gyro ROLL Bias,noOp,F,0,0,V,yes,4,3
15,59,1,Gyro HYB Bias msb2,New 1,Gyro HYB Bias,noOp,F,0,0,V,yes,4,1
16,59,1,Gyro HYB Bias LSB,New 1,Gyro HYB Bias,noOp,F,0,0,V,yes,4,3
17,59,1,Time on target lsb,New 1,Time on target,mult,S,0,3.662109375e-2,min,yes,2,1
18,59,1,Time to next trg lsb,New 1,Time to next trg,mult,S,0,3.662109375e-2,min,yes,2,1
19,59,1,Target Ra lsb,New 1,Target Ra,mult,S,0,7.32421875e-3,hours,yes,2,1
20,59,1,Target Dec lsb,New 1,Target Dec,mult,S,0,5.493164062e-2,deg,yes,2,1
21,59,1,Target Az lsb,New 1,Target Az,mult,S,0,0.109863281,deg,yes,2,1
22,59,1,Target El lsb,New 1,Target El,mult,S,0,2.746582031e-2,deg,yes,2,1
23,59,1,Tracker1 fix t. lsb,New 1,Tracker1 fix time,mult,S,0,3.051757812e-4,min,yes,2,1
24,59,1,Tracker2 fix t. lsb,New 1,Tracker2 fix time,mult,S,0,3.051757812e-4,min,yes,2,1
25,59,1,Gyro AZ Bias msb2,New 1,Gyro AZ Bias,noOp,F,0,0,V,yes,4,1
26,59,1,Gyro AZ Bias LSB,New 1,Gyro AZ Bias,noOp,F,0,0,V,yes,4,3
27,59,1,Gyro EL Bias msb2,New 1,Gyro EL Bias,noOp,F,0,0,V,yes,4,1
28,59,1,Gyro EL Bias LSB,New 1,Gyro EL Bias,noOp,F,0,0,V,yes,4,3
29,59,1,Gyro ROLL Bias msb2,New 1,Gyro ROLL Bias,noOp,F,0,0,V,yes,4,1
30,59,1,Gyro ROLL Bias LSB,New 1,Gyro ROLL Bias,noOp,F,0,0,V,yes,4,3
31,59,1,Gyro HYB Bias msb2,New 1,Gyro HYB Bias,noOp,F,0,0,V,yes,4,1
32,59,1,Gyro HYB Bias LSB,New 1,Gyro HYB Bias,noOp,F,0,0,V,yes,4,3
33,59,1,Time on target lsb,New 1,Time on target,mult,S,0,3.662109375e-2,min,yes,2,1
34,59,1,Time to next trg lsb,New 1,Time to next trg,mult,S,0,3.662109375e-2,min,yes,2,1
35,59,1,Enc bias rate cap,New 1,Enc bias rate cap,mult,S,0,3.051757812e-4,V,yes,2,1
36,59,1,Enc bias clamp,New 1,Enc bias clamp,mult,S,0,3.051757812e-4,V,yes,2,1
37,59,1,Enc bias weight,New 1,Enc bias weight,mult,S,0,1.508789e-3,mV,yes,2,1
38,59,1,Enc point weight,New 1,Enc point weight,mult,S,0,3.051757812e-4,V,yes,2,1
39,59,1,Enc 1 offset,New 1,Enc 1 offset,mult,S,0,6.103515625e-3,deg,yes,2,1
40,59,1,Enc 2 offset,New 1,Enc 2 offset,mult,S,0,6.103515625e-3,deg,yes,2,1
41,59,1,Gyro AZ Bias msb2,New 1,Gyro AZ Bias,noOp,F,0,0,V,yes,4,1
42,59,1,Gyro AZ Bias LSB,New 1,Gyro AZ Bias,noOp,F,0,0,V,yes,4,3
43,59,1,Gyro EL Bias msb2,New 1,Gyro EL Bias,noOp,F,0,0,V,yes,4,1
44,59,1,Gyro EL Bias LSB,New 1,Gyro EL Bias,noOp,F,0,0,V,yes,4,3
45,59,1,Gyro ROLL Bias msb2,New 1,Gyro ROLL Bias,noOp,F,0,0,V,yes,4,1
46,59,1,Gyro ROLL Bias LSB,New 1,Gyro ROLL Bias,noOp,F,0,0,V,yes,4,3
47,59,1,Gyro HYB Bias msb2,New 1,Gyro HYB Bias,noOp,F,0,0,V,yes,4,1
48,59,1,Gyro HYB Bias LSB,New 1,Gyro HYB Bias,noOp,F,0,0,V,yes,4,3
```

Appendix D

Gyro software

This Appendix details the gyro correction routines. The flow charts D.1 and D.2 describe the flow of the correction routines. The routine names are given in the circles, and the parameter and variable names from the programs are maintained in the flow charts. Gyro1 is the elevation gyro and gyro2 is the azimuthal and roll gyro.

The routine **get_gyros** is the main routine. It first spawns the gyro calculation routines **calc_gyro1** and **calc_gyro2** then after the gyro update, it runs the appropriate corrections. If it is the first time the routine runs, as in startup, the gyro gets reset to the gps, if it is the azimuthal gyro, and if the gps is not working then the magnetometer. In the case of the gyro1 it gets set to the value of the encoder.

```
/* heft_gyro.c */
/*
 * Rotation matrices that correct gyro reads for earth drift assume:
 *  +x axis points due north
 * +y axis points due west
 * +z axis points towards zenith
 * Pitch (AZ-like) axis points along -z (this is the gyro2's -x output)
 * Yaw (EL-like) axis points along -y
 * Roll axis points along +x  (this is gyro2's +y output)
 *
 * The signs on W_EARTH are correct for gyro#2: verification was on 11/16/01
 * Orientation:  When the circuitry side of the gyro is viewed face-on,
 *   the roll axis points along the wires.
 *   the pitch axis points 90 degrees clockwise from there
 */

#include <math.h>
#include <stdio.h>
#include <fcntl.h>
#include "heft_const.h"
#include "heft_struct.h"
#include "heft_gyro.h"
#include "heft_servo.h"
```

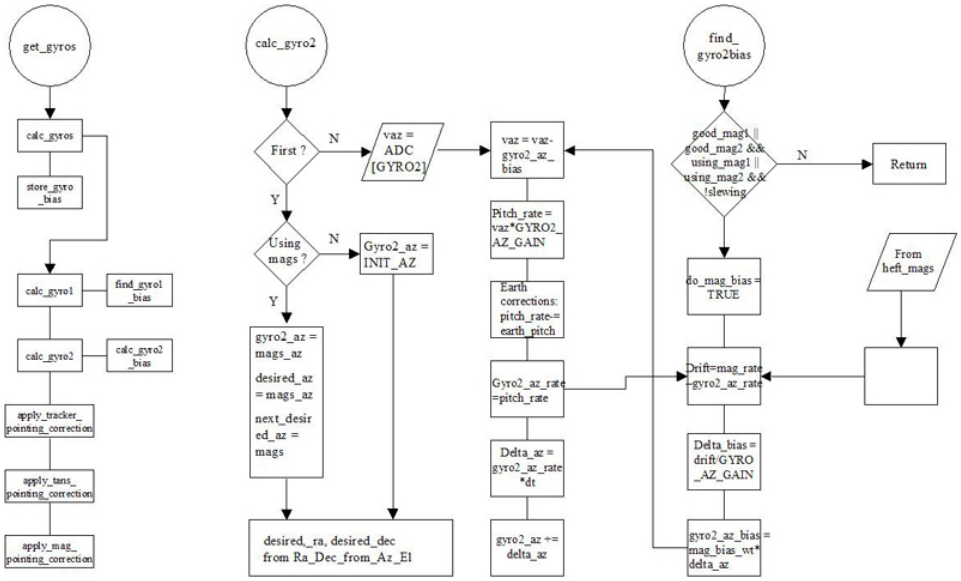

Figure D.1: Flow chart of the gyro2 correction software routines. Names of the routines are given in the circles.

```
void *get_gyros(void *arg)
  {
  heftdata *pd=(heftdata *)arg;

  pd=(heftdata *)calc_gyros(arg);
  pd=(heftdata *)store_gyro_bias(arg);
  return((void *)pd);
  }

// NOTE: gyro 2 is fixed to the gondola frame
void *calc_gyro2(void *arg)
  {
  heftdata *pd=(heftdata *)arg;
  float vaz, vroll;
  float delta_az, delta_roll;
  float w_earth_pitch, w_earth_roll;
  float pitch_rate, roll_rate;
  static unsigned char first=TRUE;
  static float last_roll_sign=0.0, last_az_sign=0.0;
  //static float vazav=0.0, vrollav=0.0;
  //static float nav=0.0;
  //float pitch_dummy;
  float vaz_dummy;
  //const float TH_OFF=3.0;
```

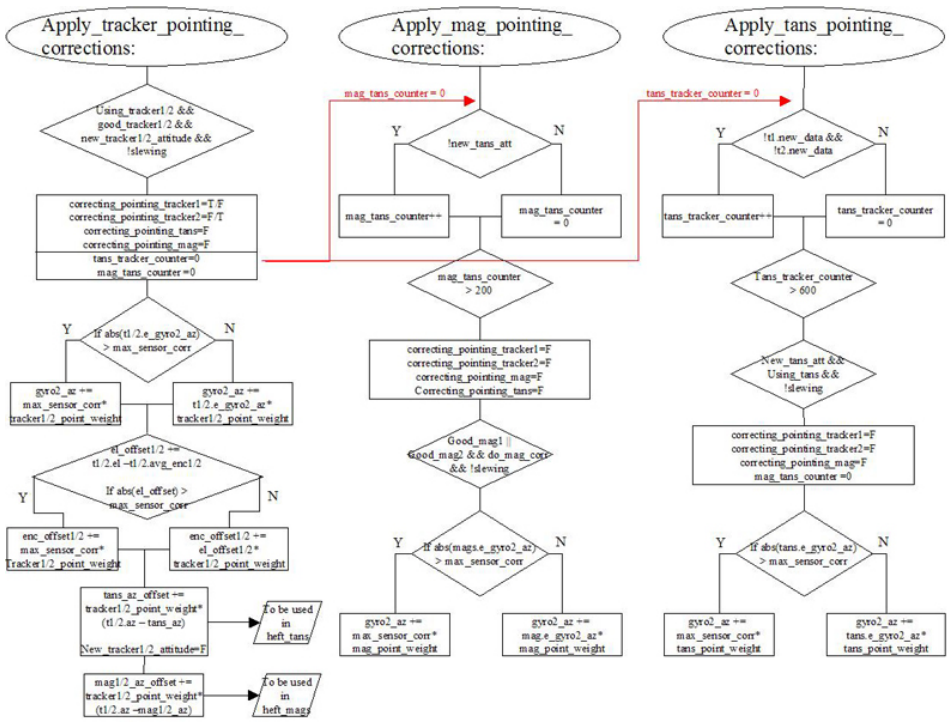

Figure D.2: Correction routines. Names of the routines are given in the circles.

```
/* Set up the gyro, it doesn't start out knowing anything absolute,
   we have decided to set things up initially on mags so that the
   gondola locks on, in azimuth, to where it is according to the mags,
   this allows time for the TANS to come up and thus doesn't
   immediately put us into slewing mode....no jerks allowed. */
if(first)
  {
  if(pd->data.status.using_mag1==TRUE &&
     pd->data.status.using_mag2==TRUE)
     {
     pd->data.pointing.gyro2_az =
     (pd->data.pointing.mag1_az+pd->data.pointing.mag2_az)/2.;
     pd->data.pointing.desired_az =
     (pd->data.pointing.mag1_az+pd->data.pointing.mag2_az)/2.;
     pd->data.pointing.next_desired_az = pd->data.pointing.desired_az;
     }
  else if(pd->data.status.using_mag2==TRUE)
     {
     pd->data.pointing.gyro2_az =
     pd->data.pointing.mag2_az;
     pd->data.pointing.desired_az =
     pd->data.pointing.mag2_az;
     pd->data.pointing.next_desired_az = pd->data.pointing.desired_az;
     }
  else if(pd->data.status.using_mag1==TRUE)
     {
     pd->data.pointing.gyro2_az =
     pd->data.pointing.mag1_az;
     pd->data.pointing.desired_az =
     pd->data.pointing.mag1_az;
     pd->data.pointing.next_desired_az = pd->data.pointing.desired_az;
     }
  else pd->data.pointing.gyro2_az=INIT_AZ;
  Ra_Dec_from_Az_El(
  &(pd->data.pointing.next_desired_ra),
  &(pd->data.pointing.next_desired_dec),
  (pd->data.pointing.tans_lat),
  (pd->data.pointing.tans_long),
  (pd->data.dateandtime.yr),
  (pd->data.dateandtime.mo),
  (pd->data.dateandtime.dy),
  (pd->data.pointing.ut),
  (pd->data.pointing.desired_az),
  (pd->data.pointing.desired_el));
  }  // end of if(first)

vaz = -pd->data.b2.adc[GYRO2_AZ];
vroll = -pd->data.b2.adc[GYRO_ROLL];

// derotate voltages by TH_OFF
vaz_dummy = vaz*cos(GYRO2_TH_OFF)-vroll*sin(GYRO2_TH_OFF);
vroll = vroll*cos(GYRO2_TH_OFF)+vaz*sin(GYRO2_TH_OFF);
vaz = vaz_dummy;

// this is now for the roll
if (first)
```

```
{
  last_roll_sign = (float)(vroll>=0.0) - (float)(vroll<0.0);
  last_az_sign = (float)(vaz>=0.0) - (float)(vaz<0.0);
  first = FALSE;
}

// check for saturation and set appropriate flags
// assume that last valid value's sign is the same as the saturated
// value's sign
pd->data.status.good_gyro2=TRUE;

if( (fabs(vaz) >= V_LIMIT) ||
    (pd->multsamp.b2ngood[GYRO2_AZ] != ADC_NSAMPLES) )
  {
  vaz=last_az_sign*V_LIMIT;
  pd->data.status.good_gyro2=FALSE;
  }
else
  {
  last_az_sign=(float)(vaz>=0.0)-(float)(vaz<0.0);
  pd->data.status.good_gyro2=TRUE;
  }

if( (fabs(vroll) >= V_LIMIT) ||
    (pd->multsamp.b2ngood[GYRO_ROLL] != ADC_NSAMPLES) )
  {
  vroll=last_roll_sign*V_LIMIT;
  pd->data.status.good_gyro2=FALSE;
  }
else
  {
  last_roll_sign=(float)(vroll>=0.0)-(float)(vroll<0.0);
  pd->data.status.good_gyro2*=TRUE;
  }

vaz = vaz - pd->data.pointing.gyro2_az_bias;
vroll = vroll - pd->data.pointing.gyro_roll_bias;

// these are the raw rates on the gyro axes, not the gondola axes
pitch_rate = vaz * GYRO2_AZ_GAIN;  // rate on gyro x axis
roll_rate = vroll*GYRO_ROLL_GAIN;  // rate on gyro y axis

w_earth_pitch = W_EARTH
             * (-sin(D2R*pd->data.pointing.tans_lat) *
                 cos(D2R*pd->data.pointing.roll) *
                 cos(D2R*pd->data.pointing.platform_el)
               + cos(D2R*pd->data.pointing.tans_lat)  * (
                    sin(D2R*pd->data.pointing.az) *
                    cos(D2R*pd->data.pointing.platform_el) *
                    sin(D2R*pd->data.pointing.roll)
                  + cos(D2R*pd->data.pointing.az) *
                    sin(D2R*pd->data.pointing.platform_el)  ) );
w_earth_roll = W_EARTH
              * (
                sin(D2R*pd->data.pointing.tans_lat) *
                cos(D2R*pd->data.pointing.roll) *
```

```
                  sin(D2R*pd->data.pointing.platform_el)
                + cos(D2R*pd->data.pointing.tans_lat) * (
                     cos(D2R*pd->data.pointing.platform_el) *
                     cos(D2R*pd->data.pointing.az)
                   - sin(D2R*pd->data.pointing.az) *
                     sin(D2R*pd->data.pointing.roll) *
                     sin(D2R*pd->data.pointing.platform_el) ) );
  pitch_rate -= w_earth_pitch;
  roll_rate  -= w_earth_roll;

  pd->data.pointing.gyro2_az_rate = pitch_rate;
  pd->data.pointing.gyro_roll_rate = roll_rate;

  delta_az =   (pd->data.pointing.gyro2_az_rate) *
          pd->timerdat.loop_period *
          (float)(pd->timerdat.adc_nsamples);
  delta_roll = (pd->data.pointing.gyro_roll_rate) *
          pd->timerdat.loop_period *
          (float)(pd->timerdat.adc_nsamples);

// the code below has been changed to eliminate the else, no gyro 2
// means sayonara heft-san
  //if(pd->data.status.good_gyro2)
   // {

    pd->data.pointing.gyro2_az += delta_az;
//printf("delta az %f \n",delta_az);
    pd->data.pointing.gyro_roll += delta_roll;
    pd->data.pointing.gyro_cumulative_roll += delta_roll;
    pd->data.pointing.gyro_roll *= (float)(!pd->data.status.slewing);
    //}

  /**********
    else
    {
    if(pd->data.status.using_tracker1 && pd->trackers.t1.status.good_packet)
       pd->data.pointing.gyro2_az = pd->trackers.t1.new_aspect.az;
    //if(pd->data.status.using_tracker2)
     //  pd->data.pointing.gyro2_az = pd->data.pointing.tracker1_az;
    }
***************/
  pd=(heftdata *)find_gyro2_bias((void *)pd);
  pd->data.pointing.gyro2_az -= ((float)(pd->data.pointing.gyro2_az >= 360.))*360.;
  pd->data.pointing.gyro2_az += ((float)(pd->data.pointing.gyro2_az < 0.0))*360.;
  return((void *)pd);

  }

// NOTE: gyro 1 is fixed to the telescope frame
// "vaz" is not linked uniquely to the pitch rotation rate:  it includes
// "roll rate" info also (as the telescope slews), and is accounted for
// in the rate assignments.

void *calc_gyro1(void *arg)
  {
  heftdata *pd=(heftdata *)arg;
```

```
float vel, vaz;
float yaw_rate;
//float pitch_rate, roll_rate, delta_hybrid;
float w_earth_pitch, w_earth_yaw, w_earth_roll;
float delta_el, delta_az, delta_roll;
static float last_el_sign, last_az_sign;
static float velav=0.0, vazav=0.0;
static unsigned char first=TRUE;
unsigned char print_running_average=TRUE;
static long n=0;
float hybrid_rate, vel_dummy;
float cross_th=GYRO1_TH_OFF;

// set the gyro position's zero point if 'first' is true
// average the two if possible, otherwise use one or the other.
// we also hack in desired_el = encoders here....no jerks allowed
if (first)
  {
  if(pd->data.status.using_encoder1 &&
     pd->data.status.using_encoder2)
     {
     pd->data.pointing.gyro_el =
     (pd->data.pointing.encoder1+pd->data.pointing.encoder2)/2.;
     // This so that it starts up and stays steady
     pd->data.pointing.desired_el =
     (pd->data.pointing.encoder1+pd->data.pointing.encoder2)/2.;
     pd->data.pointing.next_desired_el = pd->data.pointing.desired_el;
     }
  else if(pd->data.status.using_encoder2==TRUE)
     {
     pd->data.pointing.gyro_el =
     pd->data.pointing.encoder2;
     // This so that it starts up and stays steady
     pd->data.pointing.desired_el =
     pd->data.pointing.encoder2;
     pd->data.pointing.next_desired_el = pd->data.pointing.desired_el;
     }
  else if(pd->data.status.using_encoder1==TRUE)
     {
     pd->data.pointing.gyro_el =
     pd->data.pointing.encoder1;
     // This so that it starts up and stays steady
     pd->data.pointing.desired_el =
     pd->data.pointing.encoder1;
     pd->data.pointing.next_desired_el = pd->data.pointing.desired_el;
     }
  if(pd->data.status.using_accel1==TRUE)
     pd->data.pointing.gyro1_roll =
     pd->data.pointing.acc1_roll;
  else pd->data.pointing.gyro1_roll = 0.0;
  }

// get adc values for proper orientation
vaz=-pd->data.b2.adc[GYRO1_AZ];
vel=-pd->data.b2.adc[GYRO_EL];
```

```
//rotate voltages here so that bias finder will work ok
vel_dummy = vel*cos(cross_th*D2R) + vaz*sin(cross_th*D2R);
vaz = vaz*cos(cross_th*D2R) - vel*sin(cross_th*D2R);
vel = vel_dummy;

// get and keep track of signs of gyro outputs
if (first)
  {
  last_el_sign = (float)(vel>=0.0) - (float)(vel<0.0);
  last_az_sign = (float)(vaz>=0.0) - (float)(vaz<0.0);
  }

// check for saturation and set appropriate flags
// assume that last valid value's sign is the same as the saturated
// value's sign
pd->data.status.good_gyro1=TRUE;
if( (fabs(vaz) >= V_LIMIT) ||
    (pd->multsamp.b2ngood[GYRO1_AZ] != ADC_NSAMPLES) )
  {
  vaz=last_az_sign*V_LIMIT;
  pd->data.status.good_gyro1=FALSE;
  }
else
  {
  last_az_sign = (float)(vaz>=0.0) - (float)(vaz<0.0);
  pd->data.status.good_gyro1=TRUE;
  }
if( (fabs(vel) >= V_LIMIT) ||
    (pd->multsamp.b2ngood[GYRO_EL] != ADC_NSAMPLES) )
  {
  vel=last_el_sign*V_LIMIT;
  pd->data.status.good_gyro1=FALSE;
  }
else
  {
  last_el_sign=(vel>=0.0)-(vel<0.0);
  pd->data.status.good_gyro1*=TRUE;
  }


 // figure out earth drift corrections
 // assume the order pitch rot, roll rot, yaw rot
 //  (based on gondola geometry and degrees of freedom
 w_earth_pitch = W_EARTH  * (
            -sin(D2R*pd->data.pointing.tans_lat) *
            cos(D2R*pd->data.pointing.el) *
            cos(D2R*pd->data.pointing.roll) +
            cos(D2R*pd->data.pointing.tans_lat) * (
               sin(D2R*pd->data.pointing.az) *
               cos(D2R*pd->data.pointing.el) *
               sin(D2R*pd->data.pointing.roll) +
               cos(D2R*pd->data.pointing.az) *
               sin(D2R*pd->data.pointing.el) ) );
 w_earth_yaw   = -W_EARTH * (
            cos(D2R*pd->data.pointing.tans_lat) *
            sin(D2R*pd->data.pointing.az) *
```

```
            cos(D2R*pd->data.pointing.roll) +
            sin(D2R*pd->data.pointing.tans_lat) *
            sin(D2R*pd->data.pointing.roll) );
 w_earth_roll  = W_EARTH * (
            sin(D2R*pd->data.pointing.tans_lat) *
            cos(D2R*pd->data.pointing.roll) *
            sin(D2R*pd->data.pointing.el) +
            cos(D2R*pd->data.pointing.tans_lat) * (
               cos(D2R*pd->data.pointing.az) *
               cos(D2R*pd->data.pointing.el) -
               sin(D2R*pd->data.pointing.az) *
               sin(D2R*pd->data.pointing.roll) *
               sin(D2R*pd->data.pointing.el) ) );

// turn voltages into rates
yaw_rate =
    ((vel - pd->data.pointing.gyro_el_bias) * GYRO_EL_GAIN);
hybrid_rate =
    ((vaz - pd->data.pointing.gyro_hybrid_bias) * GYRO1_AZ_GAIN);

yaw_rate -= w_earth_yaw;
hybrid_rate -= w_earth_roll*cos(D2R*pd->data.pointing.el) -
               w_earth_pitch*sin(D2R*pd->data.pointing.el);

pd->data.pointing.gyro_el_rate = yaw_rate;
pd->data.pointing.gyro1_az_rate =
  -hybrid_rate*sin(D2R*pd->data.pointing.el);
pd->data.pointing.gyro1_roll_rate =
   hybrid_rate*cos(D2R*pd->data.pointing.el);
pd->data.pointing.gyro1_hybrid_rate = hybrid_rate;

// calculate attitude increment
// protect el against azim slewing
delta_el =   (pd->data.pointing.gyro_el_rate) *
         pd->timerdat.loop_period *
         (float)(pd->timerdat.adc_nsamples) *
         (float)(!pd->data.status.slewing);
delta_az =   (pd->data.pointing.gyro1_az_rate) *
         pd->timerdat.loop_period *
         (float)(pd->timerdat.adc_nsamples);
delta_roll = (pd->data.pointing.gyro1_az_rate) *
         pd->timerdat.loop_period *
         (float)(pd->timerdat.adc_nsamples);

// Add some more delta_el to sync the

// increment elevation
if(pd->data.status.good_gyro1)
  {
  pd->data.pointing.gyro_el += delta_el;
  pd->data.pointing.gyro1_az += delta_az;
  pd->data.pointing.gyro1_roll += delta_roll;
  // protect gyro elevation against large cross-axis coupling errors
  if(pd->data.status.slewing)
    pd->data.pointing.gyro_el =
       (pd->data.pointing.encoder1+pd->data.pointing.encoder2)/2.0;
```

```
    }
  else
    {
    if(pd->data.status.using_encoder1)
      pd->data.pointing.gyro_el = pd->data.pointing.encoder1;
    else if(pd->data.status.using_encoder2)
      pd->data.pointing.gyro_el = pd->data.pointing.encoder2;
    }
  if(pd->data.status.slewing)
    {
    pd->data.pointing.gyro_el_rate = 0.0;
    pd->data.pointing.gyro_el = 0.5 * (pd->data.pointing.encoder1 +
         pd->data.pointing.encoder2);
    }

  // bias correction
  pd = (heftdata *)find_gyro1_bias((void *)pd);

  // update the running average for ground testing
  if(print_running_average)
    {
    if(first)
      {
      velav=vel;
      vazav=vaz;
      }
    else
      {
      velav = (velav*n + vel)/(n+1);
      vazav = (vazav*n + vaz)/(n+1);
      }
    n++;
    }

  first=FALSE;
  return((void *)pd);
  }

void *calc_gyros(void *arg)
  {
  heftdata *pd=(heftdata *)arg;

  //Finally, do some real work, get the gyros
  pd = (heftdata *)calc_gyro1(arg);
  pd = (heftdata *)calc_gyro2(arg);
  // Then apply the pointing corrections
  pd=(heftdata *)apply_tracker_pointing_correction((void *)pd);
  //pd=(heftdata *)apply_encoder_pointing_correction((void *)pd);
  pd=(heftdata *)apply_tans_pointing_correction((void *)pd);
  pd=(heftdata *)apply_mag_pointing_correction((void *)pd);
  return((void *)pd);
  }

void *find_gyro1_bias(void *arg)
  {
  heftdata *pd=(heftdata *)arg;
```

```
  //static unsigned char first_el=TRUE, first_hyb=TRUE;
  static float last_enc_el;
  float enc_rate, gyr_rate;
  //float dbias;
  float dt=(float)pd->timerdat.loop_period*((float)pd->timerdat.adc_nsamples);
  //const float timescale=PENDULUM_PERIOD*10.0; // seconds
  //static float t=0.0, t_last_roll_cor=0.0;
  //static float old_inc1;
  //static float dbiasaz, azrate, azdrift;
  //float new_inc1;
  //unsigned char crossed, inc1_status;
  static unsigned long n=0;

  // for tracker/EL correction
  float delta_el_bias;
  n++;

  // el bias method:
  //      every iteration compare the "encoder rate" to gyro rate
  //      assume that discrepancies are due to drift, but scale down
  //      corrections with a boxcar average of width "timescale".
  //      timescale should exceed expected pendulum periods
  //   Note that the gyro has been set equal to the encoder previously

    // Do a correction based on the encoders if we are using either one.
    if((pd->data.status.using_encoder1 || pd->data.status.using_encoder2)
      && !pd->data.status.slewing)
     {
        // here is the instantaneous rate
      enc_rate = (pd->data.pointing.encoders - last_enc_el)/dt;
      last_enc_el = pd->data.pointing.encoders;

  // Only correct for bias drift here if it is credible that
        // the rate error is due to bias drift...otherwise let the pointing
        // loop handle it... 0.1 degrees per second is reasonable

if(fabs(enc_rate)  < pd->data.pointing.encoder_bias_rate_cap){
      gyr_rate = pd->data.pointing.gyro_el_rate;
      delta_el_bias = (gyr_rate - enc_rate)/GYRO_EL_GAIN;
// Now constrain this so we add no more than a tenth of
// a millivolt per time through this fast loop
if(fabs(delta_el_bias) > pd->data.pointing.encoder_bias_clamp){
  if(delta_el_bias > 0)
delta_el_bias =
pd->data.pointing.encoder_bias_clamp;
  if(delta_el_bias < 0)
delta_el_bias =
-1.0*pd->data.pointing.encoder_bias_clamp;
}
        pd->data.pointing.gyro_el_bias +=
pd->data.pointing.encoder_bias_weight*delta_el_bias;
        delta_el_bias = 0.0;
     } //endif enc_rate < encoder_bias_rate_cap

    // this gets bias...but we are tracking off of encoders so need
    // to correct gyro to the encoders...the encoders are corrected using
```

```
    // the trackers...though they can also be corrected using the filtered
    // accelerometers

   // you've done the bias with encoders...
   // gyros are now always pinned to encoder.  10/2/2004.
   // The good_tracker_attitude flag is now meaningless.
   // to the encoders.  Changed

   pd->data.pointing.gyro_el -=
pd->data.pointing.encoder_point_weight*(pd->data.pointing.gyro_el -
pd->data.pointing.encoders);

   //if(!pd->data.status.good_tracker_attitude)  {
   //         pd->data.status.correcting_pointing_encoder = TRUE;
   //}
   // else {
   //   pd->data.status.correcting_pointing_encoder = FALSE;
   //}
  } // end of good/using encoders if
  return((void *)pd);
  } // end of find_gyro1_bias

void *find_gyro2_bias(void *arg)
  {
  heftdata *pd=(heftdata *)arg;
  //static unsigned char first=TRUE;
  //static unsigned char last_had_first_tracker_fix=FALSE;
  //unsigned char got_bias=FALSE;

  /* FOR ROLL BIAS CORRECTIONS */
  //float cycles=0.38;
  //float weight=powf(.1,1.0/cycles);
  //static unsigned char gyro_roll_bias_cor=GYRO_ROLL_BIAS_COR;
  float dt;

  /* FOR GYRO AVERAGE ROLL OVER A PENDULUM PERIOD */
  static unsigned char good_avg=TRUE;
  static float int_roll=0.0, t=0.0;
  //float t3=0.0;
  float drol;
  //float new_bias, old_bias;
  //float wt=0.05;  // weight to be used for the leaky average
  float swing_thresh=20.0/60.;  // limit over which averages are ok

  /* FOR CONSTANT ZERO ROLL ASSUMPTION */
  //float gyr_rate, dbias;

  /* holders for the gyro bias correction values */
  float delta_roll_bias=0.0;
  float delta_az_bias=0.0;
  //float delta_az_bias_tracker1=0.0;
  //float delta_az_bias_tracker2=0.0;
  //float delta_az_bias_tans=0.0;
  //float delta_az_bias_mag=0.0;

  /* FOR TRACKER/TANS BIAS STUFF */
```

```
  float drift;
  //float wt_tans=0.00015;
  //float wt_mag=0.009;
  //float wt_track=(1./77.);

  // * * * * * *  ROLL BIAS * * * * * * * * * * * * * * *
  // keep track of roll rates: average roll rate over a long period
  // must be zero for a non-tumbling gondola.
  // the period should be set according to:
  //   stabilization time for roll bias (see notes from 1/18/02)
  //    pendulation period of gondola (average over several of these)
  //    stabilization time:   ~200 sec (roll); ~400 sec (az)
  //    pendulation time: ~20 sec
  // comparisons with the accelerometer or inclinometer will be
  // beneficial when they are available

    // average over roll period to find corrections because we should
    // average to zero and want to have enough time to do that.

      dt = pd->timerdat.loop_period * pd->timerdat.adc_nsamples;
      if(t < PENDULUM_PERIOD*10.0)
{ //this is 50 seconds or so
       t+=dt;
       int_roll += dt*pd->data.pointing.gyro_roll;
       if(fabs(pd->data.pointing.gyro_roll) > swing_thresh)
       good_avg=FALSE;
       } //endif PENDULUM_PERIOD
      else  // time for bias update
        {
        if(good_avg)
          {
           drol = int_roll/t;
           pd->data.pointing.gyro_roll -= 0.5*drol;
           delta_roll_bias = drol/t/GYRO_ROLL_GAIN;
          } //endif good_avg
          t=0.0;
          int_roll=0.0;
          good_avg=TRUE;
        }  //endelse time for bias update
  // Now apply the bias
  pd->data.pointing.gyro_roll *=
(float)pd->data.status.slewing; //don't apply if slewing
  delta_roll_bias =  -delta_roll_bias;  //Sign change needed here for flip?? XXX

  // Clamp this at 1arcsecond /second rate change per application (every 50 s)

  if(fabs(delta_roll_bias) > 0.001){
if(delta_roll_bias > 0) delta_roll_bias = 0.001;
if(delta_roll_bias < 0 ) delta_roll_bias = -0.001;
  } //endif delta_roll_bias
// soften this and make the roll_weight settable,
  pd->data.pointing.gyro_roll_bias -=
    pd->data.pointing.roll_weight*delta_roll_bias;
   delta_roll_bias=0.0;

  // Starting az bias correction, only use the mag for this...the other sensors
```

```
  // aren't as good...the tans is just as inaccurate and slower...the trackers
  // don't come often enough...we use them only for pointing corrections

    if ((pd->data.status.good_mag1 || pd->data.status.good_mag2)  &&
       (pd->data.status.using_mag1 || pd->data.status.using_mag2) &&
        !pd->data.status.slewing)
       {
            pd->data.status.do_mag_bias=TRUE;
        //only go here if the rate is not too large...
        if(fabs(pd->data.pointing.mags_rate)
< pd->data.pointing.mag_bias_rate_cap)
        {
        dt=pd->mag_new_fix.new_time -
pd->mag_new_fix.last_time;
        drift=pd->data.pointing.mags_rate -
pd->data.pointing.gyro2_az_rate;
        delta_az_bias =
drift/GYRO2_AZ_GAIN; //this is voltage
        } //endif mags_rate < mag_bias_rate_cap
       } //endif good/using mags
    if(fabs(delta_az_bias) > pd->data.pointing.mag_bias_clamp)
{
if(delta_az_bias > 0) delta_az_bias =
pd->data.pointing.mag_bias_clamp;
if(delta_az_bias < 0 ) delta_az_bias =
-1.0*pd->data.pointing.mag_bias_clamp;
   }
// Soften, and make az_weight settable,
   pd->data.pointing.gyro2_az_bias -= pd->data.pointing.mag_bias_weight*delta_az_bias;
   delta_az_bias=0.0; // must set this to 0 now, don't want to use it again.
    pd->data.status.do_mag_bias=FALSE;
  return((void *)pd);
} // end of find_gyro2_bias


void *apply_tracker_pointing_correction(void *arg)
  {
  heftdata *pd=(heftdata *)arg;
  //static unsigned char last_had_first_tracker_fix=FALSE;
  //float weight=pd->trackers.pointwt;
  //float old1, old2;
  //float az_error,el_error;
  float max_sensor_corr;
  float el_offset_correction_1, el_offset_correction_2;
  float mag_offset_corr;

  max_sensor_corr = pd->data.pointing.max_sensor_corr;
  //Note that we've eliminated the first jerking...but that
  // means we should set the offsets once everything is happy
  // we can do from ground but should allow unattended?? XXX

  // first lets do tracker 1
  if(pd->data.status.using_tracker1 &&
     pd->data.status.good_tracker1_attitude &&
     pd->data.status.new_tracker1_attitude &&
     !pd->data.status.slewing)
```

```
    {
pd->data.status.correcting_pointing_tracker1 = TRUE;
pd->data.status.correcting_pointing_tracker2 = FALSE;
pd->data.status.correcting_pointing_tans = FALSE;
pd->data.status.correcting_pointing_mag =  FALSE;
    // we have already calculated the errors elsewhere, weighted for times
    // when things were done.
pd->data.pointing.tans_tracker_counter = 0; // don't let the tans do nuthin
pd->data.pointing.mag_tans_counter = 0; // don't let the mag do nuthin

// First put a clamp on the corrections
      // Az
    if (fabs(pd->trackers.t1.new_aspect.e_gyro2_az) >
   pd->data.pointing.max_sensor_corr)
  {
  if(pd->trackers.t1.new_aspect.e_gyro2_az > 0)
pd->trackers.t1.new_aspect.e_gyro2_az = max_sensor_corr;
  if(pd->trackers.t1.new_aspect.e_gyro2_az < 0)
pd->trackers.t1.new_aspect.e_gyro2_az = -max_sensor_corr;
  }

    // Old elevation stuff.
      // El
      //if (fabs(pd->trackers.t1.new_aspect.e_gyro_el) >
     // pd->data.pointing.max_sensor_corr)
  //{
  //if(pd->trackers.t1.new_aspect.e_gyro_el > 0)
      // pd->trackers.t1.new_aspect.e_gyro_el = max_sensor_corr;
      // if(pd->trackers.t1.new_aspect.e_gyro_el < 0)
      // pd->trackers.t1.new_aspect.e_gyro_el = -max_sensor_corr;
      // }

      // Now apply them....suitably weighted
  // don't actually apply except on az. we track on the encoders, so don't want to use
      // trackers to correct the gyros, but rather the encoders.
      pd->data.pointing.gyro2_az +=
pd->data.pointing.tracker1_point_weight*pd->trackers.t1.new_aspect.e_gyro2_az;
//printf("gyro2_az %f and correction %f \n", pd->data.pointing.gyro2_az,
//                    pd->trackers.t1.new_aspect.e_gyro2_az);
     el_offset_correction_1 = pd->trackers.t1.new_aspect.el -
pd->trackers.t1.new_aspect.avg_enc1;
     if (el_offset_correction_1 > pd->data.pointing.max_sensor_corr) {
           el_offset_correction_1 = pd->data.pointing.max_sensor_corr;
     }
     if (el_offset_correction_1 < -pd->data.pointing.max_sensor_corr) {
           el_offset_correction_1 = -pd->data.pointing.max_sensor_corr;
     }

     el_offset_correction_2 = pd->trackers.t1.new_aspect.el -
pd->trackers.t1.new_aspect.avg_enc2;
     if (el_offset_correction_2 > pd->data.pointing.max_sensor_corr) {
           el_offset_correction_2 = pd->data.pointing.max_sensor_corr;
     }
     if (el_offset_correction_2 < -pd->data.pointing.max_sensor_corr) {
           el_offset_correction_2 = -pd->data.pointing.max_sensor_corr;
     }
```

```
    //printf("Encoder average1 %f, tracker el %f, encoder offset %f, encoder change %f\n",
//pd->trackers.t1.new_aspect.avg_enc1,
//pd->trackers.t1.new_aspect.el,
//el_offset_correction_1,
//pd->data.pointing.tracker1_point_weight*el_offset_correction_1);


      // need to fix encoder offsets so they'll drift in, must
     pd->data.pointing.enc_offset1 +=
     pd->data.pointing.tracker1_point_weight*el_offset_correction_1;
     pd->data.pointing.enc_offset2 +=
     pd->data.pointing.tracker1_point_weight*el_offset_correction_2;

     // Now the Tans
     // 4/19/05 KKM. We will no longer correct the TANS and instead believe
     // that it is always - when working - telling us the truth. If we need
     // to correct this value we will do it by uplink.
     //pd->data.pointing.tans_az_offset +=
 // pd->data.pointing.tracker1_point_weight*
 // (pd->trackers.t1.new_aspect.az - pd->data.pointing.tans_az);

     // we don't want to use this solution again
     pd->data.status.new_tracker1_attitude = FALSE;

     // Now the magnetometer
     // 4/19/05 KKM. These correction are now capped by the max sensor
     // correction to prevent large jerks.

     if (fabs(pd->trackers.t1.new_aspect.az - pd->data.pointing.mag1_az)
          > max_sensor_corr)
       {
       if ((pd->trackers.t1.new_aspect.az - pd->data.pointing.mag1_az)>0)
           mag_offset_corr = max_sensor_corr;
       if ((pd->trackers.t1.new_aspect.az - pd->data.pointing.mag1_az)<0)
           mag_offset_corr = -1.0*max_sensor_corr;
       }
     else mag_offset_corr = (pd->trackers.t1.new_aspect.az - pd->data.pointing.mag1_az);

     pd->data.pointing.mag1_az_offset +=
pd->data.pointing.tracker1_point_weight*mag_offset_corr;

     if (fabs(pd->trackers.t1.new_aspect.az - pd->data.pointing.mag2_az)
          > max_sensor_corr)
       {
       if ((pd->trackers.t1.new_aspect.az - pd->data.pointing.mag2_az)>0)
           mag_offset_corr = max_sensor_corr;
       if ((pd->trackers.t1.new_aspect.az - pd->data.pointing.mag2_az)<0)
           mag_offset_corr = -1.0*max_sensor_corr;
       }
     else mag_offset_corr = (pd->trackers.t1.new_aspect.az - pd->data.pointing.mag2_az);

     pd->data.pointing.mag2_az_offset +=
pd->data.pointing.tracker1_point_weight*mag_offset_corr;

     // This is the old uncapped magcode. KKM 4/19/05
```

```
     //pd->data.pointing.mag1_az_offset +=
 // pd->data.pointing.tracker1_point_weight*
     //(pd->trackers.t1.new_aspect.az - pd->data.pointing.mag1_az);
     //pd->data.pointing.mag2_az_offset +=
 // pd->data.pointing.tracker1_point_weight*
     //(pd->trackers.t1.new_aspect.az - pd->data.pointing.mag2_az);

     } //end of tracker 1

  // now lets do tracker 2
  if(pd->data.status.using_tracker2 &&
     pd->data.status.good_tracker2_attitude &&
     pd->data.status.new_tracker2_attitude &&
     !pd->data.status.slewing)
    {
pd->data.pointing.tans_tracker_counter =0; // don't let the tans do nuthin
pd->data.pointing.mag_tans_counter = 0; // don't let the mag do nuthin

    // we have already calculated the errors elsewhere, weighted for times
    // when things were done.

// First put a clamp on the corrections
      // Az
      if (fabs(pd->trackers.t2.new_aspect.e_gyro2_az) >
   pd->data.pointing.max_sensor_corr)
{
if(pd->trackers.t2.new_aspect.e_gyro2_az > 0)
pd->trackers.t2.new_aspect.e_gyro2_az = max_sensor_corr;
if(pd->trackers.t2.new_aspect.e_gyro2_az < 0)
pd->trackers.t2.new_aspect.e_gyro2_az = -max_sensor_corr;
}
    // El
    //  if (fabs(pd->trackers.t2.new_aspect.e_gyro_el) >
   // pd->data.pointing.max_sensor_corr)
//{
//if(pd->trackers.t2.new_aspect.e_gyro_el > 0)
    // pd->trackers.t2.new_aspect.e_gyro_el = max_sensor_corr;
    // if(pd->trackers.t2.new_aspect.e_gyro_el < 0)
    // pd->trackers.t2.new_aspect.e_gyro_el = -max_sensor_corr;
    // }

      // Now apply them....suitably weighted...but only to azimuth
      // not elevation.
    pd->data.pointing.gyro2_az +=
  pd->data.pointing.tracker2_point_weight*pd->trackers.t2.new_aspect.e_gyro2_az;

      // This piece of code has been copied from tracker 1 part so that they are
      // alike. This was not the case before, and as seen in the code above, this
      // allowed the for large encoder changes.KKM 11 april 2005
     el_offset_correction_1 = pd->trackers.t2.new_aspect.el -
pd->trackers.t2.new_aspect.avg_enc1;
     if (el_offset_correction_1 > pd->data.pointing.max_sensor_corr) {
           el_offset_correction_1 = pd->data.pointing.max_sensor_corr;
     }
     if (el_offset_correction_1 < -pd->data.pointing.max_sensor_corr) {
           el_offset_correction_1 = -pd->data.pointing.max_sensor_corr;
```

```
    }

    el_offset_correction_2 = pd->trackers.t2.new_aspect.el -
pd->trackers.t2.new_aspect.avg_enc2;
    if (el_offset_correction_2 > pd->data.pointing.max_sensor_corr) {
          el_offset_correction_2 = pd->data.pointing.max_sensor_corr;
    }
    if (el_offset_correction_2 < -pd->data.pointing.max_sensor_corr) {
          el_offset_correction_2 = -pd->data.pointing.max_sensor_corr;
    }

     // need to fix encoder offsets so they'll drift in, must
     pd->data.pointing.enc_offset1 +=
  pd->data.pointing.tracker2_point_weight*el_offset_correction_1;
     pd->data.pointing.enc_offset2 +=
  pd->data.pointing.tracker2_point_weight*el_offset_correction_2;

     // This piece of code goes with the elevation piece commented out above.
     // and is replaced by the piece just above. KKM 11. april 2005
     // pd->data.pointing.enc_offset1 +=
  // pd->data.pointing.tracker2_point_weight*(pd->trackers.t2.new_aspect.el -
     // pd->trackers.t2.new_aspect.avg_enc1);
     // pd->data.pointing.enc_offset2 +=
  // pd->data.pointing.tracker2_point_weight*(pd->trackers.t2.new_aspect.el -
     // pd->trackers.t2.new_aspect.avg_enc2);

    // Now the Tans offset correction
    // 4/19/05 KKM. We will no longer correct the TANS and instead believe
    // that it is always - when working - telling us the truth. If we need
    // to correct this value we will do it by uplink.
    //pd->data.pointing.tans_az_offset +=
 // pd->data.pointing.tracker2_point_weight*
 // (pd->trackers.t2.new_aspect.az - pd->data.pointing.tans_az);
    // don't use this solution again please

    pd->data.status.new_tracker2_attitude = FALSE;

    // Now the magnetometers.
    // 4/19/05 KKM. These correction are now capped by the max sensor
    // correction to prevent large jerks.

    if (fabs(pd->trackers.t2.new_aspect.az - pd->data.pointing.mag1_az)
         > max_sensor_corr)
      {
      if ((pd->trackers.t2.new_aspect.az - pd->data.pointing.mag1_az)>0)
          mag_offset_corr = max_sensor_corr;
      if ((pd->trackers.t2.new_aspect.az - pd->data.pointing.mag1_az)<0)
          mag_offset_corr = -1.0*max_sensor_corr;
      }
    else mag_offset_corr = (pd->trackers.t2.new_aspect.az - pd->data.pointing.mag1_az);

    pd->data.pointing.mag1_az_offset +=
pd->data.pointing.tracker2_point_weight*mag_offset_corr;

    if (fabs(pd->trackers.t2.new_aspect.az - pd->data.pointing.mag2_az)
         > max_sensor_corr)
```

```
       {
       if ((pd->trackers.t2.new_aspect.az - pd->data.pointing.mag2_az)>0)
           mag_offset_corr = max_sensor_corr;
       if ((pd->trackers.t2.new_aspect.az - pd->data.pointing.mag2_az)<0)
           mag_offset_corr = -1.0*max_sensor_corr;
       }
     else mag_offset_corr = (pd->trackers.t2.new_aspect.az - pd->data.pointing.mag2_az);

     pd->data.pointing.mag2_az_offset +=
pd->data.pointing.tracker2_point_weight*mag_offset_corr;

     // This is the old uncapped magcode. KKM 4/19/05
     //pd->data.pointing.mag1_az_offset +=
 // pd->data.pointing.tracker2_point_weight*
     //(pd->trackers.t1.new_aspect.az - pd->data.pointing.mag1_az);
     //pd->data.pointing.mag2_az_offset +=
 // pd->data.pointing.tracker2_point_weight*
     //(pd->trackers.t1.new_aspect.az - pd->data.pointing.mag2_az);

    } //end of tracker 2

  return((void *)pd);
} //end of apply tracker pointing


void *apply_tans_pointing_correction(void *arg)

 // only do this if the trackers are no good...they are much better.
  {
  heftdata *pd=(heftdata *)arg;
  // this corrects for tans pointing errors and also modifies it's
  // own offsets

  //float weight=0.5;
  float max_sensor_corr,e_gyro_az;

  max_sensor_corr = pd->data.pointing.max_sensor_corr;
  e_gyro_az = pd->tans_new_fix.new_e_gyro2_az;

  // first check the trackers and see if they are doing things for us
  if(!pd->trackers.t1.status.new_data && !pd->trackers.t2.status.new_data) {
// we have no tracker solutions so wait a bit
pd->data.pointing.tans_tracker_counter++;
}
  else{
pd->data.pointing.tans_tracker_counter = 0;
  }
   if(pd->data.pointing.tans_tracker_counter > 600)
// then no trackers for a minute or so
        // thus we, oh so reluctantly, begin to
        // do pointing corrections with the tans
{
  if(pd->data.status.new_tans_att &&
    !pd->data.status.slewing &&
    pd->data.status.using_tans)
    {
```

```
pd->data.status.correcting_pointing_tracker1 =  FALSE;
pd->data.status.correcting_pointing_tracker2 =  FALSE;
pd->data.status.correcting_pointing_mag =  FALSE;
pd->data.pointing.mag_tans_counter = 0; // don't let the mag do nuthin
    // clamp this...and get the sign right.
    if(fabs(pd->tans_new_fix.new_e_gyro2_az) > max_sensor_corr)
      {
      pd->tans_new_fix.new_e_gyro2_az = -1.0*(e_gyro_az<0)*max_sensor_corr+
                                        (e_gyro_az>0)*max_sensor_corr ;
      }
     //now apply it
     pd->data.pointing.gyro2_az +=
       pd->data.pointing.tans_point_weight*(pd->tans_new_fix.new_e_gyro2_az);
//please don't use this solution again....
pd->data.status.new_tans_att = FALSE;
} //end of if no trackers statement
  }
  return((void *)pd);
  }

void *apply_mag_pointing_correction(void *arg)
 // only do this if the trackers and tans are no good...they are much better.
  {
  heftdata *pd=(heftdata *)arg;
  // this corrects for mag pointing errors and also modifies the mag's
  // own offsets
  float max_sensor_corr,e_gyro_az;

  max_sensor_corr = pd->data.pointing.max_sensor_corr;
  e_gyro_az = pd->mag_new_fix.new_e_gyro2_az;

  // first check the tans and see if it is doing things for us
  if(!pd->data.status.new_tans_att) {
// we have no tans solutions so wait a bit
pd->data.pointing.mag_tans_counter++;
}
   if(pd->data.pointing.mag_tans_counter > 200)
// then no tans for 20 seconds or so
        // thus we do pointing corrections with the mag
{
pd->data.status.correcting_pointing_tracker1 =  FALSE;
pd->data.status.correcting_pointing_tracker2 =  FALSE;
pd->data.status.correcting_pointing_tans =  FALSE;
pd->data.status.correcting_pointing_mag = TRUE;
    if((pd->data.status.good_mag2 || pd->data.status.good_mag1) &&
      !pd->data.status.slewing && pd->data.status.do_mag_corr)
       {
     // clamp this...and get the sign right.
     if(fabs(pd->mag_new_fix.new_e_gyro2_az) > max_sensor_corr)
         {
              pd->mag_new_fix.new_e_gyro2_az = -1.0*(e_gyro_az<0)*max_sensor_corr+
                     (e_gyro_az>0)*max_sensor_corr ;
              }
     //now apply it
        pd->data.pointing.gyro2_az +=
        pd->data.pointing.mag_point_weight*pd->mag_new_fix.new_e_gyro2_az;
```

```
    // now fix the error signal to make sure we don't go trying to correct
    // bias for the pointing correction

    //pd->mag_new_fix.new_e_gyro2_az =
    //pd->mag_new_fix.new_e_gyro2_az*(1.0-pd->data.pointing.mag_point_weight);

         }
   } // end of if no tans
  return((void *)pd);
  }

// called by heft_loop.c
void *InitGyroBias(void *arg)
  {
  heftdata *pd=(heftdata *)arg;
  struct stat stbuf;
  int fd, nread;
  FILE *fp;
  unsigned char have_file;
  float biasarr[4];

  pd->data.status.using_stored_gyro_bias = FALSE;

  if(stat(GYRO_BIAS_FILENAME,&stbuf)==-1)
    {
    fd = creat(GYRO_BIAS_FILENAME,
       S_IWUSR | S_IRUSR | S_IWGRP | S_IRGRP);
    close(fd);
    have_file = FALSE;
    }
  else have_file=TRUE;

  fp = fopen(GYRO_BIAS_FILENAME,"r+");
  fd = fileno(fp);

  // if file already existed, read its contents
  if(have_file && USE_STORED_GYRO_BIAS && !pd->data.status.filling_gyro_default)
    {
    fseek(fp, 0, SEEK_SET);
    nread = read(fd, (void *)&biasarr[0], sizeof(biasarr));
    if(nread==sizeof(biasarr))
      {
      pd->data.pointing.gyro_el_bias = biasarr[0];
      pd->data.pointing.gyro_hybrid_bias = biasarr[1];
      pd->data.pointing.gyro2_az_bias = biasarr[2];
      pd->data.pointing.gyro_roll_bias = biasarr[3];
      pd->data.status.using_stored_gyro_bias = TRUE;
      //printf("heft_gyro.c: Gyro bias file found. ");
      //printf("V(EL,HYB,AZ,ROLL)=(%1.5f, %1.5f, %1.5f, %1.5f)\n",
        //pd->data.pointing.gyro_el_bias,
        //pd->data.pointing.gyro_hybrid_bias,
        //pd->data.pointing.gyro2_az_bias,
        //pd->data.pointing.gyro_roll_bias);
      }
     else pd->data.status.filling_gyro_default = TRUE;
```

```
    }
  if (pd->data.status.filling_gyro_default)
    {
  //printf("i am in gyro bias init\n");
    pd->data.pointing.gyro_el_bias = INIT_GYRO_EL_BIAS;
    pd->data.pointing.gyro_hybrid_bias = INIT_GYRO_HYBRID_BIAS;
    pd->data.pointing.gyro2_az_bias = INIT_GYRO2_AZ_BIAS;
    pd->data.pointing.gyro_roll_bias = INIT_GYRO_ROLL_BIAS;
    pd->data.status.using_stored_gyro_bias = TRUE;
    pd->data.status.filling_gyro_default = FALSE;
    pd=(heftdata *)store_gyro_bias(arg);
    // fix the gyro values
    pd->data.pointing.gyro2_az = pd->data.pointing.mag1_az;
    pd->data.pointing.gyro_el = pd->data.pointing.encoders;
    }

  pd->fpbias = fp;

  return((void *)pd);

  }

// called locally to write to bias file
// is no longer used while flying.
void *store_gyro_bias(void *arg)
  {
  heftdata *pd=(heftdata *)arg;
  static unsigned char first=TRUE;
  static unsigned short n=0;
  FILE *fp=pd->fpbias;
  int fd=fileno(pd->fpbias);
  float biasarr[4];
  float nwritten;
  if(!first && ((n % 20) == 0))
    {
    // write biases to start of bias file
    biasarr[0] = pd->data.pointing.gyro_el_bias;
    biasarr[1] = pd->data.pointing.gyro_hybrid_bias;
    biasarr[2] = pd->data.pointing.gyro2_az_bias;
    biasarr[3] = pd->data.pointing.gyro_roll_bias;
    fseek(fp, 0, SEEK_SET);
    nwritten=write(fd, (void *)&biasarr[0], sizeof(biasarr));
//printf("heft_gyro.c: bias=(%1.5f,%1.5f,%1.5f,%1.5f) nwritten=%d\n",
 //biasarr[0],biasarr[1],biasarr[2],biasarr[3],nwritten);
    }
  n++;
  first=FALSE;
  return((void *)pd);
  }
```

Bibliography

[1] Trimble Navigation Limited, 645 North Mary Avenue,Sunnyvale, CA 94086, *TANS VECTOR, GPS Attitude Determination System,Specification and User's Manual*, 2.0 ed., 1995. P/N 20997-00 Rev C.

[2] K. Dietz and et al. *Opt. Eng.* **41**, p. 2641, 2002.

[3] J. Chonko. PhD thesis, 2006. Columbia University.

[4] J. E. Koglin and et al. *proc. SPIE* **4851**, p. 607, 2003.

[5] C. P. Jensen, K. K. Madsen, H. C. Chen, F. E. Christensen, and E. Ziegler *Proceedings SPIE* **4851**, p. 724, 2003.

[6] K. K. Madsen and et al. *Proceedings SPIE* **5168**, p. 41, 2004.

[7] J. E. Koglin and et al. *proc. SPIE* **5168**, p. 1000, 2004.

[8] C. M. Chen and et al. *Proceedings SPIE* **5198**, p. 7, 2004.

[9] Private communication with F. E. Christensen, Danish National Space Center.

[10] Private communication with W. Craig, Lawrence Livermore National Laboratory.

[11] Private communication with M. Pivovaroff, Lawrence Livermore National Laboratory.

[12] R. M. Rogers, *Applied Mathematics in Integrated Navigation Systems, Second Edition*, 2.0 ed., 2003.

[13] INTEGRAL General Reference Catalog, http://isdcul3.unige.ch/Data/cat/.

[14] Private communication with F. A. Harisson, California Institute of Technology.

[15] J. E. Davis *AJ* **458**, p. 1010, 2001.

[16] Private communication with W. Baumgartner, California Institute of Technology.

[17] http://www.physics.nist.gov/PhysRefData/XrayMassCoef/ComTab/air.html.

[18] J. Wilms, M. Nowak, K. Pottschmidt, G. G. Pooley, and S. Fritz *A&A* **447**, p. 245, 2006.

[19] M. C. Weisskopf and et al. *ApJ* **536**, p. 81, 2000.

[20] A. N. Parmar and et al. *proc. SPIE* **6266**, p. 62661R, 2006.

[21] G. Hasinger and et al. *proc. SPIE* **6266**, p. 62661N, 2006.

[22] K. Joenson, P. Voutow, A. Szentgyorgyi, J. Roll, P. Gorenstein, P. H. ghøj, and F. Christensen *Appl. Opt.* **34**, p. 7935, 1995.

[23] H. Wolter, "Spiegelsysteme streifenden einfalls als abbildende optiken fur rontgensrtahlen," *Annalen der Physik* **10**, p. 94, 1952.

[24] H. Wolter, "Verallgemeinerte schwarzschildsche spiegelsysteme streifender reflexion als optiken fur rontgensrtahlen," *Annalen der Physik* **10**, p. 286, 1952.

[25] R. Petre and P. J. Serlemitsos, "Conical imaging mirrors for high-speed x-ray telescopes," *appl optics* **24**(12), 1985.

[26] P. H. Mao, F. A. Harisson, D. L. Windt, and F. E. Christensen, "Optimization of graded multilyaer designs for astronimical x-ray telescopes," *Appl. Opt.* **38**(22), 1999.

[27] L. Névot and P. Croce *Revue Phys, Appl* **15**, p. 761, 1980.

[28] T. W. Barba, S. Mrowka, and M. C. Hettrick, "Molybdenum-silicon multilayer mirrors for the extreme ultraviolet," *Appl Opt.* **24**, p. 883, 1985.

[29] K. Misaki and et al. *Appl. Opt.* **44**, p. 916, 2005.

[30] Private communication with C. P. Jensen, Danish National Space Center.

[31] D. H. Lumb, M. Bavdaz, F. E. Christensen, A. Dariel, P. Hoghoj, C. P. Jensen, M. Krumrey, K. K. Madsen, E. Ziegler, B. Albertin, S. Hedacq, M. Collon, and E.-J. Buis *proc. SPIE* **6266**, p. 626614, 2006.

[32] C. P. Jensen, K. K. Madsen, and F. E. Christensen *Experimental Astronomy, Springer* **20**, p. 93, 2005.

[33] D. L. Windt, S. Donguy, C. J. Hailey, J. Koglin1, V. Honkimaki, E. Ziegler, F. E. Christensen, and F. A. Harrison *Proc. SPIE* **5168**, p. 6, 2003.

[34] C. P. Jensen, K. K. Madsen, and F. E. Christensen *proc. SPIE* **6266**, p. 626611, 2006.

[35] F. E. Christensen, C. P. Jensen, K. K. Madsen, M. J. Pivovaroff, H. Chen, A. Dariel, and P. H. ghœj *proc. SPIE* **6266**, p. 626611, 2006.

[36] W. Press, S. Teukolsky, W. Vetterling, and B. Flannery, *Numerical Recipes*, Cambridge, 2'nd ed., 1992.

[37] A. Laor *MNRAS* **246**, p. 369L, 1990.

[38] A. C. Fabian, M. J. Rees, L. Stella, and N. E. White *mnras* **238**, p. 729, 1989.

[39] K. Nandra and K. A. Pounds *MNRAS* **268**, p. 405N, 1994.

[40] C. S. Reynolds *MNRAS* **286**, p. 513, 1997.

[41] P. W. Guilbert and M. J. Rees *MNRAS* **233**, p. 475, 1988.

[42] I. M. George and A. C. Fabian *MNRAS* **249**, p. 352, 1991.

[43] K. Iwasawa and et al *MNRAS* **282**, p. 1038, 1996.

[44] S. Vaughan and A. C. Fabian *MNRAS* **348**, p. 1415, 2004.

[45] K. Nandra, I. M. George, R. F. Mushotzky, T. J. Turner, and T. Yaqoob *ApJ* **477**, p. 602, 1997.

[46] P. Uttley, S. Vaughan, and M. McHardy *ApJ* **568**, p. 610E, 2002.

[47] A. R. Green, I. M. McHardy, and H. J. Letho *MNRAS* **265**, p. 664, 1993.

[48] M. D. et al *MNRAS* **350**, p. 745, 2004.

[49] R. W. Goosmann, B. Czerny, M. Mouchet, G. Ponti, M. Dovciak, V. Karas, A. Rozinska, and A.-M. Dumont *A&A* **454**, p. 741, 2006.

[50] K. Nandra, I. M. George, R. F. Mushotzky, T. J. Turner, and T. Yaqoob *ApJ* **523**, p. L17, 1999.

[51] T. J. Turner, S. B. Kraemer, I. M. George, J. N. Reeves, and M. C. Bottorff *ApJ* **618**, p. 155T, 2005.

[52] T. Yaqoob *ApJ* **593**, p. 85, 2003.

[53] K. A. Pounds, J. N. Reeves, K. L. Page, C. A. Wynn, and P. T. O'Brien *MNRAS* **342**, p. 1147, 2003.

[54] K. Leighly, R. F. Mushotzky, T. Yaqoob, H. Kunieda, and R. A. Edelson *MNRAS* **238**, p. 729, 1996.

[55] G. Matt, G. C. Perola, F. Fiore, M. Guainazzi, F. Nicasatro, L. Piro, and M. Cappi *A&A* **363**, p. 863, 2000.

[56] L. Miller, T. J. Turner, J. N. Reeves, D. Porquet, K. Nandra, and M. Dovciak *A&A* **453L**, p. 13M, 2006.

[57] S. T. Meyers, D. Rusin, and C. D. Fassnacht *ApJ* **117**, p. 2565, 1999.

[58] S. Toft, J. Hjorth, and I. Burud *AA* **153**, p. 205, 2004.

[59] D. Rusin, M. Norbury, A. D. Biggs, D. R. Marlow, N. J. Jackson, Browne, I. W. A., P. N. Wilkinson, and S. T. Myers *MNRAS* **330**, p. 205R, 2002.

[60] R. B. Metcalf *AJ* **580**, p. 696, 2002.

[61] The Chandra X-ray Center, ChaRT, http://cxc.harvard.edu/chart/threads/index.html.

[62] K. Pedersen *ApJL* **In Press**, 2007.

[63] A. Eliasdottir, J. Hjorth, S. toft, I. Burud, and D. Paraficz *ApJS* **166**, p. 443, 2006.

[64] Dickey and Lockman *ARAA* **28**, p. 215, 1990.

[65] K. A. Pounds, K. Nandra, H. H. Fink, and F. Makino *MNRAS* **267**, p. 193, 1994.

[66] K. A. Pounds and K. L. Page *MNRAS* **360**, p. 1123, 2005.

[67] K. A. Pounds and S. Vaughan *MNRAS* **368**, p. 707, 2006.

[68] K. A. Weaver, J. H. Krolik, and E. A. Pier *AJ* **498**, p. 213, 1998.

[69] R. Edelson, T. J. Turner, K. Pounds, S. Vaughan, A. Markowitz, H. Marshall, P. Dobbie, and R. Warwick *ApJ* **568**, p. 610E, 2002.

[70] M. Dovciak, V. Karas, and T. Yaqoob *ApJS* **153**, p. 205, 2004.

[71] A. Laor and H. Netzer *MNRAS* **238**, p. 897, 1989.

[72] A. Laor, H. Netzer, and T. Piram *MNRAS* **242**, p. 560, 1990.

[73] J. M. Bardeen, W. H. Press, and S. A. Teukolsky *ApJ* **178**, p. 347, 1972.

[74] X. Dai, G. Chartas, E. Agol, M. W. Bautz, and G. P. Garmire *AJ* **589**, p. 100, 2003.

[75] N. Ota, N. Inada, and et al *ApJL* **0**, p. 0, 2006.

[76] G. Chartas, M. Eracleous, and et al *ApJ* **606**, p. 78, 2004.

[77] L. G. Parratt *Phys.rev.* **95**(2), p. 359, 1954.

[78] J. Als-Nielsen and D. McMorrow, *Elements of Modern X-ray Physics*, Wiley, New York, 2001.